UNIVERSITY OF OKLAHOMA

GRADUATE COLLEGE

RATIONAL DESIGN AND ADVANCED CHARACTERIZATION OF NANOCOMPOSITE GLASSY POLYMER MEMBRANES WITH ENHANCED STABILITY AND SELECTIVITY IN AGGRESSIVE GAS AND LIQUID SEPARATIONS

A DISSERTATION

SUBMTTED TO THE GRADUATE FACULTY

in partial fulfillment of the requirements for the

Degree of

DOCTOR OF PHILOSOPHY

By LUCAS COLLIN CONDES

Norman, Oklahoma

2025

Downloaded from SHAREOK. Persistent Handle URL: https://hdl.handle.net/11244/341747

RATIONAL DESIGN AND ADVANCED CHARACTERIZATION OF NANOCOMPOSITE GLASSY POLYMER MEMBRANES WITH ENHANCED STABILITY AND SELECTIVITY IN AGGRESSIVE GAS AND LIQUID SEPARATIONS

A DISSERTATION APPROVED FOR THE
SCHOOL OF SUSTAINABLE, CHEMICAL, BIOLOGICAL, AND MATERIALS ENGINEERING

BY THE COMMITTEE CONSISTING OF

Dr. Michele Galizia, Chair

Dr. Reza Foudazi

Dr. Ngoc T. Bui

Dr. Mrinal C. Saha

©Copyright by Lucas C. Condes 2025

All Rights Reserved.

ACKNOWLEDGEMENTS

There are many people I need to thank and recognize for being a part of my journey to becoming a scientist. I am incredibly lucky to have had wonderful friends, colleagues, and teachers along the way. Firstly, I would like to thank my advisor, Dr. Michele Galizia, for his unwavering and unconditional support of myself and my colleagues in our scientific and personal growth. From my first contact with him and his lab, I recognized the unique creative and collaborative spirit that he fosters, and I'm excited to have contributed and taken a part in this lab. I also thank my committee, Dr. Ngoc Bui, Dr. Reza Foudazi, and Dr. Mrinal Saha for their service and encouragement.

Going back a bit, I'd like to thank the teacher who ignited my passion for chemistry and science: the late Mr. Jackie Caseboldt (*aka*, "Mr. K"). Mr. K was my high school chemistry teacher, and his endless chemistry jokes, interesting labs, and thought-provoking lectures drew me into the world of science. He was the first teacher to recognize my potential as a scientist, challenging me to learn and to be curious, and it is the attitude and habits I formed during my time as his student that I attribute to my eventual success.

I'd like to thank my undergraduate research advisors and mentors: Dr. Jimmy Lawrence at LSU, who, as an assistant professor, gave a generous amount of his time to mentoring and teaching me- an undergraduate student, in their first year of research, there for 10 weeks on REU funding- all about the world of polymer chemistry and how to think about the broader context in research; Dr. Kayla Foley, a PhD student at OU at the time, who mentored me and taught me the value of careful and methodical scientific investigation; and Dr. Jeffrey Harwell, who served as a wise and

humble role model of an accomplished scientist. My undergraduate research mentors laid a strong foundation for my PhD journey.

I'm grateful for the generous mentors in graduate school who helped me: Dr. Naga Rama Kothapalli, who met with me every week my first semester of graduate school to review and help me refine my GRFP application- I owe my success in getting the GRFP to your dedication to mentorship; Laura Matesanz-Niño, a visiting PhD student from Spain, who taught me many of the foundational polymer synthesis techniques I needed for my dissertation; Youngjoo Lee and Dr. Ryan Lively at Georgia Tech, who graciously hosted me and taught me about the design, construction, and operation of their membrane organic solvent crossflow apparatus and thin film composite membrane fabrication; and Dr. Preston Larson at the Samuel Roberts Noble Microscopy Laboratory, who is a stellar teacher and expert in microscopy sciences, and helped me develop a comfortable expertise in SEM that was instrumental in my studies.

Many collaborators came together to make this possible: at the University of Valladolid Spain and/or the National Institute of Carbon: Angel Lozano, Cristina Álvarez, Leoncio Garrido, and Laura Matesanz-Niño; at CSIRO: Anita Hill, Cara Doherty, and Durga Acharya; at OSU: Dr. Margaret Eastman; at OU: Alberto Striolo, Tran Le, and Caitlin Hodges; and at the University of North Texas: Marco Buongiorno Nardelli. Thank you for all the dedicated studies and access to techniques that have expanded the scientific impact of our works.

I would like to thank the friends and colleagues who collaborated with me in the Membrane Lab at OU: Will Box, Matthew Webb, Harold Ly, Aditi Gali, Shivam Patel, Adriana Landry, Bryce Goodin, Keen Nguyen, Luke Wilson, Jing Deng, Grant Smith, Salome Tavera, Minh Pham, Ghiath Al Hafez, and Shiwen Dong.

Additionally, I'd like to thank Andrew D'Amico and Buck Sullivan for their shop work expertise and for taking the time to teach me shop skills, which were both instrumental for my research projects and left me with practical skills for my future.

I want to thank my parents, Anne and Caesar Condes, who always tried to answer my unending questions and created a home where my curiosity could flourish. Their investment in my hobbies, education, and upbringing have allowed me to become someone who approaches problems with a curious and playful mindset.

Finally, I'd like to thank my partner, Kendall, who has supported me and cheered me on for the past five years. You have been my shelter and foundation in shaky times, the reason why I strive, and my most trusted companion.

My PhD and the work in it would not have been possible without the support of the National Science Foundation (NSF), both through the NSF CAREER program (Grant No. 2043648) and the NSF GRFP program (Grant No. 10557390). Thank you, as well, to the School of Sustainable Chemical, Biological and Materials Engineering (SCBME), and the University of Oklahoma for creating opportunities for education and innovation.

TABLE OF CONTENTS

ACKNOWLEDGEMENTS ..... **iv**
LIST OF TABLES ..... **xii**
LIST OF FIGURES ..... **xv**
ABSTRACT ..... **xxiii**
Chapter 1. Motivation, Introduction, and Theory **1**
1.1. Motivation 1
1.2. Small Molecule Transport in Dense Polymer Membranes 5
1.2.1. The Solution-Diffusion Model 5
1.2.2. Separation Mechanisms 7
1.2.3. Transport in Glassy vs. Rubbery Polymers 8
1.2.4. Partial Immobilization 10
1.2.5. Energetics of Sorption 11
1.3. Challenges and Limitations of Membrane Technology 12
1.3.1. The Permeability-Selectivity Tradeoff 12
1.3.2. Plasticization 14
1.3.3. Physical Aging 15
1.4. Nanocomposite Membranes 16
1.4.1. Interfacial Compatibility 16
1.4.2. Porous Polymer Networks 16
1.5. Polymer Crosslinking 18
1.6. Summary of Dissertation Chapters 20
Chapter 2. Inter-crosslinked spirocyclic mixed matrix membranes exhibiting enhanced gas permeability, selectivity, and plasticization resistance **23**
2.1. Abstract 23
2.2. Introduction 24
2.3. Experimental Methods 29
2.3.1. Materials 29
2.3.2. Synthesis of PIM-1 29
2.3.3. Acid Hydrolysis of PIM-1 30
2.3.4. Synthesis of Triptyene-Isatin Porous Polymer Network 30
2.3.5. Membrane Fabrication 31
2.3.6. Structural Characterization 32

2.3.7. Sorption/Transport Measurements and Plasticization Study 32
2.4. Results and Discussion 33
2.4.1. Synthesis and Characterization of PIM-1 33
2.4.2. Membrane Formation and Thermal Crosslinking 36
2.4.3. Pure Gas Permeability and Selectivity 43
2.4.4. Pure Gas Sorption, Diffusion, and Dual Mode Modeling 45
2.4.5. CO_2-induced Plasticization Study 50
2.5. Conclusions 56
Chapter 3. Elucidating the Molecular Mechanisms by which Porous Polymer Networks Affect Structure, Aging Propensity, and Selectivity of Microporous Glassy Polymer Membranes using a Multiscale Approach 59
3.1. Abstract 59
3.2. Introduction 60
3.3. Experimental Methods 63
3.4. Results and Discussion 64
3.4.1. Membrane Fabrication, Characterization, and Modeling 64
3.4.2. Physical Aging Study 69
3.4.3. Free Volume Analysis and Possible Mechanism of PTMSP-PPN Physical Interaction 72
3.4.4. ^{13}CP/MAS NMR Spectroscopy 76
3.4.5. Pure Gas Transport Properties 78
3.5. Conclusions 84
Chapter 4. Thin-film nanocomposite membranes based on microporous polymers with long-term organic solvent separation performance stability exhibiting facile formation of a solvent-resistant interlayer 86
4.1. Abstract 86
4.2. Introduction 87
4.3. Experimental Methods 89
4.3.1. Materials 89
4.3.2. Material Characterization 89
4.3.3. Free-Standing CPIM Membrane Casting 90
4.3.4. Porous Support Fabrication 90
4.3.5. Thin-Film Composite Membrane Fabrication 91
4.3.6. Organic Solvent Nanofiltration (OSN) and Organic Solvent Reverse Osmosis (OSRO) Tests 91

4.4. Results and Discussion 95
4.4.1. Defect-free, inter-crosslinked thin film composite membranes 95
4.4.2. Highly Solvent-Resistant Nanofiltration Performance 99
4.4.3. Performance After Extended Solvent Exposure 103
4.4.4. Formation of a Solvent-Resistant Interfacial Layer 109
4.4.5. Probing Interlayer Transport Behavior 115
4.5. Conclusions 121
Chapter 5. Summary and Recommendations for Future Research 122
5.1. Summary 122
5.2. Future Work 124
Appendix A 127
A1. Materials 127
A2. Synthesis of PIM-1 127
A3. Synthesis and Properties of Triptycene-Isatin Porous Polymer Network 128
A4. Membrane Casting 130
A5. Fourier-Transform Infrared Spectroscopy 132
A6. Scanning Electron Microscopy 132
A7. Thermogravimetric Analysis/Mass Spectrometry (TGA-MS) and DSC 136
A8. Nuclear Magnetic Resonance (NMR) Spectroscopy 138
A9. Powder Brunauer-Emmett-Teller (BET) Analysis 138
A10. Elemental Analysis 139
A11. Gel Fraction Tests 139
A12. Gel Permeation Chromatography 140
A13. Pure Gas Permeation Measurements 141
A14. Pure Gas Sorption Measurements 142
A15. TGA of CPIM and Triptycene Isatin PPN 143
A16. FTIR-ATR of MMM30 and IcMMM30 144
A17. Pure Gas Permeability, Diffusivity, and Solubility 145
A18. Partial Immobilization Fittings 147
A19. Comparison of CO_2 Plasticization Pressure Points 148
Appendix B 150
B1. Materials 150
B2. Synthesis of Triptycene-isatin porous polymer network 150

B3. Structural Characterization Techniques 151
B3.1. Fourier Transform Infrared Spectroscopy (FTIR) 151
B3.2. Thermogravimetric Analysis (TGA) 151
B3.3. Scanning Electron Microscopy (SEM) 152
B3.4. Positron Annihilation Lifetime Spectroscopy (PALS) 152
B3.5. Density and Fractional Free Volume Measurements 153
B4. Membranes Fabrication 153
B5. FTIR Spectra Discussion 154
B6. Positron Annihilation Lifetime Spectroscopy Results 155
B7. Molecular Dynamics Simulation Procedures and Details 156
B7.1. Simulation Setup 156
B7.2. Molecular Models and Force Fields 159
B7.3. Simulation Algorithms 160
B7.4. Self-Diffusion Coefficients 161
B8. Experimental Gas Transport and Physical Aging Measurement Protocol 161
B9. Fitting of the Permeability/Fractional Free Volume Relationship 164
B10. Estimation of Uncertainty for Fitted Parameters 165
B11. Solid State ^{13}C T_1 NMR Relaxation Measurements 166
B12. Permeability, Diffusivity, and Solubility Results 168
B13. Thermogravimetric Analysis 173
Appendix C 174
C1. Chemicals and Materials 174
C1.1. Materials for Synthesis 174
C1.2. Support Materials 174
C1.3. Transport Test Materials 174
C2. Basic Material Properties 175
C3. Material Characterization Methods 176
C3.1. Fourier-Transform Infrared Spectroscopy 176
C3.2. X-Ray Diffraction 176
C3.3. Positron Annihilation Lifetime Spectroscopy 177
C3.4. Scanning Electron Microscopy 178
C3.5. Combustion Elemental Analysis 179
C3.6. Ninhydrin Assay 179

C3.7. Liquid Dilation Measurements 180
C4. Organic Solvent Crossflow Apparatus Description 180
C5. OSN and OSRO Performance Data 182
C6. OSN Performance Stability at 578 Da 185
C7. Mechanism of Free Amine Formation 185
C8. Data for Toluene Permeability-Sorption Correlation 187
C9. Elemental Analysis Results 189
C10. Solution-Diffusion Prediction of Toluene Permeabilities 190
C11. Normalized Toluene Liquid Dilation Curves 194
C12. Correlation of Dilation to Solvent Molar Volume 195
References 198

LIST OF TABLES

Table 1. Elemental analysis, in terms of atomic weight percents, of the synthesized PIM-1 and CPIM. The degree of hydrolysis is the percentage of nitrile groups in PIM-1 that have been converted into carboxylic acids. Sulfur (S) was tested to determine whether residual sulfuric acid was retained in the final product..... 35

Table 2. Summary of the dual mode model fittings. Error bars were obtained using the Jackknife resampling technique. Parameters were fit with respect to penetrant fugacity and were constrained using the technique reported in [23,122]. 49

Table 3. Comparison of the pressures, permeabilities, and concentrations at which CO_2-induced plasticization occurs in CPIM, CPIMTT, MMM30, IcMMM30 and state of the art materials. Literature data are taken from ref. [129]..... 54

Table 4. Struik Model parameters for the various PTMSP / PPN blends considered. Parameter uncertainties were found using the Hessian matrix method described in Appendix B, Section B10. 72

Table 5. Experimental densities and fractional free volume values of neat PTMSP, the PTMSP-5PPN blend, the PTMSP-20PPN blend, and neat PPN. Errors are calculated using linear error propagation..... 73

Table 6. Summary of the dual mode parameters for the samples considered in this study. Uncertainties were calculated using the Jackknife resampling technique. 82

Table 7. Calculated resistances to toluene transport for the various layers in the developed TFC membranes..... 120

Table A1. Properties of the Triptycene-Isatin PPN..... 130

Table A2. Calculated gas permeation properties of the pure triptycene-isatin PPN using the effective medium model approach [46]..... 130

Table A3. Thicknesses, densities, and fractional free volumes (FFVs) of the membranes used for permeability and sorption measurements. Errors were calculated using linear error propagation [202]..... 131

Table A4. Gel fractions of various membranes after soaking in THF. Errors were calculated using linear error propagation [202]. 140

Table A5. Pure gas permeability at 1 atm and 35 °C. Errors were calculated using the standard error of linear regression followed by linear error propagation [202]. 145

Table A6. Pure gas solubility coefficients given by the dual-mode sorption model at 1 atm and 35 °C. Error bars were calculated using linear error propagation [89,204]. 145

Table A7. Pure gas diffusivity coefficients at 1 atm and 35 °C calculated using experimental permeability data and dual-mode solubility coefficients. Errors were calculated using linear error propagation[202] 146

Table A8. Partial immobilization analysis for CH_4 and CO_2, as well as the calculated fractional diffusivity through the Langmuir's mode. 147

Table A9. Review of CO_2 plasticization pressures for the materials considered in this study, as well as state of the art materials. 148

Table B1. Results of the PALS analysis for PTMSP, PTMSP-5PPN, PTMSP-15PPN and neat PPN, including orthopositronium (oPs) lifetimes (τ_3, τ_4 and τ_5), intensities (I_3, I_4 and I_5), and average free volume element radii (R_3, R_4 and R_5). 155

Table B2. Simulated densities of the neat PTMSP and PTMSP-PPN blend. 159

Table B3. Data used for the empirical permeability fitting. 165

Table B4. Transport properties of PTMSP and PTMSP-5PPN at 35°C (308.15 K) and 1 atm. Uncertainty was determined using the standard deviation from 3-4 measurements per point... 169

Table C1. Material properties of the CPIM batch used in this study. 175

Table C2. Material properties of the triptycene-isatin PPN batch used in this study. 175

Table C3. OSN performance of fresh TFC membranes. Δp = 31 bar, ambient temperature, <3% stage cuts, with <500 ppm styrene oligomers. Error bars are calculated using linear error propagation. 183

Table C4. OSN performance of TFC membranes as in Table C3 after 6 months exposure to toluene, using the same testing conditions. Error bars are calculated using linear error propagation. *183*

Table C5. OSRO performance of samples after ~18 months exposure to toluene. Error bars are calculated using linear error propagation. *184*

Table C6. Hydrocarbon rejection of IcMMM30 after ~21 months of exposure to toluene in a crossflow permeation test of a dilute 9-component mixture (1 mol% each dissolved in toluene, Δp = 50 bar). The permeance of IcMMM30 during this test was 0.038 L m^{-2} h^{-1} bar^{-1} *184*

Table C7. Experimental datapoints used to validate the toluene permeability-sorption correlation. *187*

Table C8. Combustion elemental analysis results for supports crosslinked with varying crosslinking solutions, before and after washing repeatedly with 50:50 v:v toluene/methanol solutions to remove adsorbed diamine. *189*

Table C9. Polymers, solvent uptakes, and volumetric dilation data used to validate the derived expression used to convert dilation to solvent uptake. *197*

LIST OF FIGURES

Figure 1. Qualitative depiction of the difference between glassy and rubbery polymers using representative relationships between the specific volume and temperature.[22] 9

Figure 2. Structure of PIM-1..... 13

Figure 3. Structure of the triptycene-isatin porous polymer network...... 18

Figure 4. Structure of carboxylated PIM-1 (CPIM)...... 19

Figure 5. Synthetic routes to (A) PIM-1, (B) CPIM, and (C) triptycene isatin PPN. (D and F) defect-free CPIM membranes, (E) a defect-free MMM30 membrane, (G) the synthesized triptycene isatin powder, (H) color comparison of a MMM30 membrane before (top) and after (bottom) thermal treatment, and (I) demonstration of CPIMTT's insolubility after soaking in THF for 24h...... 29

Figure 6. Molecular structures with numbered carbon assignments and lettered proton assignments for (A) PIM-1 and (B) CPIM. (C) ATR-FTIR, (D) 1H NMR, and (E) ^{13}*C NMR spectra of the synthesized materials are shown.*..... 34

Figure 7. Study of the thermal treatment by (A) FTIR-ATR of MMM30 and IcMMM30, (B) ^{13}*C-CP/MAS NMR spectra of CPIM, CPIMTT, MMM30 and IcMMM30, (C) TGA mass loss analysis of MMM30 and IcMMM30, and (D) mass spectrometry signals corresponding to the TGA experiments in (C).*..... 38

Figure 8. (A) Proposed crosslinking mechanism, with the final C-C crosslinked structures highlighted in blue. (B) Artwork depicting the structure of IcMMM30...... 42

Figure 9. Upper bound plots for the (A) H_2/CH_4 *(35°C, 10 atm) and (B)* CO_2/CH_4 *(35°C, 1 atm) gas pairs. State of the art polymer membranes are denoted in gray and include cellulose acetate (CA)* [88]*, polysulfone (PSf)* [111,112]*, polycarbonate (PC)* [113]*, PIM-1* [23]*, Matrimid®* [114,115]*, and Pebax* [116]*. Previously reported PIM-based composite membranes are shown as green triangles: 1- PIM-1/POSS* [117]*, 2- PIM-1/CC3* [118]*, 3- PIM-1/COF(SNW-1)* [119]*, 4- PIM-1/pDCX* [120]*, 5- PIM-1/UiO-66-*NH_2 [56]*, 6 – CPIM/UiO-66-*NH_2 [56]*, 7 – CPIM/diacetyl biphenyl PPN* [121]*.*..... 43

Figure 10. Pure (A) CO_2 and (B) CH_4 sorption isotherms in CPIM, CPIMTT, MMM30 and IcMMM30. (C) Pure CO_2 solubility coefficients and CO_2/CH_4 ideal solubility-selectivity. (D) Pure CO_2 diffusivity and CO_2/CH_4 ideal diffusivity-selectivity. (E) Henry's and Langmuir's mode CO_2/CH_4 diffusivity-selectivity (i.e., $DDCO2DDCH4$ and $DHCO2DHCH4$). *47*

Figure 11. CO2 plasticization test for (A) untreated samples (i.e., CPIM and MMM30) and (B) thermally treated samples (i.e., CPIMTT and IcMMM30). (C) Review of CO2 plasticization pressures for the materials reported in this study, as well as state of the art materials. Stars represent crosslinked films, and half-filed symbols are thin films (< 1 μm). Data for non-crosslinked film are from ref. [125], and data for crosslinked and mixed-matrix films are tabulated in Table A9. ..... *52*

Figure 12. Isosteric heats of sorption for (A) CH_4 and (B) CO_2 in CPIM, CPIMTT, MMM30, and IcMMM30. Continuous lines denote experimentally determined values, and the shaded region surrounding each line is the experimental error determined, at each concentration, via linear error propagation and the standard error of linear regression [128]. *54*

Figure 13. Plasticization CO_2 permeability vs. plasticization pressure and plasticization CO_2 concentration in several glassy polymers of interest in membrane separations. IcMMM30 outperforms other materials in all three axes. *56*

Figure 14. Chemical structure of PTMSP (A) and the triptycene-isatin PPN (B). Scanning Electron Micrographs of the membrane cross-section after fracture in liquid nitrogen: PTMSP (C), PTMSP-5PPN (D), and PTMSP-20PPN (E) (scale bar: 10 μm). (F) Results from Positron Annihilation Lifetime Spectroscopy (PALS) plotted as pore size distributions for PTMSP, PTMSP-5PPN, and PTMSP-15PPN. *66*

Figure 15. Simulation snapshots prepared with densities matching the experimental data for PTMSP (A) and PTMSP-20PPN (B). Color code: cyan (carbon), white (hydrogen), and orange (silicon). For better visual distinction, in (B), atoms belonging to the PPN are colored in purple. Box side lengths are approximately 8 nm. *68*

Figure 16. Physical aging of approximately ~20-40 μm thick films of PTMSP, PTMSP-5PPN, and PTMSP-20PPN blends, tracked via pure N_2 permeability measurements conducted at 35°C

(308.15 K) and 1.4 atm (A), where the dotted line are the permeabilities calculated from Eqs. 1 and 2. The corresponding reduction in free volume is also shown (B). A modified Struik model[136,160] was fit and plotted for each sample; the results are shown using dotted lines. The fitted values for the modified Struik model are provided in Table 4. 69

Figure 17. (A) Fractional free volumes of the PTMSP-PPN blends vs. blend composition. The dotted line is the ideal volumetric mixing rule. A MD simulation snapshot of a PTMSP-PPN interaction is shown in (B), where the white molecules are PTMSP, and the yellow/blue are individual PPN particles. As can be seen, PTMSP chains are partially adsorbed on the PPN molecularly rough surface. 74

Figure 18. Spin-lattice relaxation times measured in air for the carbons in PTMSP (for both neat PTMSP and PTMSP-20PPN). The labels for carbons A, B, C indicated on the structure of PTMSP correspond to the accordingly labeled plots. Relaxation times measured under pure N_2 are shown in Figure B6. 78

Figure 19. (A) Pure N_2, CH_4, and CO_2 permeability and (B) ideal gas selectivity for CO_2/CH_4, CO_2/N_2, and CH_4/N_2 at 1 bar and 35 °C (308.15 K), and C) Infinite dilute sorption coefficients for N_2, CH_4, and CO_2 at 35 °C (308.15 K). (D) Radial distribution functions calculated from MD simulated trajectories, between sorbed gases (i.e., CO_2 and CH_4) and the Si atoms in PTMSP and PTMSP-PPN blends, as well as between the gases and the N atoms in PTMPS-PPN blends. Simulations were run for neat PTMSP and PTMSP-20PPN. Heat density maps of E) PPN nitrogen atoms, F) CO_2 gas molecules, and G) CH_4 gas molecules found within a 2D slice of PTMSP-20PPN from MD simulations. H) Experimentally determined CO_2 and CH_4 diffusion coefficient changes in PTMSP-5PPN (red) and PTMSP-20PPN (green) relative to neat PTMSP, along with MD predictions for PTMSP-20PPN (purple). Experimental uncertainty was calculated using linear error propagation.[173] 79

Figure 20. Membrane materials, TFC membrane fabrication, and FVE properties. (A) Materials used to fabricate membranes, as well as sample nomenclature. (B) Depiction of the two types of crosslinks resulting from thermal treatment in the CPIM-PPN systems. (C) SEM image of the IcMMM5 membrane depicting the selective layer coated on the porous Matrimid® support. The inlay plot for (C) depicts the trend of selective layer thickness with PPN weight loading. XRD

spectra of (D) bulk non-crosslinked films and (E) crosslinked films. (F) PALS of non-crosslinked films (top panel), crosslinked films (middle panel), and comparison between a CPIM and CPIMTT membrane (bottom panel). *97*

Figure 21. (A) Polystyrene oligomer rejection (i.e., MWCO) curves in toluene. Data for PIM-1[186] *and SBAD-1*[177] *are shown for comparison. (B) OSN trade-off curve for polystyrene oligomers in toluene. All data in this plot uses polystyrene oligomers with the exception of Torlon®, which used other aromatic hydrocarbons, but is included as a representative comparison.*[19,177,186–189] *(C) Comparisons of toluene uptake and molecular weight cutoff among membranes, including those reported in this study, and state-of-the-art membranes* *101*

Figure 22. (A) Polystyrene oligomer rejection curves in toluene comparing initial performance to 6-month performance. (B) OSN trade-off curve demonstrating changes in thermally treated samples exhibiting different filler loading. (C) Performance of selected samples after extended toluene exposure for ~18 months in the OSRO toluene/triisopropylbenzene separation. The feed contained 1 mol% TIPB in toluene. Gray symbols stand for state-of-the-art materials.[14,15,17,19,177,178,183] *(D) Percent changes in permeance after the 6-month stability test. (E) Percent changes in rejection for the 266 Da oligomer after the 6-month stability test.* *104*

Figure 23. (A) Depiction of the interlayer hypothesis, where free amines couple with the acid groups in CPIM to form a locally immobilized 'interlayer' with solvent-resistant properties. (B) Chemical structures and solutions in ethanol of ninhydrin before and after reaction with primary amines. (C) Ninhydrin test on non-crosslinked supports (i.e., neat Matrimid®) and crosslinked supports. *110*

Figure 24. (A) Procedure used to fabricate supports with different free amine content, as well as the corresponding amine loading. Adsorbed amine refers to amine content that is not chemically bound to the polymer at either end, and is just physically adsorbed to the support. (B) Comparison of polystyrene oligomer rejection profiles in toluene for CPIM TFC membranes derived from the two supports. (C) Comparison of the selectivity and permeance of the CPIM TFC membranes derived from the two supports. (D) Correlation of intrinsic toluene permeability with toluene weight fraction in the membrane across different polymer types and membrane configurations. Half-filled symbols are thin films and filled symbols are bulk (free-standing)

films. A table containing all of the correlation information and datapoints is provided in Appendix C, Section C8. 112

Figure 25. (A) Fabrication procedure for the interlayer proxy materials. (B) ATR-FTIR spectra of CPIM, DACPIM, and DACPIMTT highlighting the chemical changes occuring during interlayer formation. (C) Toluene liquid dilation of the bulk selective layer materials (CPIM, CPIMTT) and the interlayer proxy materials (DACPIM, DACPIMTT). (D) Interlayer transport resistance modeling demonstrating the requisite interlayer volumetric dilation given the assumed interlayer thickness to match the experimentally observed permeance anomaly. 116

Figure A1. SEM micrographs depicting cross-sectional images of (A),(B) CPIM; (C),(D) CPIMTT; (E),(F) MMM30; (G),(H) IcMMM30, and (I),(J) triptycene-isatin PPN particles dispersed on a silicon wafer. 134

Figure A2. (Top) SEM micrograph of an MMM30 membrane with the line scan and point analyses indicated by tick marks along the scan direction. (Bottom) A line graph showing the relative C,N,O, and Ir (sputtercoating substrate) molar % along the length of the line scan. ... 135

Figure A3. DSC thermograms of the four membranes studied, during the third heating cycle. The minor bump in the data at 70°C is an artifact due to contamination of the furnace. 137

Figure A4.Thermogravimetric mass loss, and mass loss first derivative of neat CPIM (casted membrane) and the synthesized triptycene-isatin PPN. 143

Figure A5.The left panel shows FTIR-ATR of MMM30 and IcMMM30, as appears in the main manuscript, and the middle and right panels are magnifications of the same spectra in the single-bond C-H and O-H stretching regions and C-O-C stretch regions, respectively. 144

Figure A6. (A) CH_4 and (B) H_2 permeability vs. fugacity at 35 °C. Error bars from linear error propagation are too small to show. Fugacity was calculated using the Peng-Robinson equation of state. 145

Figure A7. Partial immobilization fittings for (A) CH_4 and (B) CO_2. Error bars were calculated by linear error propagation using the standard error of linear regression[202] and the dual-mode errors given in Table 2 in the main manuscript. 147

Figure B1. A) Chemical structure of PTMSP. B) Synthesis route and chemical structure of triptycene-isatin PPN. *151*

Figure B2. FTIR spectra of the PTMSP-PPN blends in range A) 600-3750 cm^{-1} and B) 1300-2000 cm^{-1}. *155*

Figure B3. Atomistic models of (A) a single PTMSP polymer chain (101-mer) and (B) a PPN molecule with 22 triptycene units and 45 isatin units. Color code: cyan (C), white (H), red (O), blue (N), and orange (Si). *157*

Figure B4. Snapshots showing the final configurations of (A) neat PTMSP and (B) the PTMSP-PPN. Color code: cyan (C), white (H), and orange (Si). For better visual distinction, atoms belonging to the PPN are colored periwinkle blue. The snapshots reveal the presence of voids within the structures, indicating a porous and amorphous morphology in both membranes. These membranes are not uniformly packed. *159*

Figure B5. Exponential fit of permeability to inverse fractional free volume for the PTMSP and PTMSP-PPN systems. *164*

*Figure B6. Spin-lattice relaxation times measured in pure N_2 for the carbons in PTMSP. The labels for carbons **A**, **B**, **C** indicated on the structure of PTMSP correspond to the accordingly labeled plots.* *167*

Figure B7. (A) Ideal diffusivity selectivity and (B) ideal solubility selectivity for CO_2/CH_4, CO_2/N_2, and CH_4/N_2 at 1 bar and 35 °C (308.15 K). *168*

Figure B8. Permeability isotherms of CO_2 (A), CH_4 (B), and N_2 (C) in PTMSP (blue), PTMSP-5PPN (red), and PTMSP-20PPN (green) in Barrer as a function of pure gas pressure, ranging up to 20 atm. Error bars were calculated via the standard deviation from 3-4 measurements. *169*

Figure B9. Concentration averaged diffusivity coefficients of CO_2 (A) and CH_4 (B) in PTMSP (blue) and PTMSP-5PPN (red) in cm2s *as a function of pure gas pressure in atm. Error bars were found via linear error propagation and values were calculated via the solution-diffusion model from experimentally available permeability and solubility data.* *170*

Figure B10. Sorption isotherms of CO_2 (A) and CH_4 (B) in PTMSP (blue) and PTMSP-5PPN (red) in $cm^3STP cm^3Pol.$ as a function of pure gas pressure in atm. Error bars were found via linear error propagation.[89] 171

Figure B11. Kinetic (left Y-axis; Dashed lines/Circles) and thermodynamic factors (right Y-axis; Solid lines/Squares) of CO_2 (A), CH_4 (B) and N_2 (C) in PTMSP (blue), PTMSP-5PPN (red), and PTMSP-20PPN (green) as a function of pure gas pressure in atm. Error bars were found via linear error propagation.[89] 172

Figure B12. TGA thermogram of PTMSP, PPN, PTMSP-5PPN, and PTMSP-20PPN blends, heated at 10 °C/min (10 K/min) from 25-800℃ (298.15-1073.15 K). 173

Figure C1. X-ray diffractograms of neat CPIM and PPN powder. 177

Figure C2. Images of the synthesized triptycene-isatin particles dispersed on a silicon wafer. 179

Figure C3. (A) Setup used to track liquid dilation of polymer samples. (B) Image from a CPIMTT dilation run in toluene...... 180

Figure C4. (A) flow diagram and (B) picture of the organic solvent crossflow apparatus. 181

Figure C5. Trends in TFC membrane performance with thermal treatment, filler loading, and solvent exposure time. TFC membranes toluene permeance of (A) fresh samples and (B) after 6 months exposure to toluene. Rejection of the 266 Da Styrene oligomer of (C) fresh samples and (D) after 6 months exposure to toluene...... 182

Figure C6. Changes in rejection for the 578 Da styrene oligomer after the 6-month stability test. 185

Figure C7. Mechanism of free amine formation during support crosslinking...... 186

Figure C8. Solution-diffusion a priori predictions of experimental toluene permeabilities...... 193

Figure C9. Volumetric dilation curves of CPIM, CPIMTT, DACPIMTT, and DACPIM in liquid toluene plotted against a normalized time parameter. The purpose of normalization is to create kinetically comparable curves (since thicker samples will dilate more slowly)...... 194

Figure C10. Validation of the derived relationship between volumetric dilation and incorporated solvent volume. The labelled point for CPIM was cross-validated using gravimetric uptake measurements and optical liquid dilation measurements. 196

ABSTRACT

Polymer membranes are transforming modern separation technologies by providing substantial energy and cost advantages over traditional thermal-based processes. Among them, glassy polymers stand out for their outstanding molecular size-sieving capabilities. However, three fundamental limitations continue to hinder their widespread use: the permeability–selectivity tradeoff, physical aging, and plasticization. Overcoming these interconnected challenges is critical for enabling robust, high-performance membrane systems for chemically aggressive industrial separations.

To address these issues, this work reports a class of nanocomposite membranes in which glassy polymers are blended with a rigid porous organic filler—the triptycene–isatin porous polymer network (PPN). This PPN is an optimized, highly crosslinked network material developed by Iglesias et al.[1] in 2018 that demonstrates extreme rigidity due to the incorporation of triptycene, a highly rigid and contorted 3D monomer; high BET surface areas (~790 m^2 g^{-1}), and an excellent distribution of micropores that enable size-sieving separation performance. Importantly, PPNs are fully organic, allowing compatibility with organic polymers and facile fabrication of defect-free nanocomposite membranes.

Triptycene-isatin PPNs were synthesized and processed into nanoparticles exhibiting sizes of 150-700 nm, then incorporated into two different polymers. The first polymer used was carboxylated polymer of intrinsic microporosity 1 (CPIM), a rigid ladder polymer with pendant carboxylic acid groups. While CPIM has excellent separation performance, it suffers from plasticization by CO_2 at relatively low pressures (5-10 atm). To solve this problem, the CPIM-based nanocomposite membranes containing up to 30 wt.% PPN were fabricated and subjected to a 200 °C treatment for 24h under vacuum, resulting in the CPIM crosslinking to itself as well as

to the PPN particles by radical decarboxylation of the acid groups in CPIM, resulting in what is termed "inter-crosslinked membranes" due to the CPIM/PPN interfacial crosslinking. It was found that particle incorporation alone nor crosslinking of neat CPIM significantly enhanced plasticization resistance. Only inter-crosslinked membranes, which exhibit the polymer/particle interfacial crosslinks, had significantly enhanced plasticization resistances, with these membranes exhibiting no signs of plasticization up to CO_2 partial pressures of 50 atm. In addition, these PPN-containing membranes had enhanced gas separation performance relative to neat CPIM. The individual and synergistic roles of PPN incorporation and crosslinking were elucidated using a variety of material characterization and transport measurement techniques.

The second polymer that was blended with the triptycene-isatin PPN was poly(1-trimethylsilyl-1-propyne) (PTMSP), a highly permeable, microporous glassy polymer that exhibits rapid physical aging and that, as such, has been used, over the years, as a model polymer for aging studies. Thus, PPN incorporation into PTMSP (5-20 wt. %) was studied and found to slow physical aging: over the course of three weeks, neat PTMSP lost 41 % of its N_2 permeability, while PTMSP blended with 5 wt. % PPN lost only 15% of its N_2 permeability. Positron Annihilation Lifetime Spectroscopy (PALS), free volume measurements, cross polarization/magic angle spinning (CP/MAS) ^{13}C NMR T1 measurements, transport measurements and molecular dynamics (MD) simulations revealed that an adsorptive interaction at the PTMSP-PPN interface suppressed backbone carbon relaxations, slowing the collapse of larger micropores, and that decreases in gas diffusivity due to micropore-blocking induced by PPN incorporation can be offset by increasing PPN loading, resulting in an increased sorption capacity.

The exceptional rigidity and stability of the inter-crosslinked CPIM/PPN membrane platform prompted further exploration for challenging and aggressive chemical separations, particularly for

organic solvent nanofiltration (OSN) and organic solvent reverse osmosis (OSRO) in hydrocarbon media. Hydrocarbons severely soften and plasticize glassy polymers, limiting their long-term stability and separation efficiency, yet CPIM/PPN membranes were able to fractionate hydrocarbons with greater efficiencies than observed in conventional polymeric membranes in OSN tests and were exceptionally stable, exhibiting enhanced OSN performance after 6 months of exposure to liquid toluene. Remarkably, after almost two years of exposure to liquid toluene, inter-crosslinked CPIM/PPN membranes still exhibited excellent hydrocarbon fractionation performance in OSRO tests. As a matter of fact, the material platform discovered in this project exhibits unprecedented long-term stability in the harshest chemical environments, creating promising opportunities for fundamental understanding and translational purposes. In addition to the inter-crosslinking, a novel interfacial interaction between primary amine functionalities on the porous support and the acid groups in the CPIM were found to form a thin interfacial layer that significantly enhances the overall membrane selectivity. Transport modeling, liquid dilation tests, and correlation of literature data were used to elucidate the transport mechanism of these membranes, offering insights into future optimization and utilization of the chain immobilization and functionalization approaches developed in this work.

Overall, this dissertation combines synthesis, advanced characterization, transport modeling, and long-term stability studies to develop a mechanistic understanding of how porous polymer networks (PPNs) can stabilize and enhance the separation performance of glassy polymer membranes in aggressive chemical environments. The findings establish design principles for creating nanocomposite membranes that simultaneously achieve high selectivity, permeability, and resistance to aging and plasticization. These insights aid the broader goal of expanding the

implementation of polymer membranes in chemically aggressive gas and liquid separation environments, providing a foundation for more energy-efficient industrial separations.

Chapter 1. Motivation, Introduction, and Theory

1.1. Motivation

Energy is the pivotal resource that has enabled industrialization and modernization over the past ~250 years. It has enabled the production of massive quantities of chemicals, minerals, and consumer goods; efficient long-distance transport of people and materials; and the continual advancement and development of advanced technologies. For over a hundred years, civilization has exponentially increased its energy expenditure, with an average 2.3% yearly growth rate, all while increasing efficiency, with energy intensity (measured in terms of energy produced normalized by economic expenditure) declining at a rate of approximately 1% per year.[2,3] The continual decline in energy intensity is directly tied to the efficiency of physical technology: the development of more efficient lighting, chips, energy production methods, cars, etc., all collectively contribute to this 1% improvement in energy intensity per year. All physical technologies, however, have theoretical efficiency limits: light-emitting diodes, in use today, are 10x more efficient than their incandescent predecessors, yet are only ~4x below the theoretical efficiency limit, meaning that further development of such technologies will have diminishing returns.[3] Continuing this trend of technological efficiency improvement is critical to ensure a sustainable and just future for all. While many other technologies are far along the path towards maximal efficiency, certain categories are still operating far below their efficiency limit. The industrial separation of chemicals is one of those categories. Many liquid chemical mixtures utilize thermal-based distillation or evaporation techniques to separate or concentrate compounds, techniques which are estimated to use approximately 50 times the theoretically required energy

limit. Membrane-based separations, in which pressure is used to force select chemicals through thin films, only use approximately 1.25x the theoretical required energy limit.[4]

One question that arises from this discussion, then, is: why haven't membranes been ubiquitously implemented in all sorts of chemical separations? In broad context, membranes and other sustainable separation technologies (such as adsorption-based technologies) appear to be slowly transforming and intensifying separations, but implementation has been dependent on steady research and development efforts combined with pinpoint technological breakthroughs relevant only to select applications. Reverse-osmosis desalination of seawater using membranes is one example: widespread adoption and the resulting dominant position of this technology hinged on developments in fabrication of scalable thin-film manufacturing techniques, material discovery, and practical engineering advancements.[5,6] In 2019, global production of desalinated water using reverse-osmosis membranes accounted for 69% of all production, with 65.5 million m^3/day produced, delivering fresh water to millions of people.[7] A similar development story took place for membrane-based gas separations, which as of today represents a >$1 billion/year industry for separations such as hydrogen recovery, N_2 production, natural gas treatment, and light hydrocarbon vapor recovery.[8]

While the stories of membrane-based water desalination and gas separations demonstrate the stellar success of membranes in significantly improving the energy intensity and sustainability of certain separations, there are a large number of potential applications that membranes have not broken into.[4,8] One of the most cited reasons for this lack of implementation is that current membrane materials are not productive, selective, and stable enough to be technologically superior to the currently implemented methods. One recurring pattern with a number of these applications is that harsh operating conditions tend to degrade the separation performance of polymer

membranes (which are foreseeably the dominant membrane material given their scalability), a phenomenon known as *plasticization*. Plasticization is commonly observed in applications involving high partial pressures of CO_2, condensable hydrocarbon vapors, high temperature applications, or separations involving organic solvents.[4,8–10] Additionally, many of the high-performing membranes that exhibit the performance desired to be technologically competitive are intrinsically unstable, and their performance decays over time due to a phenomenon known as *physical aging*. Thus, to expand the array of viable membrane applications, material and membrane scientists must tackle the issue of engineering membranes to perform under highly plasticizing conditions and membranes with excellent and stable performance.

Some of the most highly plasticizing separations are organic solvent separations, namely, membrane-based organic solvent nanofiltration (OSN) and organic solvent reverse osmosis (OSRO). These are relevant to applications such as pharmaceutical recovery from solution, refining of crude oil, recovery of organic solvents from chemical synthesis, and purification of chemical feedstocks and fine chemicals.[4,11–13] Recent efforts and studies have shown that both nanocomposite membranes (i.e., membranes with some sort of nanoparticle blended into the polymer matrix) and crosslinked membranes have the most potential to resist plasticization, with some of these membranes successfully demonstrating their potential in applications such as refining crude oil or separating benzene derivatives from each other.[10,14–19] However, the number of these studies is relatively limited, and there is an extremely wide variable space regarding nanoparticle design and function, polymer structure, fabrication approach, and crosslinking strategy. While some strategies perform better than others, they often require complex synthesis or fabrication approaches, potentially limiting their manufacturing scalability and impact on the environment. From a naïve perspective, more studies are required to gain understanding of the

material design and performance space, and further efforts in balancing membrane fabrication complexity with performance in aggressive environments are required. Additionally, the long-term separation behavior in these aggressive applications is not widely studied, which is problematic given that glassy polymers are non-equilibrium materials that can exhibit slow yet dramatic changes in separation performance over long time periods.

To simultaneously attempt to produce a simply fabricated and high-performance membrane system for use in highly plasticizing environments that demonstrates long-term stability, while also individuating the fundamental structural properties responsible for performance, is the primary goal of this dissertation. Crosslinked nanocomposite membranes are designed by combining a spirocyclic ladder polymer- the carboxylated polymer of intrinsic microporosity-1 (CPIM)- with high surface area, rigid, entirely organic porous polymer networks (PPNs) composed of the monomers triptycene and isatin. The effect of PPN incorporation, polymer-polymer crosslinking, and polymer-PPN crosslinking are elucidated in terms of transport performance, long-term stability, and plasticization susceptibility. The triptycene-isatin PPN was also studied for its potential to inhibit physical aging and demonstrated a significant hindering of physical aging in a model microporous polymer, poly(1-trimethylsilyl-1-propyne) (PTMSP). Final application-oriented OSN and OSRO tests are performed to determine the success of the material design approach and effect of each variable in contributing to the membrane performance, providing structure-property insights, novel membrane chemistries, and new benchmark methodologies for studying long-term membrane performance to the material design space for next-generation membrane applications.

1.2. Small Molecule Transport in Dense Polymer Membranes

1.2.1. The Solution-Diffusion Model

The permeability of a component *i* (P_i) in dense membranes is defined as follows:

$$P_i = \frac{J_i}{\left(\frac{\Delta p_i}{l}\right)} \quad (1)$$

Where J_i is the molar flux of component *i* through the membrane, Δp_i is the partial pressure difference of component *i* between the high-pressure (i.e., 'upstream') and low-pressure side (i.e., 'downstream') of the membrane. The partial pressure difference of *i* translates to a chemical potential gradient along which component *i* diffuses through as it transports through the membrane. For the case of gas transport in dense polymers (i.e., polymers with no permanent pores), the mechanism of transport abides by the solution-diffusion mechanism:

$$P_i = \bar{D}_i \times S_i \quad (2)$$

where $\bar{D}_i$ is the concentration-averaged diffusion coefficient and S_i is the solubility coefficient of component *i* in the membrane given by the fugacity-normalized penetrant concentration in the polymer phase (i.e., *C*), so that $S = C/f$. Thus, the overall rate of transport of a molecule through a membrane is a product of how quickly it moves through the membrane ($\bar{D}_i$) and how much of it sorbs within the membrane (S_i). Equation 2 is derived assuming that the low-pressure side of the membrane is at a perfect vacuum, i.e., the concentration in the polymer at the downstream side of the membrane ≈ 0, an assumption which can be satisfactorily met in most lab-scale membrane gas permeation tests.

The case for solvent (i.e., liquid) transport through membranes, though still abiding by the solution-diffusion mechanism, is complicated by the fact that both faces of the membrane are in

contact with solvent mixtures, meaning that the downstream concentration in the membrane is almost never nonexistent. For the case of the solution-diffusion model for solvent transport through membranes, we begin formulation with Fick's law of diffusion:

$$J_i = -\rho D_i \frac{d\omega_i}{dx} \tag{3}$$

where J_i is the diffusive flux of penetrant i in the membrane with respect to the center of mass of the polymer-penetrant system, ρ is the mass density of the solvent/membrane mixture, ω_i is the solvent mass fraction in the membrane, and x is the coordinate direction along which transport is occurring, assuming a unidirectional gradient that runs along the membrane thickness.[20]

Since ω_i can reach significant values in solvent-swollen polymers, any flux in the polymer-penetrant system will carry the laden solvent with it. This is expressed in the 'frame-of-reference' correction[20]:

$$n_i = J_i + \omega_i n_i \tag{4}$$

where n_i is the total flux in the membrane system. Combining the two above equations and integrating from $x = 0$ to $x = l$, the following expression can be derived:

$$n_i l = \rho \bar{D}_i \ln\left(\frac{1-\omega_i|_{x=l}}{1-\omega_i|_{x=0}}\right) \tag{5}$$

where $\bar{D}_i$ is the average diffusion coefficient of penetrant i in the membrane. This can be combined with the definition of permeability:

$$P_i = \frac{\rho \bar{D}_i \, ln\left(\frac{1-\omega_i|_{x=l}}{1-\omega_i|_{x=0}}\right)}{\Delta p} \tag{6}$$

Although not as elegant and simple as the solution-diffusion formulation for gas transport, Equation 6 demonstrates that solvents transport is fundamentally controlled by the product of diffusive and solubility contributions.

For the case in both gas and liquid separations, permeability is an intrinsic material property of the membrane being used, making it a powerful tool for comparing the performance of different membrane materials.

1.2.2. Separation Mechanisms

The ability of a membrane to separate compound A from compound B can be measured using the selectivity (α_{AB}), which is defined as the permeability ratio of A to B:

$$\alpha_{AB} = \frac{P_A}{P_B} = \frac{D_A}{D_B} \times \frac{S_A}{S_B} \tag{7}$$

where $(\frac{D_A}{D_B})$ and $(\frac{S_A}{S_B})$ are the diffusivity-selectivity (i.e. size-sieving ability) and the solubility-selectivity, respectively, which emerge due to the substitution of the solution-diffusion relationship into the definition for permeability. Selectivity can be defined using the ratios of the pure permeability values (i.e., the P_A and P_B values measured using only their respective component), or real selectivity values (i.e., the P_A and P_B values determined when separating a real mixture of A and B using the membrane). In mixtures, the presence of one compound may affect the diffusion and solubility behavior of other compounds, resulting in a complex relationship between mixture composition and selectivity. Understanding the transport and separation behavior of complex multicomponent mixtures is essential to translating membrane processes into industrial processes capable of replacing conventional separation processes.

Thus, the diffusivity-selectivity and solubility-selectivity characterize the two fundamental mechanisms by which membranes can separate compounds: by distinguishing them by size or

shape (diffusivity-selectivity) or by their tendency to sorb within the polymer the membrane is made of (solubility-selectivity). Various classes of membrane materials have emerged to leverage each of these mechanisms.

1.2.3. Transport in Glassy vs. Rubbery Polymers

Polymer membranes can be broadly classified into rubbery and glassy polymers, both of which abide by the solution-diffusion mechanism of small molecule transport, but yet exhibit vastly different transport properties. Glassy polymers are defined as polymers which exist below their glass transition temperature (T_g), which is a temperature that marks when a polymer experiences a step change in its coefficient of thermal expansion during cooling or heating (Figure 1). Explained from the perspective of cooling a polymer, this step change occurs as the thermal energy required for the polymer to collapse to its equilibrium specific volume exceeds the thermal energy available, and thus the polymer becomes kinetically sluggish in approaching its theoretical equilibrium volume. As a glassy polymer is further cooled below its T_g, the chain mobility further decreases, and the polymer further deviates from its equilibrium volume, resulting in a large quantity of what is called "excess free volume" to be captured in the polymer matrix. These two qualities- a rigid polymer matrix (characterized by low chain mobility) and significant excess free volume- are what distinguishes the transport properties of glassy polymers from those of rubbery polymers.[21]

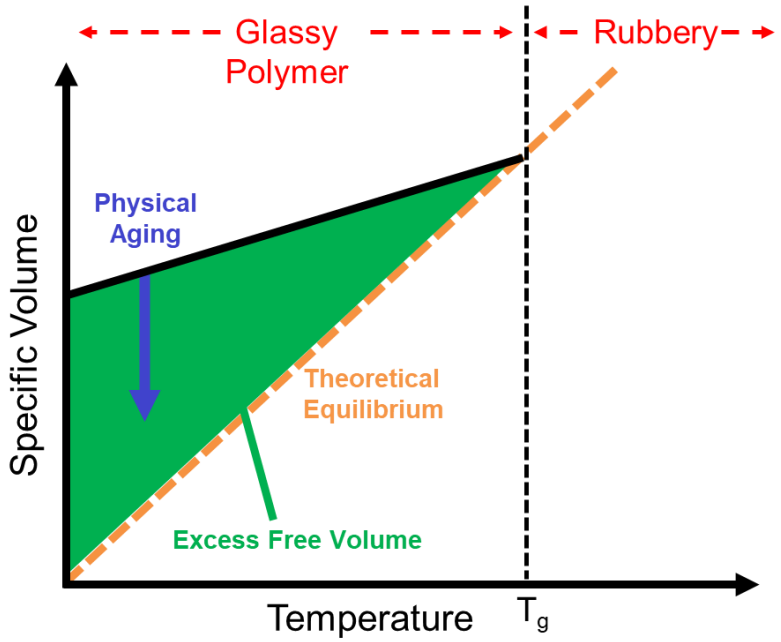


Figure 1. Qualitative depiction of the difference between glassy and rubbery polymers using representative relationships between the specific volume and temperature.[22]

In the case of gas separations, glassy polymers typically have higher permeabilities than rubbery polymers due to their higher sorption capacity for gases.[21] This is captured in the dual mode sorption/transport model. This model describes small molecules sorption and transport in glassy polymers by envisioning the polymer phase as a heterogeneous medium (i.e, Henry's and Langmuir's contributions):

$$C = k_D\, f + \frac{C_H'\, b\, f}{1 + b\, f} \tag{8}$$

where C is the penetrant concentration in the polymer, f is the fugacity in the external gas phase, k_D is the Henry's solubility coefficient, C_H' is the Langmuir sorption capacity, and b is the Langmuir affinity parameter [23,24].

In contrast to glassy polymers, rubbery polymers only have a Henry's mode contribution to their gas sorption, which demonstrates the overall solubility advantage that glassy polymers have

over rubbery polymers that translates to their overall higher permeability. In terms of diffusivity, rubbery polymers, having a higher chain mobility, tend to have higher diffusivity coefficients than glassy polymers, yet this does not overcome the large solubility difference between glassy and rubbery polymers.[21] Despite glassy polymers having higher permeabilities, they suffer from physical aging, which will be discussed further in Section 1.3.3.

The separation mechanisms of glassy and rubbery polymers differ significantly, as well. Due to having overall high diffusion coefficients for various gases, the diffusivity-selectivity in rubbery polymers is lackluster, resulting in the solubility differences between gases to control their overall permeability, resulting in the solubility selectivity being the primary separation mechanism in rubbery membranes.[25] Glassy polymers, however, exhibit the opposite trend: their rigid structure reduces the diffusion coefficients of gases, yet creates greater differences in the diffusion coefficients of different gases, resulting in the primary separation mechanism for glassy polymers relying on diffusivity-selectivity.[26] Thus, the difference in dominating separation mechanism between glassy and rubbery polymers allows for each respective membrane type to be applied to applications in which one mechanism is more favorable over another. Glassy polymers are highly sought after for harsh separation environments (such as high-pressure gas processing or organic solvent separations), since they can be engineered to resist such conditions by creating very rigid polymer architectures, and are thus the topic for the remainder of the dissertation.

1.2.4. Partial Immobilization

Besides equilibrium gas uptake, the dual-mode model has also been adapted to describe the diffusion of gases in each of the two modes, assuming the existence of a distinct contribution of penetrant mobility from each sorbed mode in the polymer rather than a single representative

diffusion coefficient [24,27]. Therefore, according to the partial immobilization model, the gas permeability P can be expressed as follows:

$$P = k_D\, D_D + \frac{C'_H\, b\, D_H}{1 + b\, f} \tag{9}$$

where D_D and D_H are the Henry mode and Langmuir mode diffusion coefficients, respectively. The ratio of the two diffusion coefficients is given as the parameter F, where $F = D_H/D_D$. A value of $F = 0$ represents the 'total immobilization' case wherein gases sorbed in Langmuir sites do not contribute to the measured diffusivity, whereas a value of $F = 1$ corresponds to 'no immobilization' wherein the diffusion behavior of gases does not depend on which sorbed mode the gas occupies.

1.2.5. Energetics of Sorption

Fundamental insights into the penetrant-polymer and penetrant-penetrant interactions responsible for the membrane transport behavior can be gained by examining the energetics of penetrant sorption in the membrane material. Isosteric heats are the enthalpy of sorption at constant penetrant concentration in the polymer phase. The enthalpy of sorption is the difference in enthalpy between a penetrant in the bulk gas phase and the same penetrant when condensed in the polymer phase. The isosteric heat is related to energetic changes due to condensation of the penetrant, interaction of the penetrant with the polymer, and interaction of the penetrant with other penetrants already in the polymer phase [28]. In this work, isosteric heats are used to base the membrane plasticization propensity on a rational thermodynamic basis. Isosteric heats of sorption can be determined by collecting gas sorption isotherms at multiple temperatures, as follows [28]:

$$\left(\frac{d(\ln p)}{d\left(\frac{1}{T}\right)}\right)_C = \frac{\Delta H_S}{R} \tag{10}$$

where p is the pressure at which the penetrant concentration C is achieved, T is the temperature, R is the gas constant, and ΔH_S is the isosteric heat.

1.3. Challenges and Limitations of Membrane Technology

1.3.1. The Permeability-Selectivity Tradeoff

The ideal membrane would exhibit a maximally high combination of selectivity and permeability values. However, it has been found that permeability and selectivity exhibit an intrinsic tradeoff, wherein membranes that are highly selective demonstrate low permeability, and membranes that are highly permeable demonstrate low selectivity. This relationship was first empirically observed for gas separation membranes by Lloyd Robeson[29] in 1991 and was later found to be fundamental in nature by Benny Freeman in 1999.[30] A collection of membranes were found to sit along a frontier with maximal permeability and selectivity values, which became known as the "Robeson Upper Bound" and is formulated for two components i and j as follows:

$$\alpha_{ij} = kP_i^n \tag{11}$$

Where k and n are found to be constants relating to the physical properties of components i and j. Over time, membrane scientists have worked to develop materials that push the upper bound frontier, resulting in the 1991 upper bound line being superseded by a 2008 upper bound relationship, and recently a 2019 upper bound was established. Additionally, the permeability-selectivity tradeoff has been shown to apply in organic solvent-based liquid separations, as well.[9,15,17]

One dominant molecular engineering approach that enabled the continual "pushing up" of the upper bound was to reduce the flexibility of the polymer backbone while simultaneously incorporating motifs that hindered molecular packing of the polymer matrix. Polymer backbone

flexibility is greatly reduced by designing backbones that consist of fused ring systems (resulting in the concept of 'ladder polymers'), and packing was hindered by incorporating bulky side groups (e.g., -CF_3) and introducing contortion sites in the polymer backbone. These contortion sites orient rigid monomer structures in various directions in 3D space, resulting in an overall more 'open' molecular structure for gas transport that was still selective due to the highly rigid nature of the polymers. One of the earliest examples of this approach is the polymer of intrinsic microporosity-1 (PIM-1), which is also one of the most widely studied polymers in membrane science.[31] The structure in PIM-1 is shown in Figure 2. PIM-1 exhibits repeating units of 7 fused rings joined by spirocyclic carbon centers, which orient the sequential fused rings approximately 90 degrees from each other in space, resulting in hindered packing.

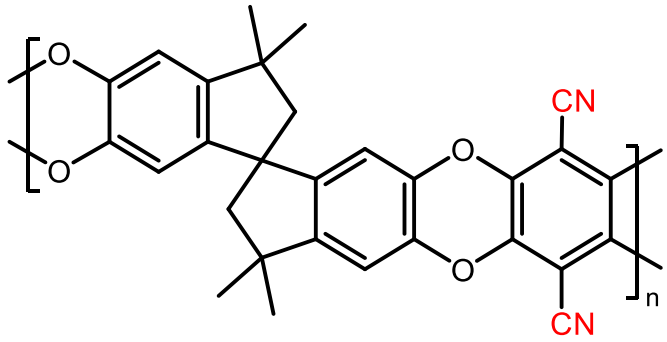


Figure 2. Structure of PIM-1.

The abovementioned molecular engineering approaches, demonstrated in principle by PIM-1, paved the way forward to membranes with continually higher permeability/selectivity combinations. Post-functionalization of PIM-1 through the chemistry of its nitrile groups (-CN) has been a popular approach to tailor and improve on its favorable properties. Though maximizing both permeability and selectivity is desirable, as will be discussed in the following sections, other relevant issues such as plasticization and long-term stability must be simultaneously considered

and addressed. As laid out in Chapter 2 of this dissertation, functionalization of PIM-1 forms the basis for creating high-performance polymers that can also overcome such issues.

1.3.2. Plasticization

As diffusion in polymers is an activated process depending on transient thermal fluctuations in the polymer medium,[30] it is highly sensitive to changes in polymer relaxation dynamics. Stiffer polymers tend to have lower diffusivity coefficients, yet higher diffusivity selectivity values, as in accordance with the upper bound tradeoff relationship.[29,30,32] However, highly condensable penetrants such as CO_2, C_{2+} hydrocarbons, alcohols, and other solvents, when sorbed into polymers, tend to "soften" the polymer matrix, increasing the chain mobility. This consequently dilates the polymer matrix and increases the polymer chain mobility, significantly raising the diffusivity coefficients of all incorporated components while simultaneously lowering the diffusivity selectivity between components, as well.[8–10] This phenomenon is known as penetrant-induced plasticization, and is one of the primary challenges restricting the broad implementation of membranes in various applications where highly plasticizing conditions are found. Plasticization occurs in both rubbery and glassy polymers, however, glassy polymers, which rely heavily on their size-sieving capabilities, suffer the most from this issue.

Approaches to mitigate plasticization all center around reducing polymer chain mobility, ranging from filler incorporation, crosslinking, hydrogen-bonding incorporation, and rigid monomer design.[10] As explained in Chapter 2, scalable nanocomposite membranes exhibiting all four of these qualities were rationally designed and thoroughly examined for their ability to resist plasticization in gas and liquid separations throughout this work.

1.3.3. Physical Aging

Glassy polymers, as mentioned, tend to have superior sorption capacity and thus higher permeability values than rubbery polymers due to their nonequilibrium excess free volume. This excess free volume, however, collapses over time, resulting in diminished permeability values. Although these diminished permeability values are often accompanied by increased selectivity values, the relative gain of selectivity is typically small and outweighed by the loss of permeability.[33] Additionally, in membrane process technology, high permeabilities are highly sought after, as capital expenditure/module size scale down directly with productivity, while diminishing returns are observed for monotonically increasing the selectivity.[34] Physical aging, additionally, is difficult to predict and track, making it difficult to produce membranes that reliably operate and meet the desired production specifications.[8,22] Thus, it is highly desirable to limit or halt physical aging in order to take advantage of the desirable performance of glassy polymers for advanced membrane technologies. The general approach to limiting physical aging is to either (i) reduce the amount of excess free volume present (i.e., reduce the driving force for physical aging), capping the extent of physical aging, or (ii) hinder the relaxation mechanisms responsible for physical aging by limiting segmental mobility and local relaxations.[22,33,35,36] One successfully demonstrated approach to reduce the segmental mobility and slow physical aging is the incorporation of nanoparticle fillers into the polymer matrix to form nanocomposite membranes.[36,37] In Chapter 3, the potential of an organic polymer network to inhibit physical aging in glassy polymer membranes is evaluated, and in the coming sections, the broad challenges that have arisen in the development of nanocomposite membranes will be introduced.

1.4. Nanocomposite Membranes

1.4.1. Interfacial Compatibility

Beginning in the 90s, researchers began incorporating zeolitic or carbonaceous molecular sieving particles into polymer membranes in order to imbue the resulting mixed matrix membrane (MMM) with the superior intrinsic transport properties of the chosen filler particle.[38] Theoretical predictions were promising, and the studies incorporating zeolites demonstrated some success in improving the selectivity of the MMMs relative to the neat matrix polymer, but there were several issues mostly relating to the interfacial incompatibility of inorganic materials like zeolites and organic polymers. Filler loading had to be limited, and complex multistep fabrication strategies were employed to prevent defects from forming at the polymer-filler interface.[38] These defects often led to membranes with enhanced permeabilities and decaying selectivity values.[8,38,39] Due to these limitations, researchers turned their attention to incorporation of organically derived porous particles as the filler phase in MMM, such as metal organic frameworks (MOFs), porous organic cages (POCs), and covalent organic frameworks (COFs).[8,40,41]

1.4.2. Porous Polymer Networks

A recently developed class of porous organic networks have been developed, known as porous polymer networks (PPNs).[1] In contrast to MOFs, POCs, and COFs, porous polymer networks are amorphous materials, and don't have the high regularity and exact pore size distribution of these other materials. Due to this irregularity, PPNs do not crystallize, and this lack of strong self-interaction make them exceedingly easy to incorporate into various polymer matrices through simple blending and casting procedures.[18,42–48] Additionally, since geometrically precise and tailored monomers are not required, PPNs are typically significantly simpler and cheaper to

synthesize than other organic frameworks. An example in Chapter 3, for example, places the cost of synthesizing the PPN in this work at around ~$50/g, while a state-of-the-art porous aromatic framework (PAF) costs > $500/g to synthesize, demonstrating that, although the pore sizes are not as precise, PPNs offer significant translatable benefits.

PPN properties depend significantly on what monomers are used to construct them. A 2018 study by Lopez-Iglesias and colleagues compared the synthesis of various PPNs using trifunctional aromatic monomers paired with bifunctional activated ketones coupled by the superacid catalyzed hydroxylalkylation reaction.[1] They found that, among the monomers tested, the combination of triptycene and isatin (shown in Figure 3) resulted in the highest BET surface areas (~790 m^2 g^{-1}) with the highest proportion of ultramicropores (molecular pores with aperture < 7 Å)., which are on a competitive level with many of the tailor-made MOFs, COFs, and POCs. The triptycene-isatin PPN was found in a separate study to form defect-free MMMs up to 30 wt.% loading with various polyimide polymers, significantly increasing their permeability without sacrificing selective performance.[43] The intrinsic rigidity of the triptycene-isatin PPN due to its highly crosslinked structure, as well as its hydrogen bonding moieties, makes it an interesting platform for enhancing plasticization and mitigating physical aging in polymer membranes, which, before this work, has not been investigated. Thus, one of the primary focal points of this dissertation is to understand how PPN incorporation can be used to mitigate plasticization and physical aging in ultra-glassy polymer membranes.

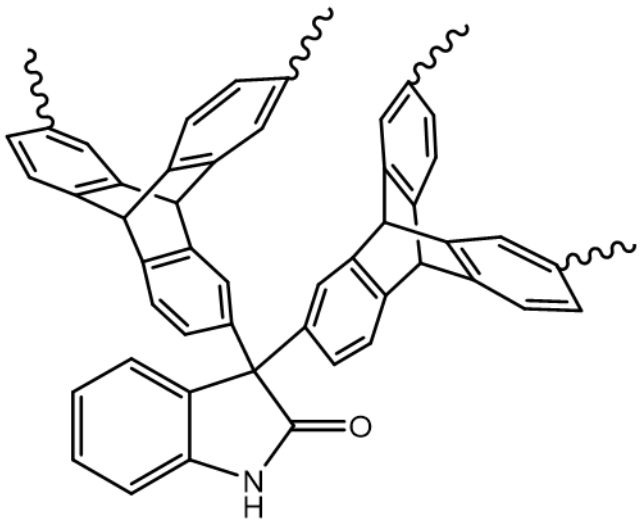


Figure 3. Structure of the triptycene-isatin porous polymer network.

1.5. Polymer Crosslinking

In addition to filler loading to form nanocomposite membranes, polymer crosslinking is a useful and popular approach to improve the long-term performance stability of polymer membranes. By molecularly linking adjacent polymer chains, the relative motion of chains is inhibited, reducing the dilatory and plasticizing effects of highly condensable penetrant incorporation into the polymer matrix. Crosslinking can be accomplished by adding functional groups into the polymer that bond upon being exposed to some stimulus (e.g., heat, light, etc.) or introduce multifunctional crosslinking agents that bond to the polymer at multiple functional points in the polymer structure.[8,15,17,49–53] This approach has successfully shown to significantly enhance plasticization resistance in both aggressive gas and liquid separations.

Although crosslinking may be reasonably called a general purpose aid to improve the plasticization resistance of polymer membranes, the complexity and scalability of the crosslinking approach matters, as well. Complex strategies or harmful crosslinking agents significantly harm the translatable value of the crosslinking approach, therefore simplicity and scalability are highly

desirable. One exceptionally simple approach is to incorporate pendant carboxylic acid groups in the polymer backbone, then thermally crosslink the polymer. This was successfully done with polyimides containing diaminobenzoic acid as a comonomer in 2008 and has been demonstrated to occur with other acid containing polymers, such as carboxylated PIM-1.[51,52] The lowest crosslinking temperature employed in these studies was ~330 °C, which is a relatively high temperature that is expected to degrade conventional polymers used for supports in thin film composites, such as PDMS or PAN.[53] In Chapter 2, it's shown for the first time that carboxylated PIM-1 (CPIM, Figure 4) can be thermally crosslinked at a temperature as low as 200 °C with reasonable efficiency while still reaping the benefits of enhanced plasticization resistance.

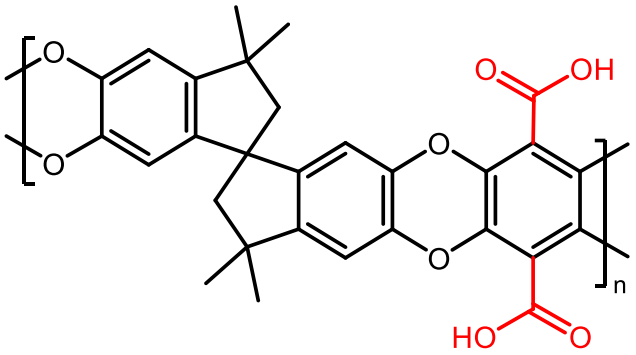


Figure 4. Structure of carboxylated PIM-1 (CPIM).

Additionally, it was found that the radical-based decarboxylation mechanism likely leads to covalent crosslinking between the CPIM and aromatic substrates on the triptycene-isatin PPN, which is denoted herein as a distinct class of nanocomposite membranes called *inter-crosslinked mixed matrix membranes* (IcMMMs). Crosslinking between the polymer-filler interface in nanocomposites is a small but growing field of study,[54–56] and this dissertation adds a number of insights into the effects of engineering the polymer-filler interface through interfacial bonding.

1.6. Summary of Dissertation Chapters

This dissertation details the development and understanding of glassy polymer membranes that, even under chemically aggressive conditions, (i) exhibit excellent permeability and selectivity combinations for gas and organic solvent separations, (ii) resist physical aging and plasticization, and (iii) exhibit long-term performance stability, especially in application-relevant thin-film membrane configurations. The overall strategy utilized to achieve this was to utilize and fundamentally understand the individual and synergistic effects of filler incorporation, polymer crosslinking, and filler-polymer crosslinking on the resulting nanocomposite membrane material properties, followed by detailed structure-property correlations with advanced transport characterization and separation tests.

Chapter 2 lays the theoretical foundation and introduces the material design strategy for designing highly stable nanocomposite membranes. Carboxylated PIM-1 (CPIM) and the triptycene-isatin porous polymer network (PPN) are selected as a functional platform allowing for understanding the individual and synergistic effects of filler incorporation and thermal crosslinking. A simple thermal crosslinking protocol consisting of a 200 °C treatment under vacuum was studied in detail, and it was found that CPIM uniquely undergoes thermal decarboxylation up to ~25% after 24 hours of this treatment, resulting in the mildest temperature this reaction has been found to occur in the literature. Additionally, the molecular mechanism of this thermal decarboxylation is laid out by utilizing earlier studies by chemists, allowing the identification of a potential mechanism by which grafting from CPIM to the PPN would occur to form IcMMMs. In short, Chapter 2 demonstrates that IcMMMs exhibit a unique plasticization resistance owing to the multimodal chain immobilization enabled by both polymer-polymer and polymer-filler interaction, while also exhibiting excellent separation performance. Fundamental

understanding of how CPIM and PPN interact and how to leverage this interaction lays the foundation for carrying them into more advanced applications.

Chapter 3 continues the investigation of how the triptycene-isatin PPN affects long-term membrane stability, specifically with respect to the issue of physical aging. Triptycene-isatin PPN is incorporated into poly(1-trimethylsilyl-1-propyne) (PTMSP), a polymer known for its rapid physical aging. It was found that as little as 5 wt.% PPN in PTMSP resulted in a drastic reduction of physical aging; this result is thoroughly investigated for its fundamental mechanism through a variety of macroscopic and molecular characterization techniques, molecular dynamics modeling, and transport tests. It was found that an adsorptive interaction between the PTMSP and PPN, leading to reduced segmental mobility of the backbone carbons in PTMSP, was responsible for the diminished physical aging observed in the PTMSP-PPN composites. Chapter 3 demonstrates that PPNs are a cost-effective microporous filler that could significantly hinder physical aging in polymers and lays the foundation for future investigation and material development for tackling the grand challenge of physical aging in ultrathin polymer films.

Chapter 4 returns to the CPIM-PPN platform to extend their application to some of the most challenging membrane separations: organic solvent separations. Due to the highly plasticizing nature of liquid organic solvents, polymer membranes have traditionally suffered from poor selectivities in organic solvent separations. One such area is that of hydrocarbon fractionation: mixtures of hydrocarbons don't exhibit many mechanisms by which sorption selectivity can be utilized, and thus aggressive size-sieving membranes must be utilized, but as discussed, plasticization specifically targets and diminishes the size-sieving capability of membranes. CPIM-PPN membranes were adapted into thin-film composite (TFC) membranes and tested for their ability to fractionate hydrocarbons after extended exposure to liquid toluene. It was found that

crosslinking and filler incorporation both extend the long-term durability of membranes and significantly improve their selective performance, even after almost 2 years of exposure to liquid toluene. Additionally, unique interactions at the support-selective layer interface (i.e., between CPIM and the support) were found to spontaneously occur, which offered further enhancements in the long-term stability and separation performance of the TFC membranes. The fundamental mechanisms underlying the long-term stability and separation performance of the membranes are elucidated through several material and transport characterizations, resulting in further development and understanding of how the material design strategy studied in this dissertation can be utilized to tackle the issues of long-term stability of glassy polymer membranes in chemically aggressive environments.

Chapter 2. Inter-crosslinked spirocyclic mixed matrix membranes exhibiting enhanced gas permeability, selectivity, and plasticization resistance

2.1. Abstract

Poor interfacial compatibility is the most common issue inhibiting performance enhancement in mixed matrix membranes (MMM) for gas and liquid separations. To address this issue, we fabricated highly selective and permeable inter-crosslinked mixed matrix membranes (IcMMMs) based on carboxylic-acid functionalized polymer of intrinsic microporosity-1 (CPIM) containing up to 30 wt. % triptycene-isatin polymer porous network (PPN) particles. Polymer-filler inter-crosslinking is accomplished *via* thermal decarboxylation at 200 °C, which is the lowest temperature this reaction has been found to occur in the literature. This low temperature circumvents potential issues with degradation of porous supports or gutter layer materials, and thus enables these materials to be integrated into traditional membrane processes. The resulting IcMMMs exhibit gel fractions above 90%. Beyond IcMMMs, membranes based on neat CPIM, thermally crosslinked CPIM, as well as non-crosslinked CPIM-PPN mixed matrix membranes were fabricated to elucidate the individual and synergistic effects of filler inclusion and thermal treatment. In addition to showing upper bound permeability-selectivity performance, IcMMMs also exhibit an almost unprecedented stability against plasticization upon extended exposure to CO_2 up to 50 atm or above. This study shows that crosslinking across the polymer-filler interface is the key feature to achieve simultaneous enhancement in permeability, selectivity, and stability. To elucidate the molecular mechanism of these enhancements in the IcMMMs with respect to the baseline materials, permeability was broken into its sorption and diffusion contributions and an energetic analysis of sorption was performed. The low cost of PPNs coupled with the mild

crosslinking temperature make this approach highly scalable, resulting in materials exhibiting high rigidity and structural stability with the potential to excel in aggressive separations, such as organic solvent separations or high-CO_2 content, high-pressure natural gas sweetening.

2.2. Introduction

Chemical separations account for a significant fraction of global energy consumption, which is estimated to be 8 GJ per person on the hearth every year.[4] Although membrane separations hold promise as energy efficient and sustainable alternatives to thermal-based separations, their large-scale implementation has been hindered by long-standing challenges, such as poor selectivity and stability. These challenges are especially difficult to solve within the context of the chemically and thermally harsh operating conditions in applications such as sour gas processing, carbon capture, hydrogen production, and organic solvent separation.[4,8,57]

A trade-off relationship between permeability and selectivity exists in polymer membranes, wherein attempts to enhance permeability are typically accompanied by a loss in selectivity, and vice-versa.[29,30] While strides in enhancing permeability while maintaining modest selectivity have continually been made by synthesizing extremely rigid polymer architectures, improving selectivity without significantly compromising permeability has proven to be a challenge.[8,58,59]

As recommended by the US National Academies in 2019,[60] enhancing permeability and selectivity, while important, is not sufficient. The long-term stability of membrane permeability and selectivity remains a mostly unsolved challenge. Many existing state-of-the-art polymer membranes based on linear glassy polymers, despite exhibiting adequate separation performance in the short term, suffer from poor long-term stability due to plasticization and physical aging [33,61]. A generally accepted idea is that the suppression of chain rotation *via* the use of monomers

exhibiting fused rings, such as those found in polybenzimidazoles (PBIs), might help fix this issue. However, these polymers still exhibit a marked aging and plasticization propensity [22,62]. Spirocyclic polymers, such as polymers of intrinsic microporosity (PIMs), are another example of functional materials designed to exhibit high permeability and rigidity. PIMs typically consist of a combination of rigid kinked moieties, such as spiro centers, which generate internal microporosity, and fused rings, which hamper chain rotation. Since their discovery, a plethora of functionalization approaches have been devised to engineer their properties by direct substitution of the nitrile groups. A large variety of substitutions have been proposed, such as amidoximes [63,64], carboxylic acids [23,65], amines [66–68], amides [69,70], thioamides [71], and tetrazoles [72]. Despite their positive effects on permeability and selectivity in the short time frame, these approaches alone are not sufficient to fix long-term stability issues [23,61,64,66,67].

Although increasing monomer rigidity inhibits atomic-scale fluctuations, polymer chain mobility must be halted to guarantee a stable performance in chemically and thermally harsh environments [61]. The core challenge to be addressed is to synthesize materials exhibiting, even in harsh environments, a permanent structure at multiple length scales, while maintaining a free volume architecture capable of offering adequate size sieving ability. Solving this challenge requires simultaneous freezing of local atomic fluctuations to preserve permeability and selectivity (i.e., rigid/kinked monomers) [73], as well as reduction of the chain mobility responsible for plasticization and physical aging. Thus, a *combination* of both rigid molecular architectures and chain immobilization techniques could be a favorable strategy to produce membranes meeting the expected needs.

Fabricating immobilized molecular architectures presents a distinct challenge when considering that polymers should be solvent-soluble and go through a vitrification process during

fabrication as a thin film. This process inherently produces non-equilibrium (i.e., glassy) materials with some degree of chain mobility. Given this conflict between the nature of membrane processing and the need for stable materials, fabrication of highly stable membranes often requires post-modification chemical treatments, thermal treatments, or the incorporation of additives [8,74–76].

Crosslinking is an effective approach to immobilize polymer chains, leading to membranes exhibiting enhanced plasticization resistance [49,51–53,77–79]. Polyimides (PIs) exhibiting carboxylic groups were crosslinked using various diols or multivalent metal ion coordination to the carboxylate form. This result was generally successful and resulted in films exhibiting adequate plasticization resistance upon exposure to CO_2 up to 30-40 atm [49,77,78]. In 2008, Kratochvil and Koros used thermal decarboxylation at 389°C to crosslink diamino benzoic acid (DABA) containing PIs, followed by rapid quenching [52]. This decarboxylation approach was more effective than the diol crosslinking, as it produced membranes exhibiting plasticization resistance up to 45 atm, with a CO_2 permeability at plasticization of 450 Barrer. Of equal importance, these membranes resisted hydrolysis and did not require external crosslinking agents. The crosslinking temperature, however, was above the polymer's T_g, which may be problematic if the polymer experiences degradation below its glass transition. Decarboxylation crosslinking has been successfully extended and combined into hybrid approaches to modify polyimides [50,79–81], PIMs [51], Tröger's base polymers [82], and thermally rearranged polymers [83]. All these approaches, however, rely on crosslinking temperatures above 300 °C, which makes the processing and scale-up of these membranes difficult, as conventional gutter layers or porous support materials do not withstand such high temperatures. Additionally, many of these crosslinked films still exhibit performance instabilities under harsh conditions, especially when fabricated as thin films [79]. In this

study, we propose a fabrication approach capable of producing fully crosslinked spirocyclic polymers at temperatures as low as 200°C, where most of porous support will not experience any degradation issues.

Another approach to enhance selectivity and stability relies on the incorporation of porous materials in polymers to fabricate mixed matrix membranes (MMM). While zeolites were initially considered, researchers have turned to designing metal organic frameworks (MOFs) and other hybrid porous materials due to their better compatibility with polymers. Overall, the MMM approach offers the well-defined and permanent structure of the incorporated particles, but it also introduces the need to engineer polymer-filler interactions, find optimal filler loadings, and design new fabrication routes. Solving the problem of poor polymer-filler compatibility, which compromises selectivity due to the formation of defects at filler-polymer interfaces, has been of particular focus [56,84]. Recently, the discovery of new synthetic routes made it possible to fabricate fully organic porous fillers, such as porous organic cages (POCs), porous aromatic frameworks (PAFs), and porous polymer networks (PPNs) [1,43]. These materials exhibit some key features, such as *i)* lack of inorganic components, *ii)* tunable porosity and microporosity, and *iii)* capability of being functionalized. These features tend to eliminate the structural defects typically observed in conventional MMMs by promoting intimate polymer-filler blending. In some instances, these organic additives establish physical and chemical interactions with the polymer, such that the blend resembles a single phase rather than a heterogeneous medium. For this reason, these material systems have been called molecularly mixed composite membranes (MMCMs). Lively et al. fabricated MMCMs for organic solvent separations exhibiting molecular weight cut-off below 236 g/mol in methanol, ethanol, and toluene in organic solvent nanofiltration (OSN) tests [16]. Noteworthy, this approach may also benefit membrane's long-term stability. Indeed, as shown by

Noble et al., incorporation of PAFs significantly reduces the aging propensity of high free volume microporous glassy polymers, such as PTMSP and PIM-1 [36,85].

In this study, we combine the crosslinking and mixed matrix membrane approaches to design polymer membranes exhibiting simultaneously high selectivity, high stability and superb plasticization resistance. We demonstrate that PPNs synthesized from isatin and triptycene can be blended with carboxylic-acid functionalized PIM-1 (CPIM) to form defect-free MMMs at loadings as high as 30 wt. %. Thermally induced decarboxylation crosslinking is then utilized to crosslink not only CPIM to itself, but the CPIM to the PPN. These composite membranes, wherein the filler and continuous phase are chemically bonded, are thus specified as *inter-crosslinked mixed matrix membranes* (IcMMMs). Notably, crosslinking is accomplished at 200°C, which is the lowest temperature this reaction has been found to occur in the literature. This low temperature circumvents potential issues with degradation of porous supports or gutter layer materials, thus facilitating the scale up and integration of these materials into membrane processes. The low cost of PPNs compared to other fillers, such as PAFs (50 vs 500 $/g), improves the scalability of the proposed approach. The resulting IcMMMs exhibit upper bound permeability-selectivity performance for several gas pairs and an impressive CO_2 plasticization resistance up to at least 50 atm for extended exposure times, which places these membranes among the most stable ever reported. Finally, fundamental structure-property correlations are presented to explain the molecular origin of the observed behaviors.

2.3. Experimental Methods

2.3.1. Materials

Details about the chemicals used and their purification routes are provided in Appendix A, Section A1.

2.3.2. Synthesis of PIM-1

PIM-1, the precursor material for carboxylated PIM-1 (CPIM), was synthesized as shown in Figure 5A, via high-temperature polycondensation. Details are provided in Appendix A, Section A2.

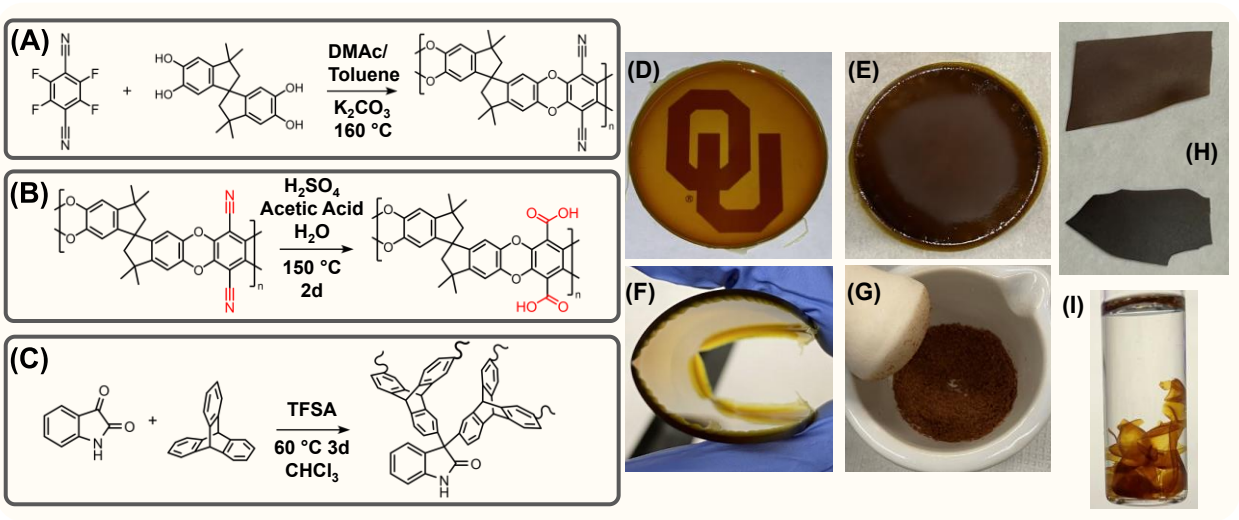


Figure 5. Synthetic routes to (A) PIM-1, (B) CPIM, and (C) triptycene isatin PPN. (D and F) defect-free CPIM membranes, (E) a defect-free MMM30 membrane, (G) the synthesized triptycene isatin powder, (H) color comparison of a MMM30 membrane before (top) and after (bottom) thermal treatment, and (I) demonstration of CPIMTT's insolubility after soaking in THF for 24h.

2.3.3. Acid Hydrolysis of PIM-1

Carboxylated PIM-1, denoted herein as CPIM, was prepared via the acid hydrolysis method with minor modifications (cf., Figure 5B) [23]. Specifically, 0.8 g of PIM-1 was combined with 48 mL of deionized (DI) water, 16 mL of glacial acetic acid, and 48 mL of sulfuric acid in a 250 mL single neck round-bottom flask equipped with a water-cooled condenser and magnetic stir bar. The reaction was heated by submersion of the flask in an oil bath at 150°C under stirring at 200 rpm. After 48h, the reaction mixture was decanted into 500 mL of water. The resulting solution was filtered to recover a brown-colored product. To retain the protonated form of the acid groups, the product was refluxed in 200 mL of DI water with 3-4 drops of sulfuric acid for 24h. Finally, the final product was recovered by filtration and dried in a vacuum oven at 110°C overnight. The degree of carboxylation, determined via elemental analysis, was about 90% (Table 1).

2.3.4. Synthesis of Triptyene-Isatin Porous Polymer Network

Porous polymer networks (PPN) were synthesized in-house via the hydroxyalkylation reaction between triptycene and isatin (cf., Figure 1C). Details regarding the synthesis procedure are provided in Appendix A, Section A3. The rationale for selecting triptycene-isatin PPN to be mixed with CPIM is that carboxy moieties in the CPIM backbone are expected to produce, upon thermal treatment, radical crosslinking with the triptycene moieties in the PPN to favor the formation of IcMMMs. Also, triptycene units provide their unique internal free volume, referred to as configurational free volume [32,86,87], which exhibits extremely uniform distribution, offering high selectivity as well as long-term stability [1]. Finally, isatin, which is an activated ketone exhibiting high reactivity in the hydroxyalkylation reaction, is cheap, readily available, and contains amide groups that can favorably interact with gases such as CO_2.

2.3.5. Membrane Fabrication

In this study, four kinds of membranes were fabricated: neat CPIM, thermally treated (i.e., thermally crosslinked) CPIM, mixed matrix membranes comprising CPIM and 30 wt. % PPN (MMM), and thermally treated membranes of CPIM and 30 wt. % PPN (i.e., IcMMMs). A loading of 30 wt. % PPN is the previous highest successful loading achieved in the literature, and this loading was used throughout this study to serve as a benchmark for comparison [43]. All membranes were fabricated via solution casting. Details, including membranes' thickness, are reported in Appendix A, Section A4.

After fabrication via the solution-casting procedure, dense, self-standing (i.e., support-free) membranes were thermally crosslinked by placing them in a glass petri dish in a room-temperature vacuum oven equipped with a cold trap, which was filled with liquid nitrogen. Vacuum was pulled for 30 minutes to remove gases and any residual moisture. Following this step, the oven was heated to 200 °C over the course of one hour. The samples were held at this temperature under vacuum for 24h and then were allowed to slowly cool to room temperature. This procedure avoids any potential oxidation processes that could complicate the crosslinking process. Regarding sample nomenclature, the uncrosslinked MMM containing 30 wt.% PPN will be denoted MMM30, and the thermally crosslinked IcMMM containing 30 wt. % PPN will be called IcMMM30 throughout the manuscript. Thermally crosslinked CPIM will be denoted CPIMTT. PPN-containing samples had a darker appearance, and the color darkened further upon thermal treatment, as shown in Figure 5D-H. As shown in Figure 5I, both thermally crosslinked membranes (i.e., CPIM-TT and IcMMM30) are insoluble in THF.

2.3.6. Structural Characterization

Details regarding the compositional (NMR, FTIR, elemental analysis), thermal (DSC, TGA-MS), and physical (BET, gel fraction) characterization are provided in Appendix A, Sections A5-A12.

2.3.7. Sorption/Transport Measurements and Plasticization Study

Pure gas H_2, CH_4, and CO_2 permeability was measured at 35 °C and up to 30 atm using a constant volume, variable pressure apparatus. Details are provided in Appendix A, Section A13.

High pressure CO_2 permeability measurements were run, up to 50 atm at 35 °C, to assess membrane plasticization resistance. Membranes were first exposed to a low CO_2 pressure (0.2-0.5 atm), which was increased stepwise until a discernible minimum in permeability was observed. Permeability rise due to CO_2-induced plasticization is a transient dynamic process dependent on polymer relaxation, and steady increases in permeability can be observed to occur for multiple days at constant CO_2 pressures [77,79,88]. Thus, a standard procedure was determined to equalize the membrane exposure time to each CO_2 pressure, wherein each CO_2 pressure was held for 24 hours, and the downstream side of the membrane was vacuumed out until measurement at the end of each 24 hours.

To gain fundamental insights into the transport mechanism via the dual-mode model, pure gas CO_2 and CH_4 sorption was measured at temperatures between 15-50°C and up to 40 atm, using the pressure decay method [89]. H_2 was excluded from sorption measurements, due to its extremely low condensability [90]. Details regarding the sorption measurements are provided in Appendix A, Section A14. Diffusion coefficients were determined from experimental sorption and permeation data, using the solution-diffusion model.

2.4. Results and Discussion

2.4.1. Synthesis and Characterization of PIM-1

Successful synthesis of PIM-1, CPIM, and the triptycene-isatin PPN was confirmed by ATR-FTIR, 1H NMR, and ^{13}C NMR spectroscopy. Chemical structures of PIM-1 and CPIM are shown in Figure 6A-B, where they are labelled with the corresponding NMR proton or carbon assignments.

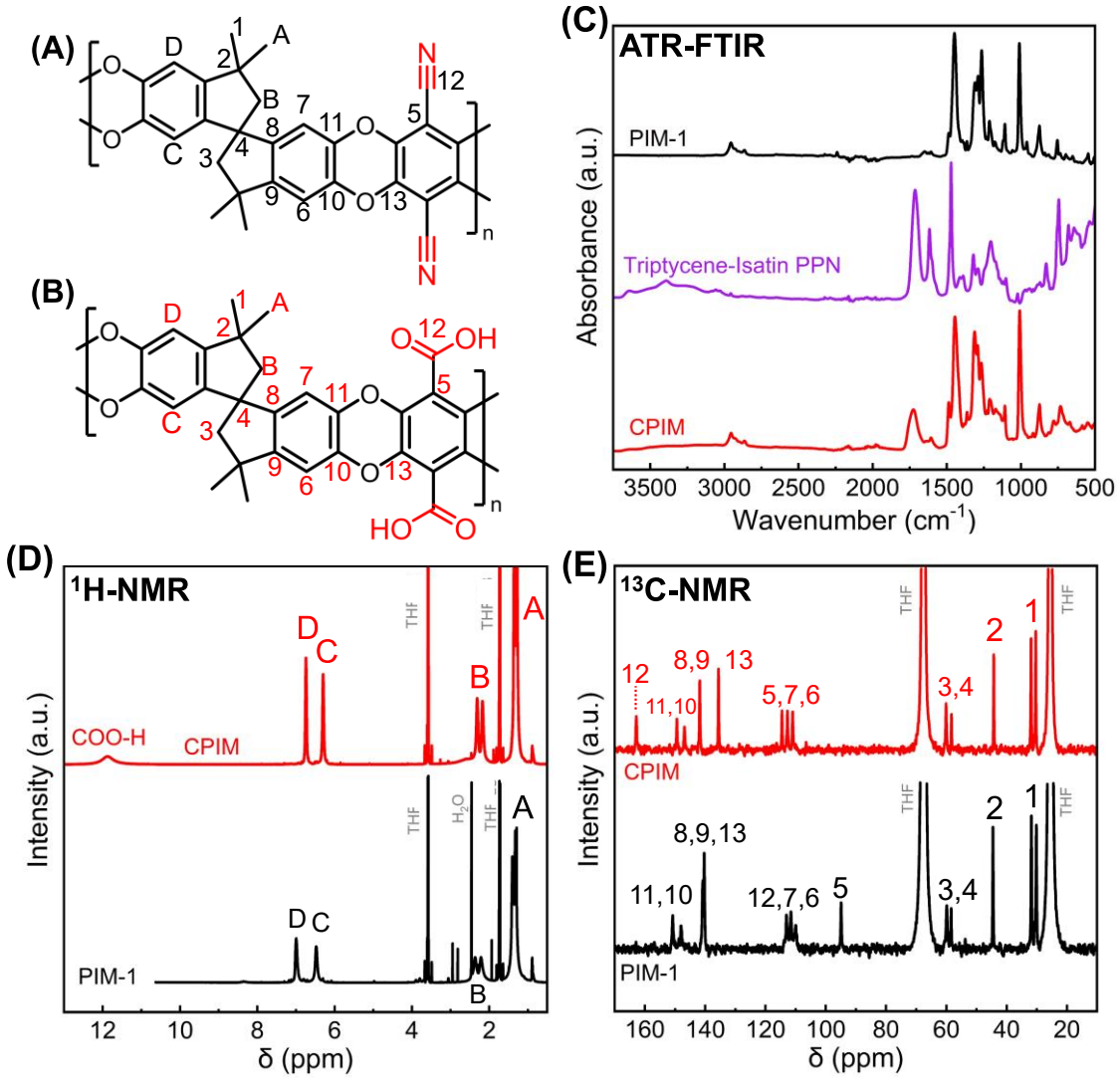


Figure 6. Molecular structures with numbered carbon assignments and lettered proton assignments for (A) PIM-1 and (B) CPIM. (C) ATR-FTIR, (D) 1H NMR, and (E) ^{13}C NMR spectra of the synthesized materials are shown.

In Figure 6C, the ATR-FTIR spectra of the synthesized materials are shown. Both PIM-1 and CPIM exhibit the characteristic IR absorption bands, namely, the C=C aromatic stretching at 1600 cm^{-1} [91,92], the dibenzodioxane C-O-C stretch at 1010 cm^{-1} [93,94], as well as the methyl, methylene bridge, and aromatic stretching and bending peaks at 2840-3000 cm^{-1} and 1360-1490 cm^{-1}, respectively [92,95,96]. PIM-1 exhibits the characteristic nitrile C≡N stretch at 2238 cm^{-1}, which disappears in CPIM. The latter, instead, exhibits new peaks appearing as a broad -OH stretch near 3500 cm^{-1}, as well as a carbonyl stretch at 1720 cm^{-1} corresponding to the carboxylic acid -COOH group [23]. The triptycene-isatin PPN exhibits the typical C=O stretch at 1708 cm^{-1}, N-H bend at 1469 cm^{-1}, and C-N stretch at 1320 cm^{-1} characteristic of the lactam moiety [1]. Details about the PPN thermal stability (Appendix A, Section A15) and BET area (Appendix A, Section A9) are provided in Appendix A.

^{1}H NMR spectra for CPIM and PIM-1 are shown in Figure 6D. The peaks for the PIM-1 backbone (labeled A, B, C, D) are invariant between the PIM-1 and CPIM spectra and correspond to the expected structures for these materials [23,97]. Successful carboxylation of PIM-1 is confirmed by the appearance of the acidic proton signal in the ^{1}H NMR spectrum for CPIM at 11.9 ppm. In the ^{13}C spectra for PIM-1 and CPIM (cf., Figure 6E), the corresponding backbone peaks are preserved as in the case of the ^{1}H NMR spectra, and the almost complete shifting/disappearance of the signal at 95 ppm (i.e. carbon 5) and appearance of a signal at 162.9 ppm characteristic of the -COOH group in the ^{13}C spectrum of CPIM further confirm a successful carboxylation reaction [23,97,98].

To determine the degree of hydrolysis of CPIM (i.e., number of nitriles in PIM-1 converted to carboxylic acid groups in CPIM), combustion elemental analysis was performed. Elemental analysis was chosen since direct quantification by integration of ^{1}H NMR peaks is difficult to achieve due to exchange of the acidic protons with water [23,99]. Moreover, estimates from mass losses during decarboxylation would underestimate the degree of decarboxylation [23,97] since this process is self-catalyzed by nearby acid groups, therefore complete decarboxylation is not generally observed to occur in a single isolated mass loss during TGA analysis [52,100]. As shown in Table 1, the experimental *N/C* mass ratio in neat PIM-1 matches theoretical predictions, and the calculated degree of hydrolysis of the synthesized CPIM is 92.0%. This conversion is in agreement with literature data [23]. Since a dilute sulfuric acid solution is applied in the last processing step, a certain amount of sulfur is expected to be retained in the final CPIM product. Consistently, a slight increase in the sulfur content between PIM-1 and CPIM (~0.3 wt. %) is apparent. Some implications of this residual acid content will be discussed in Section 2.4.2.

Table 1. Elemental analysis, in terms of atomic weight percents, of the synthesized PIM-1 and CPIM. The degree of hydrolysis is the percentage of nitrile groups in PIM-1 that have been converted into carboxylic acids. Sulfur (S) was tested to determine whether residual sulfuric acid was retained in the final product.

sample	*data source*	*% C*	*% N*	*% S*	*N/C*	*degree of hydrolysis (%)*
PIM-1	*Experimental*	*72.97*	*5.83*	*0.21*	*0.08*	*0*
	Theory	*75.64*	*6.08*	*0*	*0.080*	*0*
CPIM	*Experimental*	*63.7*	*0.41*	*0.504*	*0.00637*	*92.0*
	Theory	*69.9*	*0*	*0*	*0*	*100*

2.4.2. Membrane Formation and Thermal Crosslinking

Decarboxylation crosslinking has been successfully used on various acid-containing polyimides and microporous polymers, including CPIM, but usually at temperatures in excess of 300 °C [50,52,53,82]. Significant losses in crosslinking efficiency and plasticization resistance have been reported as crosslinking temperature is decreased from 425 °C to as low as 300 °C for both polyimides and microporous PIMs [50,53,82]. Given that the temperature used in this study (200 °C) for the decarboxylation crosslinking reaction is relatively low, gel fraction analysis, FTIR, ^{13}C CP/MAS NMR, and TGA-MS were used to confirm that crosslinking successfully occurred, as well as to analyze the extent of crosslinking.

The gel fraction characterizes the amount of insoluble material of a crosslinked gel. By using THF, a good solvent for CPIM, soluble material was leached out of crosslinked membranes (i.e., CPIMTT and IcMMM30), and the fraction of remaining mass gives an estimate of the crosslinking efficiency. Du et al. previously reported, for CPIMs crosslinked at 375 °C for 40 minutes, gel fractions of 85-92% with degrees of hydrolysis of 85-100% [51]. For the CPIM reported herein, with a 92% degree of hydrolysis, the gel fraction of the resulting crosslinked (i.e., thermally treated) membrane, CPIMTT, is 90 ± 1%. The thermally crosslinked IcMMM30 exhibits a gel fraction of 94.1 ± 0.7%. Remarkably, these results confirm that crosslinking efficiency is not sacrificed by the lower crosslinking temperature. To the best of our knowledge, this is the first time that thermal crosslinking of PIM derivatives has been achieved at temperatures as low as 200 °C [51,101,102].

One possibility is that crosslinking occurs by formation of anhydrides, rather than by formation of covalent C-C bonds. However, the presence of anhydrides as primary crosslinking products was ruled out by hydrolysis testing, wherein samples of CPIMTT were boiled in water for 10 days, after which the gel fraction was measured again. Despite the aggressive hydrolytic conditions

employed, these membranes retained gel fractions close to 90% (Table A4). Therefore, despite the lower temperature, a high crosslinking efficiency, resulting in hydrolysis-resistant crosslinks, can be achieved by extending the crosslinking time.

Figure 7A shows ATR-FTIR spectra of MMM30 and IcMMM30 membranes. Two main spectral features confirm the chemical transformations occurring. First, the signals associated with the carboxylic acid -OH and C=O stretches at 3500 cm^{-1} and 1720 cm^{-1} are depressed in the thermally treated sample, indicating some degree of decarboxylation occurs during treatment. Moreover, peaks located at 1440-1480 cm^{-1} in IcMMM30 experience a 25 cm^{-1} blueshift to 1465-1513 cm^{-1}, while the C-O-C stretch at 1004 cm^{-1} present in the MMM30 sample becomes significantly diminished along with the appearance of a new peak at 975 cm^{-1} in the IcMMM30 sample. The large blueshift in the stretching region between 1440-1480 cm^{-1} in the IcMMM30 sample, which includes C=C aromatic stretching, C-O stretching, and methylene bridge -CH_2 bending modes [92,103–105], is likely the result of changes to the substitution pattern on the aromatic benzodioxin moieties in the CPIM backbone or carbon-carbon bond disruption between the methylene bridge and spiro center. Notably, the bending vibration of the methyl groups at 1369 cm^{-1} [95] is unaffected by thermal treatment, which indicates that any C-C bond scission is prone to occur close to the spiro center in the PIM backbone. Changes in the C-O-C stretch in the thermally treated sample further confirm the significant change in the substitution pattern on the aromatic moieties, namely, loss of acid groups or formation of the aromatic C-C crosslinks that typically occur during decarboxylation crosslinking [52,100].

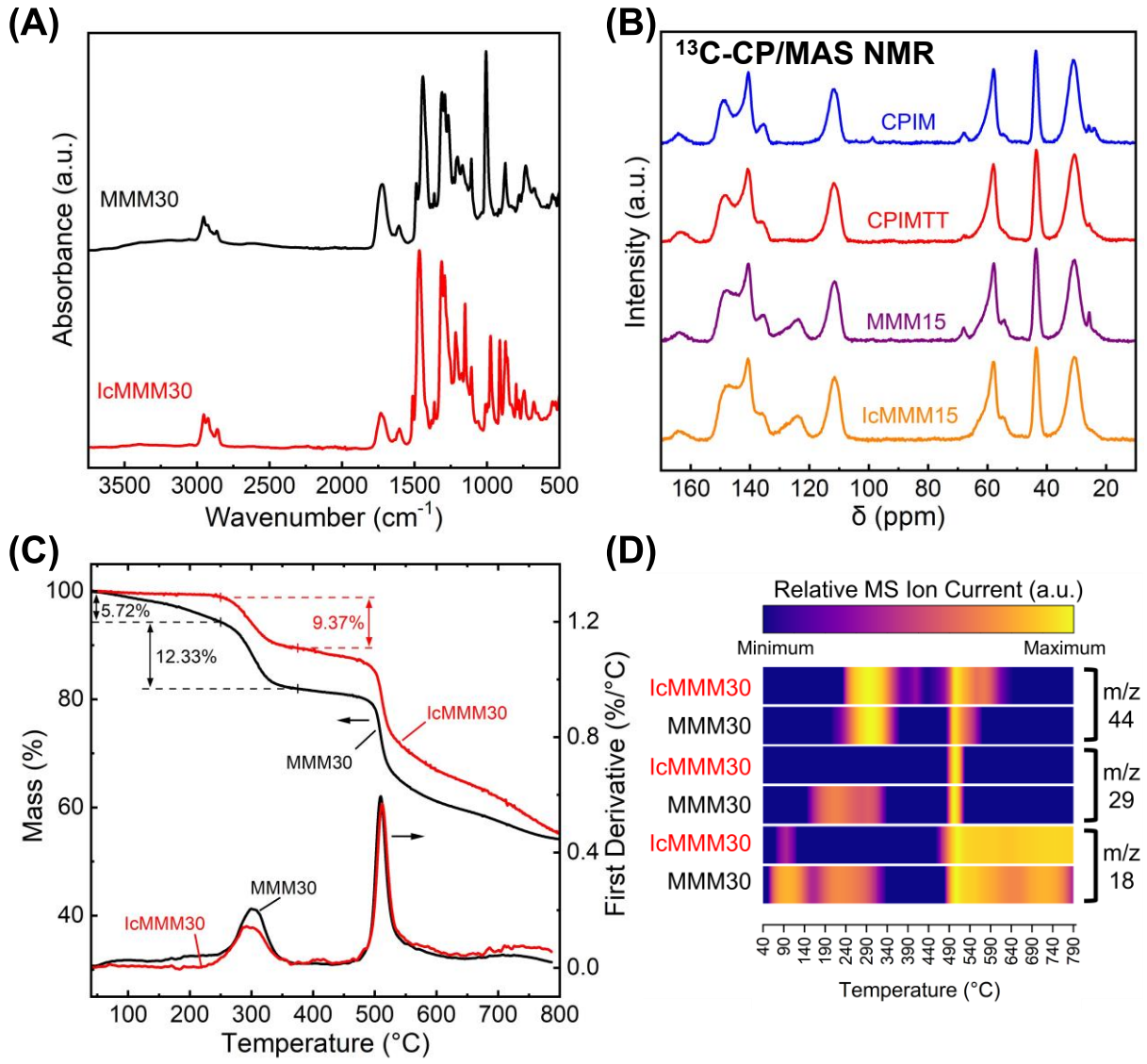


Figure 7. Study of the thermal treatment by (A) FTIR-ATR of MMM30 and IcMMM30, (B) ^{13}C-CP/MAS NMR spectra of CPIM, CPIMTT, MMM30 and IcMMM30, (C) TGA mass loss analysis of MMM30 and IcMMM30, and (D) mass spectrometry signals corresponding to the TGA experiments in (C).

^{13}C CP/MAS NMR spectra were collected on both untreated and thermally treated analogues of CPIM and MMM15 (Figure 7B). Since the thermal crosslinking process occurs due to the CPIM chemistry, 15 wt. % loading was used instead of 30% to maximize the signal due to changes

happening to the CPIM. The signals expected for the CPIM structure agree with the ^{13}C NMR presented in Section 2.4.1 and signals corresponding to the aromatic carbons in the triptycene-isatin PPN are observed at 123 and 145 ppm as a distinct peak and shoulder contribution, respectively. Additionally, the methine bridge in the triptycene group appears at 54 ppm [1]. No significant changes in the peaks corresponding to the carbon skeleton in either CPIM or the PPN are observed to occur due to the thermal annealing process. This is likely due to changes in the substitution pattern producing signals that are overshadowed by already extant signals, or that subtle changes are occurring that are beyond the limit of detection of the instrument.

Notable shoulder contributions to the aliphatic carbons in the CP/MAS spectra appear at 67 and 25 ppm in the untreated samples. These signals either greatly diminish or completely disappear upon thermal treatment. These align well with the expected ^{13}C signals for THF—the casting solvent for the samples—shown in Figure 6E. However, all samples used for the CP/MAS analysis were dried at 110°C for 12h under vacuum before analysis, so it seems unlikely that THF, with a boiling point of 66°C, would remain occluded in the samples after this treatment. Further, the signal is still weakly present in the CPIMTT sample, which was treated at 200°C for 24 hours under vacuum. These apparently contradictory observations are explained by considering the interaction between the casting solvent, THF, and the residual sulfuric acid present in the CPIM after synthesis that was detected using elemental analysis (Table 1). As mentioned earlier, a dilute acid wash is applied in the final step of the CPIM synthesis to retain the protonated acid form, and the residual sulfuric acid likely interacts with THF in the casting solutions for the membranes to form short-chain oligomers of THF (i.e., poly(THF)), which have ^{13}C signals that correspond to those seen in Figure 7B [106]. Sulfuric acid is a common catalyst in ring-opening polymerizations (ROPs) and is known to catalyze the cationic ROP of THF, leading to the production of oligomeric

species with molecular weights < 1000 Da [107]. These oligomeric polyTHF species will have a significantly higher boiling point than THF and have been shown to degrade under inert conditions at the temperatures employed [106,108]. Considering the small amount of sulfuric acid present and the relatively weak signals seen in the CP/MAS, these polyTHF species are likely removed during thermal treatment through a combination of thermal degradation and evaporation processes. The effect of the poly(THF) species on the degree of crosslinking or hydrolytic stability of the crosslinked membranes was found to be minimal. Specifically, CPIMTT membranes boiled in water and cast from either THF or DMF exhibited gel fractions close to 90% (Table A4). Possible effects of poly(THF) on membrane transport properties are discussed in Section 2.4.4.

Further confirmation of the chemical crosslinking mechanism is provided by the TGA-MS measurements on MMM30 and IcMMM30 membranes shown in Figure 7C-D. PPN, due to its thermal stability, should not contribute significantly to the observed differences, and TGA of neat CPIM closely reflects that of the MMM30 sample. TGA of neat CPIM and PPN are discussed in Appendix A, Section A15. Thus, the different mass losses exhibited by the two samples should originate from processes occurring during the thermal treatment process. Notably, the untreated MMM30 sample shows a sloping mass loss of 5.72% from 100-250 °C that is not present in the IcMMM30 sample. As both samples were dried at 110 °C overnight in a vacuum oven before analysis, it is unlikely that this difference in mass loss is due to residual moisture or solvent and is instead a combination of low-temperature decarboxylation and removal of the poly(THF) that occurs during thermal treatment.

The smaller area of the first derivative decarboxylation peak for the thermally treated sample, relative to the untreated sample, confirms the partial decarboxylation occurring during thermal treatment that was also seen in the FTIR analysis. By comparing the mass losses from 250 to 375

°C, it appears that the MMM30 membrane loses about 3% more mass during decarboxylation. For a fully carboxylated CPIM, complete decarboxylation of this sample would result in a 12.46 % mass loss (after adjusting for the 30 wt. % PPN content) [23]. After accounting for the 92.0% hydrolysis of the CPIM found from elemental analysis, this 3% mass loss difference indicates that approximately 25.8% of acid groups are lost during thermal treatment.

In the mass spectrometry signals (cf. Figure 7D), differences were observed primarily in the lower temperature degradation products. First, a m/z = 29 signal was observed from the MMM30 sample from 140-350 °C that is not observed from IcMMM30. This ion fragment was assumed to be associated with the ethyl ion fragment originating from either the evolution or decomposition of THF or poly(THF) oligomers, but would also be produced in the degradation of the main-chain PIM backbone [109,110]. The m/z = 29 signal presents as a bimodal evolution in MMM30 with peaks centered at 200 and 300 °C, which suggests that multiple pathways could be producing this signal. Minor degradation of the aliphatic C-C bonds in the aliphatic moieties of the PIM backbone could also contribute to the observed degradation behavior, as changes in these peaks were observed in the FTIR spectra (cf. Figure 6C). The absence of this signal from IcMMM30 at these lower temperatures provides direct confirmation that these species are efficiently removed during thermal treatment. For the m/z = 18 signal, which corresponds to water evolution, some differences between MMM30 and IcMMM30 are observed as well. While both samples exhibit an evolution near 100 °C, typical of physi-sorbed moisture, the untreated MMM30 sample exhibits a secondary water evolution spanning from 140-350 °C. This behavior is also consistent with the same degradation pathways discussed for the m/z = 29 signal, in addition to the expected water production as a result of condensation of adjacent acid groups to anhydride groups [52,100]. Little to

no changes were observed in the production of carbon dioxide between the two samples (m/z = 44).

Based on the observed decarboxylation, high gel fractions, and hydrolysis resistant crosslinks, it seems that the conventional decarboxylation pathway, in which a free radical process induces degradation of anhydride species leading to the formation of C-C crosslinks, is occurring in our materials. One interesting feature of this pyrolytic degradation is the ability to sustain crosslinks to external aromatic substrates, rather than just between two acid-containing sites. Eskay et al. studied in depth this chemistry and found that aromatic acids grafted to naphthalene by a free radical process [100]. Thus, since this degradative pathway has been established to be occurring in the samples studied, some degree of grafting between CPIM and the aromatic substrates on the PPN should take place. The various crosslinking pathways leading to C-C crosslinks in the membrane are illustrated in Figure 8A, with the resulting hypothesized inter-crosslinked structure portrayed in Figure 8B. The effect of inter-crosslinking on the membrane plasticization resistance and transport properties is discussed in Section 2.4.5.

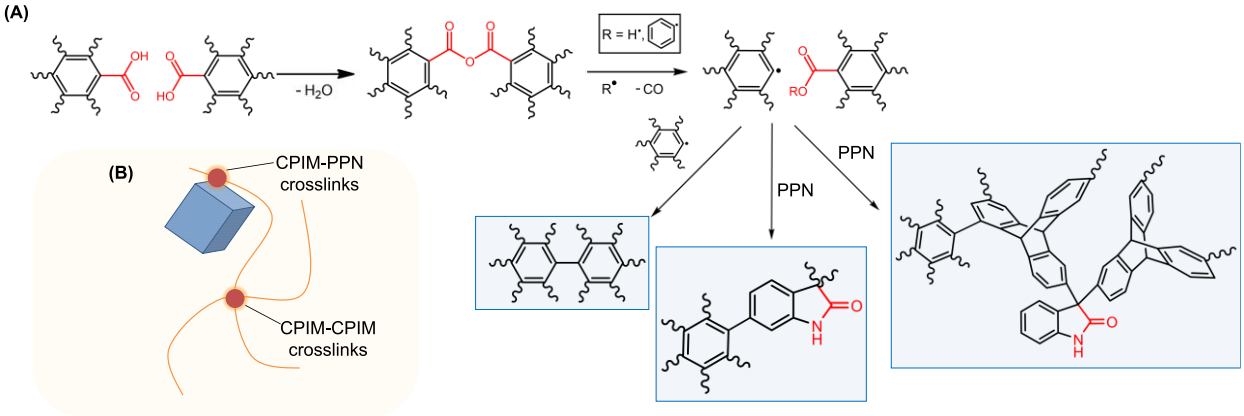


Figure 8. (A) Proposed crosslinking mechanism, with the final C-C crosslinked structures highlighted in blue. (B) Artwork depicting the structure of IcMMM30.

2.4.3. Pure Gas Permeability and Selectivity

Pure gas H_2, CH_4 and CO_2 permeabilities at 35 °C in CPIM, CPIMTT, MMM30, and IcMMM30 are tabulated in Appendix A, Section A17. CH_4 and H_2 (Figure A6) permeability isotherms exhibit the dual mode behavior typical of glassy polymers, with a constant or monotonically decreasing permeability as a function of fugacity. In the case of CO_2, the dual mode behavior is observed, in the entire pressure range, up to 50 atm, only for IcMMM30, while the other samples exhibit a clearly discernible upturn ascribed to plasticization. Details about the CO_2-induced plasticization behavior are provided in Section 2.4.5.

Pure-gas H_2/CH_4 selectivity at 35 °C and 10 atm is shown, as a function of H_2 permeability, in an upper-bound plot in Figure 9A.

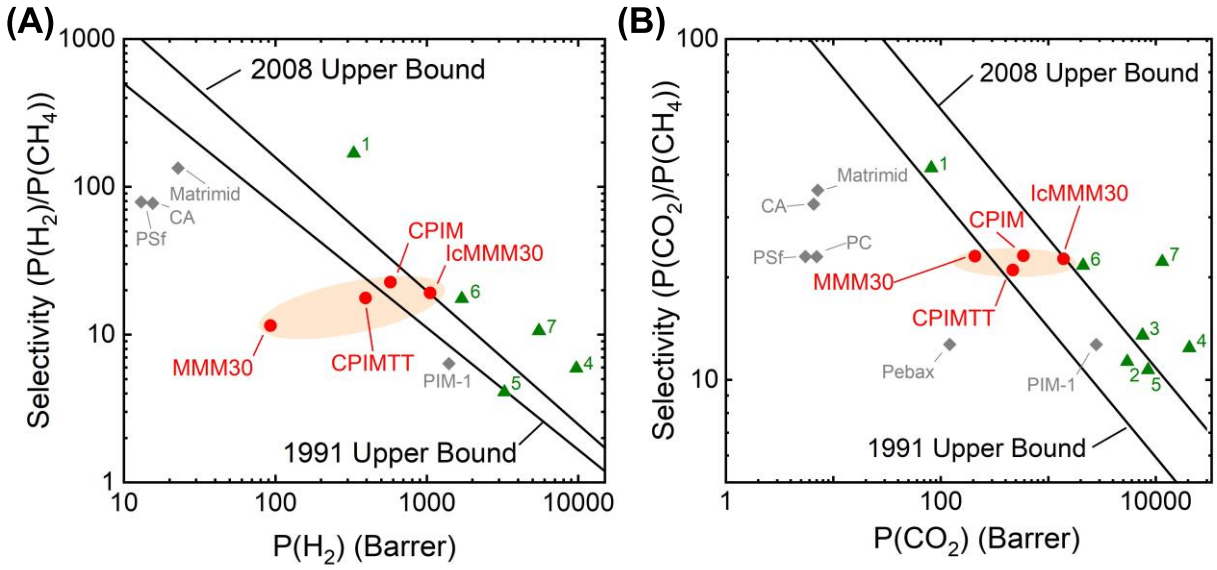


Figure 9. Upper bound plots for the (A) H_2/CH_4 (35°C, 10 atm) and (B) CO_2/CH_4 (35°C, 1 atm) gas pairs. State of the art polymer membranes are denoted in gray and include cellulose acetate (CA) [88], polysulfone (PSf) [111,112], polycarbonate (PC) [113], PIM-1 [23], Matrimid® [114,115], and Pebax [116]. Previously reported PIM-based composite membranes are shown as green triangles: 1- PIM-

1/POSS [117], 2- PIM-1/CC3 [118], 3- PIM-1/COF(SNW-1) [119], 4- PIM-1/pDCX [120], 5- PIM-1/UiO-66-NH$_2$ [56], 6 – CPIM/UiO-66-NH$_2$ [56], 7 – CPIM/diacetyl biphenyl PPN [121].

H_2 permeability and H_2/CH_4 selectivity decrease by 32% and 22%, respectively, upon thermal treatment of CPIM (i.e., CPIMTT). Upon blending with 30 wt. % triptycene-isatin PPN (i.e., MMM30), a further 84% decrease in the H_2 permeability and 49% decrease in the H_2/CH_4 selectivity is observed relative to CPIM. However, after thermal treatment of MMM30, the resulting IcMMM30 experiences a >1,000% increase in the H_2 permeability and a 66% increase in selectivity with respect to its untreated analogue MMM30 membrane, with an overall performance lying on the 2008 upper bound. As shown in Figure 9B, quantitatively similar results were observed for the CO_2/CH_4 gas pair at 35 °C and 1 atm. To note, data at 1 atm instead of 10 atm were used for the CO_2/CH_4 upper bound to avoid any artifacts due to plasticization of CPIM, CPIMTT and MMM30. To put these results in a broader perspective, in Figure 9A-B, the performance of the IcMMM30 is compared to that of state-of-the-art materials and, including other spirocyclic polymers.

As shown by Lozano et al., blending triptycene-isatin PPN with polyimides with no thermal treatment leads to an increase in permeability and a moderate drop in selectivity, while a marked permeability drop is observed in MMM30 relative to CPIM [43]. As discussed in Section 2.4.4, the ~65% CO_2 permeability decrease experienced by MMM30 relative to neat CPIM is ascribed to the presence of short-chain, oligomeric poly(THF) species, which are expected to partially occupy the PPN pores. Poly(THF) oligomers in MMM30, whose presence is confirmed by solid state ^{13}C CP/MAS NMR measurements, were found to be removed efficiently by the thermal treatment at 200°C. Interestingly, gas permeability in CPIM, which also contains poly(THF), is not significantly hindered, as it closely matches previously reported values [23]. This fact suggests that

poly(THF) preferentially occupies the PPN pores, more than the CPIM excess free volume pockets. To shed light on the fundamental origin of the observed transport behavior, in Section 2.4.4, gas permeability and selectivity were broken into their elementary sorption and diffusion contributions.

2.4.4. Pure Gas Sorption, Diffusion, and Dual Mode Modeling

Pure gas CO_2 and CH_4 sorption isotherms at 35 °C in CPIM, CPIMTT, MMM30 and IcMMM30 are shown in Figure 10A-B as a function of fugacity in the contiguous external gas phase. Fugacity was calculated using the Peng-Robinson equation of state, and experimental uncertainties were calculated using linear error propagation [89]. H_2 sorption in these polymers is below the limit of experimental detectability, therefore it could not be measured. Finally, diffusion coefficients were calculated from experimental permeability and sorption data, via the solution-diffusion model.

CO_2 and CH_4 sorption in CPIMTT are 59% and 44% higher than in neat CPIM, respectively. Similar increases in the sorption capacity have been reported in the literature for acid-containing polymers upon thermal decarboxylation [81]. More in general, thermal decarboxylation of polymers produces two competitive effects. First, it allows a more densely packed structure to form, due to free volume collapse (i.e., accelerated physical aging), which causes a moderate decrease in penetrant solubility; secondly, removing bulky -COOH groups creates new microcavities, increasing Langmuir's mode sorption. Sorption isotherms in Figure 10A-B, and solubility coefficients in Figure 10C indicate that the latter effect largely overwhelms the former. More specifically, the dual mode analysis, summarized in Figure 10A-B and Table 2, suggests that, for both CO_2 and CH_4, CPIMTT exhibits larger values of the Langmuir sorption capacity, C_H', relative

to CPIM, which confirms that thermal decarboxylation enhances, at least for these materials, sorption capacity. However, as discussed in the previous section, gas permeability decreases upon thermal treatment of CPIM, indicating that a parallel decrease of diffusivity must take place (Figure 10D). To explain this behavior on a more fundamental basis, diffusivity was broken into its Henry's (i.e., D_D) and Langmuir's (i.e., D_H) contributions using the partial immobilization model (Appendix A, Section A18). The dual mobility modeling points out two main effects. First, for both penetrants and in both CPIM and CPIMTT, D_H is one order of magnitude lower than D_D (Table 2). Moreover, in CPIMTT, the relative contribution of Langmuir's mode diffusion to the total overall diffusivity (i.e., $F = {D_H}/{D_D}$, Table 2) is almost doubled relative to CPIM, which explains why gas diffusivity and permeability decrease upon thermal treatment of CPIM. This physical picture is also consistent with the increase of the Langmuir's sorption capacity, C_H', observed in CPIMTT relative to CPIM, which causes sorption to increase upon thermal treatment.

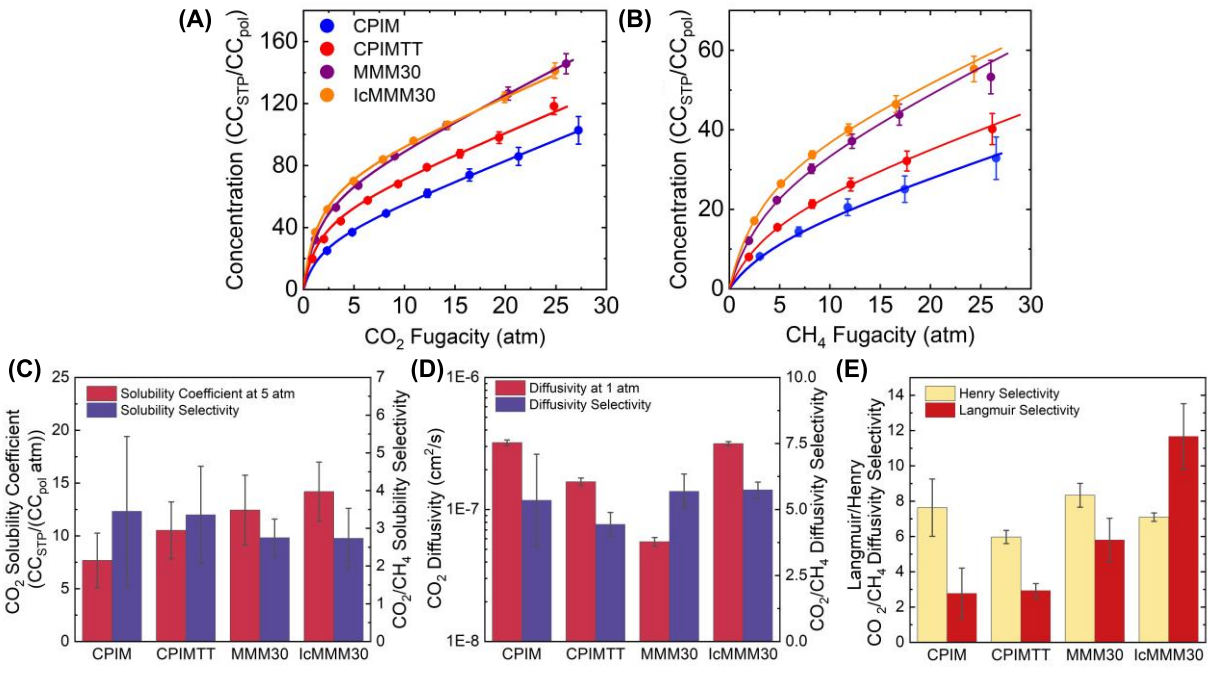


Figure 10. Pure (A) CO_2 and (B) CH_4 sorption isotherms in CPIM, CPIMTT, MMM30 and IcMMM30. (C) Pure CO_2 solubility coefficients and CO_2/CH_4 ideal solubility-selectivity. (D) Pure CO_2 diffusivity and CO_2/CH_4 ideal diffusivity-selectivity. (E) Henry's and Langmuir's mode CO_2/CH_4 diffusivity-selectivity (i.e., $D_D^{CO_2}/D_D^{CH_4}$ and $D_H^{CO_2}/D_H^{CH_4}$).

To avoid mathematical artifacts and enhance the physical meaning of the parameters, the dual mode fit of sorption data was run by constraining the slope of *ln(k_D)* and *ln(b)* versus gas critical temperature to be the same as the slope of *ln(S)* versus gas critical temperature at 10 atm, according to the procedure recommended by Smith et al. [23,122].

Incorporating 30 wt. % PPN causes a 37% increase in CO_2 sorption in MMM30 relative to CPIM, which is consistent with the much larger surface area exhibited by PPN relative to CPIM, as shown by BET measurements (PPN S_{BET} = 695 m^2/g > CPIM S_{BET} = 373 m^2/g). Notably, this fact indicates that CPIM is not extensively infiltrating and occupying the PPN's pores, thus ruling out any possible polymer interlocking through the PPN's porosity. This picture is also supported by simple geometric considerations. More specifically, the PPN cavities' diameter is less than 0.7 nm [1], while the cross-sectional diameter of bulky CPIM is expected to be 0.75 nm or higher, based on the end-to-end distance of the carbonyl oxygens in terephthalic acid. The lack of CPIM interlocking through the PPN porosity is also confirmed by the plasticization study, as discussed in Section 2.4.5.

However, gas permeability in MMM30 is lower than in CPIM, which can only be caused by a parallel decrease in diffusivity (Figure 10D). The CO_2 diffusion coefficient in MMM30 is almost six times lower than in CPIM due to *i)* the presence of triptycene units, which, as previously shown, slow down gas diffusion [86] and *ii)* oligomeric poly(THF) partially occupying the PPN pores, as discussed in Section 2.4.2. For both CO_2 and CH_4, MMM30 exhibits lower values of D_D and D_H

relative to neat CPIM. In the case of D_H, a larger decrease is observed for CH_4 (-82%), which is a bulkier penetrant relative to CO_2 (-70%).

Finally, IcMMM30 experiences no significant changes in gas sorption relative to MMM30, especially in the case of CO_2. In the case of CH_4 a slight increase is apparent within the experimental uncertainty. Therefore, the large permeability increase exhibited by IcMMM30 relative to the non-thermally treated MMM30 is essentially due to the diffusion behavior. This fact is confirmed by the simultaneous increase in D_H and D_D observed in IcMMM30 for both penetrants relative to MMM30. Interestingly, if we take CPIM as the basis of comparison, the larger permeability exhibited by IcMMM30 mirrors its larger gas sorption capacity relative to CPIM, while diffusivity is essentially the same for the two materials. In other words, while sorption tends to increase in the order CPIM < CPIMTT < MMM30 ≈ IcMMM30, diffusion first decreases in the order CPIM > CPIMTT > MMM30, and then for IcMMM30 it recovers a similar value as for the original CPIM sample. As shown in Table 2, the increase in CO_2 sorption observed from CPIM to IcMMM30 is due to a 114% increase in the Langmuir sorption capacity, C_H', while the Henry's mode contribution, k_D, exhibits a much smaller increase of 8.14%. Therefore, the increased sorption capacity exhibited by IcMMM30 relative to the baseline material, CPIM, is likely caused by *i)* the elimination of bulky -COOH groups, and *ii)* the additional surface area provided by the microporous PPN.

D_D and D_H values for CO_2 in IcMMM30 recover and slightly surpass the values observed in CPIM. In the case of CH_4, D_D recovers almost the same value as for CPIM, while D_H surpasses the value observed in CPIM by 170%. This trend is consistent with the increase in Langmuir capacity offered by the PPN and with the efficient removal of poly(THF) and subsequent pore activation of the PPN, as discussed in the structural analysis. Overall, CO_2/CH_4 diffusion

selectivity increases by 7.3% in IcMMM30 relative to CPIM, while solubility-selectivity experiences a 4.4% decrease. Fractional free volume (FFV) calculations seem to confirm this physical picture, with both CPIM and IcMMM30 exhibiting essentially similar FFVs of 21.0% (Table A3). A further discussion on the role and interpretation of FFV values can be found in Appendix A, Section A4.

Interestingly, while Henry's CO_2/CH_4 diffusion selectivity (i.e., $D_D^{CO_2}/D_D^{CH_4}$) remains approximately constant among samples, Langmuir's CO_2/CH_4 selectivity (i.e., $D_H^{CO_2}/D_H^{CH_4}$) increases in the order CPIM ≈ CPIMTT < MMM30 < IcMMM30. This behavior is primarily attributed to the presence of triptycene units in the PPN structure, which contain configurational free volume (i.e., the intramolecular spaces within triptycene moieties), providing an effective enhancement of the size sieving ability in specifically the Langmuir mode of transport, in accordance with the mechanism discussed by Box et al. [86].

In conclusion, the observed increase in CO_2 permeability in the order MMM30 < CPIMTT ≈ CPIM < IcMMM30 is due to increases in both CO_2 sorption and diffusivity. The slight increase in diffusivity selectivity is offset by a small decrease in sorption selectivity, which renders the overall CO_2/CH_4 permeability selectivity essentially constant across samples.

Table 2. Summary of the dual mode model fittings. Error bars were obtained using the Jackknife resampling technique. Parameters were fit with respect to penetrant fugacity and were constrained using the technique reported in [23,122].

sample	*gas*	k_D *(CC_{STP} /(CC_{pol} atm))*	C'_H *(CC_{STP}/CC_{pol})*	b *(atm^{-1})*	$D_D \times 10^7$ *(cm^2/s)*	$D_H \times 10^8$ *(cm^2/s)*	*F*
CPIM	*CO_2*	*2.58 ± 0.04*	*34.0 ± 0.98*	*0.597 ± 0.03*	*15.57 ± .03*	*3.4 ± 0.3*	*0.022*

	CH_4	0.81 ± 0.17	14.4 ± 6.4	0.192 ± 0.040	2.0 ± 0.4	1.2 ± 0.6	0.060
CPIMTT	CO_2	2.68 ± 0.1	50.7 ± 2.0	0.680 ± 0.043	9.8 ± 0.4	4.4 ± 0.4	0.045
	CH_4	0.88 ± 0.04	21.3 ± 1.2	0.226 ± 0.012	1.64 ± 0.08	1.5 ± 0.2	0.092
MMM30	CO_2	3.26 ± 0.10	64.5 ± 3.0	0.682 ± 0.070	4.0 ± 0.2	1.1 ± 0.2	0.027
	CH_4	1.20 ± 0.09	29.5 ± 2.5	0.257 ± 0.015	0.48 ± 0.03	0.18 ± 0.02	0.038
IcMMM30	CO_2	2.79 ± 0.050	73 ± 1	0.713 ± 0.028	25.4 ± 0.5	11.0 ± 0.5	0.043
	CH_4	1.10 ± 0.02	34.7 ± 0.7	0.286 ± 0.007	3.6 ± 0.1	0.9 ± 0.1	0.026

2.4.5. CO_2-induced Plasticization Study

A dedicated plasticization study was run by measuring, in the series of four materials, CO_2 permeability at 35°C up to 50 atm. In Figure 11A, the plasticization behavior of non-thermally treated samples, i.e., CPIM and MMM30, is shown as a function of pressure. CPIM plasticizes at about 7 atm, which is in reasonable agreement with previously reported data [23]. Recently, Matesanz-Niño et al. showed that hydrogen bonding between an acid-containing polyimide and triptycene-isatin PPN was able to suppress CO_2-induced plasticization up to 30 atm, thus it was hypothesized that hydrogen bonding between the -COOH groups in CPIM and amide groups in the PPN may lead to plasticization resistance [123]. In striking contrast with the expected behavior, MMM30 suffers from an even stronger plasticization propensity relative to CPIM, with the onset of plasticization showing up at about 4 atm. The stronger plasticization propensity exhibited by MMM30 relative to neat CPIM indicates that *i)* the polymer-filler physical interactions (e.g., CPIM threading through or interlocking with the PPN) is not occurring, which mirrors the results of the

sorption-diffusion study discussed in the previous section, and that *ii)* significant CPIM-PPN chemical interactions, such as hydrogen bonding, is not occurring in non-thermally treated mixed matrices.

The plasticization behavior of thermally treated samples is shown in Figure 11B. Thermally treated CPIM, i.e., CPIMTT, plasticizes at about 15 atm CO_2. The enhanced plasticization resistance exhibited by the latter polymer relative to CPIM is consistent with its crosslinked structure resulting from thermally induced decarboxylation. Remarkably, IcMMM30 does not exhibit any detectable CO_2-induced plasticization up to 50 atm, which places this material among the best reported in terms of plasticization resistance. As shown in Figure 11C, the plasticization resistance exhibited by IcMMM30 is comparable only to that of a handful of other polymeric membrane materials, such as membranes fabricated with branched MOFs [124], polymers with ultra-rigid sidechain porosity [125], and advanced crosslinked polyimides exhibiting π-stacking interactions [81]. It should be noted that, for this test, each CO_2 pressure was held for 24h, thus IcMMM30 was exposed to high pressures of CO_2 for 14 days by the end of the experiment, which makes its plasticization resistance even more remarkable. Interfacial polymer-PPN crosslinking is responsible for the excellent plasticization resistance exhibited by IcMMM30. Previously, Jiang et al. reported high plasticization resistance in membranes fabricated by mixing poly(ethylene oxide) with UiO-66 MOFs exhibiting polymer-filler crosslinking relative to composites with no interfacial crosslinking [126], a result that appears to confirm the trend observed in this study.

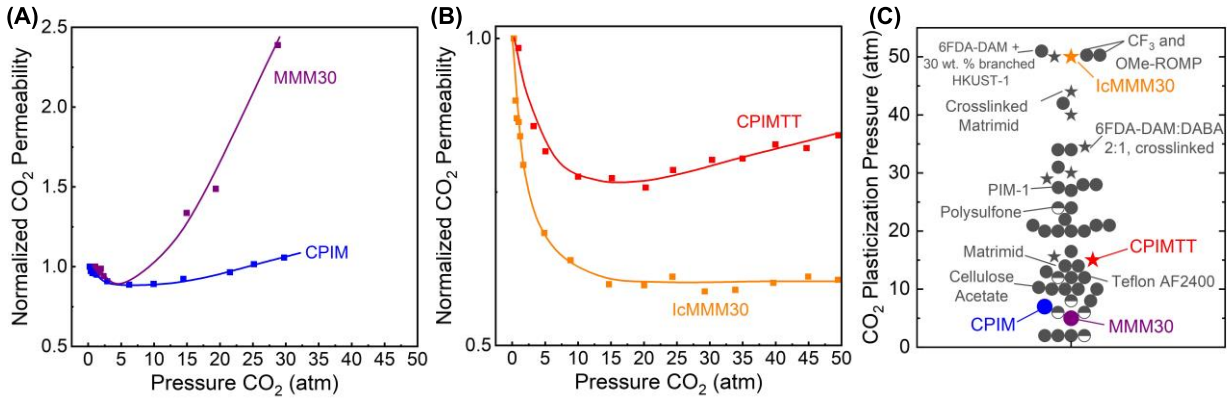


Figure 11. CO2 plasticization test for (A) untreated samples (i.e., CPIM and MMM30) and (B) thermally treated samples (i.e., CPIMTT and IcMMM30). (C) Review of CO2 plasticization pressures for the materials reported in this study, as well as state of the art materials. Stars represent crosslinked films, and half-filed symbols are thin films (< 1 μm). Data for non-crosslinked film are from ref. [125], and data for crosslinked and mixed-matrix films are tabulated in Table A9.

While polymer-filler crosslinking seems to be the key factor, any effects due to simple physical interactions between CPIM and the PPN should be ruled out. The thermal treatment was performed at 200°C, which is well below the glass transition temperature of PIM materials (i.e., > 400°C) [127]. Additionally, DSC measurements confirmed that none of the studied samples exhibited glass transitions or any relaxations below 300°C, as shown in Appendix A, Section A7. This fact, in conjunction with the rigidity exhibited by CPIM and its bulky structure, would exclude the occurrence of any CPIM interlocking or threading through the cavities of the PPN (whose microcavities are primarily <0.7 nm in diameter [1]) as a result of thermal treatment.

The plasticization resistance exhibited by IcMMM30 is confirmed, from a thermodynamic standpoint, by the analysis of the isosteric heats of sorption (Figure 12). Being a non-polar, non-plasticizing gas, CH_4 should exhibit almost no variations in the energetics of interaction with the

polymer phase, and this is seen to be the case, where the isosteric heat of CH_4 sorption is, within the experimental uncertainty, constant as a function of CH_4 concentration in the polymer (cf., Figure 12A). In contrast, CO_2, which is a more condensable quadrupolar gas, is known to plasticize polymers. As shown in Figure 12B, the isosteric heat of CO_2 sorption in CPIM, CPIMTT and MMM30 exhibit a well detectable minimum as a function of CO_2 concentration in the polymer. The presence of this minimum indicates that positive deformation work is required to accommodate additional CO_2 molecules in the polymer by pulling apart polymer chains. Interestingly, the concentration at which the minimum appears substantially increases by moving from CPIM to CPIMTT as a consequence of crosslinking. Remarkably, the CO_2 isosteric heat of sorption in IcMMM30 does not exhibit any minimum, as it monotonically decreases with increasing CO_2 concentration. This fact indicates that little or no deformation work is being provided to pull polymer chains apart for accommodating additional penetrant molecules in this sample, which mirrors the results of the plasticization study, confirming that strong, irreversible polymer-filler inter-crosslinking is the key factor leading to superior plasticization resistance. Thus, engineering the polymer-filler interface with covalent bonds appears to be a viable strategy to simultaneously tackle the problems of membrane permeability, selectivity, and stability without adding too much complexity to the material synthesis or membrane fabrication process.

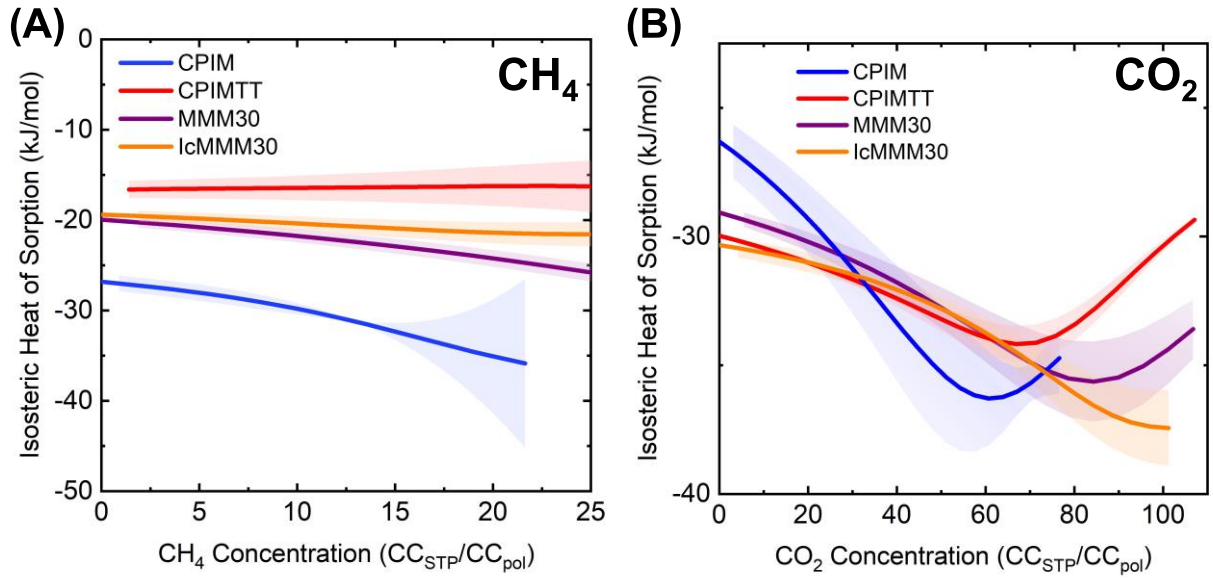


Figure 12. Isosteric heats of sorption for (A) CH_4 and (B) CO_2 in CPIM, CPIMTT, MMM30, and IcMMM30. Continuous lines denote experimentally determined values, and the shaded region surrounding each line is the experimental error determined, at each concentration, via linear error propagation and the standard error of linear regression [128].

To better highlight the excellent stability exhibited by IcMMM30 and put it in a broader perspective, in Table A9 we compare the plasticization pressures (i.e., the pressure at which a minimum in CO_2 permeability is observed) across several polymers. Although comparing each polymer's plasticization propensity on a pressure basis is easy to do, it is more interesting, from a fundamental perspective, to compare the plasticization onset across materials at a given number of CO_2 molecules accommodated in the polymer matrix (i.e., at a given concentration), as shown in Table 3.

Table 3. Comparison of the pressures, permeabilities, and concentrations at which CO_2-induced plasticization occurs in CPIM, CPIMTT, MMM30, IcMMM30 and state of the art materials. Literature data are taken from ref. [129].

polymer	*CO_2 plasticization pressure (atm)*	*CO_2 permeability at plasticization (Barrer)*	*CO_2 concentration at plasticization (CC_{STP}/CC_{pol})*	*temperature (°C)*
CPIM	*7*	*546 ± 14*	*45 ± 2*	*35*
CPIMTT	*15*	*368 ± 16*	*83 ± 2*	*35*
MMM30	*5*	*196 ± 4*	*66 ± 4*	*35*
IcMMM30	*> 50*	*976 ± 26*	*> 193 ± 2*	*35*
Polysulfone	*34*	*3.6*	*47*	*23*
Matrimid®	*12*	*4.8*	*47*	*22*
P84	*22*	*0.92*	*48*	*23*
Cellulose acetate	*11*	*6*	*31*	*27*
Cellulose triacetate	*10*	*7.3*	*31*	*24*

All polymers presented in this study, apart from the neat CPIM, plasticize at higher CO_2 concentrations relative to previously reported polymers, indicating that PIM derivatives provide an excellent platform of materials to design highly stable membranes. Interestingly, MMM30, which is the lowest performance material among those studied in this work (Figure 11), exhibits a much better stability when its performance is evaluated on concentration basis. Specifically, MMM30 plasticizes at a CO_2 content of about 66 CC_{STP}/CC_{pol}, while P84 polyimide, one of the most rigid materials used for organic solvent separations, plasticizes at a CO_2 content of 48 CC_{STP}/CC_{pol}. This comparison is useful to put our results in broader perspective and indicates that comparing plasticization propensity on solubility basis is formally more correct than pressure-based comparisons.

Data in Table 3 are summarized in Figure 13, where plasticization CO_2 permeability is compared across polymers in a 3D plot, as a function of plasticization pressure and plasticization

CO_2 concentration. Remarkably, IcMMM30 stands out among state-of-the-art materials, exhibiting, simultaneously, no plasticization up to 50 atm, high plasticization CO_2 permeability, and superb CO_2 plasticization concentration.

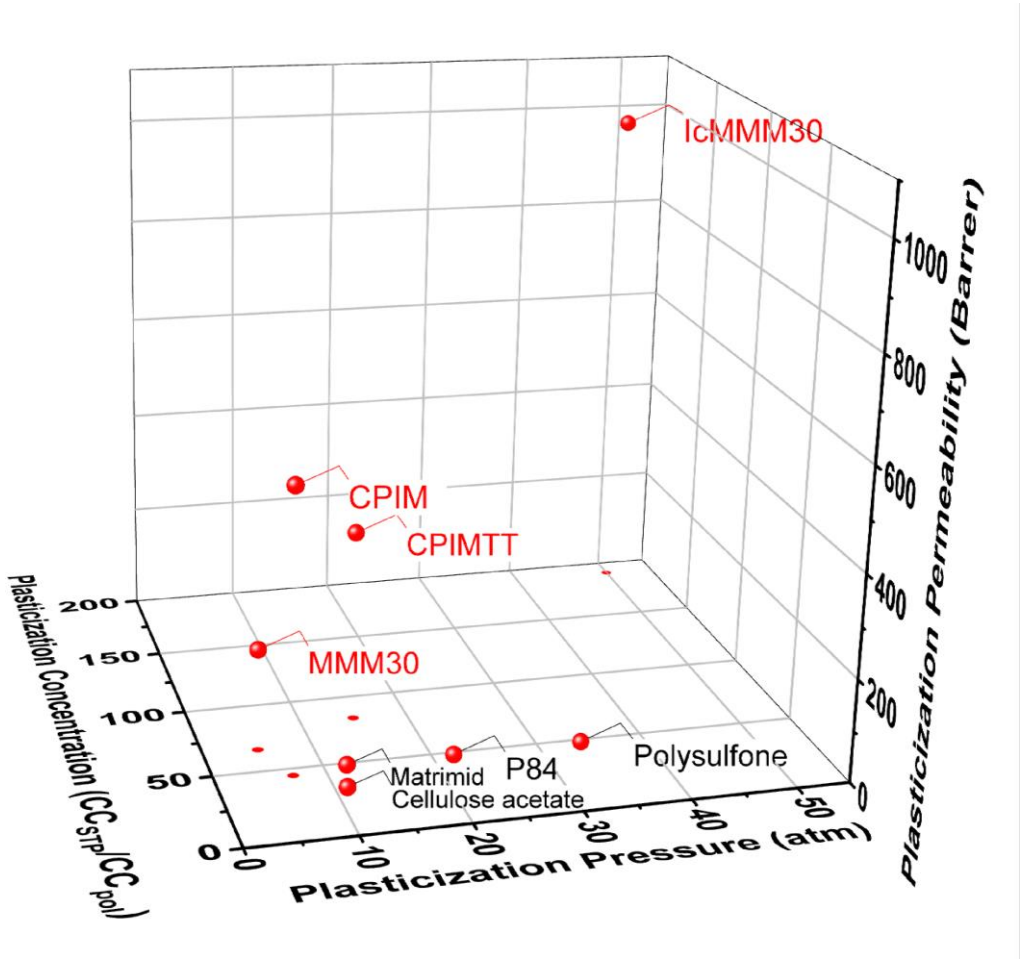


Figure 13. Plasticization CO_2 permeability vs. plasticization pressure and plasticization CO_2 concentration in several glassy polymers of interest in membrane separations. IcMMM30 outperforms other materials in all three axes.

2.5. Conclusions

Free-standing, mechanically robust inter-crosslinked mixed matrix membranes (IcMMMs) based on carboxylated polymer of intrinsic microporosity-1 (CPIM) and triptycene-isatin porous

polymer networks (PPNs) were synthesized and characterized. Mutual polymer-filler crosslinking, through a free-radical decarboxylation mechanism, was accomplished via a mild thermal treatment at 200 °C under vacuum for 24h. It was shown that the main compositional changes resulting from the crosslinking process were minor decarboxylation, removal of low-molecular weight contaminants, and formation of hydrolytically stable crosslinks. The resulting IcMMMs perform on the 2008 upper bound for a variety of gas separation applications and exhibit ultra-high stability against plasticization upon prolonged CO_2 exposure up to 50 atm.

To isolate and quantify the individual and synergistic contributions of physical vs chemical polymer-filler interactions to the IcMMMs performance, their structure and properties were compared *vis-à-vis* with those of neat CPIM, thermally treated CPIM, and CPIM-PPN mixed matrix membranes. The individual and synergistic effects of PPN incorporation and thermal treatment were studied via a detailed structural and transport analysis to demonstrate that polymer-filler crosslinking is the key factor enabling simultaneously high permeability, high selectivity, and superior long-term stability against plasticization. It was shown that the high permeability and selectivity exhibited by IcMMM30 stem from its high sorption capacity, and Langmuir's size-sieving ability, respectively. Removal of the low-molecular weight contaminants was also found to have an activating effect on the IcMMMs. IcMMMs stand out in terms of plasticization CO_2 permeability, plasticization pressure, and plasticization CO_2 concentration relative to conventional rigid glassy polymers, such as polyimide P84, Matrimid®, cellulose acetate and polysulfone.

One advantage of the fabrication approach developed in this work, due to the lower crosslinking temperature employed relative to prior studies, is its compatibility with conventional thin-film composite support layers such as PDMS or PAN. With the foundational understanding

of this material platform established, the following chapters investigate the physical aging and organic solvent transport characteristics of the newly synthesized materials.

Chapter 3. Elucidating the Molecular Mechanisms by which Porous Polymer Networks Affect Structure, Aging Propensity, and Selectivity of Microporous Glassy Polymer Membranes using a Multiscale Approach

3.1. Abstract

Microporous glassy polymer membranes suffer from physical aging, which adversely affects their performance in the short timeframe. We show that the aging propensity of a model microporous polymer, poly(1-trimethylsilyl-1-propyne) (PTMSP), can be effectively mitigated by blending with as little as 5 wt % porous polymer network (PPN) composed of triptycene and isatin. The aging behavior of these materials was monitored via N_2 pure gas permeability measurements over the course of three weeks, showing a 14% decline in PTMSP blended with 5 wt. % PPN vs. a 41% decline in neat PTMSP. Noteworthy, PPNs are two orders of magnitude cheaper than the porous aromatic frameworks previously used to control PTMSP aging.

A variety of experimental and computational techniques, such as Positron Annihilation Lifetime Spectroscopy (PALS), free volume measurements, cross polarization/magic angle spinning (CP/MAS) ^{13}C NMR, transport measurements and molecular dynamics (MD) simulations were used to uncover the molecular mechanisms leading to enhanced aging resistance. We show that partial PTMSP chain adsorption into the PPN surface porosity reduces the PTMSP local segmental mobility, leading to improved aging resistance. Permeability coefficients were broken into their elementary sorption and diffusion contributions, to elucidate the mechanism by which the reduced PTMSP local segmental mobility affects selectivity in gas separation applications. Finally, we demonstrate that in these systems, where both chemical and physical interactions take

place, transport coefficients must be corrected for thermodynamic non-idealities to avoid erroneous interpretation of the results.

3.2. Introduction

The 6th Assessment Report by the Intergovernmental Panel on Climate Change (IPCC) highlighted that the global average temperature increase relative to pre-industrial levels will likely exceed 1.5 °C by 2050, which threatens transgression of a variety of global physical and ecological tipping points.[130,131] To avoid this scenario, net carbon emissions must be drastically reduced by implementing carbon capture and by adopting more energy-efficient separation processes. Membrane-based technologies could revolutionize separation processes by enhancing their efficiency by up to 90% and, as such, they represent a viable alternative to conventional thermal-based separations.[4]

Despite their promise, several issues stand in the way of high performance membrane materials, such as their unstable behavior under long-term industrial operations and harsh conditions,[22,57] a lack of economically attractive permeability-selectivity combinations,[58] and difficulty encountered in processing and scaling up materials into defect-free membrane modules.[8,22] In this scenario, microporous glassy polymers have become desirable membrane materials due to their higher permeability-selectivity combinations relative to rubbery polymers.[21] However, the conformational free volume in conventional glassy polymers, which is a categorization of excess free volume, is due to inefficient chain packing during membrane fabrication and, as such, it relaxes over time.[132–135] This phenomenon, known as physical aging, is particularly pronounced when the membrane is fabricated as a thin film ($\leq$ 1 μm thick).[136,137]

Physical aging causes a permeability loss that reduces the membrane productivity, typically within the first few weeks of operation.[22]

A plethora of synthesis and post-synthesis modification approaches have been devised to control physical aging in glassy polymers and tailor their transport properties. Incorporating iptycenes (e.g., triptycene and pentiptycene groups) into polymer backbones has been one successful approach, due to the intrinsic molecular cavities inside iptycenes, which provide *configurational free volume*.[32,86,135] In contrast to conformational free volume, configurational free volume is non-collapsible and exhibits a highly regular size distribution.[32,86] Hence, microporous glassy polymers containing iptycenes have emerged as a broad class of materials that guarantees performance exceeding the Robeson upper bound[58,59,138–142] while exhibiting improved resistance to physical aging relative to conventional polymers containing only conformational free volume.[32,143,144]

Another very successful approach to manage physical aging in high free volume microporous glassy polymers, proposed in 2014 by Lau et al.,[36] consists of blending with porous fillers. For example, adding 10 wt. % of a porous aromatic framework (PAF) into 100 μm thick poly(1-trimethylsilyl-1-propyne) (PTMSP) films reduces the CO_2 permeability loss from -38% (neat PTMSP) to -7% (PTMSP+10% PAF-1) over 240 days, while increasing the CO_2 permeability by ~30% at essentially constant CO_2/N_2 selectivity (~7), relative to neat PTMSP. Despite this impressive result, PAF-1 costs more than $500/g,[145] which is one order of magnitude above the industrially acceptable cost of $20-50/g for selective layer materials[146]. Thus, there is a strong drive to discover *i)* cheaper fillers exhibiting a performance comparable to PAFs, as well as *ii)* the molecular mechanism by which these fillers control the aging rate.

To fill this knowledge and technological gap, porous polymer networks (PPNs) are considered here. PPNs are highly-crosslinked, amorphous, microporous materials derived from the polymerization of readily available organic precursors.[1] Due to their high surface areas, tunable surface properties, low cost, and compatibility with organic polymers, PPNs have the potential to tame the physical aging of glassy polymers and the compatibility issues experienced by mixed matrix membranes containing porous inorganic fillers.[43,147,148] However, the mechanism by which PPNs affect physical aging when incorporated into glassy polymers is poorly understood. The overarching goal of this study is to shed fundamental light on this mechanism, providing an opportunity to design aging-resistant membrane systems in a rational fashion.

In this study, a PPN synthesized using triptycene and isatin as monomers[1] was blended with a model high free volume microporous glassy polymer, PTMSP, at 5 and 20 wt. %. The two blends are denoted as PTMSP-5PPN and PTMSP-20PPN, respectively.[149] Blending resulted in a significant reduction in the physical aging rate of PTMSP. Specifically, N_2 permeability dropped from -41% for neat PTMSP to only -14% in the PTMSP-PPN blends after 21 days, an effect that is ascribed to the unique structure of the PPN used and its interaction with PTMSP. First, the triptycene units incorporated in the PPN provide aging resistance in the form of non-collapsible configurational free volume. Moreover, we hypothesize that the PPN network may reduce the PTMSP local segmental mobility by an interaction between the PTMSP backbone and surface cavities in the PPN.[36,150] To test this hypothesis, the structure of PTMSP-PPN blends was thoroughly investigated using scanning electron microscopy (SEM), positron annihilation lifetime spectroscopy (PALS), free volume analysis, and cross polarization/magic angle spinning (CP/MAS) ^{13}C NMR. Pure gas (N_2, CH_4, and CO_2) permeability, solubility and diffusivity were also measured. Molecular dynamics (MD) simulations were also implemented to interrogate the

PTMSP-PPN structure, their interactions, the effect of PPN incorporation on the transport properties, and the mechanism underlying physical aging inhibition.

3.3. Experimental Methods

Details pertaining to materials, synthesis and characterization protocols are provided in Appendix B, Section B1 (materials), B2 (Triptycene-Isatin synthesis, Figure B1), and B3 (characterization protocols). Neat PTMSP and blends of PTMSP containing up to 20 wt.% triptycene-isatin PPN will be considered in this study. The membrane fabrication protocol is provided in Appendix B, Section B4.

Fourier Transform Infrared Spectroscopy (FTIR) (Appendix B, Section B3.1 and Section B5, Figure B2), Thermogravimetric Analysis (TGA) (Appendix B, Section B3.2 and Section B13, Figure B12), Scanning Electron Microscopy (SEM) (Appendix B, Section B3.3), and Positron Annihilation Lifetime Spectroscopy (PALS) (Appendix B, Section B3.4/B6) were used for materials characterization. For PALS measurements, PTMSP-15PPN (PTMSP with 15 wt% PPN) was used in place of PTMSP-20PPN. Density measurements were run using an Archimedes balance (*Mettler Toledo*), and fractional free volume for freshly casted membranes was estimated using the group contribution method reported by Wu et al. (Appendix B, Section B3.5, Eq. B2-3).[151]

The details of the molecular dynamics (MD) simulations are provided in Appendix B, Section B7. Neat PTMSP and PTMSP-PPN blends were simulated with densities comparable to those observed experimentally. These structures were used to simulate molecular interactions, differences in gas diffusion coefficients, and identify preferential pathways or sorption sites for gas molecules in the polymer blends.

Pure-gas CH_4, N_2, and CO_2 sorption and permeation measurements were conducted at 35°C (Appendix B, Sections B8, B10 and B12, Figures B7-10, Table B4), whilst the materials aging propensity was tested via pure-gas N_2 permeability measurements at 35 °C and 1.4 atm (i.e., 20 psi) over the course of 500 hours (Appendix B, Section B8). The rate of physical aging was modeled by incorporating a free volume term in the Struik model, as described in Section 3.4.2 and in Appendix B, Section B9, Figure B5.

Solid state ^{13}C T_1 nuclear magnetic resonance (NMR) measurements were performed using cross-polarization/magic angle spinning (CP/MAS) (Appendix B, Section B11).

3.4. Results and Discussion

3.4.1. Membrane Fabrication, Characterization, and Modeling

Defect-free membranes were fabricated via the solution casting method described in Appendix B, Section B4. The chemical structures of PTMSP and triptycene-isatin PPN, shown in Figure 14A-B, suggest that PTMSP-PPN chemical interactions, such as hydrogen bonds, are unlikely to form, since PTMSP contains no hydrogen bond donors or acceptors. This picture is confirmed by FTIR (Appendix B, Section B5, Figure B2), which revealed no significant shifts in the characteristic peaks for either PTMSP or PPN in the blends. Scanning electron microscopy on PTMSP, PTMSP-5PPN, and PTMSP-20PPN membrane cross-sections was also used to investigate the PTMSP-PPN compatibility (Figure 14C-E). Unlike in hybrid composite membranes,[8,152] no interfacial defects or significant PPN aggregation are observed. Thus, it is concluded that, despite the lack of polymer-filler specific chemical interactions, defect-free membranes can be fabricated at loadings as high as 20 wt. %. As shown later in this study, this is made possible by PTMSP-PPN physical interactions, such as polymer adsorption in the PPN surface porosity.

The PTMSP chain packing is significantly affected by the blend composition, as shown by free volume cavity size distributions studied via Positron Annihilation Lifetime Spectroscopy (PALS, Figure 14F and Table B1). Notably, PALS measurements were run one month after casting the membranes. Neat PTMSP exhibits cavities with average diameters of 0.55, 1.3, and 1.74 nm, which are referred to as cavities 1, 2, and 3, respectively. The triptycene-isatin PPN exhibits cavities with diameters of 0.32 and 0.95 nm. Lopez-Iglesias et al.[1] and Soto et al.[45] previously reported pore diameters of approximately 0.35, 0.526, and 0.824 nm for triptycene-isatin PPN based on CO_2 adsorption isotherms at 0°C (273.15 K) and DFT calculations, which are in reasonable agreement with the 0.32 nm and 0.95 nm diameter pores detected experimentally by PALS.

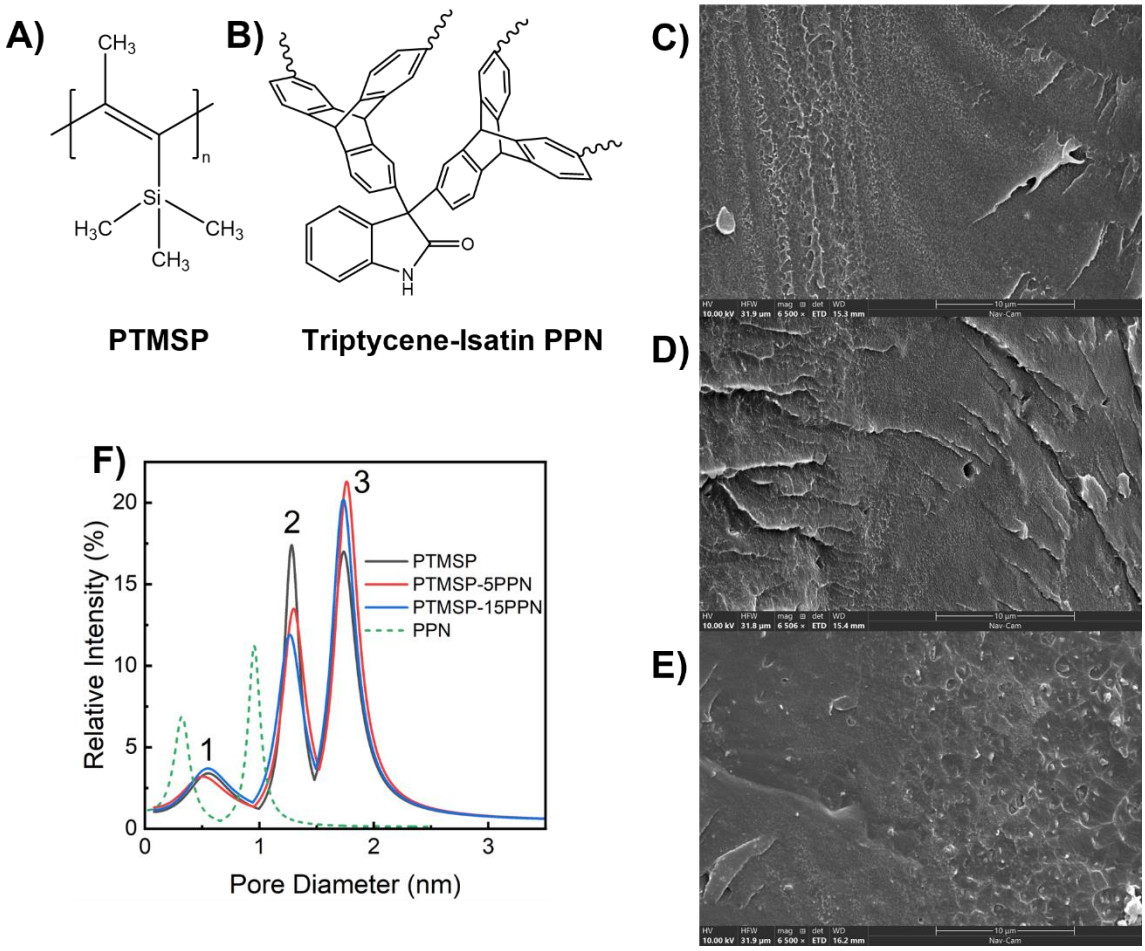


Figure 14. Chemical structure of PTMSP (A) and the triptycene-isatin PPN (B). Scanning Electron Micrographs of the membrane cross-section after fracture in liquid nitrogen: PTMSP (C), PTMSP-5PPN (D), and PTMSP-20PPN (E) (scale bar: 10 μm). (F) Results from Positron Annihilation Lifetime Spectroscopy (PALS) plotted as pore size distributions for PTMSP, PTMSP-5PPN, and PTMSP-15PPN.

In the blends, the best fit of the PALS data, using the Tao-Eldrup (RTE) equation[153,154] (Appendix B, Section B3.4, Eq. B1) reflected a cavity size distribution qualitatively similar to that exhibited by neat PTMSP, with no additional peaks corresponding to the cavity sizes of the neat

PPN. This behavior has also been reported in the PALS measurements of other nanocomposites.[155] However, the relative intensities of cavities 2 and 3 changed upon blending, which is interpreted to be the influence of the PPN on the PTMSP chain packing. For example, the intensity of cavity 3 in the PTMSP-5PPN and PTMSP-15PPN (i.e., PTMSP containing 15 wt% PPN) blends exhibit a 25% and 18% increase, respectively, relative to PTMSP. This observed preservation of larger cavities in the blend supports the hypothesis that PPN might inhibit the physical aging of PTMSP, and similar preservations of microcavity intensities upon aging in nanocomposites were observed by Koschine et al.[155] Previous studies[156–159] have demonstrated, using PALS, that physical aging of PTMSP results in a decrease of the intensity of the largest free volume elements (i.e., cavity 3) from 30% to 15% relative to freshly cast PTMSP. The hindered large cavity collapse in the PTMSP-5PPN and PTMSP-15PPN membranes suggests that PPN directly inhibits the excess free volume collapse associated with physical aging.

In sharp contrast, a decline in the intensity of cavity 2 pores was observed with increasing PPN loading, i.e., -22.4 % in PTMSP-5PPN and -31.6 % in PTMSP-15PPN relative to neat PTMSP. Consolati et al. theorized that the medium sized free volume cavities (i.e., cavity 2, 1.3 nm) are "channel-like" in that they connect the various larger sized cavities in PTMSP (i.e., cavity 3, 1.74 nm).[159] Thus, the observed reduction in the sized number of medium cavities in the PTMSP-PPN blends may indicate the disruption of connectivity between the larger cavities in the polymer blend. As discussed in Section 3.4.5**,** with this feature is correlated the decrease in the gas diffusivity and minor changes in the ideal gas selectivity for several light gas pairs.

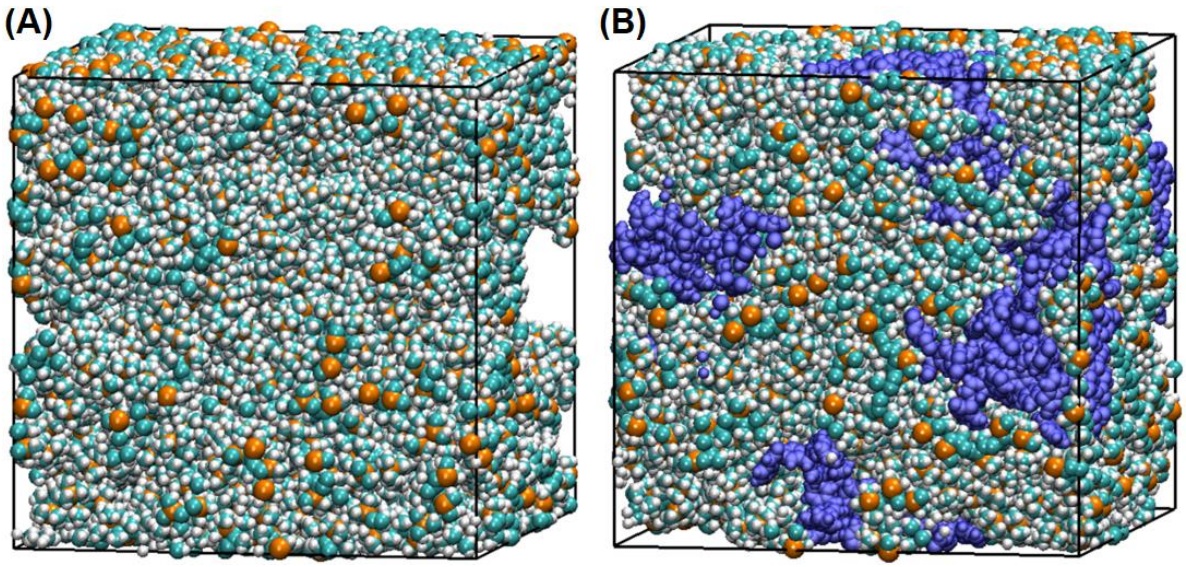


Figure 15. Simulation snapshots prepared with densities matching the experimental data for PTMSP (A) and PTMSP-20PPN (B). Color code: cyan (carbon), white (hydrogen), and orange (silicon). For better visual distinction, in (B), atoms belonging to the PPN are colored in purple. Box side lengths are approximately 8 nm.

MD simulations were run to rationalize and support the experimental findings and achieve a deeper molecular level understanding of the blended membranes. The neat PTMSP membrane was simulated with a system of 20 chains, each consisting of 101 repeat units, as shown in Figure 15A. Likewise, the PTMSP-20PPN membrane was simulated using 20 PTMSP chains and 5 PPN particles, each composed of 22 triptycene subunits and 45 isatin subunits. Dispersion of the PPN into the PTMSP matrix can be visualized from a snapshot, shown in Figure 15B, of the PTMSP-20PPN system. Figure 15B shows the amorphous arrangement of both the PTMSP chains and PPN particles, with no defects at the PTMSP-PPN interface, which further indicates their compatibility.

Further details of these simulations and the downstream analyses are provided in Section B7 of Appendix B, while the main conclusions are summarized in the forthcoming sections.

The remainder of this chapter is dedicated to investigating how the inclusion of PPN in PTMSP affects the resulting membrane material properties and to elucidating the potential molecular mechanism by which small molecule transport and physical aging are affected by PPNs.

3.4.2. Physical Aging Study

Physical aging in glassy polymers occurs due to relaxation of excess free volume as the material approaches its equilibrium density, which translates to a decline in gas permeability over the short time frame.[160] Long-term aging tests are typically run using N_2 as gas probe. Indeed, being a non-plasticizing gas, N_2 provides a reliable assessment of aging without superimposing it with other phenomena, such as swelling and plasticization, which produce the opposite effect on permeability.

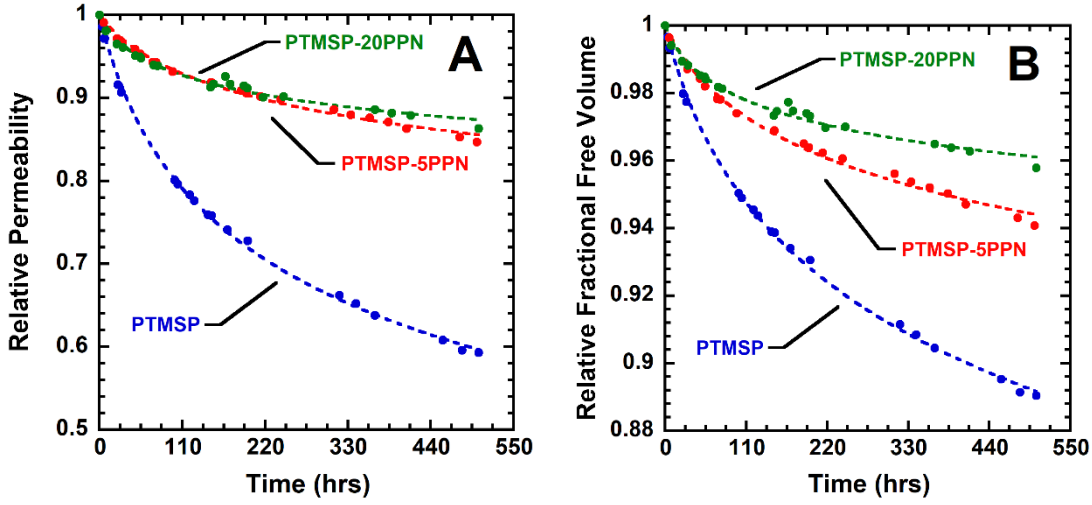


Figure 16. Physical aging of approximately ~20-40 μm thick films of PTMSP, PTMSP-5PPN, and PTMSP-20PPN blends, tracked via pure N_2 permeability measurements conducted at 35°C (308.15 K) and 1.4 atm (A), where the dotted line are the permeabilities calculated from Eqs. 1 and 2. The corresponding reduction in free volume is also shown (B). A modified Struik model[136,160]

was fit and plotted for each sample; the results are shown using dotted lines. The fitted values for the modified Struik model are provided in Table 4.

Figure 16A shows the pure N_2 permeability in PTMSP, PTMSP-5PPN, and PTMSP-20PPN measured over the course of ~500 hours (i.e., 3 weeks). All samples were between 20 and 40 μm thick. The specifics of the permeability and physical aging measurement protocols are provided in Appendix B, Section B8. A slower decrease in permeability for PTMSP-5PPN and PTMSP-20PPN blends is observed relative to neat PTMSP. Specifically, after 500 hours, the N_2 permeability in neat PTMSP drops to 59% of its original value (i.e., permeability drops by 41% from the initial value), while PTMSP-5PPN and PTMSP-20PPN retain approximately 86% of their original permeability values (i.e., permeability drops by 14% from the initial value). Notably, not much difference in the physical aging rate between PTMSP-5PPN and PTMSP-20PPN is observed, which suggests that small amounts of PPN are sufficient to delay aging, while additional PPN may not provide detectable benefit, all other experimental conditions being the same.

To shed fundamental light on the PPN-PTMSP interaction and its effect on the physical aging behavior, the Struik model was used:[136,160]

$$\frac{df}{dt} = \frac{-(f - f_e)}{\tau} = \frac{-(f - f_e)}{\tau_\infty exp[-\gamma(f - f_e)]} \tag{12}$$

where f is the fractional free volume of the polymer phase, f_e is the equilibrium fractional free volume, and τ is the characteristic relaxation time. In the Struik self-retarding aging model, relaxation becomes increasingly hindered as the polymer phase becomes denser, thus τ is expanded to include τ_∞, the relaxation time at equilibrium, and γ, a constant that characterizes how the relaxation time changes with excess free volume (i.e., $f - f_e$). Fractional free volume, f, was correlated to gas permeability, *P*, using Equation 13:

$$P = A\, e^{-\frac{B}{f}} \tag{13}$$

where P is the gas permeability, and A and B are constants that depend on the gas being used. A and B were obtained for N_2 by fitting Equation 13 to the N_2 permeability and fractional free volume data for the fresh PTMSP, PTMSP-5PPN, and PTMSP-20PPN films from this study (Figure B5), where f is calculated from density measurements and Bondi's theory (Appendix B, Section B3.3, Eq. B3), as well as fitting the N_2 permeability and fractional free volume data for a fresh and 4-year aged PTMSP film from Yampolskii et al.[158], who reported permeabilities and film densities using a similar method as the one used in this study. The linearized fitting curve for Equation 13, correlation parameters (i.e., A and B), and their uncertainties are provided in Appendix B, Section B9, Figure B5.

The Struik model parameter fittings and sample thicknesses are shown in Table 4, and the overall fittings are shown in Figure 16B. Based on the Struik model parameters, the incorporation of PPN into PTMSP appears to significantly hinder physical aging. Specifically, this phenomenon is evidenced through the trends of τ_∞ and f_e as a function of PPN content. The natural logarithm of the characteristic relaxation time increases by approximately 95.5% from neat PTMSP to PTMSP-20PPN. This increase in τ_∞ indicates a hindered local segmental mobility, resulting in a slower physical aging rate. In accordance with the PALS results, the incorporation of PPN appears to maintain open the 'Cavity 3' free volume elements in the PTMSP. Additionally, the fitted equilibrium free volume, f_e, increases due to PPN loading, with no significant differences observed between 5 wt.% and 20 wt. %, and thus the net driving force for free volume collapse could be decreased as well due to PPN incorporation.

Table 4. Struik Model parameters for the various PTMSP / PPN blends considered. Parameter uncertainties were found using the Hessian matrix method described in Appendix B, Section B10.

material	*ln(τ∞)a (--)*	*f_e (--)*	*γ (--)*	*sample thickness (μm)*
PTMSP	*22 ± 3*	*0.059b ± 0.025*	*91 ± 1*	*19.8 ± 1.1*
PTMSP-5PPN	*31 ± 1*	*0.1508b ± 0.0071*	*112 ± 4*	*23.0 ± 2.4*
PTMSP-20PPN	*43 ± 1*	*0.1571b ± 0.0046*	*276 ± 13*	*39.1 ± 6.6*
Polysulfone c	*24.64*	*0.1069d*	*350*	*0.465*
Matrimid® c	*18.27*	*0.1131d*	*200*	*0.550*

[a] τ_∞ is expressed in units of hours.
[b] f_e values for PTMSP were found as fitted parameters, since pressure-volume-temperature (PVT) data for this polymer above the glass transition temperature is not accessible.[161]
[c] from reference [136].
[d] f_e values for polysulfone and Matrimid® polyimide were found by extrapolation of PVT data above the glass transition temperature to the conditions in the study.

Interestingly, as shown in Table 4, neat PTMSP exhibits similar values of τ∞ when compared to other polymers, such as polysulfone and Matrimid®. Blending only 5% PPN into the PTMSP matrix increased the value of ln τ∞ from 22 to 31, which is well above the range reported for conventional glassy polymers (e.g., polysulfone and Matrimid® polyimide). This observation reinforces the possibility that blending PPN into other polymeric membranes is a viable approach to mitigate physical aging.

3.4.3. Free Volume Analysis and Possible Mechanism of PTMSP-PPN Physical Interaction

Density measurements (Appendix B, Section B3.5) were run to quantify free volume differences between neat PTMSP and PTMSP-PPN blends. The experimental density of neat PTMSP, PTMSP-5PPN, and PTMSP-20PPN is shown in Table 5.

Table 5. Experimental densities and fractional free volume values of neat PTMSP, the PTMSP-5PPN blend, the PTMSP-20PPN blend, and neat PPN. Errors are calculated using linear error propagation.

material	*experimental density (g/cm³)*[a]	*Fractional free volume, f*[b]	*ideal mixing density (g/cm³)*[d]
PTMSP	*0.759 ± 0.004*	*0.38 ± 0.01*	---
PTMSP-5PPN	*0.816 ± 0.020*	*0.34 ± 0.02*	*0.770*
PTMSP-20PPN	*0.864 ± 0.012*	*0.32 ± 0.01*	*0.807*
PPN[c]	*1.08*[c]	*0.31*[c]	---

[a] *PTMSP, PTMSP-5PPN, and PTMSP-20PPN density values were determined using buoyancy measurements in water at 21 °C (294.15 K). The density of PPN was estimated using the occupied volume from Bondi's method*[151] *and the total pore volume from N_2 adsorption at 77 K.*[43]
[b] *The van der Waals volume used to calculate f was derived from the group contribution technique reported by Wu et al.*[151]
[c] *Reference values used to calculate the PPN properties did not have associated uncertainties, thus uncertainty values are not available for PPN since linear error propagation could not be performed.*
[d] *Values calculated assuming no change in volume upon mixing, i.e., treating volume as an additive property*

If the excess volume of mixing for PTMSP and PPN blends was zero, the blend density would be the volumetrically weighted average of the two neat materials. The experimental results directly demonstrate non-ideal mixing, as the measured densities of the PTMSP-5PPN and PTMSP-20PPN blends, 0.816 and 0.864 g/cm^3, respectively, are larger than the ideal-mixing prediction. As a result, fractional free volume values of the PTMSP-PPN blends exhibit negative deviations from ideal mixing (Figure 17A). This result confirms a unique packing behavior in the blend, which could be ascribed to either *i)* adsorption of PTMSP to the surface of the PPN or *ii)* physical interlocking/interpenetration of the PTMSP through the PPN porosity. Either scenario is likely to

explain the reduction in local segmental mobility responsible for physical aging resistance in PTMSP-PPN blends. As discussed hereafter, partial adsorption of PTMSP chains to the PPN surface appears the most likely scenario, which is also supported by MD simulations (Figure 17B).

The drive to minimize the intramolecular free volume in the triptycene moieties (which make up the majority of the PPN used here) by occupation of adjacent functional groups or polymer backbones of appropriate size is a well-documented phenomenon.[139,162] Thus, it appears possible that the PTMSP backbone or pendant methyl groups could be absorbed into triptycene clefts or other cavities present in the triptycene-isatin PPN.

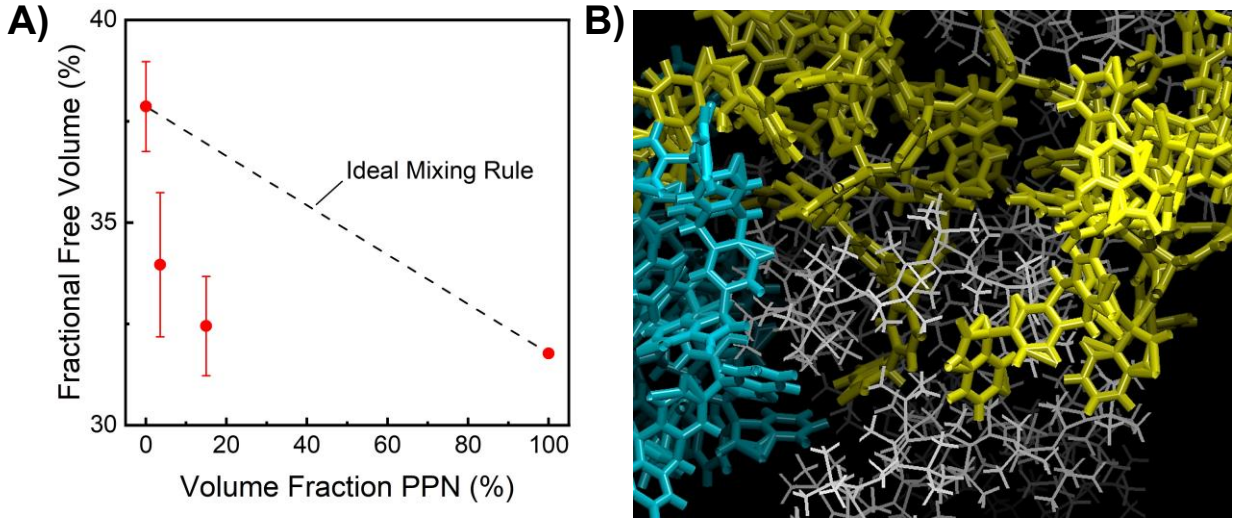


Figure 17. (A) Fractional free volumes of the PTMSP-PPN blends vs. blend composition. The dotted line is the ideal volumetric mixing rule. A MD simulation snapshot of a PTMSP-PPN interaction is shown in (B), where the white molecules are PTMSP, and the yellow/blue are individual PPN particles. As can be seen, PTMSP chains are partially adsorbed on the PPN molecularly rough surface.

Based on PALS data, PTMSP chains could occlude the 0.95 nm diameter cavities in PPN, since this peak does not appear in the PALS spectrum of the PTMSP-PPN blends. However, this would require that the PTMSP cross-sectional diameter be smaller than 0.95 nm. Boyer and Miller[163] estimated the cross-sectional diameter of forty polymers exhibiting different structures and morphologies with values ranging between 0.47 nm and 1.26 nm. This analysis includes polymers with bulky pendant groups, such as polystyrene, which has a cross-sectional diameter of 0.94 nm. The PTMSP backbone, that is, the sub-structure including the double bond and pendant methyl, but not the trimethylsilyl group, might be approximated to the structure of *cis*-1,4-polyisoprene. For this polymer, Boyer and Miller reported a cross-sectional diameter of 0.6 nm, making this sub-structure a likely candidate for absorption into PPN. Moreover, the overall cleft width of triptycene (i.e., the distance between the tips of any two of the aromatic rings), estimated from space-filling models by Tsui et al.,[162] is ~0.9 – 1.02 nm, which aligns well with the 0.95 nm peak from PALS. This combination of geometrical sizes suggests that the presence of triptycene may enable this unique lock-in interaction between PTMSP and PPN. Alternatively, pendant methyl groups such as those found in the trimethylsilyl groups or even the backbone of PTMSP have been shown by Wiegand et al.[139] to directly incorporate into triptycene cavities; therefore, adsorption of methyl groups may be partially responsible for this interaction with PPN. In this case, these "adsorption sites" would act as constraints to reduce PTMSP local segmental mobility and, as such, its aging propensity.

Regardless, there appears to be multiple sub-structures present in PTMSP that satisfy the geometric requirements to partially occupy the triptycene clefts present in PPN. Visualization of PTMSP interpenetrating small surface protrusions at the interface of PPN particles in an MD simulation is shown in Figure 17B, which confirms that the geometric requirements for PTMSP to

occupy some microcavities in the PPN are satisfied. Further evidence from NMR T_1 (relaxation) measurements will be considered in Section 3.4.4 to elucidate which PTMSP sub-structures are most affected by the proposed adsorption mechanism.

3.4.4. ^{13}CP/MAS NMR Spectroscopy

During NMR measurements, atomic nuclei are excited to a high-energy state by absorption of a radiofrequency (RF) pulse. After this excitation, nuclei undergo a phenomenon called *spin-lattice relaxation*, which brings the nucleus from a non-equilibrium, high-energy state back to thermodynamic equilibrium. The spin-lattice relaxation time, T_1, characterizes the rate at which an excited nucleus approaches thermodynamic equilibrium. Experimentally obtained values of T_1 are related to the rate or relative freedom of molecular motion as experienced by specific carbon atoms.[36,164–166] Previous studies have characterized T_1 values for the carbon atoms in PTMSP, before and after physical aging, to yield molecular-scale insights into the aging process.[36,165,167,168] The approach implemented herein builds on this literature.

T_1 measurements were performed both in air and pure N_2 to examine the effect of O_2 on the relaxation time. O_2, being paramagnetic, can reduce the T_1 time due to electron-nuclear dipolar interactions, thus measuring T_1 in the absence and presence of air decouples the competing effects of the enhanced spin-lattice relaxation due to O_2 and the hindered mobility due to physical aging (Appendix B, Section B11, Figure B6).[169,170] NMR allows us to differentiate carbon atoms in the CH_3 groups bound to the trimethylsilyl groups, the carbon atoms in the pendant CH_3 groups , and the carbon atoms in the polymer backbone, as shown in Figure 18. These carbon atoms are referred to as A, B, and C, respectively. The T_1 values obtained for PTMSP and PTMSP-20PPN, measured in air, are shown in Figure 18 for the freshly cast and 9-month aged samples. Upon aging, the T_1 values for neat PTMSP increase for carbons A and B. Increases in T_1 for these groups are typically

interpreted to be a result of denser local packing or constrained molecular motion.[36,165,167] According to our results, T_1 values for carbons A and B in PTMSP-20PPN experience no change upon aging, within experimental error. As shown in Figure 18C, carbon C (the backbone carbon) in PTMSP is affected, as well. In neat PTMSP, little to no change due to aging is observed in the backbone carbon T_1 values, while the backbone carbon T_1 values for PTMSP-20PPN increases by 30% upon aging. Thus, due to interaction with the PPN, the molecular motion of backbone carbons in PTMSP appears to become increasingly hindered with aging. The inhibition of sidechain methyl rigidification and increased backbone rigidity are consistent with the results previously reported by Lau et al. for PAF-1/PTMSP composites that resist physical aging.[36] These results suggest that an interaction between the backbone of PTMSP and PPN may be responsible for the physical aging resistance of the blends tested.

One possible interpretation for the mechanism of physical aging inhibition becomes apparent due to the observed differences between the T_1 measurements in air and in N_2 (Appendix B, Section B11, Figure B6). In N_2, unlike in air, increases in T_1 for carbons A and B are not observed for neat PTMSP upon aging; rather, only a minor increase in T_1 for carbon C is observed upon aging. Further, no significant changes in the T_1 upon aging of all the carbons are observed due to the inclusion of PPN (i.e., in PTMSP-20PPN) when measured in N_2. These results suggest that the increases in T_1 in air for neat PTMSP are not necessarily due to enhanced rigidity of the methyl groups, but rather the increasingly hindered accessibility of O_2 to interact with these groups as the polymer phase packs during physical aging.[166] This alternative explanation also supports the hypothesis that the PPN significantly affects the physical aging behavior of PTMSP by interacting with the PTMSP backbone and is supported by the fact that carbon C is the only one that exhibits differences in how T_1 changes upon aging between PTMSP and PTMSP-20PPN in both air and in

N_2.

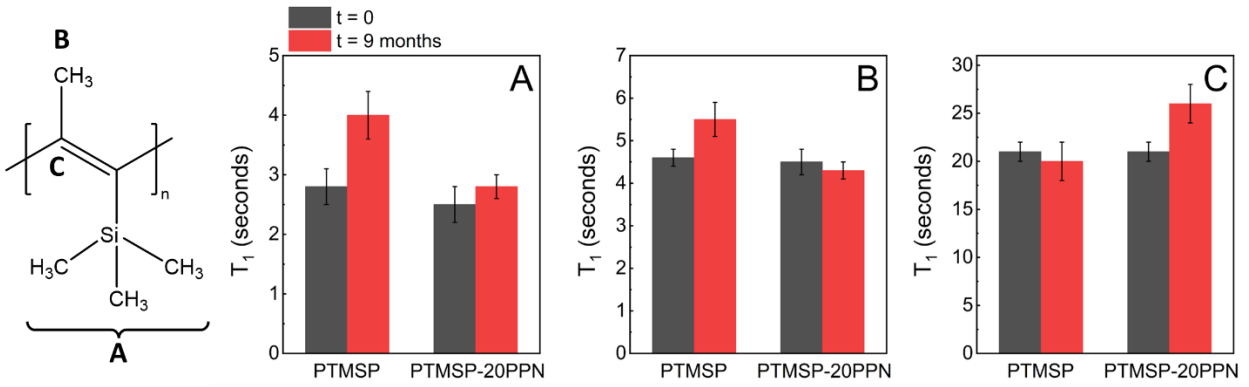


Figure 18. Spin-lattice relaxation times measured in air for the carbons in PTMSP (for both neat PTMSP and PTMSP-20PPN). The labels for carbons A, B, C indicated on the structure of PTMSP correspond to the accordingly labeled plots. Relaxation times measured under pure N_2 are shown in Figure B6.

3.4.5. Pure Gas Transport Properties

Pure-gas N_2, CH_4, and CO_2 permeability in PTMSP, PTMSP-5PPN, and PTMSP-20PPN were measured at 35°C (308.15 K) and up to 20 atm (Appendix B, Section B8 and B12, Figure B8). For all gases, permeability decreased with increasing feed pressure (Figure B8). This behavior is consistent with the dual mode transport mechanism.[171,172]

Gas permeability decreases after incorporating 5 wt. % PPN into PTMSP (Figure 19A**)**. Specifically, the permeability of N_2, CH_4, and CO_2 at 1 bar decreased, relative to that in neat PTMSP, by 36%, 52%, and 42%, respectively. Notably, the largest decline in permeability is observed for CH_4, which is the bulkier among the penetrants considered in this study. As discussed later, this result is ascribed to the parallel drop in diffusivity. Interestingly, upon adding 20 wt. % PPN, the overall CH_4 permeability showed little change, while the CO_2 permeability increased by 1.8% relative to neat PTMSP, and by 75% relative to PTMSP-5PPN.

The CO_2/CH_4, CO_2/N_2, and CH_4/N_2 ideal (i.e., pure gas) selectivity, shown in Figure 19B, exhibits a more complicated behavior. Upon incorporation of 5 wt. % PPN, CO_2/N_2 and CH_4/N_2 selectivity decreased by 9.1% and 25%, respectively, relative to those in neat PTMSP. In contrast, in the PTMSP-20PPN blend, CO_2/N_2 selectivity and CH_4/N_2 selectivity increase by 50% and 44%, respectively, relative to neat PTMSP. For both the 5 and 20 wt. % blends, an increase in CO_2/CH_4 selectivity (21.2% and 3.9%, respectively) relative to neat PTMSP is observed.

To explain these trends and rationalize the effect of PPN on gas transport, permeability was broken down into its elementary sorption and diffusion contributions. Sorption of N_2, CH_4, and CO_2 in PTMSP, PTMSP-5PPN, and PTMSP-20PPN were measured at 35°C (308.15 K) (Appendix B, Section B8 and B12, Figure B10), and diffusion coefficients (Figure B9) were estimated using the sorption-diffusion model, i.e., as the ratio P/S.

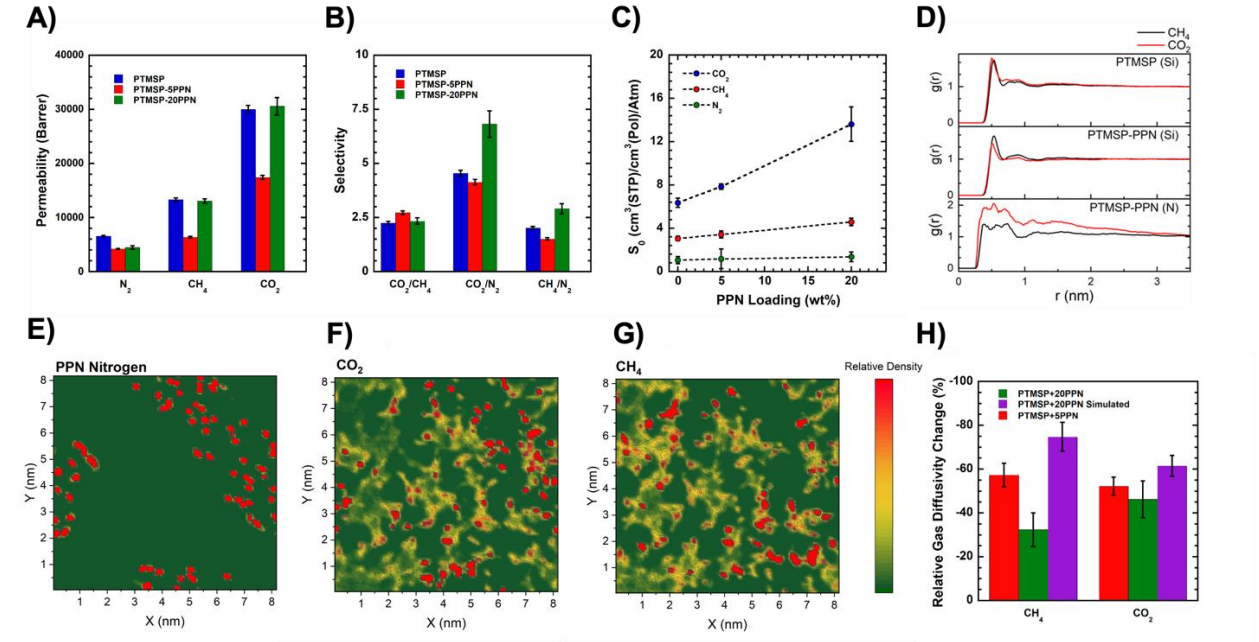


Figure 19. (A) Pure N_2, CH_4, and CO_2 permeability and (B) ideal gas selectivity for CO_2/CH_4, CO_2/N_2, and CH_4/N_2 at 1 bar and 35 °C (308.15 K), and C) Infinite dilute sorption coefficients for

N_2, CH_4, and CO_2 at 35 °C (308.15 K). (D) Radial distribution functions calculated from MD simulated trajectories, between sorbed gases (i.e., CO_2 and CH_4) and the Si atoms in PTMSP and PTMSP-PPN blends, as well as between the gases and the N atoms in PTMPS-PPN blends. Simulations were run for neat PTMSP and PTMSP-20PPN. Heat density maps of E) PPN nitrogen atoms, F) CO_2 gas molecules, and G) CH_4 gas molecules found within a 2D slice of PTMSP-20PPN from MD simulations. H) Experimentally determined CO_2 and CH_4 diffusion coefficient changes in PTMSP-5PPN (red) and PTMSP-20PPN (green) relative to neat PTMSP, along with MD predictions for PTMSP-20PPN (purple). Experimental uncertainty was calculated using linear error propagation.[173]

Pure-gas N_2, CH_4, and CO_2 sorption increased with increasing PPN loading. The infinite dilution sorption coefficients (S_0) for each material are shown in Figure 19C. The increase in gas sorption becomes more prominent with increasing penetrant condensability, i.e., S_0 showed larger increases in the order of CO_2 (+114%) > CH_4 (+50.0%) > N_2 (+30%), moving from neat PTMSP to PTMSP-20PPN. To shed light on the molecular origin of this phenomenon, each sorption isotherm was fit to the dual-mode model, whose parameters are shown in Table 6. Interestingly, the increased sorption is not related to an increase in the Langmuir sorption capacity (C_H'), but rather due to an increase in both the gas-polymer affinity factor (i.e., b) and Henry's sorption coefficient (i.e., k_D) (Table 6). Given the similarity in BET surface areas between PTMSP (i.e., 816 m^2/g)[75] and PPN (i.e., 790 m^2/g)[1], the added porosity of PPN may not be expected to have a large impact on the changes in C_H'. Instead, C_H' decreases upon PPN incorporation in PTMSP. This result is consistent with the physical picture that the PTMSP backbone is occupying parts of the PPN at the PTMSP-PPN interfaces and thus decreases the free volume and surface area available

for Langmuir mode sorption. Therefore, enhanced sorption is driven by the affinity of gases for the PPN over PTMSP. Specifically, in the case of CO_2, sorption is largely correlated with the favorable interactions between CO_2 and the lactam amide rings present in the PPN. This effective attraction is shown quantitatively by the radial distribution functions, *g(r)*, between the gases (CO_2 and CH_4) and the silicon atom in PTMSP, as well as those between the gases and the silicon and amide nitrogen atoms in PTMSP-20PPN, as obtained from MD simulations (Figure 19D). *g(r)* represents the probability of finding a certain gas molecule (i.e., either CO_2 or CH_4) at a certain distance from a specific atom (i.e., the silicon atom of PTMSP or amide nitrogen of the PPN), normalized by the probability of finding said gas molecule at an infinite distance from the atom. The simulation results show a larger value in *g(r)* for CO_2 over CH_4 near the nitrogen atom, which is consistent with the experimentally observed increase in CO_2 sorption in the PTMSP-PPN blends. This effect on individual sorption values translates to the sorption selectivity of CO_2/CH_4, CO_2/N_2, and CH_4/N_2 at 1 bar and 35 °C (308.15 K), which increases with increasing the amount of PPN blended with PTMSP (Appendix B, Section B12, Figure B7). For example, at these conditions, the CO_2/CH_4 sorption selectivity for PTMSP, PTMSP-5PPN, and PTSMP-20PPN, are 2.1 ± 0.2, 2.6 ± 0.2, and 2.7 ± 0.4, respectively. To further support this interpretation, 2D density profiles for the amide of the PPN, CO_2, and CH_4 are shown in Figure 19 E, F, and G, respectively. These figures help visualize the favorable interactions between CO_2 and the PPN amide nitrogen, as high relative local packing of CO_2 can be found at positions that correspond well to the positions near that of the PPN nitrogen. In sharp contrast, CH_4 is more distributed throughout the 2D slice, and no correlations are observed between the position of N atoms in PPN and that of the CH_4 molecules diffusing within the polymer.

Table 6. Summary of the dual mode parameters for the samples considered in this study. Uncertainties were calculated using the Jackknife resampling technique.

sample	gas	k_D ($cm^3(STP)/(cm^3(pol)atm)$)	C'_H ($cm^3(STP)/cm^3(pol)$)	b (atm^{-1})
PTMSP	CO_2	0.537 ± 0.103	179.2 ± 9.5	0.032 ± 0.002
	CH_4	0.526 ± 0.052	65.8 ± 4.1	0.038 ± 0.002
	N_2	0.200 ± 0.105	58.6 ± 19.6	0.014 ± 0.002
PTMSP-5PPN	CO_2	1.532 ± 0.042	103.7 ± 2.8	0.061 ± 0.002
	CH_4	0.532 ± 0.074	68.4 ± 5.4	0.042 ± 0.003
	N_2	0.359 ± 0.118	31.3 ± 31.8	0.026 ± 0.011
PTMSP-20PPN	CO_2	2.243 ± 0.132	65.1 ± 4.6	0.175 ± 0.021
	CH_4	0.738 ± 0.049	50.1 ± 3.0	0.077 ± 0.005
	N_2	0.225 ± 0.120	43.6 ± 14.0	0.026 ± 0.005

Interestingly, as shown in Figure 19H, incorporation of PPN into PTMSP at both 5 and 20 wt. % decreased overall gas diffusivity relative to neat PTMSP at 1 bar and 35°C. For example, CO_2 diffusivity decreased by 57 and 52% for the PTMSP-5PPN and PTMSP-20PPN blends, respectively, relative to values obtained for neat PTMSP. For the sake of completeness, it should be clarified that, although nitrogen data were excluded from Figure 19H due to large error bars, nominal values for the nitrogen diffusivity in the blends also decrease relative to those measured in neat PTMSP (Appendix B, Figure B9). These results are consistent with a reduction or a possible blockage of medium sized cavities (cavity 2) upon blending PTMSP with PPN, as shown by the PALS analysis. In other words, the loss of connectivity among large free volume cavities (i.e., cavity 3) is consistent with the reduced diffusivity in the blends relative to neat PTMSP, observed experimentally. Therefore, the permeability drop observed in PTMSP due to PPN incorporation is

ascribed solely to the diffusion contribution and is consistent with the hindered local segmental dynamics due to PTMSP lock-in mechanism with PPN.

PTMSP-20PPN exhibited an increase in gas diffusivity relative to PTMSP-5PPN, despite a slight decrease in the overall fractional free volume. To rationalize this discrepancy, given the stronger polymer-penetrant interactions (i.e., non-idealities) present upon incorporating more PPN in PTMSP, the diffusivity coefficient was separated into a mobility, or kinetic, factor (i.e., L), which is due to purely kinetic contributions, and a thermodynamic factor (i.e., α), which accounts for thermodynamic non-ideality:[20,62,174]

$$D = L \times \alpha = L \times \frac{\partial \ln(a)}{\partial \ln(\omega)} \tag{14}$$

In Eq. 14, a is the penetrant activity, and ω is the corresponding penetrant weight fraction in the material. As shown in Appendix B, Figure B11, as the weight loading of PPN is increased in PTMSP to 5 and 20 wt%, the thermodynamic factor increases (ranging from ~1 to 2), and thus, mobility (i.e., the thermodynamically corrected diffusion coefficient) decreases. This demonstrates that gas-PPN interactions impact the overall diffusion behavior. Therefore, it is not surprising that PTMSP-20PPN shows slight deviations between the fractional free volume and diffusivity trend expectations. For example, upon making this correction, the overall mobility of CO_2 in PTMSP-5PPN and PTMSP-20PPN is within error of each other, and both decrease by 53% relative to PTMSP.

Of note, the mobility factor of N_2, CH_4, and CO_2 in both PTMSP-5PPN and PTMSP-20PPN remains relatively constant with increasing pressure. However, the mobility factors decrease monotonically in neat PTMSP with increasing pressure. These results are in agreement with those reported previously by Merkel et al.[175], and are attributed to self-blocking of gases, which impede

penetrant diffusion through the relatively open polymer matrix, and are again consistent with the PALS analysis' indication that PTMSP has its 'channel like' cavities (cavity 2) occluded by the presence of the PPN.

Given the opposing changes occurring in the gas diffusivity and sorption upon adding PPN to PTMSP, the observed effects on overall pure gas selectivity become clearer: there is a competing effect between gas sorption and diffusion with increasing PPN weight loading. In the case of the PTMSP-20PPN, the overall permeability and selectivity are controlled by the sorption contribution, while permeability and selectivity in PTMSP-5PPN are largely affected by the diffusion contribution.

3.5. Conclusions

We propose a facile and cheap strategy to control polymer dynamics, free volume characteristics, physical aging propensity and transport properties of microporous glassy polymers, while providing a detailed picture of the molecular level phenomena underpinning the experimentally observed behaviors. PTMSP, a model high free volume microporous glassy polymer, was blended with a triptycene-isatin porous polymer network (PPN), a hyper cross-linked porous 3-D network. The fabrication step was followed by a detailed structural and transport characterization.

While slight reductions or enhancements in gas permeability and either an increase or decrease in selectivity were observed upon blending, physical aging resistance was significantly enhanced. PALS analysis indicates that three different sizes of free volume cavities are available in the PTMSP and PTMSP-PPN samples. In contrast, a bimodal pore size distribution was detected in the neat PPN. While the number of smaller free volume cavities is essentially the same in both the

neat polymer and the blends, the number of medium-sized free volume cavities decreases, and the number of larger free volume cavities increases upon blending PTMSP with the PPN. The preservation of these larger cavities is consistent with a hindered rate of physical aging in the PTMSP-PPN blends. PALS spectroscopy, transport measurements and theoretical modeling show that polymer-PPN physical interaction disrupts the connectivity among large free volume cavities of PTMSP, with marked effects on permeability and selectivity. MD simulations were conducted to achieve a deeper molecular level understanding of the observed phenomena.

Incorporating as little as 5 wt. % PPN in PTMSP leads to a N_2 permeability decline of only 14% over the course of 500h, as compared to the 41% decline exhibited by neat PTMSP. The hindered aging rate is ascribed to the occupation of surface cavities in the PPN by the PTMSP chains. PALS, density measurements, free volume calculations, ^{13}C CP/MAS NMR spectroscopy, as well as modeling with the Struik model, dual mode model and MD simulations support this physical picture. Finally, we show that, to correctly interpret transport data in these systems, which present a complicated pattern of physical and chemical interactions, a careful correction for thermodynamic non-idealities must be performed, absent which misleading conclusions might be drawn.

Copyright Statement

Reprinted with permission from ACS Appl. Mater. Interfaces 2024, 16, 40, 53843–53854. Copyright 2024 American Chemical Society.

Chapter 4. Thin-film nanocomposite membranes based on microporous polymers with long-term organic solvent separation performance stability exhibiting facile formation of a solvent-resistant interlayer

4.1. Abstract

While crosslinking and rigid filler incorporation are two strategies to inhibit plasticization in polymeric membranes, their effect on the separation of liquid hydrocarbons is highly dependent on the strategy employed. We show that incorporation of rigid porous polymer networks containing shape-persistent units into carboxylic acid functionalized PIM-1, followed by polymer-filler intercrosslinking, individually and synergistically enhance the overall performance, leading to a new family of membranes exhibiting unprecedented long-term stability. These newly developed materials are easy to fabricate in thin film configurations, and are intrinsically sustainable, as their manufacture requires milder operating conditions relative to state-of-the-art materials. A unique interlayer was discovered at the interface between the porous support and the selective layer that limits the local dilation propensity, leading to previously unattainable combinations of permeances and molecular weight cutoff values in hydrocarbon media. Membranes exhibiting a 300 nm thin selective layer offer superb hydrocarbon fractionation performance in organic solvent nanofiltration (OSN) and reverse osmosis (OSRO), even after 18 months of continuous exposure to liquid toluene. The molecular origin of the observed behaviors is elucidated, expanding the array of mechanisms that can be used to design next generation materials for aggressive organic phase separations.

4.2. Introduction

Chemical separations and solute purification from organic solvents are the most energy-intensive and expensive steps involved in the production of fuels, pharmaceuticals, and chemicals.[4,12] This is due to (i) the challenging nature of certain separations (e.g., isomers or compounds with similar boiling points and sizes) and (ii) the intrinsically energy-intensive nature of thermal phase-change based separations, such as distillation.[4] Membrane-based separations have arisen as a promising alternative to thermal-based separations since they do not rely on phase change and could consume up to 90% less energy than conventional separation technologies.[13]

Two primary areas have emerged in the study of membrane-based solvent separations: organic solvent nanofiltration (OSN) for the purification of large solutes (200-1000 Da) from solvents, and organic solvent reverse osmosis (OSRO) for the separation of solvent/solvent mixtures (<200 Da).[11,12] Within both these modes, polymers are the most studied membrane material due to their tunable chemistry and ability to be scaled up.[11,12] Polymers, for example, can be solubilized and then fabricated as large, continuous areas using roll-to-roll manufacturing or hollow-fiber spinning, which makes their scale-up easy to achieve.[176] The soluble nature of polymers, though advantageous for manufacturing, generally renders them 'flexible' at the molecular level when swollen in solvents, drastically reducing their ability to differentiate molecules by size. This phenomenon is known as plasticization.[9] One of the primary challenges to achieving efficient polymer-based membrane solvent separations is overcoming plasticization in order to access size-based differentiation of molecules.

Plasticization has been fundamentally studied, yielding many useful insights that have thus been translated to membrane-based organic solvent separations. Rodriguez et al.[10] recently summarized and identified four design strategies that successfully inhibit penetrant-induced

plasticization in polymer membranes, all of which have been successfully implemented to improve OSN and OSRO membrane performance: these are (i) rigid monomer design[14,177,178], (ii) hydrogen bonding[54], (iii) crosslinking[14,15,17,179–181], and (iv) filler incorporation[16,19,54] (e.g., organic/inorganic nanoparticle incorporation or polymer blending).

Among the widely explored range of monomers, crosslinking chemistries, and filler types, a few material design principles have become clear. For membrane productivity, it is necessary to uptake an adequate quantity of solvent to achieve a high intrinsic permeability. However, taking up a large quantity of solvent increases the effective micropore size by geometric dilation (i.e., swelling) and relaxation (i.e., increased chain mobility), which reduce size-sieving effects.[9] This competition between the solvent uptake (permeability) and micropore size (size-selectivity) are responsible for the observed 'upper bound' trade off in hydrocarbon-based membrane separations.[9,15,19,182] With these competing effects in mind, the ideal strategy to design efficient OSRO/OSN membranes is to maximize solvent uptake without bypassing the effective micropore size required to distinguish the molecules of choice. Ideally, the relaxation-based contribution to micropore size would be completely eliminated, allowing for size discrimination based on geometric principles alone. This would bring the polymer membrane selectivity close to that observed in inorganic materials. The best performing OSN/OSRO membranes to date utilize this design principle, featuring polymeric materials that, despite taking up significant quantities of solvents, have persistent structural features that render them plasticization resistant.[14,17,19,183]

Herein, we leverage these design principles by fabricating crosslinked polymeric membranes that incorporate rigid, fully organic fillers. Carboxylated PIM-1 (CPIM) is utilized for its rigid monomer design and the acid groups in CPIM provides a facile route to crosslinking by mild thermal treatment (200 °C).[18] Triptycene-isatin porous polymer networks (PPNs) are chosen as the

organic filler due to their (i) cheap (<$50/g) and facile synthesis; (ii) shape-persistent and rigid monomer (triptycene) and linkage chemistry (aromatic C-C linkages), both of which are expected to enhance size-sieving capabilties; and (iii) hydrophobic nature, which is expected to increase solvent uptake in hydrocarbon-based separations.[14,184] We previously showed that thermally crosslinked CPIM membranes containing PPN have a synergistic effect in resisting CO_2-induced plasticization[18], thus we expected to observe a similar effect translating to organic solvent-based separations. Finally, crosslinking across the selective layer-support interface was achieved, further boosting plasticization resistance and long-term stability. OSN and OSRO tests in toluene were performed to evaluate the material platform's performance in hydrocarbon-based separations, which present some of the most plasticizing and challenging separations currently being studied. An outstanding resistance to plasticization as well as unprecedented long-term stability of membrane performance are confirmed, and their fundamental origin is elucidated.

4.3. Experimental Methods

4.3.1. Materials

Details of the chemicals used and the PIM-1, CPIM, and triptycene-isatin PPN synthesis are reported in Appendix C, Sections C1.1-C1.2.

4.3.2. Material Characterization

Details regarding Fourier-transform infrared spectroscopy, positron annihilation lifetime spectroscopy, X-ray diffraction, combustion elemental analysis, ninhydrin assay, scanning electron microscopy (SEM), and liquid dilation measurements are reported in Appendix C, Section C3.

4.3.3. Free-Standing CPIM Membrane Casting

Dry CPIM powder (or CPIM + PPN) was dissolved at a concentration of 4 wt.% in THF. CPIM + PPN solutions were sonicated for 3-5 minutes after being fully dissolved to disperse the PPN particles and then were immediately casted. Solutions were poured onto leveled PTFE dishes in a nitrogen-purged glovebag, covered with a filter paper and glass plate to slow evaporation, and allowed to dry for 48 hours. Following this step, nascent membranes were recovered and dried at 110 °C for 24 hours in a vacuum oven and were then ready to use. Bulk CPIM membranes were primarily used to study the interaction with the diamine crosslinking agent (*p*-xylylenediamine) through Fourier-transform infrared spectroscopy and solvent sorption/dilation measurements.

4.3.4. Porous Support Fabrication

Porous supports were fabricated using a modified version of a previously reported procedure.[19] A dope solution consisting of Matrimid® (16 wt. %), tetrahydrofuran (10 wt. %), ethanol (3 wt. %), water (1 wt. %), $LiNO_3$ (1 wt. %), and N-methyl-2-pyrrolidone (69 wt. %) was prepared and mixed on a rolling mixer for 3 days and allowed to settle to remove bubbles. This dope solution was then knife-casted on a glass plate with a wet thickness of 300 μm, allowed to dry in a well-ventilated hood for 10 s, and was then immersed into deionized (DI) water at 25 °C. Ambient temperatures and relative humidities in the room during support fabrication were approximately 22 °C and 50%, respectively. After immersion, supports delaminated from the glass plate and were transferred to another DI water bath. After 24 hours, the supports were cut into 49 mm diameter round coupons and soaked in another DI water bath for 24 hours. The supports were then soaked in methanol 3 times for at least 3 hours for each soak and then immediately transferred to a 10 w/v % (g/ml) solution of *p*-xylylenediamine in methanol for crosslinking for 24h. After crosslinking,

supports were again washed with methanol 3 times (for at least 3 hours each wash) and were then stored in fresh methanol until use.

4.3.5. Thin-Film Composite Membrane Fabrication

CPIM and CPIM/PPN nanocomposite TFC membranes were fabricated by spin coating. Solutions of 1.5 w/v% CPIM (in g/ml) or 1.5 w/v% CPIM + the requisite quantity of PPN (resulting in a total solids w/v% > 1.5) dissolved in tetrahydrofuran were chilled in a refrigerator (~3 °C). After removal from the refrigerator, 0.7 ml of the coating solution was statically dispensed (i.e., before spinning) onto the porous supports and then they were immediately spun at 2000 rpm for 1 minute. Composite solutions of CPIM + PPN were briefly mixed and then sonicated for 30 seconds to disperse the PPN particles just before coating. The spin coating chamber was saturated with tetrahydrofuran vapors to slow down film formation. Resulting TFC membranes were then sandwiched between two glass plates with 1/32" spacers holding the plates apart- this was done to prevent scratching of the selective layer while keeping the membranes flat during drying. Sandwiched TFC membranes were dried in a vacuum oven at 110 °C overnight. Thermally treated TFC membranes were then held at 200 °C for 24h under vacuum. After thermal treatment, the oven was allowed to cool to at least 130 °C, and the TFC membranes were removed.

4.3.6. Organic Solvent Nanofiltration (OSN) and Organic Solvent Reverse Osmosis (OSRO) Tests

A custom crossflow membrane testing system was used to perform OSN and OSRO tests (Appendix C, Section C4). For OSN experiments, approximately 0.5 g/L of styrene oligomers dissolved in toluene were used to determine the hydrocarbon fractionation behavior over a wide range of molecular weights. Low concentrations of oligomers were used to avoid any issues with

fouling or osmotic pressure. Styrene oligomers were purchased from Agilent (PL2012-0001, PL2012-2001, PL2012-3001) and had molecular weights ranging from 162-1306 Da. An HPLC pump (Azura P2.1S, Knauer) was used to pressurize and flow the feed solution across the membranes. Feed flowrate was adjusted such that the stage cut was < 3% for all tests. After installation into cells, the transmembrane pressure was slowly brought up to 31 bar over the course of about 5 minutes. Tests were performed at ambient temperatures (21-23 °C). The crossflow system features a permeate recycling loop to allow for steady-state operation. After initial pressurization, the permeate lines were recycled for 2 days to allow the system to reach a steady state. Then, permeate lines were switched to allow collection into glass vials. 3-5 ml samples of the permeate and feed were collected and weighed. The weight and time to collect the sample were recorded and used to calculate membrane permeance. Permeance was calculated as follows:

$$Permeance = \frac{P}{l} = \frac{\Delta V}{A\,\Delta t\,\Delta p} \tag{15}$$

where ΔV is the permeate volume collected over time Δt, A is the active membrane area (14.6 cm^2), and Δp is the transmembrane pressure (31 bar for OSN tests).

OSN feed and permeate samples were analyzed using high-performance liquid chromatography (HPLC, Agilent 1100 series). Samples were first reconstituted in ethanol since toluene causes retention issues during analysis. 2-3 ml of the feed or permeate sample was transferred using a micropipette to a septum-topped vial. The septum was pierced with a 20-gauge needle and the vial was dried in a vacuum oven at room temperature. Usage of a needle limited the solvent removal rate and eliminated issues with overboiling during drying. After the toluene was removed, 2 ml of 10 v/v% THF in ethanol solution was added to redissolve the oligomers for HPLC analysis. A novel HPLC method was developed to separate and quantify the styrene

oligomers that avoids the harsh mobile phase mixture (i.e., tetrahydrofuran + trifluoroacetic acid) traditionally used for this purpose. Instead of a gradient technique, a single mobile phase consisting of 1 v/v% water and 0.1 v/v% THF in HPLC-grade reagent alcohol (90 v/v% ethanol, 5 v/v% methanol, 5 v/v% isopropanol, Fisher Chemical) was used. A 250 mm C18 reversed phase HPLC column (pore size 80 Å, particle size 3.5 μm, Agilent P/N 884950-567) was used with a flowrate of 0.75 ml/min. The amount of water in the mobile phase can be adjusted to control the degree of separation between peaks depending on the column characteristics (higher water content results in greater separation). A UV detector set at 265 nm and response time of 0.5 s was used to detect peaks. Rejection (R) for each oligomer was calculated as follows:

$$R\ (\%) = \left(1 - \frac{A_p}{A_f}\right) * 100\% \tag{16}$$

Where A_p and A_f are the integrated peak areas for the permeate and feed, respectively.

OSRO tests were performed using the same crossflow apparatus design used for the OSN tests. A 1 mol% solution of 1,3,5-triisopropylbenzene in toluene was used as the OSRO feed solution. Tests were performed at 30 bar transmembrane pressure and ambient temperatures (21-23 °C). After 2 days, feed and permeate samples were collected. OSRO samples were analyzed using gas chromatography (Thermo Scientific Trace 1310 GC). A 30m column with a 0.25 mm inner diameter and a non-polar aromatic/aliphatic stationary phase with 0.25 μm film thickness was used (Thermo Scientific TG-5SilMS). 1 μl of undiluted sample was injected into the column inlet at 250 °C with a split ratio of 40 using helium at 1 ml/min (column flow) as the mobile phase. The temperature program for an injection consisted of an isothermal hold at 60 °C for one minute followed by a 90 °C/min ramp to 300 °C. Analytes were detected using a flame ionization detector (FID). Compositions were calculated by using relative peak areas. Calibration standards of known

composition were injected on the same sequence as the feed/permeate samples and used to calibrate the relationship between peak area ratio and mass fraction ratio. 7 injections each of calibration standards and samples were performed to accurately assess the separation performance. Separation factors between component A and B ($S_{A/B}$) were calculated as follows:

$$S_{\frac{A}{B}} = \frac{\left(\frac{C_{A,p}}{C_{B,p}}\right)}{\left(\frac{C_{A,f}}{C_{B,f}}\right)} \tag{17}$$

Where $C_{A,p}$ and $C_{A,f}$ are the concentrations of component A in the permeate and feed, respectively, and $C_{B,p}$ and $C_{B,f}$ are the concentrations of component B in the permeate and feed, respectively.

Dilute 9-component hydrocarbon mixtures were separated using the same crossflow apparatus testing conditions (except Δp = 50 bar for this test) and analyzed by gas chromatography using the same GC, column, and detector as mentioned above. 0.5 µl of undiluted permeate or retentate samples were injected into the column inlet at 310 °C C with a split ratio of 40 using helium at 1 ml/min (column flow) as the carrier phase. The temperature program consisted of an initial 80 °C isothermal hold for 0.5 minutes followed by a 60 °C/min ramp to a 310 °C 5-minute isothermal hold. Compositions were calculated by using relative peak areas. Calibration standards of known composition were injected on the same sequence as the feed/permeate samples and used to calibrate the relationship between peak area ratio and mass fraction ratio. 10 injections each of calibration standards and samples were performed to accurately assess the separation performance, and rejections were calculated as shown in Equation 3. Calibration and assessment of mass fractions were performed with scripts in the Julia programming language, leveraging the package Measurements.jl for automated uncertainty propagation.[185]

4.4. Results and Discussion

4.4.1. Defect-free, inter-crosslinked thin film composite membranes

Carboxylated PIM-1 (CPIM) and triptycene-isatin porous polymer networks (PPNs), whose structures are shown in Figure 20A, were synthesized as discussed in Appendix C, Sections C1-C2, where details about the PPN particle size and CPIM degree of hydrolysis are also reported. By thermal treatment at 200 °C for 24h under vacuum, the acid groups in CPIM undergo thermal-decarboxylation, resulting in a radical-based polymer-polymer and polymer-filler crosslinking (Figure 20B).[18] Nanocomposite membranes exhibiting CPIM-PPN crosslinks are denoted as "inter-crosslinked" mixed matrix membranes (IcMMMs) due to the polymer-filler interfacial crosslinking. It has been shown that these interfacial crosslinks dramatically increase plasticization resistance upon exposure to CO_2 at high pressures.[18] Thus, a similar strategy was undertaken in this study to elucidate the individual and synergistic effects of filler incorporation, filler loading, and thermal crosslinking on organic solvent separation (i.e., OSN and OSRO) performance. As shown in Section 4.4.3, this approach leads to membranes for organic solvent separation exhibiting unprecedented long-term stability. Throughout this study, the following thin film composite (TFC) membrane samples were fabricated: neat CPIM, thermally treated CPIM (CPIMTT), neat mixed-matrix membranes with XX% weight loading of PPN (MMMXX, XX = 2.7, 5, 10, 30%, where the weight loading is expressed with respect to CPIM), and thermally treated mixed-matrix membranes with XX% weight loading of PPN (IcMMMXX, XX = 2.7, 5, 10, 30%).

TFC membranes were prepared by spincoating solutions of either CPIM or CPIM and the corresponding weight loading of PPN onto crosslinked porous Matrimid® supports prepared by knife casting followed by phase inversion. The full support fabrication protocol is provided in the experimental details. Supports were crosslinked with a 10 vol/wt.% (g/ml basis) *p*-

xylylenediamine solution in methanol. The final, crosslinked supports had surface pore sizes in excess of 10 nm and toluene permeances exceeding 100 L m^{-2} h^{-1} bar^{-1}, thus offering negligible resistance to transport and no molecular sieving capability. The resulting TFC membranes were defect-free, with selective layers thickness ranging from 300 nm to 1000 nm (Figure 20C inlay). It was observed that the selective layer thickness increases with the PPN loading, due to viscosity effects.

Free volume element (FVE) size distributions across the variables of filler loading and crosslinking were measured using X-ray diffraction (XRD, Figure 20D-E) and positron annihilation lifetime spectroscopy (PALS, Figure 20F). Although dry membrane FVE sizes can be highly indicative of gas separation performance due to the limited dilation of polymers upon exposure to light gases, their translatability to organic solvent separations may not be as direct due to the significant degree of membrane swelling that can alter the FVE sizes and distribution. Despite this limitation, correlation between the dry FVE size distribution and solvent permeance has been observed in highly plasticization-resistant membranes, wherein microporous membranes with a larger proportion of large FVEs exhibit enhanced solvent permeance.[14,184]

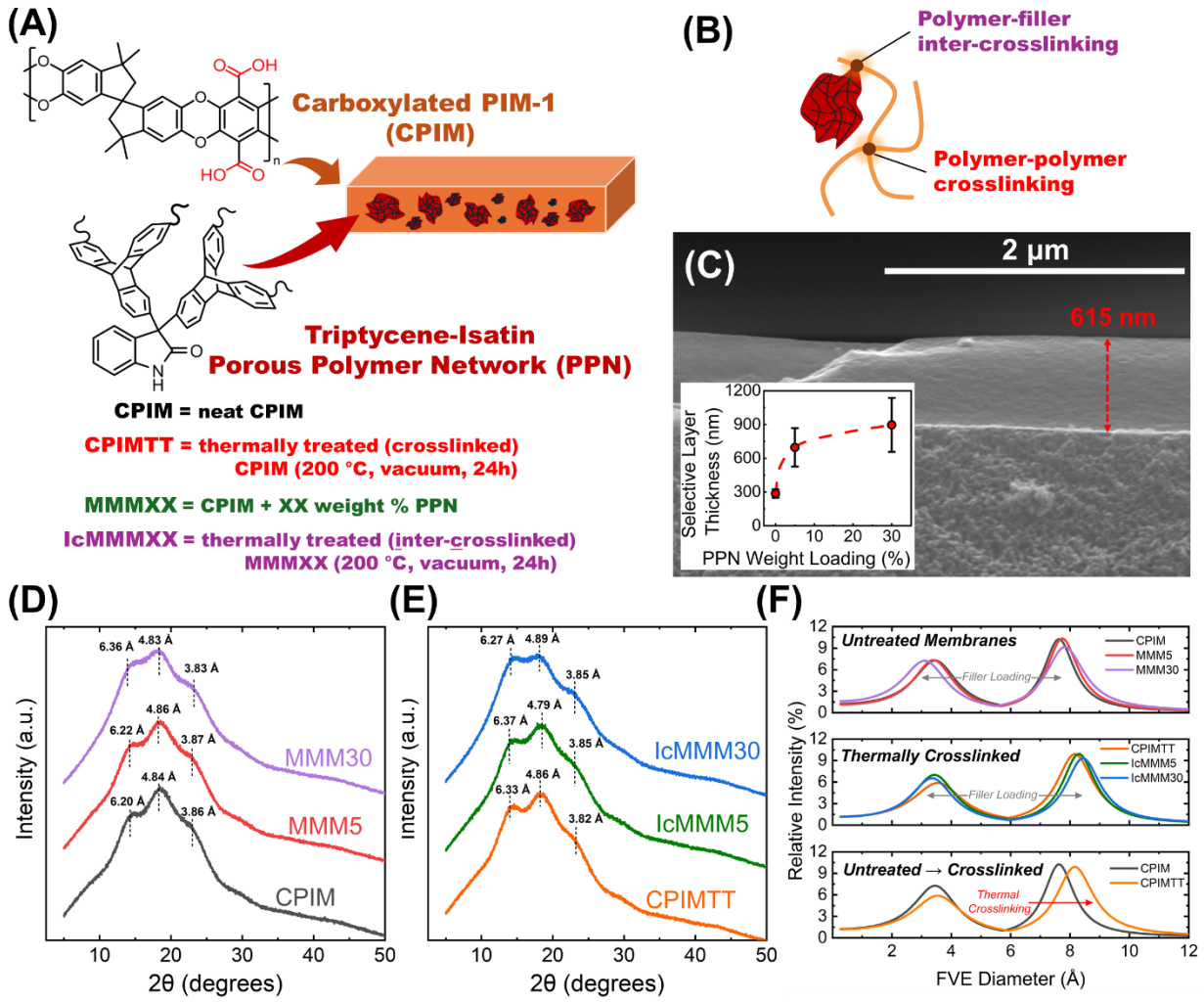


Figure 20. Membrane materials, TFC membrane fabrication, and FVE properties. (A) Materials used to fabricate membranes, as well as sample nomenclature. (B) Depiction of the two types of crosslinks resulting from thermal treatment in the CPIM-PPN systems. (C) SEM image of the IcMMM5 membrane depicting the selective layer coated on the porous Matrimid® support. The inlay plot for (C) depicts the trend of selective layer thickness with PPN weight loading. XRD spectra of (D) bulk non-crosslinked films and (E) crosslinked films. (F) PALS of non-crosslinked films (top panel), crosslinked films (middle panel), and comparison between a CPIM and CPIMTT membrane (bottom panel).

According to the XRD results, incorporation of PPN in CPIM and subsequent thermal treatment directly affects the ultramicroporosity (cavities with sizes not exceeding ~7 Å) of the resulting intercrosslinked membranes. Specifically, incorporation of PPN into CPIM increases the proportion of large FVEs, as evidenced by the growing shoulder at ~6.3 Å in Figure 20D. This is consistent with the XRD of the PPN, which indicates a large proportion of FVE at ~7.2 Å (Appendix C, Figure C1). Thermal crosslinking appears to have the same effect, where this shoulder is further enhanced, resulting in IcMMM30 having the largest proportion of large sized FVE (6.3 Å) to medium-sized FVE (4.9 Å) (Figure 20E). While XRD does not make it possible to separate and elucidate the individual and synergistic effects of filler incorporation and thermal crosslinking on the absolute FVE sizes, PALS offers this insight. PALS spectra show a bimodal FVE distribution, with two distinct peaks representative of microporosity and ultramicroporosity. The average size of micropores increases monotonically with PPN loading (Figure 20F, top/middle panels), while their number is reduced. Likewise, thermal crosslinking significantly increases the micropores size (Figure 20F, bottom panel), without changing their relative abundance. Therefore, the effects of PPN incorporation and thermal treatment on the size of micropores is synergistic. While PPN incorporation reduces the size of ultramicropores (~3 Å), the effect of thermal crosslinking on the size of ultramicropores is negligible. In contrast, thermal treatment decreases the relative abundance of micropores. As discussed in Section 4.4.3, these results directly correlate to permeability and selectivity.

Based on the outcomes of structural characterization, it can be expected that two factors will compete to affect the TFC membrane solvent permeance: (i) increases in permeance due to the micropore enlargement upon PPN incorporation and thermal treatment and (ii) decreases in overall productivity (i.e., lower permeance) due to the increased selective layer thickness observed in the

PPN-containing TFC membranes. Regarding membrane selectivity and performance stability, it is hypothesized that both thermal crosslinking and particle incorporation will inhibit chain mobility and slow molecular-scale dynamics, thus enhancing resistance to plasticization, boosting selectivity, and preserving its long-term stability.

4.4.2. Highly Solvent-Resistant Nanofiltration Performance

Hydrocarbon separation performance was tested across a wide range of molecular weights by measuring the rejection of polystyrene oligomers in toluene (**Figure 21**A). Tests were performed at 31 bar transmembrane pressure and ambient temperatures (21-23°C), with a stage cut below 3%. The total concentration of styrene oligomers in the feed was kept below 500 ppm to mitigate any possible effects of fouling and concentration polarization. Toluene was chosen as a solvent for three reasons. First, it is commonly used in refining and petrochemical applications. Second, it tends to heavily plasticize polymeric membranes.[14,177,186] Finally, a body of literature data have been reported for the toluene/styrene oligomers mixture, which makes it possible to put results from this study in broad perspective.[16,19,177,178,182,187–189] Notably, the smallest oligomer in the feed has a molecular weight of 162 Da, which is considered well within the OSRO range (<200 g mol^{-1}), while the largest oligomer has a molecular weight of 1410 Da, which falls in the upper end of the OSN range. The CPIM TFC membrane had a MWCO value of 200 Da, while that of CPIMTT had a MWCO value of at least 162 Da, both of which are significantly lower than the MWCO values of SBAD-1 (i.e., 335 Da) and PIM-1 (i.e., 786 Da).[177,187] In accordance with the tradeoffs typically observed for membrane separations, high selectivities are accompanied by lower permeances, with CPIM and CPIMTT exhibiting toluene permeances of 0.042 and 0.046 L m^{-2} h^{-1} bar^{-1} (Figure 21B), respectively, which are lower than the permeances of SBAD-1 (~0.2 L m^{-2} h^{-1} bar^{-1}) and PIM-1 (~7.1 L m^{-2} h^{-1} bar^{-1}). The composite membranes exhibit similar performances

as CPIM and CPIMTT, with MMM30 and IcMMM30 TFC membranes having a MWCO value of at least 162 and 270 Da, respectively, but had approximately five times lower permeance values than CPIM and CPIMTT; this effect is most attributable to the increased selective layer thickness of the composite membranes.

The rejection profiles of the CPIM/PPN-based membranes, both crosslinked and non-crosslinked, also outperform industry OSN standards, such as Puramem 280®, crosslinked Lenzing P84 polyimide, and Starmem™ 240 with molecular weight cutoff values that are 100-150 Da lower, while CPIM and CPIMTT TFC membranes exhibit permeance values ~200% higher than that reported for Torlon® hollow fibers,[190] which offers a comparable MWCO value of 185 Da. The membranes reported in this study exhibit some of the tightest MWCO values reported among hydrocarbon separations, resulting in MWCO values lower than that of Torlon®[190] (a plasticization resistant polyamide) and AlOx/PIM-1[19] (a PIM-1/aluminum oxide nanocomposite) for MMM30 and CPIMTT membranes, placing these samples at the upper-left corner of the OSN trade-off curve for polystyrene oligomers in toluene (Figure 21B). In general, the extremely low MWCO values observed for the membranes reported in this study suggest that they could be well-suited for more challenging hydrocarbon-based separations, such as OSRO.

As discussed, the materials reported in this study, while apparently exhibiting lower permeance relative to other membranes, offer much lower MWCO values and, as discussed in Section 4.4.3, unprecedented long-term stability, which makes them among the best membranes ever reported in terms of long-terms performance. It must be noted, however, that permeance can be improved by optimizing the fabrication protocol (i.e., selective layer thickness), while selectivity and long-term

stability are intrinsic membrane properties.

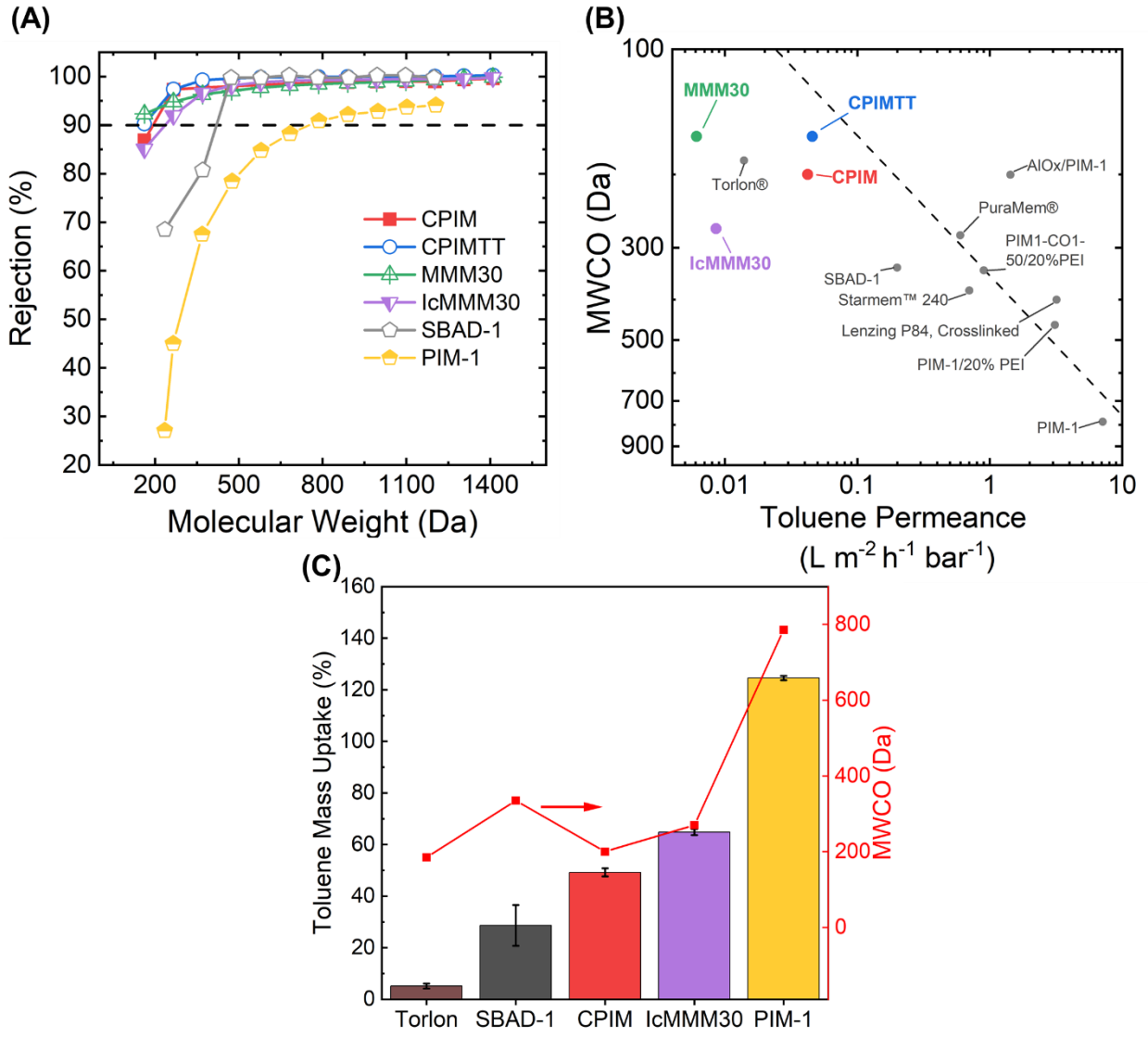


Figure 21. (A) Polystyrene oligomer rejection (i.e., MWCO) curves in toluene. Data for PIM-1[187] *and SBAD-1*[177] *are shown for comparison. (B) OSN trade-off curve for polystyrene oligomers in toluene. All data in this plot uses polystyrene oligomers with the exception of Torlon®, which used other aromatic hydrocarbons, but is included as a representative comparison.*[19,177,187–190] *(C) Comparisons of toluene uptake and molecular weight cutoff among membranes, including those reported in this study, and state-of-the-art membranes*

As noted, inclusion of PPN produces a decrease in permeance in both crosslinked and uncrosslinked membranes, due to increased thickness of the selective layer (Figure 20C, inlay). Therefore, it should be concluded that the effects of the selective layer thickness overwhelms the expected permeance boost suggested by the micropore enlargement upon PPN incorporation, as shown by PALS. Additionally, significant correlations between filler loading and selectivity are not observed, resulting in the intermediate filler loadings (2.7, 5, and 10 wt. %) having OSN performance metrics that fall in the same range as the samples shown in Figure 21. For this reason, the OSN performance data shown in Figure 21 is limited to CPIM, CPIMTT, MMM30, and IcMMM30. Filler loading, however, has a distinct effect on the long-term membrane stability, and is discussed in Section 4.4.3. Specific performance data for intermediate filler loadings are provided in Appendix C, Section C5.

Despite the excellent initial performance exhibited by the TFC membranes, further inquiry into the fundamental origin of the observed behavior reveals a number of surprising insights. A simple gravimetric uptake test demonstrates that the CPIM and IcMMM30 membranes take up between 50-60% of their mass in liquid toluene (Figure 21C). As previously discussed, ideal OSN/OSRO membranes should take up as much solvent as possible to maximize permeance while still resisting plasticization in order to preserve size-sieving performance. As shown in Figure 21C, other membranes exhibit positive correlation between their toluene uptake and MWCO values, where MWCO increases with increasing solvent uptake. In contrast, the TFC membranes reported in this study exhibit negative deviations from this trend, where large solvent uptake is associated to low MWCO values. This result is remarkable and not commonly observed in polymer membranes. Given the high liquid toluene mass uptakes, it appears at first surprising how selective the TFC membranes reported in this study are, considering that membranes with similar MWCO values,

such as Torlon®, take up only ~5% toluene by mass. In Section 4.4.4, the molecular origin of this behavior is elucidated, revealing a powerful new mechanism to engineer and control selectivity and long-term stability in polymer membranes for organic solvents separation.

4.4.3. Performance After Extended Solvent Exposure

After initial testing for polystyrene oligomer rejection, membranes were stored in toluene for 6 months at ambient conditions and were then re-tested using the same procedure. Although fresh membranes exhibited very similar rejection curves regardless of treatment (i.e., filler loading/crosslinking), the rejection curves diverge after the 6-month stability test (Figure 22A). Notably, all non-crosslinked membranes lose approximately 5-30% of their rejection values across the entire OSN range, while thermally treated membranes exhibit only a slight decrease in rejection at lower molecular weight values. Specifically, the selectivity losses in thermally treated membranes range from -12.4% to -1.3% for the 266 Da styrene oligomer, decreasing with filler loading, while maintaining almost 100% rejection for the higher molecular weight oligomers (Appendix C, Section C6). Based on these results, thermal crosslinking appears to be the most critical factor in preserving the long-term membrane performance.

Although losses in selectivity accompanied by gains in permeability were expected during the 6-month stability test, the results provided surprisingly counterintuitive trends, as shown in Figure 22B. Neat CPIM TFC membranes did not exhibit detectable MWCO values after the stability test, as significant losses in rejection were observed even for high molecular weight solutes. Shown in Figure 22B are the two extremities of thermally crosslinked samples, CPIMTT and IcMMM30. Both samples gain approximately 500% permeance after extended exposure, resulting in CPIMTT having performance very similar to SBAD-1 due to its movement parallel to the upper bound curve with an MWCO increase of 95% after 6 months. Remarkably, the performance of IcMMM30 did

not move in parallel to the upper bound, but instead directly towards it. For the latter sample, the 500% gain in permeance is accompanied by a mere 11.6% increase in the MWCO value. This unprecedented selectivity stability indicates that the previously demonstrated synergistic effect of CPIM-PPN crosslinking on plasticization resistance in gas separations translates well to organic solvent separations, making inter-crosslinked mixed matrix membranes a class of "universal" materials capable of performing equally well in both gas and organic solvent separations.[18] This result is uncommon and indicates the impressive versatility of this membrane platform in terms of its short- and long-term performance.

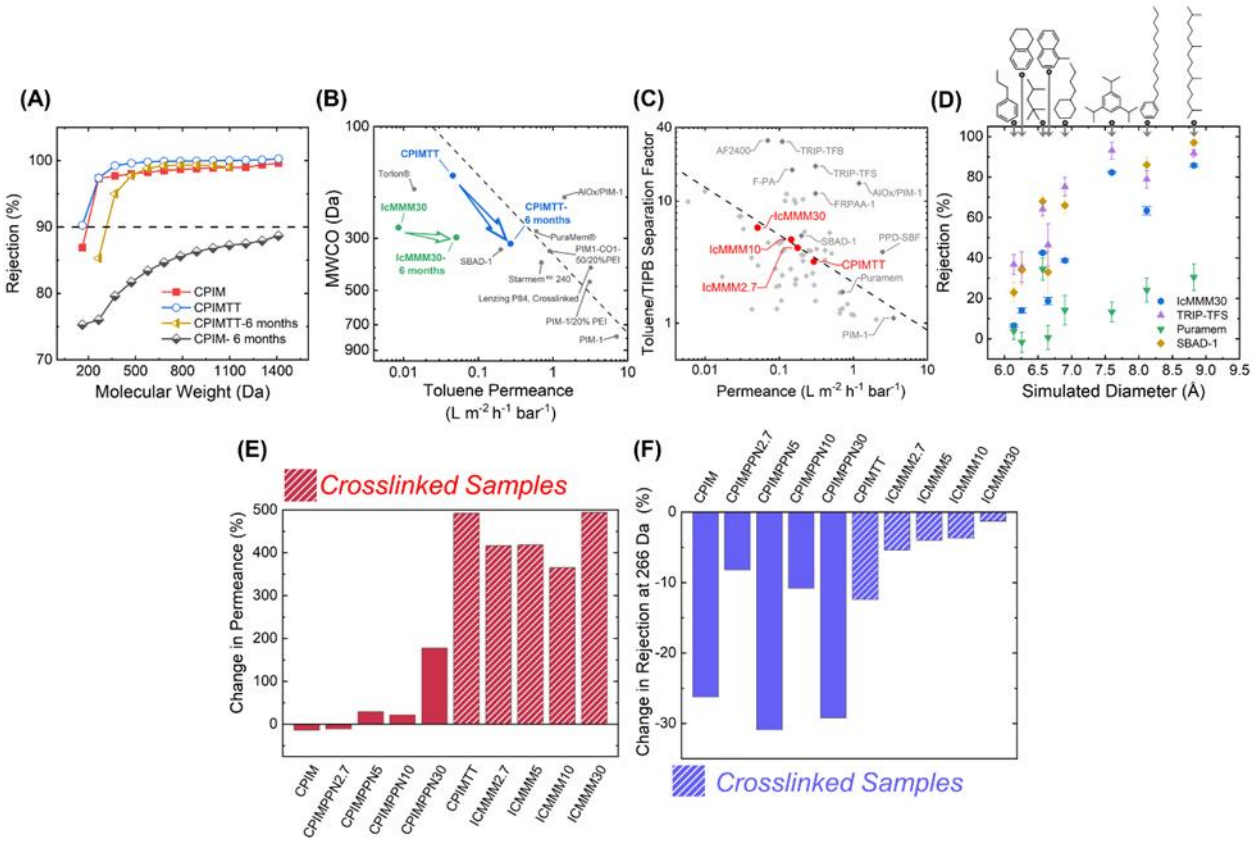


Figure 22. (A) Polystyrene oligomer rejection curves in toluene comparing initial performance to 6-month performance. (B) OSN trade-off curve demonstrating changes in thermally treated samples exhibiting different filler loading. (C) Performance of selected samples after extended

toluene exposure for ~18 months in the OSRO toluene/triisopropylbenzene separation. The feed contained 1 mol% TIPB in toluene. Gray symbols stand for state-of-the-art materials.[14,15,17,19,177,178,183] *(D) Separation performance of IcMMM30 in a dilute 9-component hydrocarbon mixture. (E) Percent changes in permeance after the 6-month stability test. (F) Percent changes in rejection for the 266 Da oligomer after the 6-month stability test.*

Given the highly selective performance of the membranes in the OSN test, an OSRO test to separate toluene (MW: 92 Da) from 1,3,5-triisopropylbenzene (TIPB, MW: 204 Da) was performed for the thermally-treated samples exhibiting systematically varied PPN content after storage in toluene for approximately 18 months. The toluene-TIPB mixture was selected for the OSRO test since it has become a benchmark OSRO separation with a widely reported body of literature data. Similar to the OSN testing procedure, all OSRO measurements were performed at 30 bar transmembrane pressure, ambient temperatures (21-23°C), with low stage cuts (<3% in all cases), and a dilute feed composition (~1 mol% TIPB in toluene) to mimic the operating conditions adopted in previously published studies. The osmotic pressure of this feed, assuming perfect selectivity, was estimated to be less than 3 bar and thus a transmembrane pressure of 30 bar provides adequate driving force for separation.[15] Even after this extended exposure, all of the thermally treated TFC membranes (except IcMMM5, which was defective after 18 months) exhibit upper bound toluene/TIPB separation performance.[15,19,182,183] The OSRO performance was characterized in terms of toluene permeance and TIPB/toluene separation factor, instead of rejection. A permeance-separation factor trade-off was observed, as separation factors monotonically increase with filler loading (i.e., IcMMM30 > IcMMM10 > IcMMM5 > CPIMTT), accompanied by the concomitant decrease in permeance (i.e., IcMMM30 < IcMMM10 < IcMMM5 < CPIMTT), with the overall performance moving along the upper bound. The

decreasing permeance values are in part due to the increasing selective layer thickness, as explained earlier, which can be corrected by optimizing the fabrication protocol. Interestingly, systematic correlations between OSRO performance and PALS data (Figure 20F) were observed: the increase in the amount of ultramicropores observed with increasing the PPN loading mirrors the increase in toluene/TIPB separation factor as PPN loading increases. These results highlight the effect of PPN incorporation: PPN acts to improve membrane selectivity by providing an effective combination of (i) improved rigidity due to inter-crosslinking between the PPN and CPIM and (ii) improved intrinsic selectivity, due to the presence of triptycene units. It has been demonstrated, indeed, that triptycene moieties greatly improve selectivity in gas separation, with a similar effect being observed in organic solvent separation.[32,86,140,191]

Finally, to simulate the fractionation of more complex hydrocarbon mixtures, the IcMMM30 membrane was tested after approximately 21 months of exposure to toluene in a separation test of a dilute 9-component mixture with molecular weights ranging from ~90 to 270 Da (1 mol% each component in toluene, Δp = 50 bar, Appendix C, Table C7). As shown in Figure 22D, IcMMM30 exhibits an overall steep rejection profile, with low molecular weight aromatic compounds like propylbenzene (120 Da), tetralin (132 Da), and 1-methylnapthalene (142 Da) exhibiting low rejections of 6.5 %, 14.1%, and 18.7%, respectively, while aliphatic compounds with similar molecular weights, such as isooctane (114 Da) and n-butylcyclohexane (140 Da), experience significantly higher rejections of 42.5% and 38.8%, respectively. Finally, higher molecular weight compounds like dodecylbenzene (246 Da) and pristane (269 Da) experience significantly higher rejections of 63.4% and 85.8%, respectively. These results demonstrate that, even after almost 2 years of exposure to toluene, IcMMM30 is still able to fractionate application-oriented hydrocarbon mixtures based on both sorption (aromatic/non-aromatic discrimination) and size-

sieving (molecular weight discrimination) mechanics. The IcMMM30 had a permeance of 0.038 L m^{-2} h^{-1} bar^{-1} for this mixture at a transmembrane pressure of 50 bar, which is 5x lower than that of TRIP-TFS, which has a permeance of 0.19 L m^{-2} h^{-1} bar^{-1}. As previously noted, though, IcMMM30 has selective layer thicknesses of approximately 900 nm, which is approximately 3.7x thicker than that reported for TRIP-TFS, so when normalized for thickness, the resulting intrinsic permeabilities of IcMMM30 and TRIP-TFS would be comparable. In comparison to other studied membranes, IcMMM30 presents a similar overall rejection profile as high-performing, plasticization resistant membranes such as TRIP-TFS[14] (an interfacially polymerized polyimine network) and SBAD-1[177] (a spirocyclic microporous polymer), with all three of these membranes exhibiting > 50% rejection of compounds with molecular weights exceeding 200 Da. In contrast to SBAD-1 and TRIP-TFS, however, IcMMM30 has <50 % rejection values for compounds with molecular weights < 200 Da, which could be advantageous for separation applications in which a fraction of this molecular weight range is desirable, such as in isolation of the lighter fuel components (gasoline, naptha, kerosene) from crude oil for further purification. A relevant conclusion is that IcMMM30, after exposure to toluene for 21 months, exhibits comparable performance to TRIP-TFS and SBAD-1, which were tested as fresh-samples.

Distinct trends in performance changes are observed in the 6-month stability test depending on the membrane treatment (i.e., incorporation of PPN, thermal crosslinking). Changes in permeance were dependent almost exclusively on whether the sample was thermally crosslinked. While non-crosslinked samples had almost no changes in permeance, crosslinked samples experienced 400-500% increases in permeance, irrespective of PPN loading (Figure 22E). The loss in selectivity after 6 months becomes smaller with increasing filler loading for inter-crosslinked samples (Figure 22F), with relative losses in rejection of the 266 Da oligomer ranging from -12.4

% for CPIMTT to only -1.3 % for IcMMM30. For the 266 Da oligomer tracked in Figure 22F, changes for CPIMTT appear similar to some of the non-crosslinked membranes, but tracking a larger oligomer with a molecular weight of 578 Da demonstrates that all thermally crosslinked samples exhibit higher stability than non-crosslinked samples (Appendix C, Section C6). Thus, crosslinking preserves the membrane performance by potentially preventing large defect formation (thus preserving rejection of the larger solutes) and long-term relaxation, while inter-crosslinking has the added benefit of preserving the performance closer to the OSRO range.

Following the 6 months aging test, the membranes were once again soaked in toluene and another OSRO test was run after one year on membranes that were aged for 18 months. The permeance changes from 6 months to 18 months were minor compared to the changes occurring in the first 6 months. The permeance changes from 0 to 6 months were: CPIMTT (+ 493%), IcMMM2.7 (+ 417 %), IcMMM10 (+ 365 %), and IcMMM30 (+ 494 %). From 6 to 18 months, permeances changed in the order of IcMMM30 (+ 0.6%) < IcMMM10 (+ 3.4%) < CPIMTT (+ 8.2%) < IcMMM2.7 (+ 23.5%). Thus, it appears that for the samples with higher loadings of PPN (≥ 10 wt.%), their permeances had stabilized after 6 months of exposure to toluene, while the samples with lower loadings of PPN continue to experience gradual increases in permeance over an extended period. This result further highlights that, although the beneficial effects of PPN do not translate into an immediately observable performance enhancement in the freshly fabricated membranes, they are remarkable if the long-term performance is considered.

Considering the 6-month performance shifts, the changes in selectivity appear reasonably correlated with the thermal crosslinking treatment and PPN loading. Changes in permeance, however, appear less correlated to the membrane structure. This is because crosslinking should stabilize performance, yet *only* crosslinked samples experience the anomalously large changes in

permeance, while non-crosslinked samples are stable in permeance, yet lose selectivity. In aggregate, the high toluene uptakes paired with the exceptionally low MWCO values, as well as the increases in permeance for only the crosslinked samples, suggest that a third structural element beyond crosslinking and filler incorporation is present in the membranes that regulates their performance and supports their unprecedented long-term stability. This aspect is discussed in Section 4.4.4.

4.4.4. Formation of a Solvent-Resistant Interfacial Layer

Although the porous Matrimid® supports used in this work have been used in previous studies,[15,19,182,183,192,193] none of them report any effect of the support on the TFC membrane separation performance. Reasonably so, as the supports have pore sizes > 10 nm and toluene permeances > 100 L m^{-2} h^{-1} bar^{-1} and thus offer negligible resistance to transport or molecular sieving capability. However, when considering the materials used in this study to fabricate the selective layer, there appears to be an opportunity for a particularly strong interaction to occur between the CPIM selective layer and the surface of the Matrimid® supports. The proposed interaction mechanism is depicted in **Figure 23**A. Porous supports are fabricated by non-solvent phase inversion and subsequently crosslinked with *p*-xylylenediamine in methanol, resulting in nucleophilic attack of the amine at the imide linkages in Matrimid®. Crosslinking of the support depends on both ends of the diamine finding and successfully linking to two different imide groups, but depending on the local concentration of diamines, the imide groups could be attacked by amines from many different diamines, resulting in a local stoichiometric deficit of imide groups to be attacked. In this scenario, some diamines would only be anchored to the support at one end with an unreacted amine group at the other end. In other words, the support could contain some free amines. A full depiction of this mechanism and structures are shown in Appendix C, Section C7.

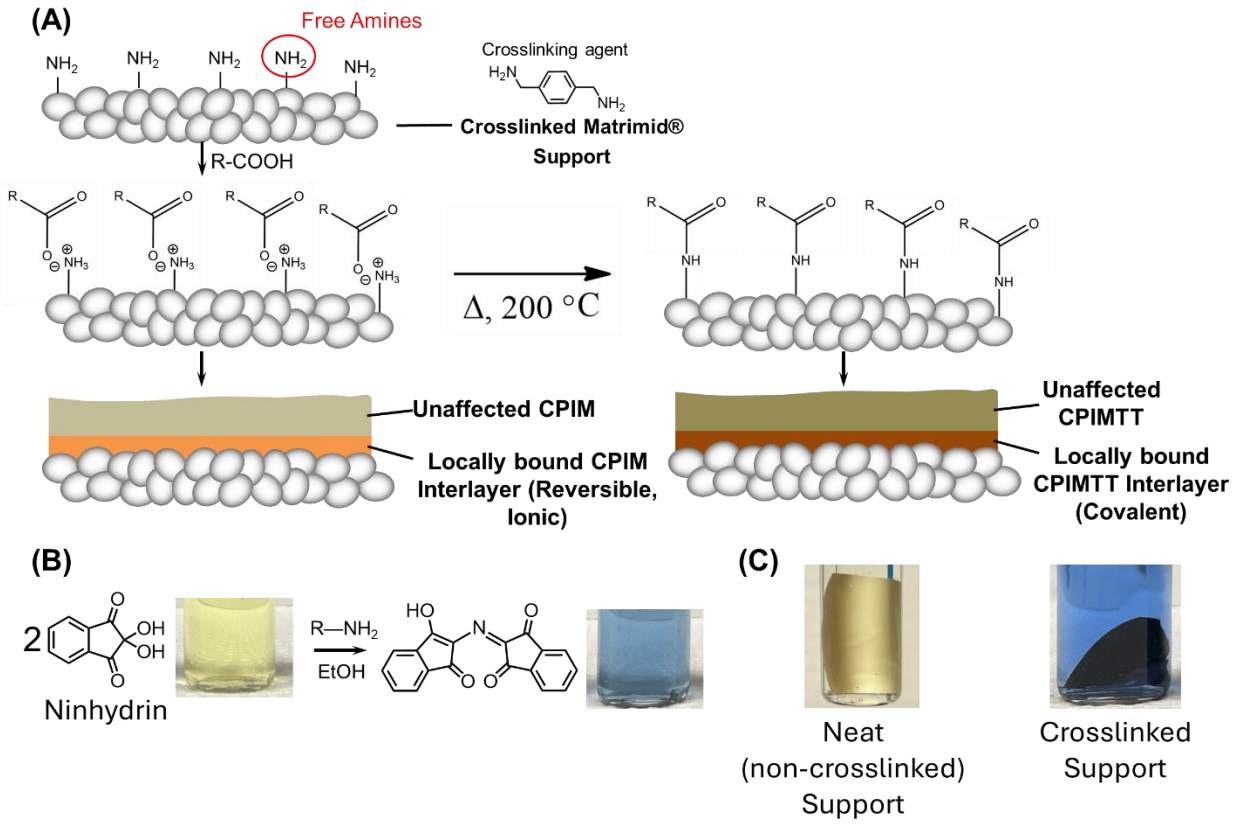


Figure 23. (A) Depiction of the interlayer hypothesis, where free amines couple with the acid groups in CPIM to form a locally immobilized 'interlayer' with solvent-resistant properties. (B) Chemical structures and solutions in ethanol of ninhydrin before and after reaction with primary amines. (C) Ninhydrin test on non-crosslinked supports (i.e., neat Matrimid®) and crosslinked supports.

The resulting free amines that are co-localized at the support surface can easily undergo proton exchange with the carboxylic acid groups in CPIM, forming an ammonium carboxylate crosslink between the CPIM and support.[194–199] Immobilization of the CPIM on the porous support may affect the local chain mobility and solvent uptake, which is expected to alter the TFC membrane performance. This locally bound region is thus called the 'interlayer', which stands for interfacial layer. Ammonium carboxylate complexes will dehydrate under the 200 °C/vacuum

treatment, resulting in transformation of the interlayer crosslinks from reversible ionic species to covalent amide linkages.[194–199] Thus, if the interlayer exists as proposed, a dramatic chemical transformation is expected to occur upon thermal treatment, resulting in stark differences between non-crosslinked and thermally crosslinked TFC membranes.

A prerequisite for the proposed interlayer to form and have distinct properties from the rest of the selective layer is a sufficiently dense concentration of free amines in the support. To test this hypothesis, we employed a chemical reagent known as ninhydrin,which is commonly used in the analysis of peptides and proteins. Ninhydrin forms a yellow solution in ethanol and reacts with primary amines to form a blue-colored complex (i.e., Ruhemann's blue, Figure 23B), making it a suitable reagent to qualitatively test for the presence of primary amines. Ninhydrin tests on non-crosslinked supports develop no color (Figure 23C), indicating ninhydrin does not react with any functional groups in Matrimid®. When tested on crosslinked supports, however, a dark blue color develops, indicating that a large quantity of free amine groups are present and available to react with the carboxylic acid groups in CPIM.

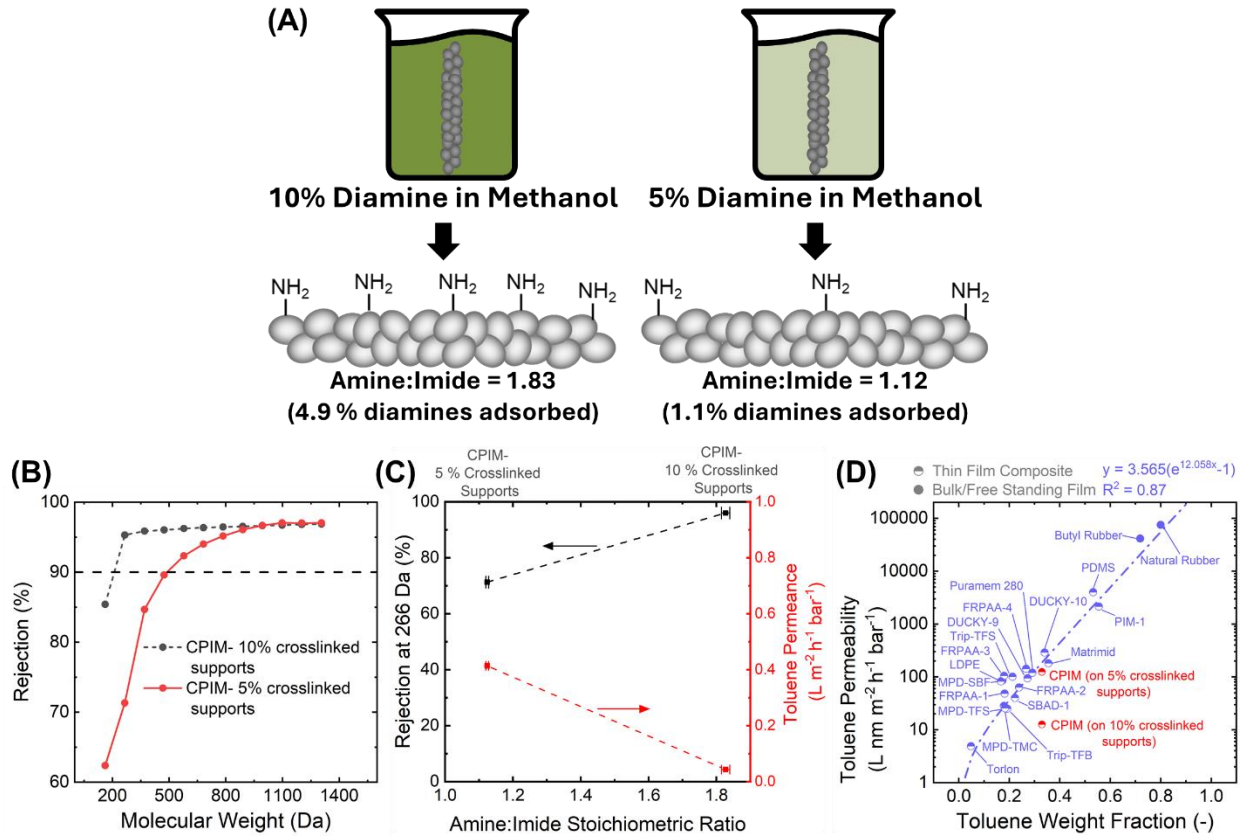


Figure 24. (A) Procedure used to fabricate supports with different free amine content, as well as the corresponding amine loading. Adsorbed amine refers to amine content that is not chemically bound to the polymer at either end, and is just physically adsorbed to the support. (B) Comparison of polystyrene oligomer rejection profiles in toluene for CPIM TFC membranes derived from the two supports. (C) Comparison of the selectivity and permeance of the CPIM TFC membranes derived from the two supports. (D) Correlation of intrinsic toluene permeability with toluene weight fraction in the membrane across different polymer types and membrane configurations. Half-filled symbols are thin films and filled symbols are bulk (free-standing) films. A table containing all of the correlation information and datapoints is provided in Appendix C, Section C8.

Confirmation of the presence of free amines on the support surface qualitatively supports the availability of the reaction pathway to form the interlayer, therefore a more rigorous quantitative test was designed to determine the degree to which the interlayer could regulate both TFC membrane selectivity and permeance. To do this, new supports containing a lower density of free amine groups were fabricated. The original supports used for the transport characterization in this study were crosslinked in a 10 w/v % (g/ml) solution of *p*-xylylenediamine in methanol. By fabricating new supports in a 5 w/v% solution of *p*-xylylenediamine, the probability of both amines in a given diamine molecule reacting with Matrimid® drastically increases, thus reducing the number of monosubstituted diamines responsible for the free amine content, as well as reducing the total number of loaded diamines. This approach was successful: as shown in **Figure 24**A, the original supports had a stoichiometric ratio of amines:imides of 1.83:1, as determined using combustion elemental analysis (Appendix C, Section C9), indicating that a large fraction of diamines were monosubstituted, while the new supports made in the 5 w/v% diamine solution had an amine:imide = 1.12:1 due to there being a higher fraction of the disubstituted diamines responsible for crosslinking. At this stage, for the sake of simplicity, TFC membranes based only on CPIM (i.e., without PPN) were analyzed.

Transport properties of CPIM TFC membranes derived from the two supports indicates that the interlayer heavily regulates the overall membrane performance (Figure 24B). Specifically, TFC membranes derived from the supports exhibiting high free amine content have a sharp rejection profile and a MWCO value of ~200 Da, while those derived from the low free amine content supports have a more gradual rejection profile, resulting in a MWCO of ~ 480 Da (Figure 24B). Remarkably, the low free amine content-derived TFC membrane exhibits an order of magnitude higher permeance than its high free amine content counterpart (Figure 24C), indicating

the interlayer presents a significantly lower permeability than the bulk selective layer while offering a greater selectivitity than the CPIM in the bulk selective layer. Zhou et al.[200] fabricated CPIM TFC membranes with amide-linked interlayers using acid-chloride modified PIM (PIM-COCl) and observed a distinct support amine content at which selectivity begins to significantly improve, indicating that the support amine content has a high influence on the overall TFC membrane performance. One advantage of the interlayer approach we propose in this work is the absence of harsh processing steps or corrosive byproducts formed during the membrane fabrication process. The ammonium carboxylate complex forms spontaneously during coating under mild conditions, and thermal conversion of the complex to the amide releases just water, thus requiring no further solvent or neutralization steps.

Further evidence of the enhanced transport resistance due to the presence of the interlayer is offered by the correlation of toluene permeabilities with selective layer material toluene uptakes (Figure 24D). Twenty different membrane materials were tabulated for their intrinsic toluene permability across a wide range of polymer chemistries, glassy and rubbery polymers, and bulk/thin films. Selective layer thicknesses for thin films were directly reported and measured using SEM. Data points for thin films were only incorporated if the selective layer thickness was clearly discernible and quantifiable, allowing for reasonably accurate conversions of permeances to permeabilities. Across this variety in material properties and compositions, the toluene permeability correlated strongly with the weight fraction of toluene in the membrane, with the equation in Figure 24D exhibiting a 35% mean absolute relative error. The explanation for this excellent correlation lies in the solution-diffusion model: the solvent weight fraction inherently accounts for the solubility contribution to permeability, while the diffusivity is strongly regulated by the volume fraction of solvent in the membrane, according to the Mackie-Meares model.[201] *A*

priori predictions from the solution-diffusion model (i.e., using only weight fraction as the experimental material property input) have an $R^2 = 0.91$ on the experimental data and thus serve to validate this hypothesis, as discussed in Appendix C, Section C10. As shown in Figure 24D, CPIM TFC membranes derived from the high free amine supports significantly deviate from this correlation (absolute relative error: 1375%) when using the weight fraction of toluene measured in bulk CPIM, while CPIM TFC membranes derived from the low free amine content supports have permeabilities in much better agreement with the correlation (absolute relative error: 50%). Thus, the interlayer offers a significant resistance to solvent transport, accomplished by resisting swelling by toluene (and thus reducing uptake). This physical picture tracks with the experimental evidence: when the source of additional resistance is gradually removed, CPIM TFC membranes start to closely follow the permeability-sorption correlation shown in Figure 24D.

As discussed in Section 4.4.5, understanding the evident correlation between toluene uptake and permeability helps elucidate the mechanism responsible for the permeance increases over time in the crosslinked samples upon prolonged exposure to toluene. From the evidence presented thus far, either the interlayer or bulk selective layer in the thermally crosslinked membranes must gradually uptake additional toluene in order to increase its intrinsic permeability. All these aspects are investigated in Section 4.4.5.

4.4.5. Probing Interlayer Transport Behavior

To better understand the transport properties of the interlayer, proxy materials were fabricated to mimic the interlayer and tested (**Figure 25**A). By taking a freestanding film of CPIM and immersing it in a 10 w/v % solution of *p*-xylylenediamine in methanol, a film containing the same ammonium carboxylate linkages expected to be found in the non-thermally crosslinked interlayer materials was obtained. These films are denoted as diamine-treated CPIM, or 'DACPIM'. Further,

DACPIM films could then be thermally treated using the same procedure as the TFC membranes (i.e., 200 °C for 24h under vacuum), resulting in dehydration of the ammonium carboxylate linkages to their corresponding amides. These films, denoted as 'DACPIMTT', are the proxy materials used to mimic the interlayer in CPIMTT TFC membranes.

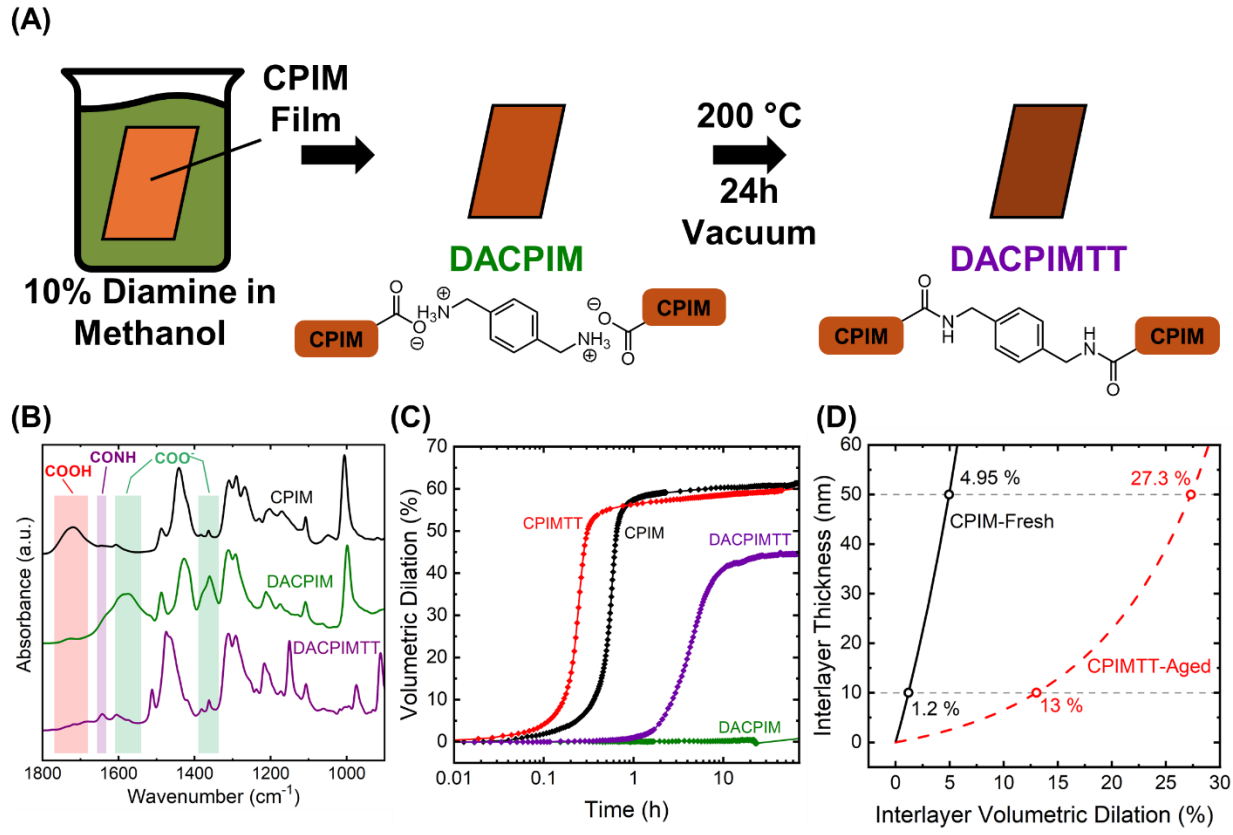


Figure 25. (A) Fabrication procedure for the interlayer proxy materials. (B) ATR-FTIR spectra of CPIM, DACPIM, and DACPIMTT highlighting the chemical changes occuring during interlayer formation. (C) Toluene liquid dilation of the bulk selective layer materials (CPIM, CPIMTT) and the interlayer proxy materials (DACPIM, DACPIMTT). (D) Interlayer transport resistance modeling demonstrating the requisite interlayer volumetric dilation given the assumed interlayer thickness to match the experimentally observed permeance anomaly.

The selective layer-support interaction proposed in Figure 23 is confirmed by the FTIR spectra of CPIM, DACPIM, and DACPIMTT, (Figure 25B). Conversion of the -COOH groups in CPIM to the ammonium carboxylate form is confirmed by the loss of the carboxylic acid C=O stretching vibration at 1720 cm^{-1} going from CPIM to DACPIM, as well as the appearance of the asymmetric and symmetric carboxylate anion ($-COO^-$) stretching at 1580 cm^{-1} and 1360 cm^{-1}, respectively.[98,202] Upon thermal treatment at 200 °C (i.e., conversion to DACPIMTT), these carboxylate anion stretching bands are diminished, and the amide (-CONH) stretching band appears at 1643 cm^{-1}, confirming the dehydration of the ammonium carboxylate complex.[70]

Volumetric dilation (i.e., $\Delta V/V_0$) curves for films of CPIM, CPIMTT, DACPIM, and DACPIMTT in liquid toluene are shown in Figure 25C (measurement details are provided in Appendix C, Section C3.7). To compare the rate of dilation between samples, the curves in Figure 25C are plotted against the square root of time divided by the thickness of each sample (Appendix C, Section C11). When normalized for thickness, CPIM and CPIMTT both dilate at approximately the same rate, reaching equilibrium dilation values of 61.9 % and 58.8 %, respectively. This result indicates that the light crosslinking resulting from the thermal treatment does not significantly inhibit toluene uptake, and thus neat CPIM and CPIMTT are expected to have similar intrinsic toluene permeability values. DACPIM, on the other hand, exhibits a dramatic rejection of toluene due to its ionic crosslinks, experiencing only ~0.4% volumetric dilation after 21 hours of exposure. This low dilation of DACPIM offers explanation for the lower-than-expected permeance of the CPIM TFC membrane (Figure 24D).

Thermal conversion of DACPIM to DACPIMTT eliminates the ionic ammonium carboxylate linkages, resulting in DACPIMTT attaining ~44 % dilation in toluene. Being densely crosslinked, DACPIMTT appears to take much longer to reach its equilibrium dilation value than CPIM and

CPIMTT, even when normalized for thickness (Appendix C, Section C11). The dilation results indicate that, while no significant difference in dilation behavior is observed between CPIM and CPIMTT, DACPIM and DACPIMTT exhibit two completely different behaviors. This divergence in toluene dilation between the interlayer materials appears to be the most responsible for the long-term permeance enhancement in *only* the thermally crosslinked materials. As we found, toluene permeability is strongly coupled to liquid toluene uptake (Figure 24D), and thus slow increases in permeance should be coupled to the slow increase in toluene uptake exhibited by DACPIMTT. It should be noted that differences in experimental timescale (i.e., days in dilation versus months for permeance) are attributed to the confinement of the interlayer materials between the support materials and bulk selective layer. In short, while the interlayer proxy materials do not provide a perfect representations of the interlayer materials, they offer useful indications of the relative properties of the interlayer materials as they undergo conversion from their ionic to covalent forms.

Having established a correlation between toluene uptake and permeability, as well as high-accuracy dilation measurements in toluene, estimates of the permeability for the interlayer can be made. A single interconversion between volumetric dilation and mass fraction is required, and it was found that, among many polymers, volumetric dilation is proportional to the incorporated solvent molar volume (Appendix C, Section C12). Dilation values can thus be converted to mass fractions and used to estimate the intrinsic toluene permeability using the empirical equation shown in Figure 24D.

With estimates of the interlayer and bulk selective layer permeabilities, the resistance offered by each layer can be calculated using the resistance-in-series model (Equation 18):

$$\boldsymbol{r_{TFC} = \frac{l_{TFC}}{P_{TFC}} = \frac{l_{BSL}}{P_{BSL}} + \frac{l_{IL}}{P_{IL}} + \frac{l_{PSL}}{P_{PSL}} = r_{BSL} + r_{IL} + r_{PSL}} \quad (18)$$

where l is the respective layer thickness, P is the layer permeability, and r is the layer resistance to transport. The overall thin film composite (TFC) membrane resistance is made up of resistances from the bulk selective layer (BSL), interlayer (IL), and porous support layer (PSL). Since, as discussed earlier, the porous supports used in this work had toluene permeances > 100 L m^{-2} h^{-1} bar^{-1}, it contributes less than 1% of the observed transport resistance, leaving only the BSL and IL as the primary transport resistances.

As the equilibrium toluene uptake of CPIM and CPIMTT from the dilation measurements were similar, and the CPIM TFC membrane made with the 5 % crosslinked supports (Figure 24D) was in agreement with the toluene permeability-sorption correlation, the BSL permeability of these materials was assumed to be consistent with this experimental measurement (i.e., the 5% crosslinked support CPIM TFC membranes). However, the exact toluene uptake of the interlayer materials is harder to pinpoint, since they are directly bonded to the support layer through the free amines, and are also confined by the BSL at the interface opposite of the support. If the thickness of the interlayer is given, however, the interlayer permeability required to match the experimentally observed transport resistance can be estimated and converted to a dilation value. This calculation was done assuming various interlayer thicknesses, as shown in Figure 25D. Specifically, the lower and upper bounds assumed for the interlayer thickness was 10 and 50 nm, respectively. Assuming a 10 nm interlayer, the originally measured neat CPIM TFC membrane must have an interlayer dilation of 1.2 % in toluene, while the CPIMTT TFC membrane after 6 months requires a DACPIMTT interlayer that has a 13 % dilation in toluene. Although the exact thickness of the interlayer would be difficult to determine, the order-of-magnitude difference between the predicted DACPIM and DACPIMTT interlayer dilation values is entirely consistent with the experimental trends observed in the dilation measurements.

Table 7. Calculated resistances to toluene transport for the various layers in the developed TFC membranes.

Sample	r_{BSL} *[L m^{-2} h^{-1} bar^{-1}]$^{-1}$*	r_{IL} *[L m^{-2} h^{-1} bar^{-1}]$^{-1}$*	r_{PSL} *[L m^{-2} h^{-1} bar^{-1}]$^{-1}$*	*Permeance Optimization Potential* [a]
CPIM-Fresh	*2.3*	*21.5*	*~.01*	*11%*
CPIMTT-Aged	*2.6*	*1.1*	*~.01*	*236%*

[a] *Defined as the permeance enhancement that would result in setting R_{BSL} = 0.*

Estimates of the resistance for each layer in the TFC membranes offer insights into how this membrane platform can be optimized. Resistances for each layer are tabulated in **Table 7.** If the bulk selective layer (BSL) could be removed, leaving only the highly selective and solvent-resistant interlayer, the permeance of the TFC membranes could be optimized without sacrificing their separation performance. For CPIM TFC membranes, removing the BSL would result in only an 11% increment in the permeance due to the high resistance of the DACPIM interlayer, which has a low toluene permeability due to its high resistance to swelling. However, CPIMTT TFC membranes stand to gain much more permeance since the DACPIMTT interlayer presents significantly less resistance, resulting in a potentially optimized CPIMTT TFC membrane having a 236% higher permeance. These calculations demonstrate the strengths of this approach if the BSL thickness can be minimized or entirely eliminated.

The main outcomes are that the proposed approach makes it possible to come up with membranes that swell enough in aggressive organic solvents to exhibit adequate productivity, while maintaining high selectivity for the desired separation over the long-time frame. Since careful tuning of productivity/selectivity tradeoffs for the desired separation process is required,

the tunability of the selectivity in these membranes by simply changing the support amine loading provides a viable approach to engineer the membrane performance over long time frames.

4.5. Conclusions

Separation of aggressively plasticizing solvents, such as the aromatic hydrocarbons found in refining and petrochemical environments, necessitates new membrane materials that can maintain adequate size-sieving capabilities over the long-time frame while still swelling enough to have reasonable productivities. By combining the thermal crosslinking of pendant acid groups in carboxylic-acid functionalized PIM-1, rigid microporous polymer network particles, and interfacial bonding at the selective-layer support interface, the membranes developed in this study completely fulfill the needs stated above, enabling highly selective separations of hydrocarbons without excessively sacrificing productivity while also maintaining unprecedented long-term stability of their separation performance.

It was demonstrated that an ultrathin interlayer region at the selective layer-support interface formed due to ionic complexation of pendant acid groups in the selective layer material with free amine content on the support surface. Noteworthy, this interlayer enables efficient separation performance and can be tuned by modulating the surface free amine content on the supports, as well as by mild thermal treatment of the membranes. Controlling the fabrication variables leading to the formation of the selective interlayer offers opportunities to create a scalable membrane platform with exquisite and precisely tunable selectivity and permeability combinations that could be tailored to suit a variety of different OSN and OSRO membrane separation applications.

Chapter 5. Summary and Recommendations for Future Research

5.1. Summary

The initial aim of this work was to discover and understand membrane systems exhibiting long-term stability and resistance under chemically harsh conditions, which would promote the adoption of highly energy-efficient membrane separation systems in currently unabated industrial chemical separations, such as thermal distillation. To this end, this dissertation documents the development of a crosslinked nanocomposite membrane platform able to withstand highly plasticizing conditions for potentially commercially relevant OSN and OSRO membrane separations, while also providing fundamental insights into the specific contributing factors leading to plasticization resistance, heuristics for fabrication of highly plasticization resistant membranes, and mechanistic aspects of gas and hydrocarbon transport in these systems.

This work began with a fundamental study of the membrane fabrication, in which it was found that carboxylic acid functionalized PIM-1 (CPIM) could be thermally crosslinked both to itself and to an incorporated porous polymer network (PPN) composed of triptycene and isatin monomers at 200 °C under vacuum. It was thusly found that the simultaneous incorporation of PPN and thermal crosslinking treatment had a synergistic effect in boosting separation performance as well as in creating outstanding plasticization resistance. These results are summarized in Chapter 2.

Next, in Chapter 3, the potential of the triptycene-isatin PPN to inhibit physical aging in glassy nanocomposite systems was evaluated. The PPN was incorporated into poly(1-trimethylsilyl-1-propyne) (PTMSP), a microporous glassy polymer known to experience rapid physical aging. It was found that incorporation of as little as 5 wt. % of the triptycene-isatin PPN into PTMSP slowed

the rate of physical aging by about a factor of three. Modeling of experimental data, as well as in-depth measurements of the free volume, molecular relaxations, molecular dynamics simulations, and transport analyses revealed that an adsorptive-type interaction between the PTMSP and PPN inhibited the segmental mobility associated with PTMSP backbone carbons, thus slowing the rate of physical aging. Fundamental insights into the molecular mechanisms for physical aging inhibition provide groundwork for engineering aging-resistant glassy polymer membranes, which is a highly relevant issue for industrial gas separation membranes, most of which are glassy polymers.

Chapter 4 returns to the highly plasticization resistant CPIM/PPN nanocomposite systems developed in Chapter 2 in order to further understand their potential for chemically aggressive separations. Thin film composite (TFC) membranes based on CPIM and CPIM/PPN nanocomposites, as well as their crosslinked counterparts were studied. Varying across filler loading and thermal treatment provided a comprehensive understanding of the contributing factors to membrane performance. Hydrocarbon fractionation OSN and OSRO tests were performed in toluene to understand how these membranes retained their size-sieving capabilities. Additionally, after initial testing, membranes were tested for their long-term stability by leaving them exposed to toluene for extended periods. Even after almost 2 years, TFC membranes that were crosslinked exhibited exceptional hydrocarbon fractionation performance in OSRO tests, especially those containing PPN. Additionally, a novel interaction between the CPIM and porous support chemistry was discovered, and detailed characterizations revealed this interaction to further contribute to the long-term stability and excellent separation performance of the membranes. Now, a host of simple treatments were identified that can be individually tuned to alter membrane properties and performance: thermal treatment, filler incorporation, and interactions with the support,

accomplishing the initial goal of developing and understanding highly stable and selective membranes for chemically aggressive separations.

This work was supported by an NSF grant and the NSF Graduate Research Fellowship Program. The content of this dissertation, findings, conclusions and recommendations are those of the author(s) and do not necessarily reflect the views of the National Science Foundation.

5.2. Future Work

While many novel material fabrication strategies and their fundamental understanding on membrane properties and performance were elucidated, there remains a number of experimental and theoretical aspects to be uncovered to further explore the potential of this material platform.

One key aspect of the material platform we developed was that the CPIM could be thermally crosslinked at 200 °C under vacuum. This leads to an adequate level of crosslinking to enhance separation performance, yet the variable space associated with the thermal treatment protocol itself was left essentially unexplored- that is, the same protocol was always used: 24 h, at 200 °C, under vacuum. Although this temperature is advantageous for manufacturing, the long treatment time could be investigated. It is uncertain what the effect of a shorter treatment time would be, for example, if 12 h is just as efficacious as 24 h, or not. Studies using thermogravimetric analysis (TGA), dynamic scanning calorimetry (DSC), and the plasticization susceptibility tests described in Chapter 2 could elucidate the impact of varying the thermal treatment protocol. Additionally, 200 °C is nice because it is compatible with most gas-sealing systems: silicone gaskets, epoxies, etc. Some silicone gaskets and epoxies can withstand slightly higher temperatures, so it would be worthwhile to expand this study to include a slightly higher temperature range, such as 220 °C.

An additionally unexplored variable space is the PPN physical particle architecture. The same batch of ball-milled PPN was used for this entire study (particle sizes ranged from 100-700 nm). This particle batch dispersed nicely with sonication and formed defect-free membranes up to high loadings, which was one of the original goals. While nice for comparison' sake, using a single batch of material leaves out the effect of the PPN particle size and shape on the outcomes of the study. For example, in thin film composite membranes, the length of certain PPN particles is close to that of the selective layer thickness itself, which means that the potential CPIM/PPN interfacial surface area has much room for improvement here by reducing particle size. Particle size and network architecture could be improved upon by undertaking a new synthetic campaign: triptycene is trifunctional, while it reacts with the bifunctional isatin, forming a three-dimensional crosslinked network. By adding other comonomers that are, for example, bifunctional or monofunctional, the connectivity and effective degree of polymerization of the network could be greatly affected. By changing the connectivity of the network, further "branching" of the PPN could improve interfacial interactions with the matrix polymer it is incorporated into. By introducing monofunctional monomers into the synthesis, the network is "capped", thus potentially creating ways that sub-100 nm particles could be synthesized from the bottom-up, overcoming the lower particle limit of grinding technologies.

Lastly, a detailed empirical and fundamental study of the interlayer formation and variable space would be the next logical step in developing the material platform. That is, what is the effect of (i) free amine content on the support surface and (ii) carboxylation degree of the CPIM on the resulting OSN/OSRO performance and long-term stability? In Chapter 4, two extremes were offered: low amine content and high amine content, and only a highly carboxylated batch of CPIM

(~90%) was utilized. A more thorough parametric study could elucidate the optimal interlayer formation conditions and provide guidance for how to best utilize this technology.

Once these aspects are addressed: the thermal treatment protocol variable space, the PPN particle physicochemical variable space, and understanding in detail the relationship of interlayer formation conditions and membrane performance, further testing on more complex mixtures would be desirable. A 9-component hydrocarbon mixture was utilized, but this is a relatively small dataset when compared to real-life refining conditions, which may have hundreds or thousands of different compounds. Expanding analytical and testing techniques to more complex and concentrated mixtures would be of technological and scientific relevance, especially if simple correlations could be made between the solvent structure and its rejection for a simple membrane. Specifically, being able to extrapolate a broad class of hydrocarbon separation performance based on a simplified mixture performance in a single membrane would be a highly desirable workflow for relatively fast screening of membrane candidates for more application-oriented testing. Beyond hydrocarbons, understanding the separation behavior for more non-ideal mixtures, such as those containing polar solvents, would also be of interest.

Appendix A

A1. Materials

Methanol (HPLC, > 99.9%) and toluene (HPLC, 99.8%) were purchased from Fischer chemical. N,N-Dimethylacetamide (DMAC, HPLC, > 99.5%), 5,5',6,6'-Tetrahydroxy-3,3,3',3'-tetramethyl-1,1'-spirobisindane (TTSBI, 97%), and Chloroform (ACS, > 99.8%) were purchased from Alfa Aesar. Tetrafluoroterephthalonitrile (TFTPN, 98%) and triptycene (98%) were purchased from TCI Chemicals. Potassium carbonate (K_2CO_3) and Isatin (97%) were purchased from Sigma Aldrich. Tetrahydrofuran (THF, HPLC, inhibitor-free) was purchased from Macron Fine Chemical. Sulfuric acid (ACS grade) was purchased from EMD, and glacial acetic acid from Research Products International.

TFTPN and TTSBI were dried at 30 °C and 110 °C, respectively, in a vacuum oven overnight before use, without any further purification. The amounts of TFTPN and TTSBI used in the synthesis of PIM-1 were adjusted for the listed purity. Potassium carbonate, which neutralizes the HF formed during the synthesis of PIM-1, was ground in a mortar and pestle, sieved through a 220 mesh (0.065 mm) Titan brand stainless-steel sieve, and dried at 110 °C in a vacuum oven overnight before use. Isatin and triptycene were dried in a vacuum oven at 30 °C overnight before use, without any further purification.

A2. Synthesis of PIM-1

PIM-1, which is the precursor material for the synthesis of the final inter-crosslinked mixed matrix membranes, was synthesized using a high-temperature polycondensation technique. All glassware was dried at 130 °C in an oven overnight before use. A 250 ml 3-neck round bottom flask was equipped with a mechanical stirrer, reflux, addition funnel, and purge gas inlets/outlets.

13.44 mmol of TFTPN, 13.43 mmol of TTSBI, and 27 ml of DMAc were added, then a 5 ml/second dry nitrogen purge was delivered to the flask. The monomers were gently stirred until they fully dissolved to form an orange-brown solution. The stir rate was then set to 200 rpm, and 40.52 mmol of the pre-dried, ground, and sieved K_2CO_3 was added using a powder funnel. Following this step, 14 ml of toluene was immediately added using the addition funnel, and the flask was submerged in a pre-heated oil bath at 160 °C. A bright yellow solution formed, and after 5 minutes, the viscosity increased. A further 9 ml of toluene was then added to dilute the solution and reduce the viscosity. After 30 minutes of stirring, another 18 ml of toluene was added, and the flask was removed from the oil bath. The reaction mixture was precipitated into 500 ml of methanol to yield bright yellow fibers. The fibers were solvent exchanged with water to remove residual salts from the reaction. Specifically, the fibers were soaked in hot water (95°C) for 1 hour. The water in this bath was decanted off and changed, repeating the exchange process 3 times. The fibers were dried at 130°C in a vacuum oven overnight. The resulting PIM-1 was then dissolved in 250 ml of chloroform and precipitated into a 1:1 (v:v) solution of acetone:THF to extract low-molecular weight residues. The solvents were decanted, and the resulting fibers were then soaked in a water bath at 95°C. The exchange process was repeated three additional times to further remove any residual salts. Finally, the fibers were dried at 130°C in a vacuum oven overnight to yield the finished product (86.4% yield).

A3. Synthesis and Properties of Triptycene-Isatin Porous Polymer Network

To a 250 mL three-neck round-bottom flask equipped with a mechanical stirrer, gas purge inlet, and addition funnel, triptycene (2.9399 g, 11.6 mmol) and of isatin (2.550 g, 17.0 mmol) were added under nitrogen flow (~5 cc/sec). Anhydrous chloroform (13 mL) was added to the flask and

stirred gently while ensuring any monomers on the flask walls were washed down. The flask was cooled in an ice bath for 5 minutes and the addition funnel was loaded with 26 mL of anhydrous trifluoromethanesulfonic acid (TFSA). TFSA was then added dropwise to the flask in the ice bath over the course of 15-20 minutes, under nitrogen flow and mild stirring, resulting in the formation of a viscous, dark-colored mass. The mixture was cooled to room temperature, the nitrogen purge was shut off, and then the reaction was stirred at 60°C for three days while isolated from the ambient atmosphere. After three days, the flask was cooled in an ice bath for 10 minutes, and the reaction was quenched by adding distilled water dropwise with the addition funnel under mild stirring. Once fume evolution ceased, the reaction mixture was transferred to a separate container, and solid chunks of product were removed. The reaction mixture was then filtered to recover any smaller solids, which were then combined with the larger solids, and the combined solid product was crushed lightly with a mortar and pestle to reduce the particle size. Finally, the product was washed three times each with water, acetone, and chloroform. The resulting mass was then wet milled in ethanol at 650 rpm for one hour using a Retsch PM 100 planetary ball mill with 3 mm stainless steel grinding balls. The resulting powder was suspended in ethanol, centrifuged at 5000 rpm, and the solid product was recovered after decanting the supernatant. Finally, the product was dried in a vacuum oven at 150°C for 12 hours and stored in ambient conditions until its use.

Relevant measured and theoretical properties of the triptycene-isatin PPN are summarized in Table A1. In Table A2, the average of extrapolated permeabilities for the pure PPN fitted to 0-30 wt.% PPN loadings in Matrimid, 6FDA-6FpDA, and 6FDA-TMPD data reported by Aguilar-Lugo et al. [43] are given. These values were fit using the effective medium approach reported by Soto et al. [46] for each polymer type, and the reported values and errors are based on the estimates derived from the three membranes. H_2 permeability was not available, so was not included.

Table A1. Properties of the Triptycene-Isatin PPN.

Property	***Value***	***Method of Determination***	***Source***
BET Surface Area	695 m^2/g	N_2 adsorption at 77 K	This work
Average Particle Size	722 ± 467 nm	Scanning Electron Microscopy	This work
Fractional Free Volume	31.8 %	Updated Bondi's method [151]	This work
Pore Sizes	.35, 0.526, 0.824 nm	NL-DFT + CO_2 adsorption at 0 °C	[1]

Table A2. Calculated gas permeation properties of the pure triptycene-isatin PPN using the effective medium model approach [46].

permeability (Barrer)				
He	***O_2***	***N_2***	***CO_2***	***CH_4***
671 ± 124	212 ± 60	47 ± 23	1069 ± 453	49 ± 39

A4. Membrane Casting

A concentration of 4 w/w % total solids (polymer + filler) was used for all casting solutions. For the non-mixed matrix materials, CPIM powder and THF were combined in a 20 ml scintillation vial and vortex mixed until a homogeneous solution formed. To prepare solutions for mixed matrix membranes, PPN powder and THF were combined in a 20 ml scintillation vial, and this solution was sonicated at 37 kHz for 2 minutes to disperse the PPN. Then, CPIM powder was added to this solution and then vortex mixed and sonicated in 2-minute intervals until the CPIM fully dissolved, and a homogeneous suspension was formed. All solutions were sonicated briefly before casting to remove dissolved gases.

All membrane casting was done in a N_2-purged glove bag on a leveled PTFE petri dish. PTFE was chosen because it facilitated the membrane formation process by allowing for even membrane shrinkage. Membrane formation could not be successfully accomplished using glass substrates. Casting solutions were poured into the PTFE dish and covered with filter paper, an aluminum disk, and a paper weight to slow down solvent evaporation and maintain a stagnant atmosphere above the nascent membrane. After 48 hours, the membranes were recovered and dried at 110°C overnight.

Table A3. Thicknesses, densities, and fractional free volumes (FFVs) of the membranes used for permeability and sorption measurements. Errors were calculated using linear error propagation [203].

sample	***thickness*** *(μm)*	***density*** *(g cm^{-3})[a]*	***FFV*** *(%)[b,c]*
CPIM	141 ± 3	1.285 ± 0.003	21.0 ± 0.6
CPIMTT	184 ± 8	1.279 ± 0.007	21.4 ± 0.7
MMM30	174 ± 3	1.267 ± 0.002	21.1 ± 0.6
IcMMM30	149 ± 4	1.244 ± 0.002	21.1 ± 0.6
Triptycene-isatin PPN	N/A	1.08[d]	31.8

[a]Density was measured by the buoyancy principle in water using a Mettler Toledo density kit.
[b]FFV was calculated using the density measurements and the updated group contribution method reported by Wu et al.[151] for the Van der Waals volume (VdW). FFV = $(V - V_{oc})/V$ where V is the specific volume of the polymer and V_{oc} = 1.3×VdW
[c]FFV calculations did not take into account the oligomeric pTHF present in the samples or the resulting crosslinked structures in the membranes. For thermally treated samples, it was assumed that 25% of the -COOH groups were missing and replaced by hydrogens, as found by thermogravimetric analysis.
[d]Estimated from the reported PPN pore volume (V_{pores} = 0.440 cm^3 g^{-1}) calculated from N_2

The fractional free volume (FFV) estimates shown in Table A3 indicate that the various membranes all have similar FFVs, however, the diffusivities of CO_2 and CH_4 in these membranes

are quite different. This may stem from the fact that certain compositional features, such as the presence of oligomeric pTHF, and the formation of crosslinked structures, are not taken into account for these materials. Thus, an extensive direct comparison of FFV values and diffusivities is not undertaken.

A5. Fourier-Transform Infrared Spectroscopy

CPIM membranes and their derivatives were analyzed using FTIR with an attenuated total reflectance (FTIR-ATR) accessory (Nicolet iS50R Fourier Transform Infrared Spectrometer) with a diamond crystal. Spectra were measured by averaging 64 scans at a resolution of 0.4821 cm^{-1}.

A6. Scanning Electron Microscopy

Cross-sectional micrographs of CPIM, CPIMTT, MMM30, IcMMM30 membranes and PPN particles were taken to determine their structural morphology using a ThermoFisher Quattro scanning electron microscope. Samples were prepared by fracturing membranes using tweezers. Prior to imaging, each sample was coated with iridium at a current of 20 mA for 45s using a Quorum Q150 sputter coater. Micrographs of all samples are shown in Fig. S1. For the PPN

particles, an average particle size of 722 ± 467 nm was measured for isolated particles.

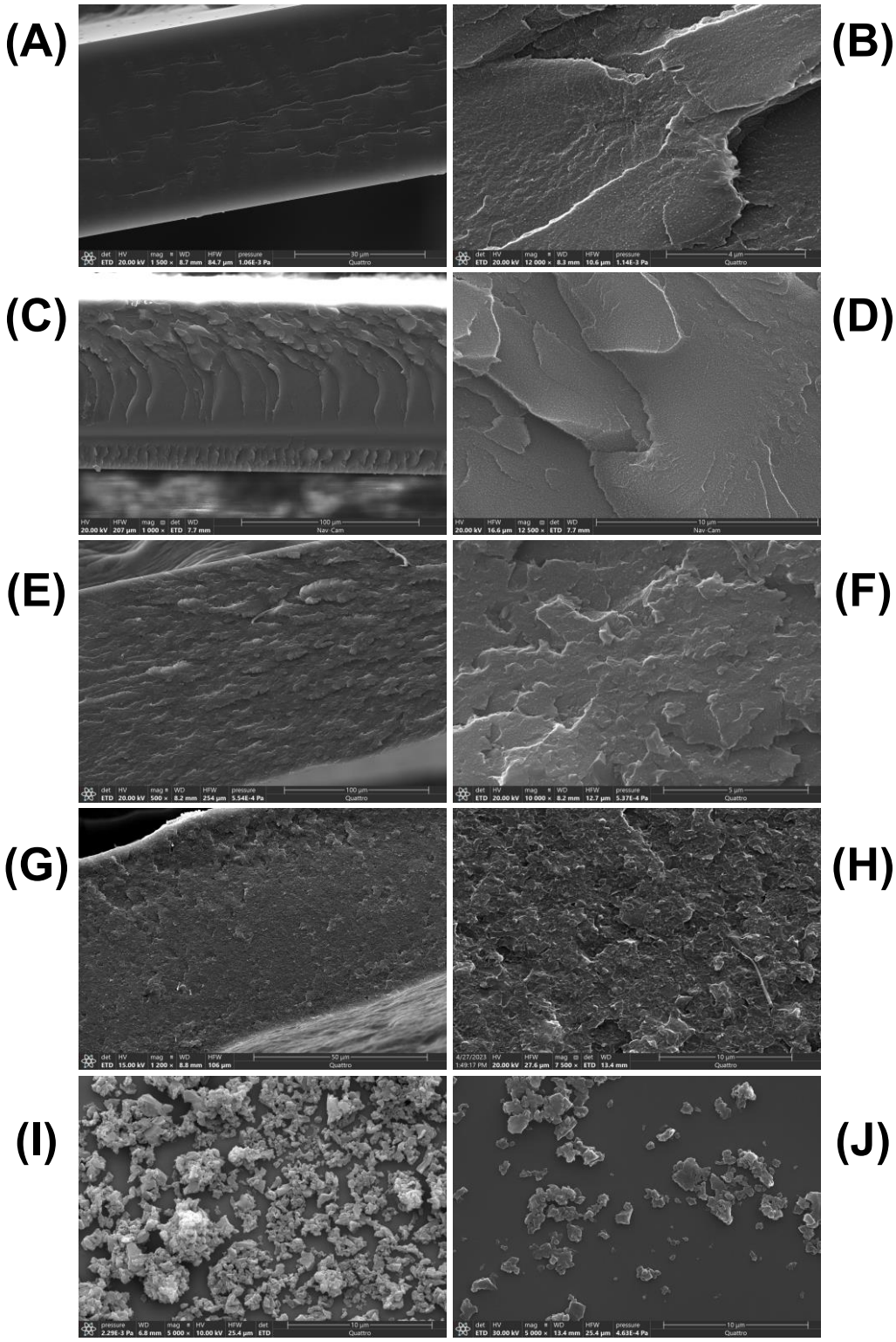


Figure A1. SEM micrographs depicting cross-sectional images of (A),(B) CPIM; (C),(D) CPIMTT; (E),(F) MMM30; (G),(H) IcMMM30, and (I),(J) triptycene-isatin PPN particles dispersed on a silicon wafer.

SEM was further used to determine the dispersion of PPN across the membrane cross-section in the z-axis (i.e., perpendicular to the membrane surface). Figure A2 shows a line scan in the z-direction, and the corresponding line plot depicts the carbon, oxygen, and nitrogen content along the line at each tick mark. Excluding hydrogen, CPIM has a 21.6% molar oxygen content, while the triptycene-isatin PPN has a 4.28% molar oxygen content. Thus, if significant agglomeration or settling occurred during solution-casting, a depletion of oxygen content should be observed while moving towards the bottom of the cross-section (i.e., higher x-values in the line plot). While a slight decrease in oxygen is apparent, it is only within 2%. More dramatic differences are expected if significant sedimentation took place: for example, if all of the PPN was deposited in the bottom half of the cross-section, the bottom half would have a molar oxygen content of 11.2%. The difference in appearance in the top and bottom of the cross-sections, then, could be due to particles of different sizes dispersing along the z-direction, but the composition of the membrane is unaffected by this behavior, indicating a good dispersion of particles.

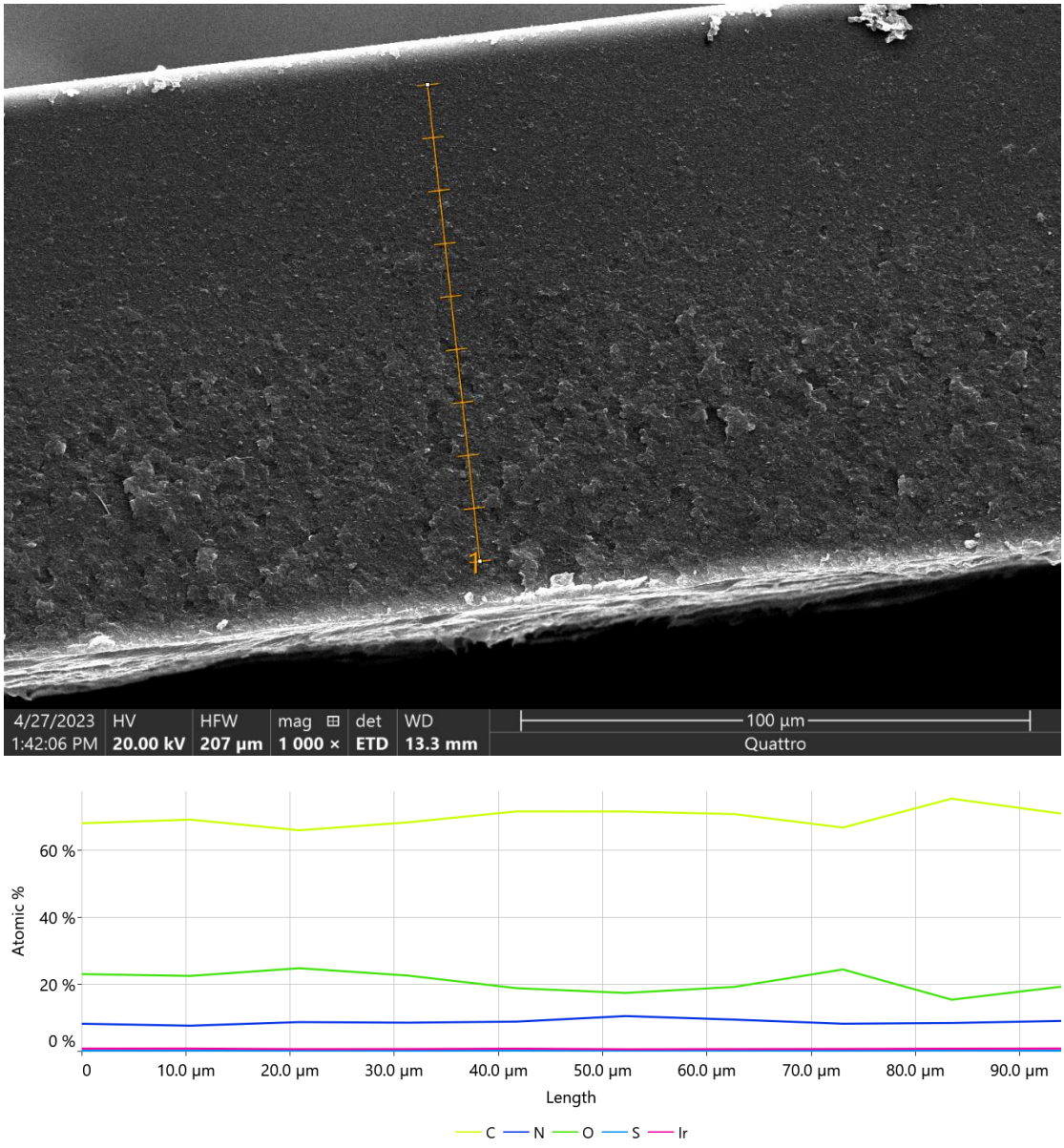


Figure A2. (Top) SEM micrograph of an MMM30 membrane with the line scan and point analyses indicated by tick marks along the scan direction. (Bottom) A line graph showing the relative C,N,O, and Ir (sputtercoating substrate) molar % along the length of the line scan.

A7. Thermogravimetric Analysis/Mass Spectrometry (TGA-MS) and DSC

TGA and TGA-MS of CPIM, CPIMTT, MMM30, and IcMMM30 membrane fragments were performed to characterize membrane thermal stability and to elucidate structural changes occurring during thermal treatment. Experiments were performed using a Netzsch STA 449 F1 Jupiter with a pin thermocouple and Netzsch nanobalance. Data was taken using a correction file for each temperature program to account for gas viscosity changes. Evolved gases were analyzed by mass spectrometry using an Aeolos QMS 403 C. For standard TGA analysis, pieces of membrane samples with masses between 8-20 mg were equilibrated in the crucible at 40 °C, then heated at a rate of 10 °C/min to 800 °C under a flow of 40 sccm Argon gas.

Dynamic scanning calorimetry (DSC) was run on cast membrane samples using a TA Instruments DSC 2500. 3-10 mg of sample were heated in standard aluminum pans with punctured tops (to allow for sorbed gases and moisture to escape) at a rate of 10°C/min from 40°C to 290 °C three times. Figure A3 shows the results of the 3rd heating scan. No transitions are observed, indicating that the PPN does not affect the polymer glass transition temperature within this range.

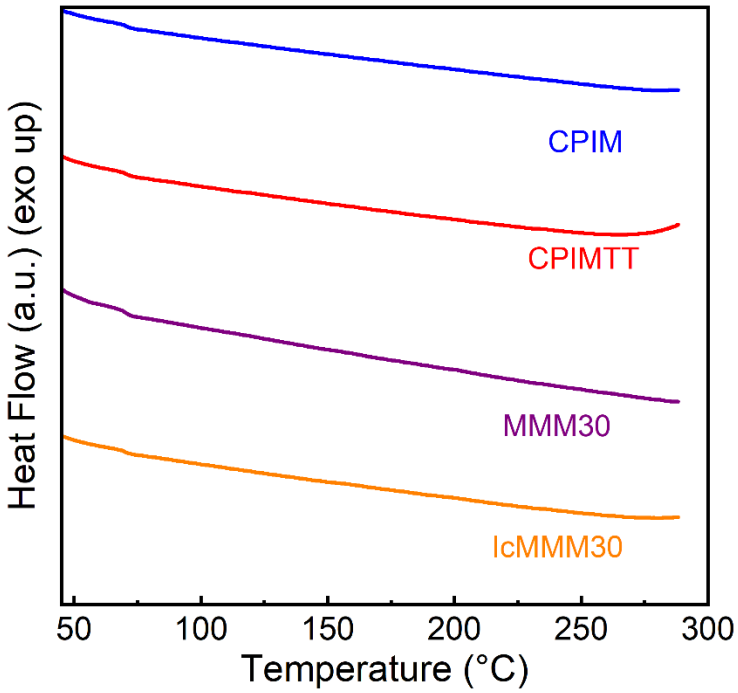


Figure A3. DSC thermograms of the four membranes studied, during the third heating cycle. The minor bump in the data at 70°C is an artifact due to contamination of the furnace.

A8. Nuclear Magnetic Resonance (NMR) Spectroscopy

NMR spectroscopy was performed on samples to determine successful synthesis and to investigate the thermal crosslinking reaction. ^{1}H NMR spectra of PIM-1 and CPIM in deuterated THF (THF-d8) was performed on an 800 MHz Bruker Neo. ^{1}H spectra were taken as the average of 16 scans at 298 K with an acquisition time of 2.6214 s, a relaxation delay of 1.0s, and a pulse width of 8.0000 μs.

^{13}C Cross-polarizaton/Magic Angle Spinning (CP/MAS) solid-state NMR was performed on a 600 MHz Bruker Neo and spectra were referenced externally to hexamethylbenzene. The ^{13}C frequency was approximately 150.57 MHz. Samples were spun at 13 kHz. Spectra were collected by averaging 1800 scans taken with an acquisition time of 0.0225 s, relaxation delay of 2.0 s, and pulse width of 3.5 μs. T1 values were determined by the T1CP method reported by Torchia [204]. Spectra for T1 determination were taken at delay times ranging from 0.005 seconds to 20 seconds. Each spectrum for T1 determination was the average of 512 scans with an acquisition time of 0.0418 seconds, a relaxation delay of 2.0 s, and a pulse width of 3.5 μs. T1 values were then determined by fitting the peak height as a function of delay time (t) to an exponential relation of the form $A\, e^{-\frac{t}{T_1}}$, where A is an arbitrary fitting constant in this case.

A9. Powder Brunauer-Emmett-Teller (BET) Analysis

BET analysis of the cryogenic N_2 adsorption isotherms for the synthesized triptycene-isatin PPN was used to determine its specific surface area and confirm successful synthesis. N_2 adsorption-desorption isotherms were measured at -196 °C in a Micromeritics Tristar II Plus. The equilibration time was 20 s. The sample was degassed at 180 °C under vacuum prior to

measurement. Apparent surface areas (S_{BET}) were determined by the BET method at an activity range (P/P_0) from 0-0.057. BET surface area of the synthesized triptycene-isatin PPN was 695 m^2/g.

A10. Elemental Analysis

Elemental analysis of PIM-1 and CPIM samples were performed to determine the successful synthesis of the materials and the degree of hydrolysis of the CPIM. Samples were analyzed using an Elementar Vario EL elemental CNS analyzer. Samples of sulfanilamide were provided by Elementar to calibrate the instrument. Three separate samples of sulfanilamide were run immediately prior to analysis to calibrate the instrument. The degree of hydrolysis (i.e., the fraction of nitriles converted to carboxylic groups) of CPIM samples were determined using the following equation:

$$degree\ of\ hydrolysis\ (\%) = \frac{\left(\frac{N}{C}\right)_{PIM-1} - \left(\frac{N}{C}\right)_{CPIM}}{\left(\frac{N}{C}\right)_{PIM-1}} \times 100\% \qquad (A1)$$

where N/C is the molar ratio of nitrogen to carbon determined.

A11. Gel Fraction Tests

Gel fractions of crosslinked membranes, CPIMTT and IcMMM30, were measured to determine the efficacy of the thermal crosslinking reaction. Membranes were first dried at 100 °C in a vacuum oven for 4 hours and then weighed to determine the initial mass, m_0. Then, membranes were soaked in THF for 24 hours, and the resulting leachate solution was discarded and replaced with new THF. This wash cycle was repeated three times, and then membranes were rinsed twice with THF after the third cycle. Finally, membranes were dried at 100 °C in a vacuum oven for 4

hours again and then weighed to determine their final mass, m_f. The gel fractions of the resulting membranes were determined according to the following equation, where a gel fraction of 100% indicates complete crosslinking of the membrane:

$$gel\ fraction\ (\%) = \frac{m_f}{m_0} \times 100 \qquad (A2)$$

To determine whether the crosslinks were the product of reversible condensation reactions, samples of CPIMTT and IcMMM30 were boiled in water for 10 days and then tested using the procedure above. Crosslinks from condensation products such as anhydrides or imides, if present, should be partially or completely hydrolyzed using this procedure, resulting in a decreased gel fraction.

Table A4. Gel fractions of various membranes after soaking in THF. Errors were calculated using linear error propagation [203].

sample	***gel fraction** (%)*
CPIM-THF Casted	90 ± 1
IcMMM30- THF Casted	94.1 ± 0.7
CPIMTT-THF Cast/Water Boiled	89 ± 1
CPIMTT-DMF Cast/Water Boiled	90 ± 1

A12. Gel Permeation Chromatography

Gel permeation chromatography (GPC) was used to determine the molecular weight of the synthesized PIM-1. MW was determined using polystyrene standards (1-500 kDa) in chloroform on a Waters™ 717 plus auto sampler with a 7.5 x 250 mm Agilent polypore column at a flowrate of 1 ml/min chloroform at 40 ºC. The eluent was detected using a Waters™ 490E UV-VIS multi-

wavelength detector set to 298 nm. After synthesis and purification, the PIM-1 used as the precursor to CPIM had a M_w = 153.4 kDa and dispersity $Đ$ = 1.59.

A13. Pure Gas Permeation Measurements

A 47 mm HP filter holder was used to separate the feed and permeate sides of the membrane. Prior to measurements, vacuum was pulled on the system overnight using a rotary vacuum pump (Welch DuoSeal 1402) to remove any sorbed species from the membrane. Measurements were performed by charging the desired gas pressure to the upstream side of the membrane. Upstream pressure was monitored using a PX-409-USHB series Omega pressure transducer (0-1000 psi). Then, gas was allowed to permeate through the membrane to the downstream volume, where the increase in pressure with time was measured using an MKS Baratron capacitance manometer (0-10 Torr). The permeability (P, in units of Barrers) was calculated as follows:

$$P = \frac{lV_{down}}{\Delta pART}\left(\left(\frac{dp}{dt}\right)_{down} - \left(\frac{dp}{dt}\right)_{leak}\right) \quad (A3)$$

where l is the membrane thickness, A is the membrane area available to gas transport at the upstream side, R is the gas constant, T is the absolute temperature, Δp is the average transmembrane pressure difference, $\frac{dp}{dt}_{down}$ is the asymptotic rate of pressure increase in the downstream volume, and $\frac{dp}{dt}_{leak}$ is the rate of pressure increase in the downstream volume whilst the charge pressure is 0. Membrane thickness was determined by the average of 10 measurements made using a Mitutoyo micrometer with 1 micron resolution. Membranes were glued with epoxy resin on a brass coupon, then scanned at a resolution of 600 dpi. The passage area was thus calculated as the average of 9 measurements collected from 3 measurements on 3 different scans

of the brass coupon at different rotations to average out any ambiguities due to shadows and color gradients.

A14. Pure Gas Sorption Measurements

The system consists of two chambers of known volume connected via a valve, which are differentiated as the "sampling" and "charge" chambers. Both chambers are equipped with PX-409-USHB series Omega pressure transducers (0-750 psi, ± 0.08% BSL accuracy). The polymer sample is first added to the sampling chamber and both chambers are evacuated of gas overnight using a rotary vacuum pump (Welch DuoSeal 1402). Gas is then introduced to the charge chamber and allowed to reach thermal equilibrium before quickly releasing it into the sampling chamber, upon opening the valve between the two chambers for a few seconds. The valve separating the two chambers is then closed, and each chamber is allowed to equilibrate. Pressure decay in the sampling chamber is observed due to gas partitioning into the polymer sample. Upon reaching sorption equilibrium, the process is repeated stepwise, without pulling vacuum. The overall sorbed gas concentration in the polymer sample is calculated using the initial charge pressure and equilibrium pressures for each chamber, at each step, as follows:

$$C_{pol,j} = \frac{\rho_{pol}}{g_{pol,dry}} \left(\sum_{i=0}^{j} \left(\frac{1}{\tilde{V}_{C0,i}} - \frac{1}{\tilde{V}_{CF,i}} \right) - \frac{V_S}{\tilde{V}_{SF,j}} \right) \tag{A4}$$

where ρ_{pol} is the polymer density (assumed constant), $g_{pol,dry}$ is the dry polymer mass, j is the current pressure step, V_s is the sample chamber volume, V_C is the charge chamber volume, and $\tilde{V}_{C0}$, $\tilde{V}_{CF}$, $\tilde{V}_{SF}$, are the gas molar volumes (calculated using the Peng-Robinson equation of state) for the initial charge state (prior to valve opening), final charge state, and final sample state,

respectively. Concentration errors were calculated by linear error propagation, according to the method reported by Box et al. [89].

A15. TGA of CPIM and Triptycene Isatin PPN

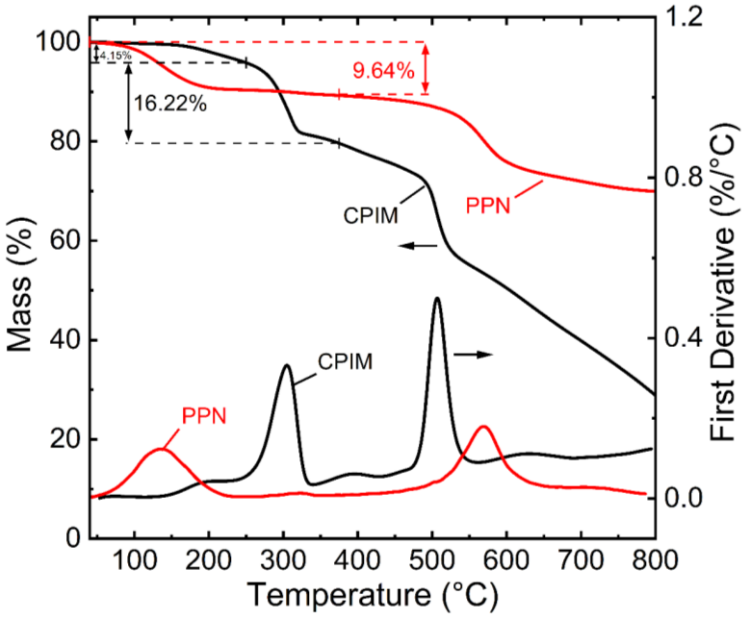


Figure A4.Thermogravimetric mass loss, and mass loss first derivative of neat CPIM (casted membrane) and the synthesized triptycene-isatin PPN.

The mass loss corresponding to the temperature range of 250-375 °C for neat CPIM is 16.22%. For a fully hydrolyzed CPIM derivative with complete substitution of acid groups, the theoretical mass loss would be 17.8% [23]. This 16.22% mass loss then predicts a 91.1% degree of hydrolysis, which is in excellent agreement with the conversion of 92% measured using elemental analysis. A minor mass loss of 4.15% from ambient temperatures to 250 °C in the CPIM sample is consistent with the analysis of the MMM30 membrane measured in the main manuscript, and is due to physisorbed moisture, gas, and residual oligomeric pTHF. Additionally, the TGA for the synthesized triptycene-isatin PPN is consistent with previous reports [1], with stability exceeding 500 °C and a high char yield of 70% at 800 °C. The PPN's exhibited mass loss of 9.64% from

ambient conditions to 375 °C is due to physisorbed moisture, gas, and residual solvent, as no pre-drying treatment was applied. Correcting the char yield for the 9.64 wt. % sorbed species gives an estimate of 77% char yield at 800 °C, which is slightly more consistent with the previously reported char yield of 75% for this material [1].

A16. FTIR-ATR of MMM30 and IcMMM30

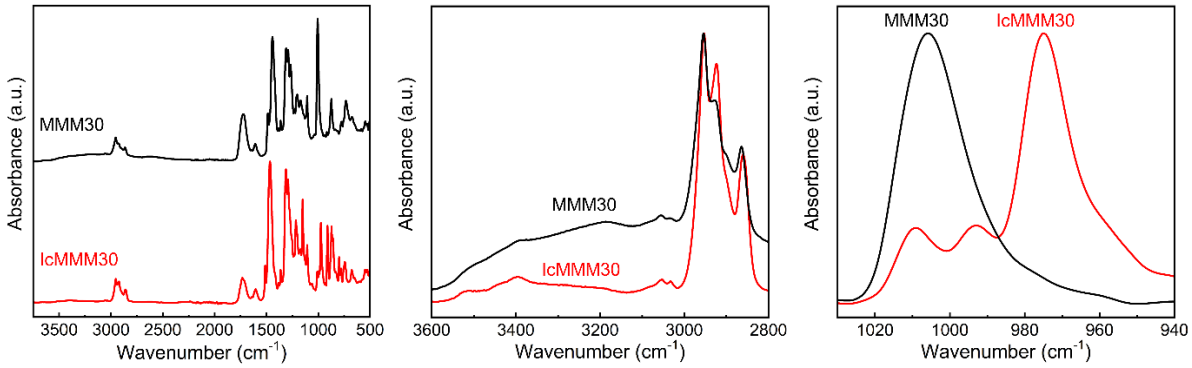


Figure A5.The left panel shows FTIR-ATR of MMM30 and IcMMM30, as appears in the main manuscript, and the middle and right panels are magnifications of the same spectra in the single-bond C-H and O-H stretching regions and C-O-C stretch regions, respectively.

As observed in Figure A5, the O-H stretch is depressed in thermally treated samples due to the decarboxylation reaction taking place. Additionally, The C-O-C stretch of membrane materials is significantly redshifted upon thermal treatment due to changes in the substitution pattern on the aromatic moieties.

A17. Pure Gas Permeability, Diffusivity, and Solubility

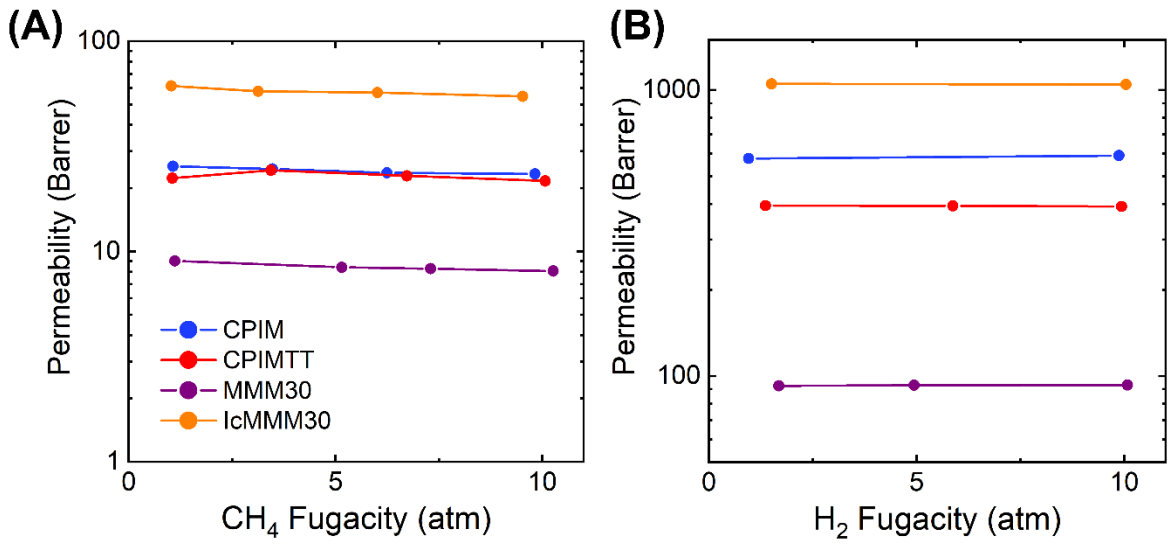


Figure A6. (A) CH_4 and (B) H_2 permeability vs. fugacity at 35 °C. Error bars from linear error propagation are too small to show. Fugacity was calculated using the Peng-Robinson equation of state.

Table A5. Pure gas permeability at 1 atm and 35 °C. Errors were calculated using the standard error of linear regression followed by linear error propagation [203].

gas	***permeability (Barrer)***			
	CPIM	***CPIMTT***	***MMM30***	***IcMMM30***
H_2	576 ± 14	394 ± 17	92.4 ± 1.7	1051 ± 28
CH_4	25.4 ± 0.6	22 ± 1	9.0 ± 0.2	61.3 ± 1.7
CO_2	588 ± 14	469 ± 20	207 ± 4	1390 ± 37

Table A6. *Pure gas solubility coefficients given by the dual-mode sorption model at 1 atm and 35 °C. Error bars were calculated using linear error propagation* [89,205].

gas	*solubility coefficient (CC_{STP} /(CC_{pol} atm))*			
	CPIM	***CPIMTT***	***MMM30***	***IcMMM30***
H_2	--	--	--	--
CH_4	3.2 ± 1.1	4.7 ± 0.7	6.9 ± 0.9	8.5 ± 0.8
CO_2	13.3 ± 2.2	21.1± 2.5	27.2 ± 3.6	32.5 ± 2.5

Table A7. Pure gas diffusivity coefficients at 1 atm and 35 °C calculated using experimental permeability data and dual-mode solubility coefficients. Errors were calculated using linear error propagation[203].

gas	*diffusivity (10^{-7} cm^2/s)*			
	CPIM	***CPIMTT***	***MMM30***	***IcMMM30***
H_2	--	--	--	--
CH_4	0.6 ± 0.2	0.37 ± 0.03	0.100 ± 0.009	0.55 ± 0.02
CO_2	3.2 ± 0.2	1.6 ± 0.1	0.57 ± .04	3.15 ± 0.1

A18. Partial Immobilization Fittings

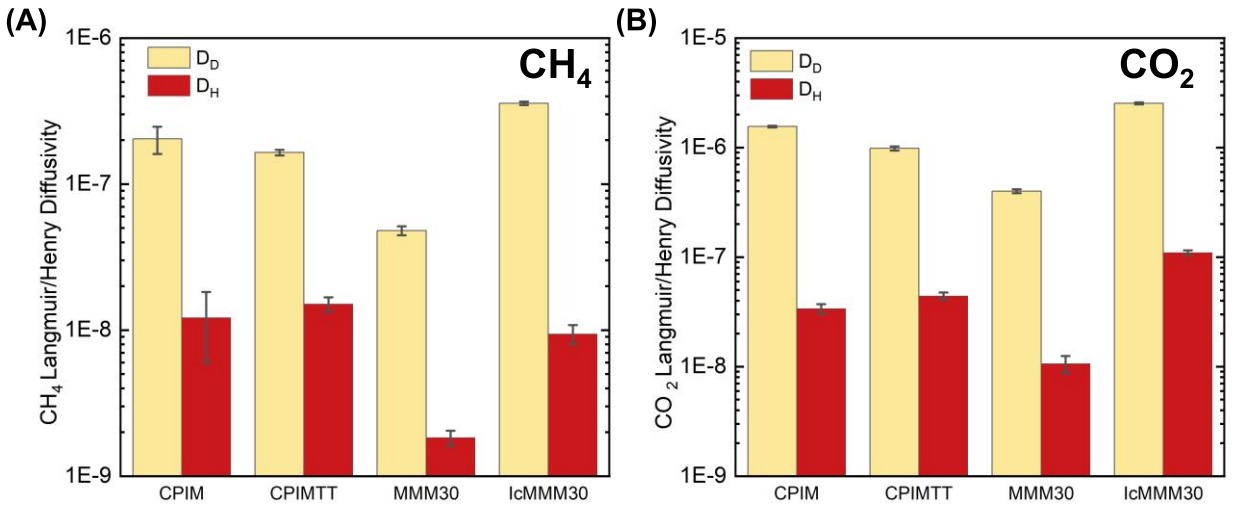


Figure A7. Partial immobilization fittings for (A) CH_4 and (B) CO_2. Error bars were calculated by linear error propagation using the standard error of linear regression[203] and the dual-mode errors given in Table 2 in the main manuscript.

Table A8. Partial immobilization analysis for CH_4 and CO_2, as well as the calculated fractional diffusivity through the Langmuir's mode.

gas	***F = D_H/ D_D***				***fractional Langmuir's diffusivity[a] (%)***			
	CPIM	***CPIMTT***	***MMM30***	***IcMMM30***	***CPIM***	***CPIMTT***	***MMM30***	***IcMMM30***
CH_4	0.060	0.092	0.038	0.026	5.6	8.4	3.7	2.6
CO_2	0.022	0.045	0.027	0.043	2.1	4.3	2.6	4.1

[a] *fractional Langmuir's diffusivity is calculated as* $D_H/(D_D + D_H)$

A19. Comparison of CO_2 Plasticization Pressure Points

Table A9. Review of CO_2 plasticization pressures for the materials considered in this study, as well as state of the art materials.

polymer	***CO_2 permeability[a] (Barrer)***	***sample details***	***CO_2 plasticization pressure (atm)***	***ref.***
IcMMM30	*1390*	*Decarboxylation crosslinked*	*>50*	*This work*
CPIMTT	*468*	*Decarboxylation crosslinked*	*15*	*This work*
CPIM	*588*	*Non-crosslinked*	*7*	*This work*
MMM30	*207*	*Non-crosslinked*	*~5*	*This work*
6FDA−6FpDA/DABA 2:1	*47*	*Crosslinked with ethylene glycol*	*29*	77
6FDA−6FpDA/DABA 2:1	*30*	*Crosslinked with Al^{3+}*	*15.6*	77
TR-PBOI-MPD5	*358*	*Thermally rearranged, decarboxylation crosslinked at 450 ° C*	*>40*	83
6FDA-CADA1-425	*917*	*Decarboxylation crosslinked at 425 ° C*	*>30*	50
PIM-COOH + 35 wt. % UiO-66-NH_2	*2110*	*Non-crosslinked*	*>42*	56
6FDA-DAM + 30 wt. % branched HKUST-1	*2480*	*Non-crosslinked*	*>51*	124

PI-Im-COOH-450-5	*2662*	*Decarboxylation crosslinked with charge transfer complex formation*	*>50*	[81]

[a] *permeability data are at 1-2 atm.*

Appendix B

B1. Materials

PTMSP was purchased from Gelest Inc. (Morrisville, USA). Anhydrous chloroform ($CHCl_3$) and isatin were purchased from Sigma-Aldrich. Triptycene and trifluoromethanesulfonic acid (TSFA) were purchased from Abcr GmbH and Apollo Scientific, respectively. Toluene (HPLC, 99.8%) was purchased from Fisher Chemical. All chemicals were used as received. Pure N_2, CO_2, and CH_4 were obtained from AirGas with a purity higher than 99%. Free standing PTMSP films, ~50-100 um thick, were prepared via solution casting from toluene.

The following materials were used for the solid-state NMR experiments: $^{13}C(1)$-labeled 99% acetic acid was purchased from Euriso-top (Gif-sur-Yvette, France), $^{13}C(1)$-labeled 99% $^{13}CO_2$ was from Cortenec (Voisins-Le-Bretonneux, France), and the nitrogen (99.9999%) and methane (99.9995%) were from Nippon Gases (Madrid, Spain).

B2. Synthesis of Triptycene-isatin porous polymer network

The synthesis procedure (Figure B1) of triptycene-isatin PPN, whose details are previously reported,[1,42,43] is briefly summarized hereafter: triptycene (1.754 g, 6.9 mmol), isatin (1.501g, 10.2 mmol) and $CHCl_3$ (8 mL) were mixed in a three-neck cylinder flask equipped with a mechanical stirrer. Following this step, the mixture was cooled to 0ºC (273.15 K) under N_2 purge, and trifluoromethanesulfonic acid (15 mL) was added dropwise. The resulting mixture was then heated up to 60ºC (333.15 K) under stirring for the following four days. The product was precipitated in water, then collected and washed using a (3:1 vol) water-methanol mixture and filtered. The product was then washed with water to remove residual acid, followed by washing with acetone and chloroform to remove residual unreacted monomers. Finally, the resulting brown powder was

milled using an UltraTurrax homogenizer in ethanol before filtered and dried in a vacuum oven at 150°C (423.15 K) for 12 h.

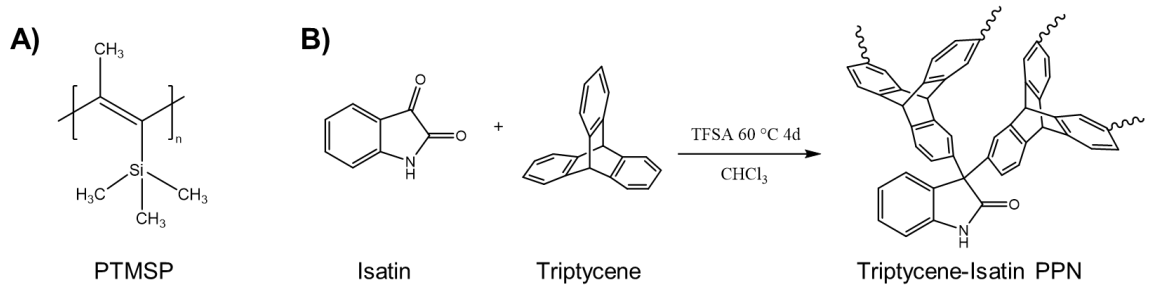


Figure B1. A) Chemical structure of PTMSP. B) Synthesis route and chemical structure of triptycene-isatin PPN.

B3. Structural Characterization Techniques

B3.1. Fourier Transform Infrared Spectroscopy (FTIR)

Neat PTMSP, PTMSP-5PPN, and the PTMSP-20PPN membranes, as well as the PPN powder were characterized by FTIR-ATR (Thermo Scientific, Nicolet™ iS50R) equipped with a diamond crystal. All spectra were averaged through 64 scans acquired over the wavenumber range 400-4000 cm^{-1}.

B3.2. Thermogravimetric Analysis (TGA)

Membrane thermal stability was analyzed by dynamic TGA using a Q500 apparatus (TA Instruments). All samples (around 10 mg) were heated from room temperature to 800 ºC (1073.15 K) with a heating rate of 10 ºC/min (10 K/min) under an N_2 purge stream.

B3.3. Scanning Electron Microscopy (SEM)

The membrane morphology was analyzed by SEM (ThermoFisher Quattro SEM). Cross-sectional images were obtained after fracturing the membranes while submerged in liquid nitrogen. Prior to imaging, samples were coated with iridium at a current of 20 mA for 45s using a Quorum Q150 sputter coater.

B3.4. Positron Annihilation Lifetime Spectroscopy (PALS)

Measurements were performed using an automated EG&G Ortec fast−fast coincidence spectrometer under vacuum (10^{-6} Torr) and at room temperature to measure the lifetimes (τ) and relative number of pores (Intensity, I) of neat PTMSP, neat PPN, and the PTMSP-PPN blends. A minimum of 4.5 x 10^6 integrated counts were collected for each spectrum and at least five spectra were collected per sample. The data were then fitted using the LT-9 software[206] with a source correction for the Na-22 source sealed in Mylar (1.478 ns, 3.24%). For PTMSP and the blends, three ortho-positronium (oPs) (τ_3, τ_4 and τ_5) lifetime components were fitted and related to radii of free volume elements (R) which are assumed spherical, through the Tao-Eldrup equation [153,154]:

$$\tau = \frac{1}{2}\left(1 - \frac{R}{R + \Delta r} + \frac{1}{2\pi} sin\left[\frac{2\pi R}{R + \Delta r}\right]\right)^{-1} \qquad (B1)$$

where Δr is the electron layer thickness (1.66 Å) which is determined empirically.[154] The adapted Relative Tao-Eldrup (RTE) calculation was used due to the longer lifetimes experienced in PTMSP, assuming a spherical pore shape and room temperature measurements.[153] For neat PNN, only two oPs lifetimes (τ_3 and τ_4) were fitted, indicating a bimodal pore distribution. The pore size distribution was calculated using the PAScual software.[207]

B3.5. Density and Fractional Free Volume Measurements

The membrane density, ρ, was measured using a Mettler Toledo balance equipped with a density kit, and was calculated after weighting the samples in air (m_{air}) and water (m_{water}) at 21 °C (294.15 K):

$$\rho = \frac{m_{air}}{m_{air} - m_{water}}(\rho_{water} - \rho_{air}) + \rho_{air} \qquad (B2)$$

where ρ_{air} is the density of air and ρ_{water} is density of water (0.997 g/cm^3 at 21°C (294.15K)). At least six measurements were taken for each sample to acquire the uncertainty.

The membrane fractional free volume (*f*) was calculated from density data as follows:

$$f = \frac{\widehat{V} - \widehat{V}_0}{\widehat{V}} \approx \frac{\widehat{V} - 1.3\widehat{V}_w}{\widehat{V}} = \frac{\widehat{V} - 1.3 \times \left((1 - x_{PPN}) \times \widehat{V}_w^{polymer} + x_{PPN} \times \widehat{V}_w^{filler}\right)}{\widehat{V}} \qquad (B3)$$

where $\widehat{V}$ is the specific volume of the polymer, obtained via density measurements, $\widehat{V}_0$ is the volume occupied by polymer chains and filler at $0K$, which is estimated as 1.3 times the van der Waals volume ($\widehat{V}w$),[208] and x_{PPN} is the filler mole fraction. Values for the van der Waals volume, which were estimated by the group contribution method reported by Wu et al.,[151] are 0.630 cm^3/g for PTMSP[209] and 0.493 cm^3/g for PPN.[43] The pore volume of PPN from N_2 uptake measurements used was reported by Aguilar-Lugo et al. as 0.44 cm^3/g,[43] and it was assumed that the pore volume plus the group contribution Van der Waals volume made up the entire phase volume for the PPN.

B4. Membranes Fabrication

Membranes based on neat PTMSP were fabricated via solution-casting from a 5 wt. % solution in toluene. To fabricate PTMSP-5PPN, PTMSP-15PPN, and PTMSP-20PPN blends, two separate solutions were prepared, the first by dissolving PTMSP in toluene at 5 wt. %, and the second by

dispersing PPN in toluene at 5 wt. % by using ultrasonication at 37 kHz. The PPN solution was then mixed into the PTMSP solution to yield a toluene mixture with a total solids content of 5 wt. % (PTMSP + PPN), where the PPN was 5 wt. % of the total solids content. The hand-mixing process was followed by 20 minutes of ultrasonication at 37 kHz. Subsequently, solutions were poured onto a clean, leveled glass plate with a glass ring mounted using silicon adhesive. The solution was covered by placing a filter paper and flat aluminum plate over the glass ring to slow the drying process, yielding flat, defect-free membranes. To ensure complete removal of toluene, the membranes were further dried under vacuum at room temperature for 24 hours. The samples were then installed immediately in the permeation apparatus or used for structural characterization analysis to control for systemic error due to the possibility of physical aging. The membrane thickness (~50-100 μm for gas transport measurements and ~20-40um for physical aging characteristics) was measured using a Mitutoyo micrometer as the average of at least ten measurements per sample. Throughout this study, membranes containing X wt. % PPN are referred to as PTMSP-XPPN.

B5. FTIR Spectra Discussion

The FTIR spectra of the neat PTMSP, PTMSP-5PPN, PTMSP-20PPN, and neat PPN are shown in Figure B2. The C=C (1560 cm^{-1}) and Si-CH_3 (1234 cm^{-1} and 830 cm^{-1}) peaks[25] are detectable in the spectra for PTMSP, PTMSP-5PPN, and PTMSP-20PPN. The peaks associated to the C=O, -NH, and -CN group in the PPN backbone are located at 1695 cm^{-1}, 1470 cm^{-1}, and 1322 cm^{-1}, respectively [12]. The FTIR spectra confirm that PPN was successfully incorporated in PTMSP. To note, no shift in the characteristic peaks associated with the spectra for neat PTMSP and neat PPN

is observed in the PTMSP-PPN blends, which indicates a lack of strong chemical (e.g., hydrogen bonding) interactions between PTMSP and PPN.

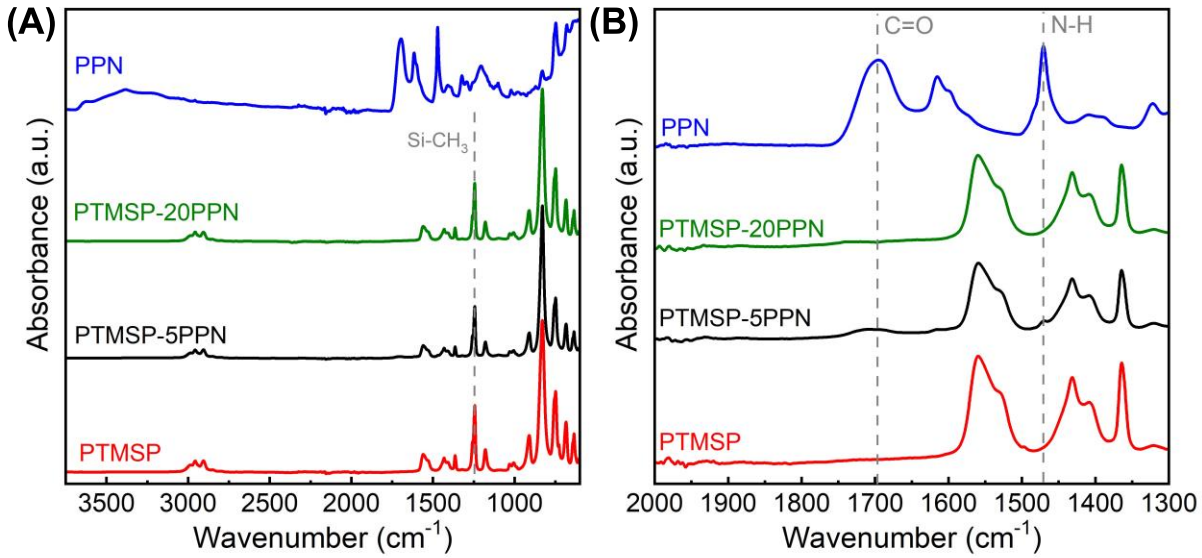


Figure B2. FTIR spectra of the PTMSP-PPN blends in range A) 600-3750 cm^{-1} and B) 1300-2000 cm^{-1}.

B6. Positron Annihilation Lifetime Spectroscopy Results

Table B1. Results of the PALS analysis for PTMSP, PTMSP-5PPN, PTMSP-15PPN and neat PPN, including orthopositronium (oPs) lifetimes (τ_3, τ_4 and τ_5), intensities (I_3, I_4 and I_5), and average free volume element radii (R_3, R_4 and R_5).

Sample	τ_3 (ns)	τ_4 (ns)	τ_5 (ns)	I_3 (%)	I_4 (%)	I_5 (%)	R_3 (Å)	R_4 (Å)	R_5 (Å)
PTMSP	1.57 ± 0.170	7.69 ± 0.546	14.81 ± 1.19	3.4 ± 0.3	17.4 ± 3.0	17.0 ± 3.2	2.77 ± 0.21	6.40 ± 0.21	8.69 ± 0.33

PTMSP-5PPN	*1.37 ± 0.103*	*7.93 ± 0.402*	*15.27 ± 0.41*	*3.2 ± 0.2*	*13.5 ± 1.5*	*21.3 ± 1.7*	*2.53 ± 0.14*	*6.50 ± 0.15*	*8.81 ± 0.11*
PTMSP-15PPN	*1.55 ± 0.128*	*7.495 ± 0.372*	*14.76 ± 0.32*	*3.7 ± 0.3*	*11.9 ± 1.1*	*20.2 ± 1.7*	*2.75 ± 0.17*	*6.33 ± 0.15*	*8.67 ± 0.09*
PPN (bimodal)	*0.97 ± 0.036*	*5.06 ± 0.064*	--	*6.9 ± 0.4*	*11.2 ± 0.2*	--	*1.61 ± 0.03*	*4.77 ± 0.06*	--

B7. Molecular Dynamics Simulation Procedures and Details

B7.1. Simulation Setup

The initial configuration of the PTMSP-PPN blend involved the construction of a pure PTMSP polymer chain consisting of 101 repeat units, with the occurrence of cis and trans monomers organized randomly (Figure B3**A**). The porous polymer network (PPN) was created by incorporating 22 units of triptycene and 45 units of isatin, also organized randomly into the chain (Figure B3**B**).

Two distinct systems were simulated: one system comprised solely of 20 PTMSP polymer chains; the second consisted of a blend of 20 PTMSP chains and 5 PPN molecules.

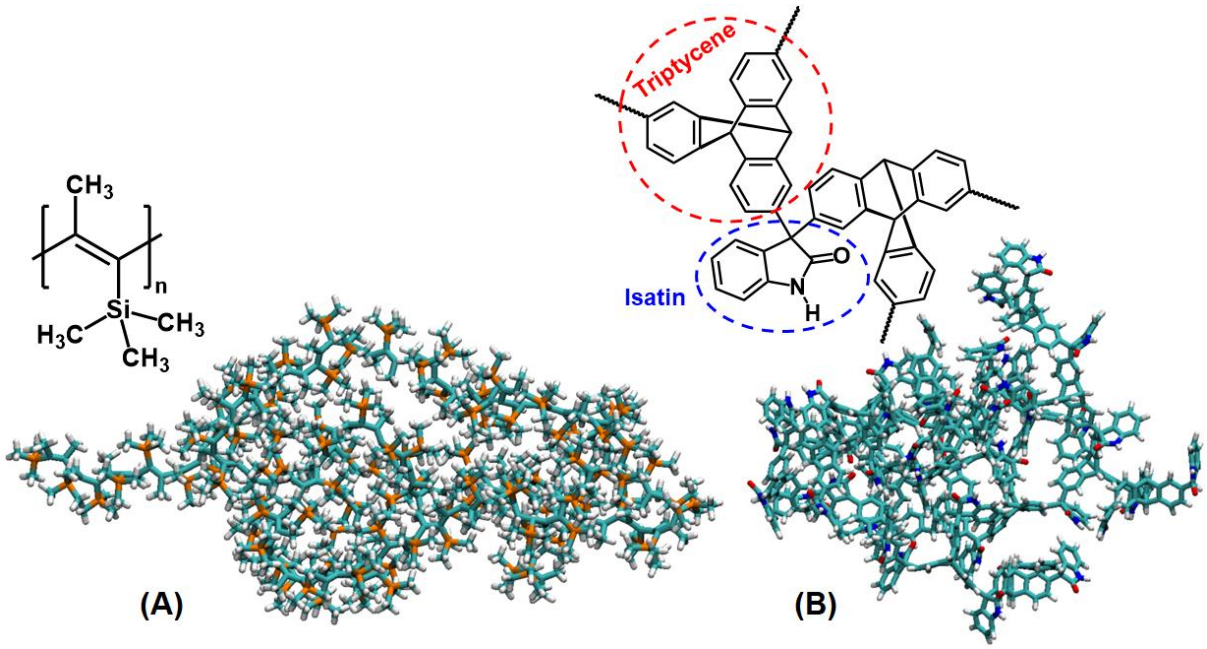


Figure B3. Atomistic models of (A) a single PTMSP polymer chain (101-mer) and (B) a PPN molecule with 22 triptycene units and 45 isatin units. Color code: cyan (C), white (H), red (O), blue (N), and orange (Si).

As the polymers considered in this study are non-equilibrium materials, care must be taken to ensure the structure of the simulated polymer matches the sample it represents. To prepare simulated systems with densities comparable to those used in the experimental portion of this work, we mimicked the solution-casting technique utilized in our experimental preparation. In the experimental approach (and as described in Section B4) the polymers were first dissolved in toluene, followed by controlled evaporation of the solvent to form the membranes. In our simulation, a system composed solely of PTMSP molecules was fabricated by dissolving 20 PTMSP polymers, such as those shown in Figure B4, in 1000 toluene molecules. These systems were simulated for 20 ns. Subsequently, 500 toluene molecules, chosen at random, were removed, after which the system was allowed to equilibrate for 5 ns. The remaining 500 toluene molecules were then removed, and the system was equilibrated for another 10 ns. During this final 10 ns, the

polymer density was monitored until it matched the target density, i.e., the density consistent with experimental data. All simulations were conducted in the NPT ensemble at ambient conditions (298 K and 1 bar).

The algorithm just described was implemented to produce pure a PTMSP membrane and a membrane incorporating a PTMSP-PPN blend, where the PPN constituted 20% of the mixture. The snapshots of the final configurations of the neat PTMSP and PTMSP-PPN blend are presented in Figure B4 **A/B**. Table B2 summarizes the simulated density data for both the neat PTMSP and the PTMSP-PPN blend.

Of note, these simulations were conducted in cubic simulation boxes, in which periodic boundary conditions were implemented in all directions. The final size of the simulation boxes obtained for the two systems considered are shown in Table B2. As the density was targeted to match experimental values, subsequent simulations were conducted in the NVT ensemble, where the density is maintained constant. These subsequent simulations allowed us to quantify the porous structure of the polymeric systems, and to investigate the transport of the pure gases CO_2 and CH_4.

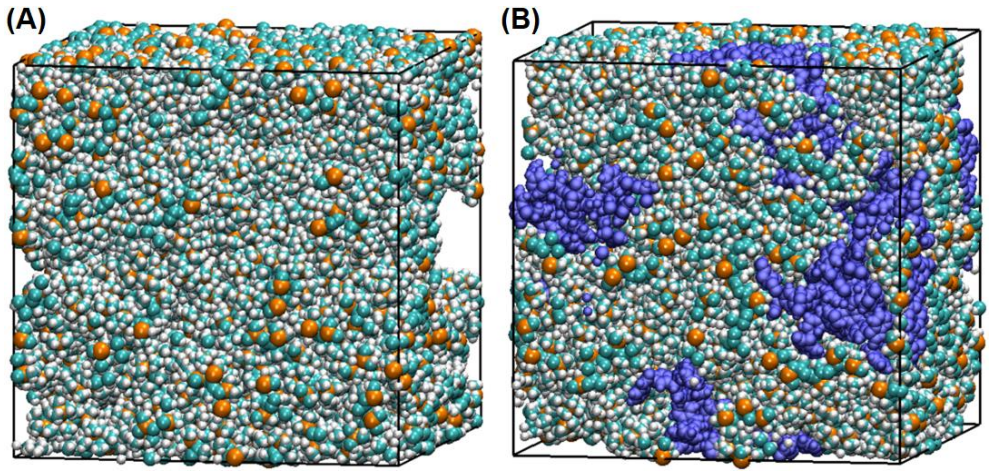


Figure B4. Snapshots showing the final configurations of (A) neat PTMSP and (B) the PTMSP-PPN. Color code: cyan (C), white (H), and orange (Si). For better visual distinction, atoms belonging to the PPN are colored periwinkle blue. The snapshots reveal the presence of voids within the structures, indicating a porous and amorphous morphology in both membranes. These membranes are not uniformly packed.

Table B2. Simulated densities of the neat PTMSP and PTMSP-PPN blend.

Material	***Box length (Å)***	***Density (g/cm^3)***
PTMSP	*79.28 ± 0.08*	*0.758 ± 0.002*
PTMSP-PPN	*81.82 ± 0.40*	*0.866 ± 0.010*

B7.2. Molecular Models and Force Fields

The GROMOS G54A7 all-atom force field[210] was used to model PTMSP, PPN, and toluene. The force field parameters were generated using the ATB (Automated Topology Builder) server[211], which combines a knowledge-based approach and quantum mechanical calculations. This approach enables the production of topologies and parameters that are compatible with the GROMOS family of force fields. CH_4 was modeled using the all-atom version of the TraPPE-EH

force field[212], which exhibits superior performance in predicting single-component phase diagrams and outperforms the TraPPE united-atom model in multicomponent equilibria. The flexible version of the EPM2 model of Cygan et al.[213] was used to describe CO_2. Compared to rigid models, the inclusion of molecular flexibility enhances predictive accuracy for interfacial and thermodynamic properties, as well as correctly describing the vibrational spectra of CO_2.[213]

In all simulations, non-bonded interactions were characterized by employing a 12-6 Lennard-Jones (LJ) potential to account for dispersive forces, alongside the Coulombic potential to model electrostatic forces. The cut-off distance for interatomic interactions was set at 14 Å, and corrections for the long-range electrostatic interactions were obtained using a smooth particle mesh Ewald method.[214] The LJ parameters for all cross interactions between different atoms were determined by applying Lorentz–Berthelot mixing rules.[215]

B7.3. Simulation Algorithms

The molecular dynamics (MD) simulations were conducted using the Groningen Machine for Chemical Simulations (GROMACS) package, version 2023.3[216,217]. The equations of motion were integrated employing the leapfrog algorithm,[218] with a timestep of 1.0 fs. Throughout the study, MD simulations were performed under consistent conditions, maintaining a temperature of 298 K and a pressure of 1 bar. To maintain constant temperatures during the MD runs, the Nosé–Hoover thermostat[219,220] was employed with a fixed temperature-damping factor of 0.1 fs. The pressure was coupled in all three dimensions using an isotropic Parrinello–Rahman barostat[221] with a relaxation time of 0.5 ps which allows realistic deformation of polymer matrices and helps maintain constant pressure throughout the simulations.

To investigate the diffusion of pure CH_4 and CO_2 in the polymeric systems, 400 molecules of each gas were randomly inserted into either the neat PTMSP and PTMSP-PPN blend matrices. Following this, MD simulations were conducted with a total duration of 60 ns to equilibrate the systems. Equilibration was confirmed when the gas diffusion coefficients stabilized to constant values, while both the system's energy and temperature remained within 10% of their average values. Subsequently, a production run of 4 ns was employed for data analysis. Each simulation was replicated at least three times to ensure the reliability of the results.

B7.4. Self-Diffusion Coefficients

The self-diffusion coefficients were calculated from the mean square displacement by implementing the Einstein equation[222]:

$$D = lim_{t\to\infty} \frac{\langle |r_i(t) - r_i(0)|^2 \rangle}{2td} \qquad (B4)$$

where $r_i(t)$ and $r_i(0)$ are the positions of particle i at time t and time zero, respectively, and d is the number of degrees of freedom. As our system is 3-dimensional, d=3.

B8. Experimental Gas Transport and Physical Aging Measurement Protocol

Pure CO_2, CH_4, and N_2 permeability and solubility were measured at 35 °C (308.15 K) via the constant-volume, variable pressure method. Physical aging of ~20-40 μm thick films was tracked via pure gas N_2 permeability measurements at 1.4 atm and 35 °C (308.15 K).

Membrane samples were prepared for permeability measurements by masking small sections of membranes over a brass disc using Devcon 5 Minute Epoxy Gel. Filter paper was used as a backing to reduce the risk of sample breakage. The assembly is then placed into the membrane module (47mm HP filter holder, Millipore) and held at vacuum for 24 hours, followed by a leak

test prior to the start of the permeability experiment. The experiment begins by filling an upstream ballast with the permeating gas to a target pressure, then opening the upstream valve to expose the membrane to the upstream ballast. During the experiment, the upstream and downstream pressures are tracked using an Omega pressure transducer (with a range of 0-1000 PSI) and an MKS Absolute Pressure Transducer (0-10 Torr), respectively. This data is then recorded by an Upper Bound 200-X Permeation Analyzer (Maxwell Robotics®). Permeability is calculated from this raw data as follows:

$$P = \frac{V_D \ell}{(p_U - p_D)ART}\left[\left(\frac{dp_D}{dt}\right)_{perm.} - \left(\frac{dp_D}{dt}\right)_{leak}\right] \qquad (B5)$$

where V_D is the downstream volume, ℓ is the membrane thickness, p_U is the upstream volume, A is the membrane area available for permeation, calculated using an optical scanner, R the ideal gas constant, T the absolute temperature, and finally p_D is the downstream pressure.

The constant-volume variable pressure gas sorption system consists of two chambers of known volume connected via a valve, which are differentiated as the "sampling" and "charge" chambers. Both chambers are equipped with PX-409-USHB series Omega pressure transducers (0-750 psi, ± 0.08% BSL accuracy). The polymer sample is first added to the sampling chamber and both chambers are evacuated of gas overnight using a rotary vacuum pump (Welch DuoSeal 1402). Gas is then introduced to the charge chamber and allowed to reach thermal equilibrium before quickly releasing it into the sampling chamber by briefly opening the valve separating the two chambers. The valve separating the two chambers is then closed, and each chamber is allowed to equilibrate.

Pressure decay in the sampling chamber is observed due to gas partitioning into the polymer sample. Upon reaching sorption equilibrium, the process is repeated stepwise, without pulling vacuum. The overall sorbed gas concentration in the polymer sample is calculated using the initial charge pressure and equilibrium pressures for each chamber, at each step, as follows:

$$C_{pol,j} = \frac{\rho_{pol}}{g_{pol,dry}} \left(\sum_{i=0}^{j} \left(\frac{1}{\tilde{V}_{C0,i}} - \frac{1}{\tilde{V}_{CF,i}} \right) - \frac{V_S}{\tilde{V}_{SF,j}} \right) \quad (B6)$$

where ρ_{pol} is the polymer density (assumed constant), $g_{pol,dry}$ is the dry polymer mass, j is the current pressure step, V_s is the sample chamber volume, V_C is the charge chamber volume, and $\tilde{V}_{C0}$, $\tilde{V}_{CF}$, $\tilde{V}_{SF}$, are the gas molar volumes (calculated using the Peng-Robinson equation of state) for the initial charge state (prior to valve opening), final charge state, and final sample state, respectively. Concentration errors were calculated by linear error propagation, according to the method reported by Box et al. [89].

Gas sorption into PTMSP was then fit to the dual-mode sorption model, where gas concentration in the polymer (i.e., sorption, *C*) is parametrized as a function of pressure (i.e., *p*) as follows:

$$C = k_D p + \frac{C'_H b p}{1 + bp} \quad (B7)$$

where b is the affinity factor, C'_H is the Langmuir capacity, and k_D is the Henry's sorption coefficient. The parameters corresponding to the fitting of each gas isotherm can be found in Section B12.

For the physical aging measurements, membranes about 20-40 μm thick were solution cast using the same procedure reported in Section B4. After fabrication, films were immersed in methanol for 24 hours to reset their physical aging. Upon removal from methanol, samples were dried at ambient temperature in a vacuum oven for 1 hour and then placed in a gas permeation apparatus. The upstream side of the membrane was quickly vacuumed out before being charged with 20 psi of pure N_2 gas, and vacuum was pulled on the downstream side. After 24 hours, the permeability was measured, and this was considered t = 0 for all samples used in this study. The membranes were kept under 20 psi N_2 for the next three weeks, with flux being measured periodically.

B9. Fitting of the Permeability/Fractional Free Volume Relationship

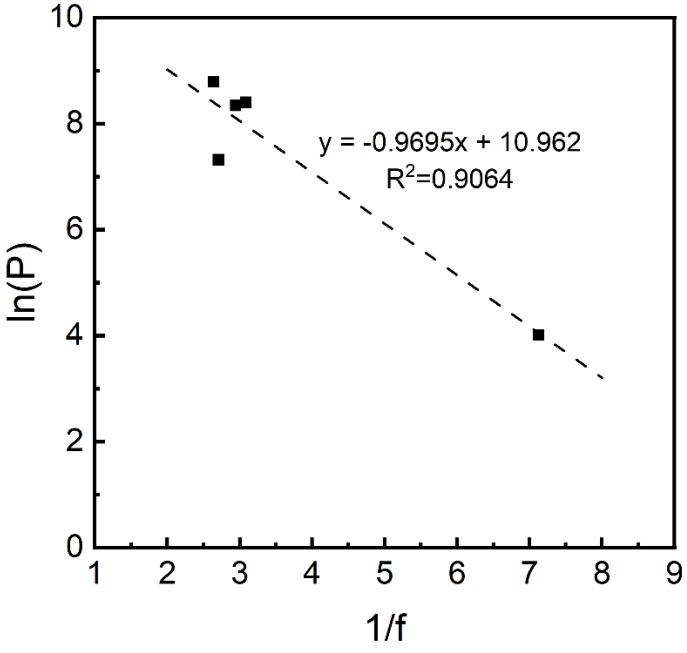


Figure B5. Exponential fit of permeability to inverse fractional free volume for the PTMSP and PTMSP-PPN systems.

The empirical permeability fit to Equation 13 is shown in Figure B5. Parameter values came out to A = 57663.5 ± 42295.1 and B = 0.9695 ± 0.180. The data used for the fitting is provided in Table B3.

Table B3. Data used for the empirical permeability fitting.

Membrane Material	*Age*	*Density (g cm^{-3})*	*N_2 Permeability (Barrer)*	*Reference*
PTMSP	*Fresh*	*0.77*	*1514*	[223]
PTMSP	*4 years*	*1.05*	*55.4*	[223]
PTMSP	*Fresh*	*0.759*	*6593*	*This work*
PTMSP-5PPN	*Fresh*	*0.816*	*4208*	*This work*
PTMSP-20PPN	*Fresh*	*0.864*	*4477*	*This work*

B10. Estimation of Uncertainty for Fitted Parameters

The Struik model parameters were found using nonlinear regression via the L-BFGS algorithm [224–226], where the residual error (SSE) function is:

$$SSE(x) = \sum_{i=0}^{n} (model(x) - obs_i)^2 \qquad (B8)$$

In Eq. S8, *obs* is a set of *n* experimentally produced data and *model* is a function which predicts the experimental observations using a set of fitted parameters *x*. The covariance matrix of the fitted parameters (*x*) can then be found through the scaled inverse of the Hessian matrix of the total residual error (SSE) function taken with respect to the fitted parameters[227–230]. This method, informally termed the "Hessian Method" of parameter uncertainty estimation, is given as:

$$COV(x) = \frac{H^{-1}}{DOF} = \frac{\left[\left.\frac{\partial^2(SSE(x))}{\partial x_i \partial x_j}\right|_{min(SSE(x))}\right]^{-1}}{n-p} \qquad (B9)$$

where the resulting uncertainties of the fitted parameters, neglecting covariance terms, are simply found via the root of the diagonal terms of the covariance matrix:

$$\sigma_{x_i} = \sqrt{diag\big(COV(x)\big)_i} \qquad (B10)$$

B11. Solid State ^{13}C T_1 NMR Relaxation Measurements

NMR measurements were performed in a Bruker Avance Neo™ 400 spectrometer (Bruker BioSpin GmbH, Rheinstetten, Germany) equipped with a 89 mm wide bore, 9.4 T superconducting magnet (^1H and ^{13}C Larmor frequencies at 400.14 and 100.61 MHz, respectively). A standard Bruker double resonance 4 mm cross-polarization/magic angle spinning (CP/MAS) probe was used to measure the ^{13}C T_1 solid-state NMR relaxation times of the PTMSP-based membranes at 298.0 ± 0.1 K with Torchia's method.[204] Relaxation (T_1) measurements were performed both in air and pure N_2 to examine the effect of O_2 on the relaxation time. O_2, being paramagnetic, can reduce the T_1 due to electron-nuclear dipolar interactions.[169,170] Measurements in air are discussed in Section 3.4.4 of the main manuscript, and the T_1 values measured in N_2 of fresh and aged PTMSP and PTMSP-20PPN are shown below in Figure B6.

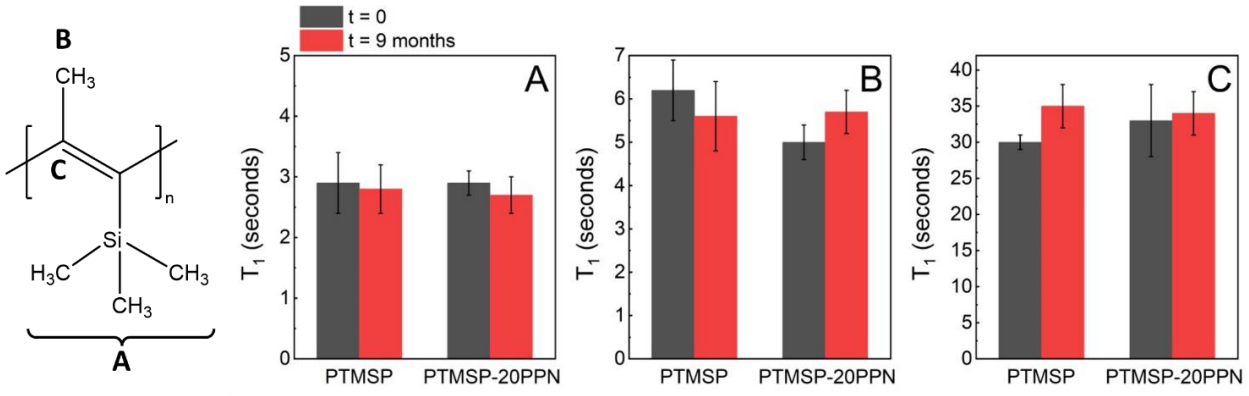


*Figure B6. Spin-lattice relaxation times measured in pure N_2 for the carbons in PTMSP. The labels for carbons **A**, **B**, **C** indicated on the structure of PTMSP correspond to the accordingly labeled plots.*

To prepare the samples for the relaxation measurements in the absence of molecular oxygen (paramagnetic), 4 mm Ø rotors were loaded with strips of membranes (~2 x 14 mm^2), placed in a glass container with a Teflon™ valve and the air removed by vacuum before loading pure nitrogen at room temperature and 0.94 ± 0.01 bar. The gas pressure was monitored with a transducer working in the range 0 – 10 bar. After allowing 24 h to reach equilibrium, the closed container was opened in a dry glove box under the same gas and pressure, and the rotor capped. The ^{13}C NMR spectra were acquired with 1.8 ms CP contact time, a recycle delay of 3 s, proton decoupling of 62.5 kHz and spinning rate of 8.5 kHz. The signal decay was monitored for delay times ranging from 0.05 ms to 60 s and was fitted to a mono-exponential function. The ^{13}C NMR spectra were referenced to adamantane (38.5 ppm) secondary to tetramethylsilane (TMS, 0.0 ppm).

B12. Permeability, Diffusivity, and Solubility Results

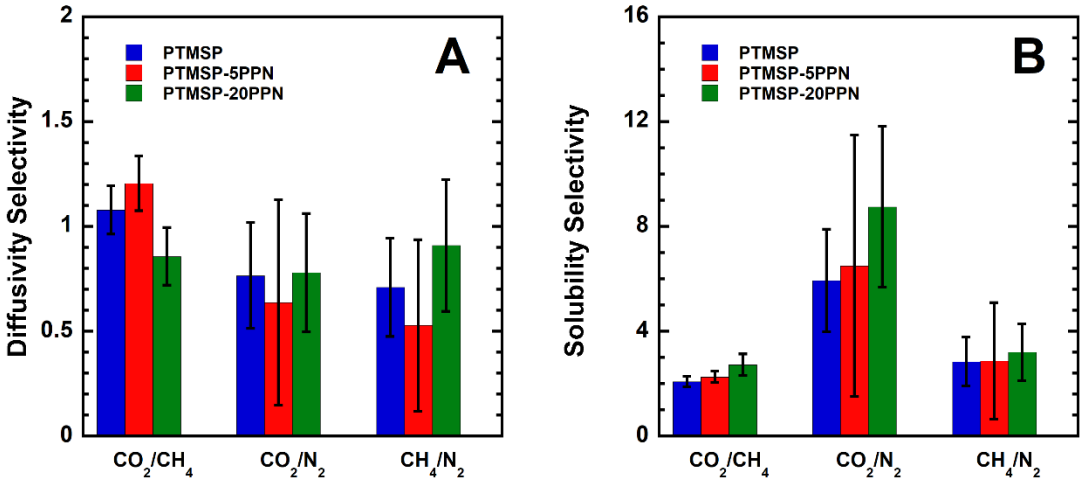
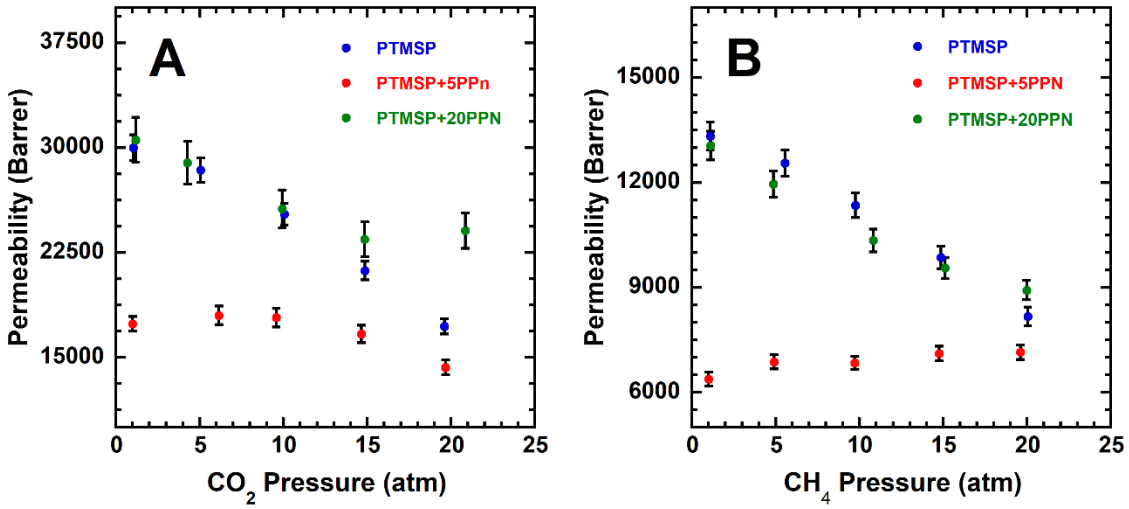


Figure B7. (A) Ideal diffusivity selectivity and (B) ideal solubility selectivity for CO_2/CH_4, CO_2/N_2, and CH_4/N_2 at 1 bar and 35 °C (308.15 K).



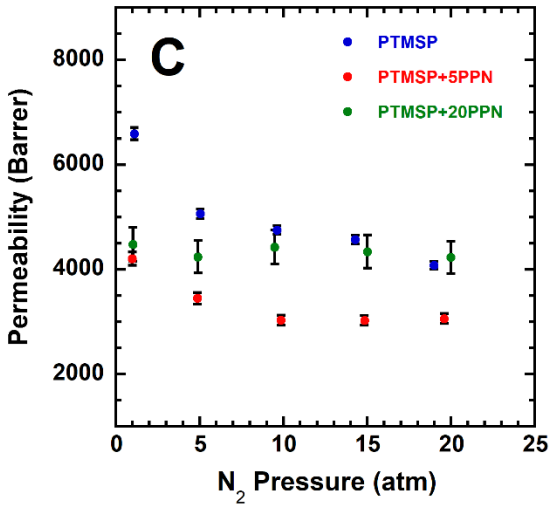


Figure B8. Permeability isotherms of CO_2 (A), CH_4 (B), and N_2 (C) in PTMSP (blue), PTMSP-5PPN (red), and PTMSP-20PPN (green) in Barrer as a function of pure gas pressure, ranging up to 20 atm. Error bars were calculated via the standard deviation from 3-4 measurements.

Table B4. Transport properties of PTMSP and PTMSP-5PPN at 35°C (308.15 K) and 1 atm. Uncertainty was determined using the standard deviation from 3-4 measurements per point.

Transport Properties (1 atm, 35 °C)	***PTMSP***	***PTMSP-5PPN***	***PTMSP-20PPN***
CO_2 Permeability (Barrer)	*29990 ± 710*	*17400 ± 372*	*30548 ± 1611*
CH_4 Permeability (Barrer)	*13330 ± 323*	*6380 ± 148*	*13057 ± 408*
N_2 Permeability (Barrer)	*6593 ± 119*	*4210 ± 94*	*4477 ± 327*
CO_2/CH_4 Selectivity	*2.25 ± 0.08*	*2.73 ± 0.09*	*2.34 ± 0.14*
CO_2/N_2 Selectivity	*4.55 ± 0.14*	*4.14 ± 0.13*	*6.82 ± 0.61*
CH_4/N_2 Selectivity	*2.02 ± 0.06*	*1.52 ± 0.05*	*2.92 ± 0.23*

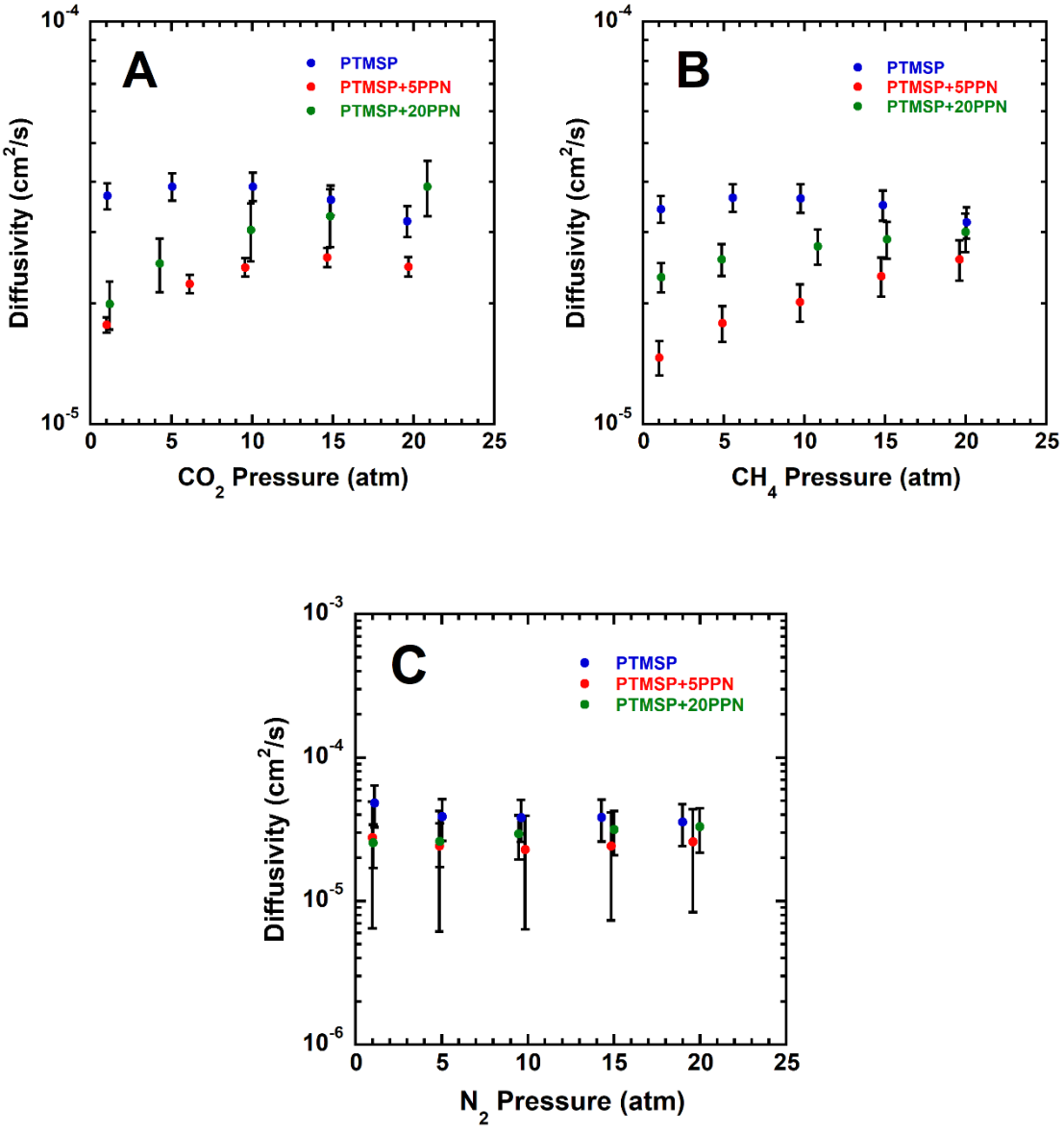


Figure B9. Concentration averaged diffusivity coefficients of CO_2 (A) and CH_4 (B) in PTMSP (blue) and PTMSP-5PPN (red) in $\frac{cm^2}{s}$ as a function of pure gas pressure in atm. Error bars were found via linear error propagation and values were calculated via the solution-diffusion model from experimentally available permeability and solubility data.

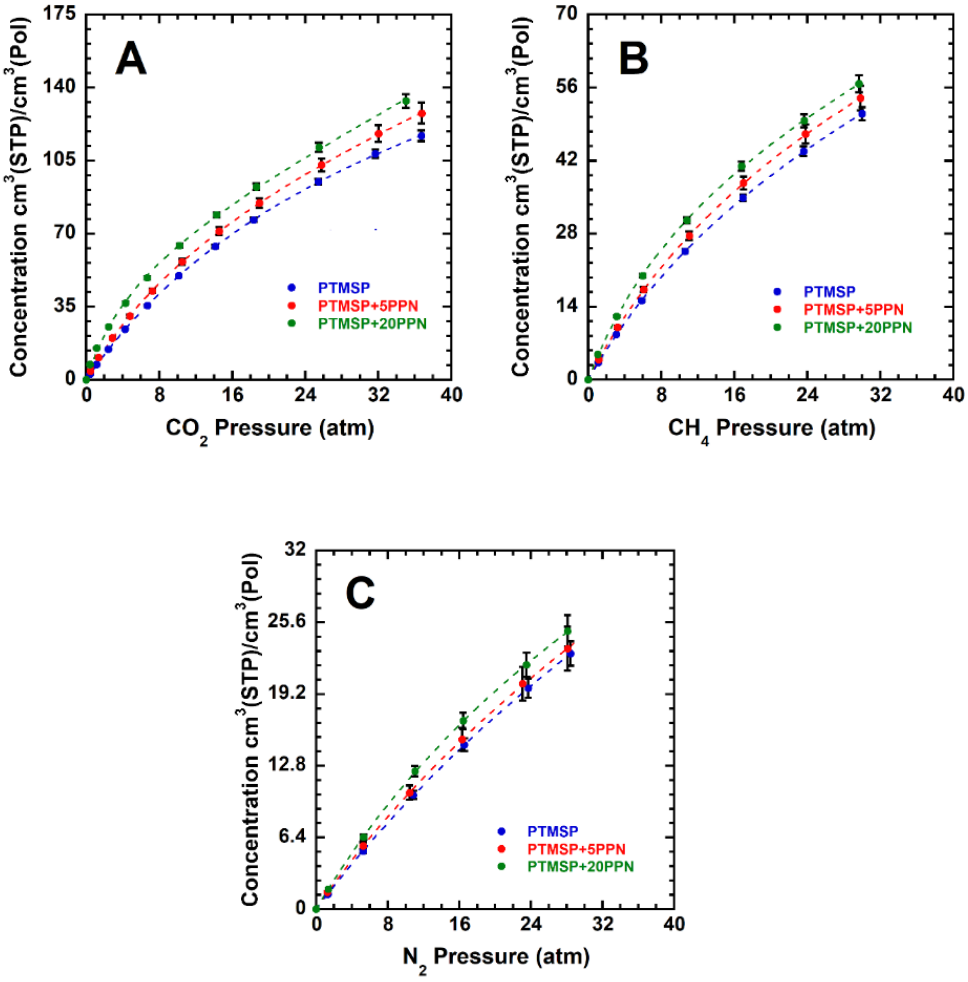


Figure B10. Sorption isotherms of CO_2 (A) and CH_4 (B) in PTMSP (blue) and PTMSP-5PPN (red) in $\frac{cm^3(STP)}{cm^3(Pol.)}$ as a function of pure gas pressure in atm. Error bars were found via linear error propagation.[89]

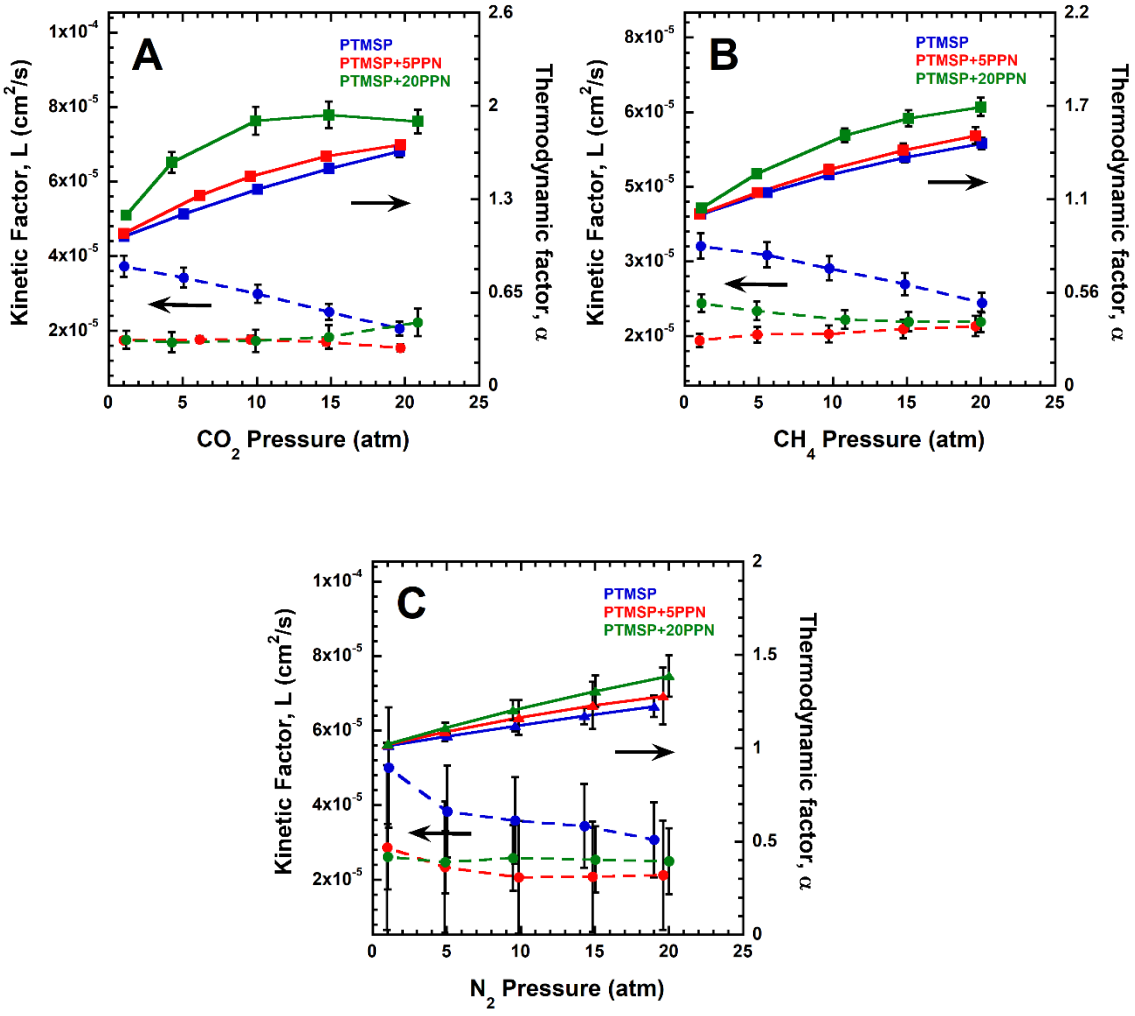


Figure B11. Kinetic (left Y-axis; Dashed lines/Circles) and thermodynamic factors (right Y-axis; Solid lines/Squares) of CO_2 (A), CH_4 (B) and N_2 (C) in PTMSP (blue), PTMSP-5PPN (red), and PTMSP-20PPN (green) as a function of pure gas pressure in atm. Error bars were found via linear error propagation.[89]

B13. Thermogravimetric Analysis

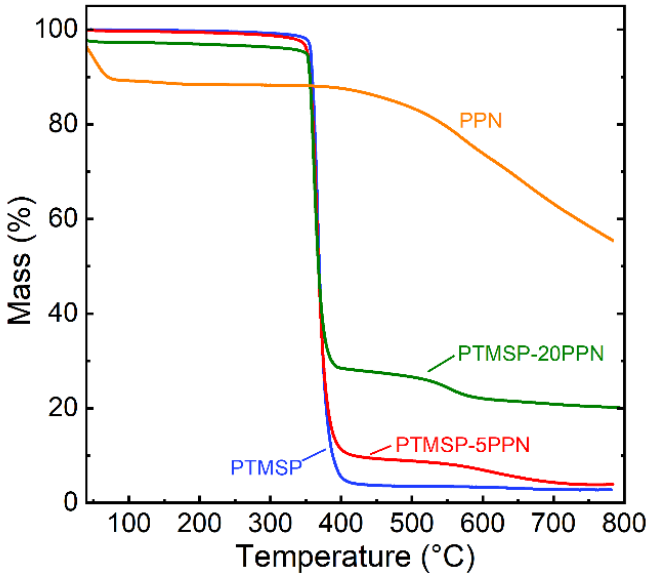


Figure B12. TGA thermogram of PTMSP, PPN, PTMSP-5PPN, and PTMSP-20PPN blends, heated at 10 °C/min (10 K/min) from 25-800℃ (298.15-1073.15 K).

Appendix C

C1. Chemicals and Materials

C1.1. Materials for Synthesis

Methanol (HPLC, > 99.9%) and toluene (HPLC, 99.8%) were purchased from Fischer chemical. N,N-Dimethylacetamide (DMAC, HPLC, > 99.5%), 5,5',6,6'-Tetrahydroxy-3,3,3',3'-tetramethyl-1,1'-spirobisindane (TTSBI, 97%), and Chloroform (ACS, > 99.8%) were purchased from Alfa Aesar. Tetrafluoroterephthalonitrile (TFTPN, 98%) and triptycene (98%) were purchased from TCI Chemicals. Potassium carbonate (K2CO3) and Isatin (97%) were purchased from Sigma Aldrich. Tetrahydrofuran (THF, HPLC, inhibitor-free) was purchased from Macron Fine Chemical. Sulfuric acid (ACS grade) was purchased from EMD, and glacial acetic acid from Research Products International. PIM-1, CPIM, and the triptycene-isatin PPN were synthesized according to the methods reported in Appendix A and Appendix B.

C1.2. Support Materials

Matrimid 5218® was kindly supplied by Huntsman corporation. $LiNO_3$ (99%, anhydrous) and Ninhydrin (ACS reagent) was purchased from Thermo Scientific. *N*-methyl-2-pyrrolidone (99.0+%, low water content) and *p*-xylylenediamine (99.0+%) was purchased from TCI America. Ethanol (200 proof) was purchased from Fisher Scientific.

C1.3. Transport Test Materials

The same toluene used in the PIM-1 synthesis (HPLC, 99.8%) was used as the solvent for the OSN and OSRO tests. Styrene oligomers were purchased from Agilent (PL2012-0001, PL2012-2001, PL2012-3001) and had molecular weights ranging from 162-1306 Da. 1,3,5-Triisopropylbenzene (95%) was purchased from Sigma-Aldrich.

For the 9-component OSRO test, the following solvents were purchased (the same toluene and TIPB were used as above):

- 2,2,4-Trimethylpentane (Isooctane, 99.8%, TCI)
- *n*-propylbenzene (99.7%, TCI)
- 1,2,3,4-tetrahydronaphthalene (tetralin, 99.3%, TCI)
- 1-methylnaphthalene (96.4%, TCI)
- n-butylcyclohexane (99%, TCI)
- *n*-dodecylbenzene (99.2%, TCI)
- 2,6,10,14-Tetramethylpentadecane (pristane, 99.5%, Thermo Scientific)

C2. Basic Material Properties

Table C1. Material properties of the CPIM batch used in this study.

Density	*Fractional Free Volume (%)*	*Typical BET Surface Area (m^2 g^{-1})*	*Degree of Hydrolysis[b] (%)*
1.285 ± 0.003	*21.0 ± 0.6*	*373[a]*	*84*

[a]Value is for a typical batch of CPIM with a high degree of hydrolysis, as reported in reference [23], not the specific batch used in this study.

[b]This is the % of nitrile groups in PIM-1 that have been converted to carboxylic acid groups. Determined using combustion elemental analysis.

Table C2. Material properties of the triptycene-isatin PPN batch used in this study.

Density	*Fractional Free Volume (%)*	*BET Surface Area (m^2 g^{-1})*	*Particle Size[c] (nm)*
1.08[a]	*31.8*	*695[b]*	*722 ± 467*

[a]Estimated from the reported PPN pore volume (V_{pores} = 0.440 $cm^3 g^{-1}$) calculated from N_2 adsorption at 77 K[43] and the Van der Waals volume (V_{VdW} = 0.486 $cm^3 g^{-1}$) estimated from Wu et al.'s updated group contribution theory,[151] where specific volume $V = V_{pores} + V_{VdW}$. Experimental error of the original pore volume estimate was not available. [b,c]The BET and particle sized determined using SEM for this PPN batch was measured and reported in the study corresponding to Chapter 1.

C3. Material Characterization Methods

C3.1. Fourier-Transform Infrared Spectroscopy

CPIM membranes and their derivatives were analyzed using FTIR with an attenuated total reflectance (FTIR-ATR) accessory (Nicolet iS50R Fourier Transform Infrared Spectrometer) with a diamond crystal. Spectra were measured by averaging 64 scans at a resolution of 0.4821 cm^{-1}.

C3.2. X-Ray Diffraction

Samples were dry ground in a corundum mortar and pestle then loaded into Si zero background inserts housed within stainless steel sample holders prior to the collection of data. A Bruker D8 Advance A25 X-ray Diffractometer operating under CuKα radiation (40kV, 40mA) equipped with a Lynx Eye XE-T detector was employed to obtain the X-ray diffractograms. The samples were scanned over the 2θ range 5° to 85° with a step size of 0.02° and a count time of 1.6 second per step, and were spun at 15 RPM during data collection. D-spacing values were calculated using Bragg's law.

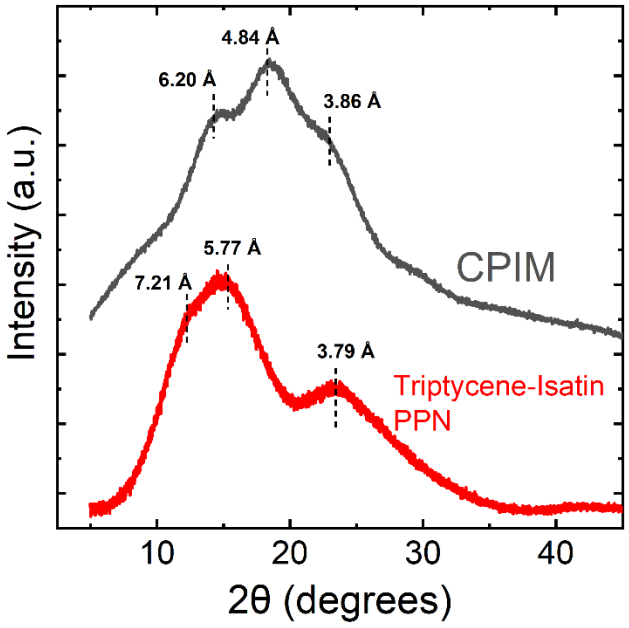


Figure C1. X-ray diffractograms of neat CPIM and PPN powder.

C3.3. Positron Annihilation Lifetime Spectroscopy

TFC membranes were measured using PALS before and after thermal treatment at 200℃ for 24 hours in vacuum. The membranes were cut and stacked into 3 mm thick bundles and the Mylar sealed positron source (1.4 MBq, ^{22}NaCl) was placed in the center of the bundle. The membrane samples were then measured under vacuum and the lifetime spectra was collected on Ortec EG&G spectrometers with a minimum of five files, each with 4.5 x 10^6 integrated counts collected. The resulting spectra were analyzed using the LT_v9 software[206] using a source corrector of 1.41 ns and 3.6%. The spectra were fit to 4 lifetimes with the first lifetime fixed to 0.125 ns which is attributed to para-positron annihilation where the positron forms a bound state with an electron within the sample of opposite spin. The second lifetime, approximately 0.4 ns was due to free annihilation where the positron directly annihilates with a free electron within the sample. The two longer lifetime components are related to ortho-positronium annihilation from the bound state of

a positron with an electron in the sample of the same spin. These semi-stable components' lifetimes are correlated to the free volume within the sample. The larger the free volume pores, the longer the lifetimes are. The sizes of the free volume elements are related to the semi-empirical Tau-Eldrup relationship (Equation C1), where the average pore size, $\boldsymbol{r}$, is related to the lifetime, $\boldsymbol{\tau}$.[154,231]

$$\tau_3 = \frac{1}{2}\left(1 - \frac{r}{r + \Delta r} + \frac{1}{2\pi} sin\left[\frac{2\pi r}{r + \Delta r}\right]\right)^{-1} \quad (C1)$$

Where $\boldsymbol{\Delta r}$, is determined empirically from the electron layer thickness (1.66 Å). The two component oPs fit indicated a bimodal pore distribution for the samples. The pore size distribution was adapted using PAScual software.[232]

C3.4. Scanning Electron Microscopy

Cross-sectional micrographs of TFC membranes and PPN particles were taken to determine their structural morphology using a ThermoFisher Quattro scanning electron microscope. Samples for cross-sectional analysis were prepared by first briefly submersing TFC membranes in toluene followed by freezing in liquid nitrogen and fracturing using tweezers. Prior to imaging, each sample was coated with iridium at a current of 20 mA for 45s using a Quorum Q150 sputter coater. Selective layer thicknesses for each TFC membrane measured were determined using 10 measurements from different points in two different images. For the PPN particles, an average particle size of 722 ± 467 nm was measured for isolated particles.

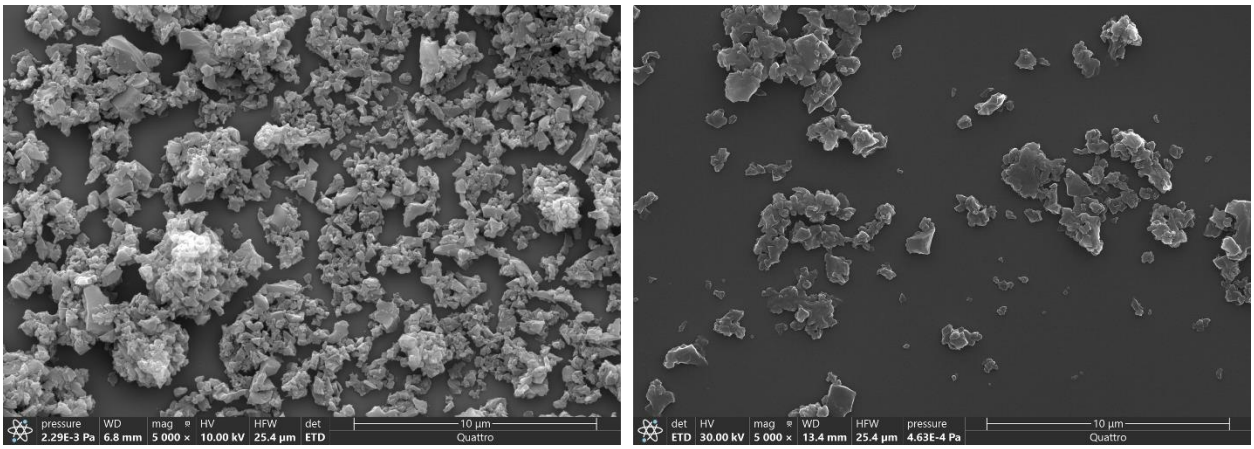


Figure C2. Images of the synthesized triptycene-isatin particles dispersed on a silicon wafer.

C3.5. Combustion Elemental Analysis

An Elementar Vario EL Cube elemental analyzer (Elementar Americas, Ronkonkoma, NY, USA) was used to determine the elemental composition of support samples and back out the free amine content, as well as the degree of hydrolysis of the CPIM. The carbon to nitrogen ratio decreases as more *p*-xylylenediamine is loaded into the supports. Analytical-grade sulfanilamide was used as the check and calibration standard. Check standards were run every 15 samples to ensure calibration quality, and each unique sample was ran three times consecutively to determine the experimental uncertainty. The relative error (i.e., precision) for both carbon and nitrogen repeat mass content measurements was approximately 2%, while the sulfanilamide check standards indicated an accuracy of within 0.1 mass %.

C3.6. Ninhydrin Assay

Ninhydrin was dissolved in 200 proof ethanol at a concentration of 5 w/v% (g/mL). After dissolving, a small section of support was immersed in 1 mL of the ninhydrin solution and heated at 50 °C on a hot plate. After 5-10 minutes, blue color developed if free amines were present. In absence of amines, the solution remained a yellow color.

C3.7. Liquid Dilation Measurements

Liquid dilation was tracked using the setup and equation depicted in Figure C3. The sample, sandwiched between microscope slides, was placed in a clear petri dish. This dish was placed on a ring stand and positioned above a camera. Enough toluene was added such that the sample was entirely submersed, and images were automatically taken. The area of the sample was tracked as a function of time using ImageJ (optical analysis software).

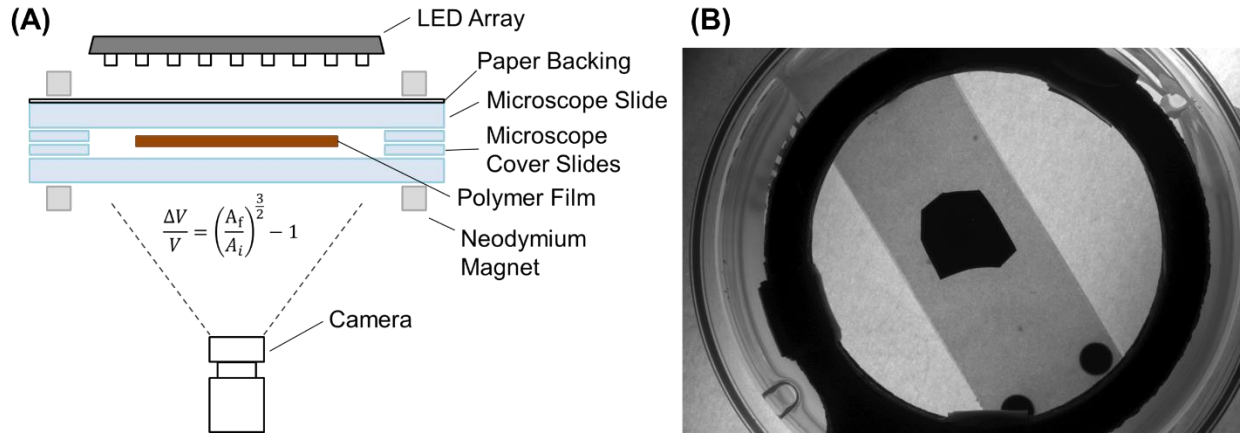


Figure C3. (A) Setup used to track liquid dilation of polymer samples. (B) Image from a CPIMTT dilation run in toluene.

C4. Organic Solvent Crossflow Apparatus Description

The crossflow apparatus used to perform OSN and OSRO measurements for this study is shown in Figure C4**.** 3-way valves are used to direct the flow either across the membrane surface or through a bypass route (in the case of a cell not having a membrane installed), as well as to control the flow of permeate either to recycle to the feed bottle or to be collected in vials. Septum-capped vials are used as the permeate collection receptacles. Septa are pierced with high gauge needles to prevent pressure buildup during permeate collection while minimizing solvent

evaporation. Oil-filled pressure gauges are installed between cells for operating pressure determination. A backpressure regulator is used to adjust the pressure in the system.

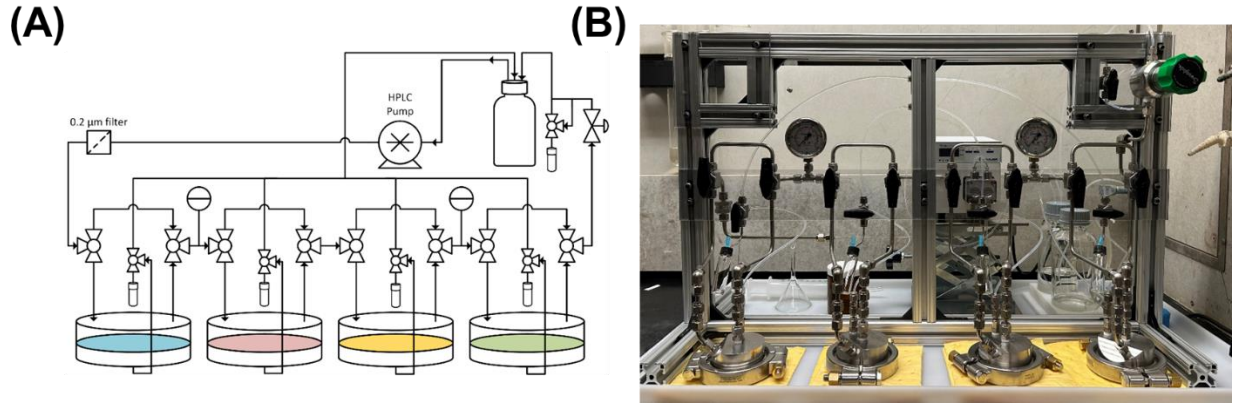


Figure C4. (A) flow diagram and (B) picture of the organic solvent crossflow apparatus.

C5. OSN and OSRO Performance Data

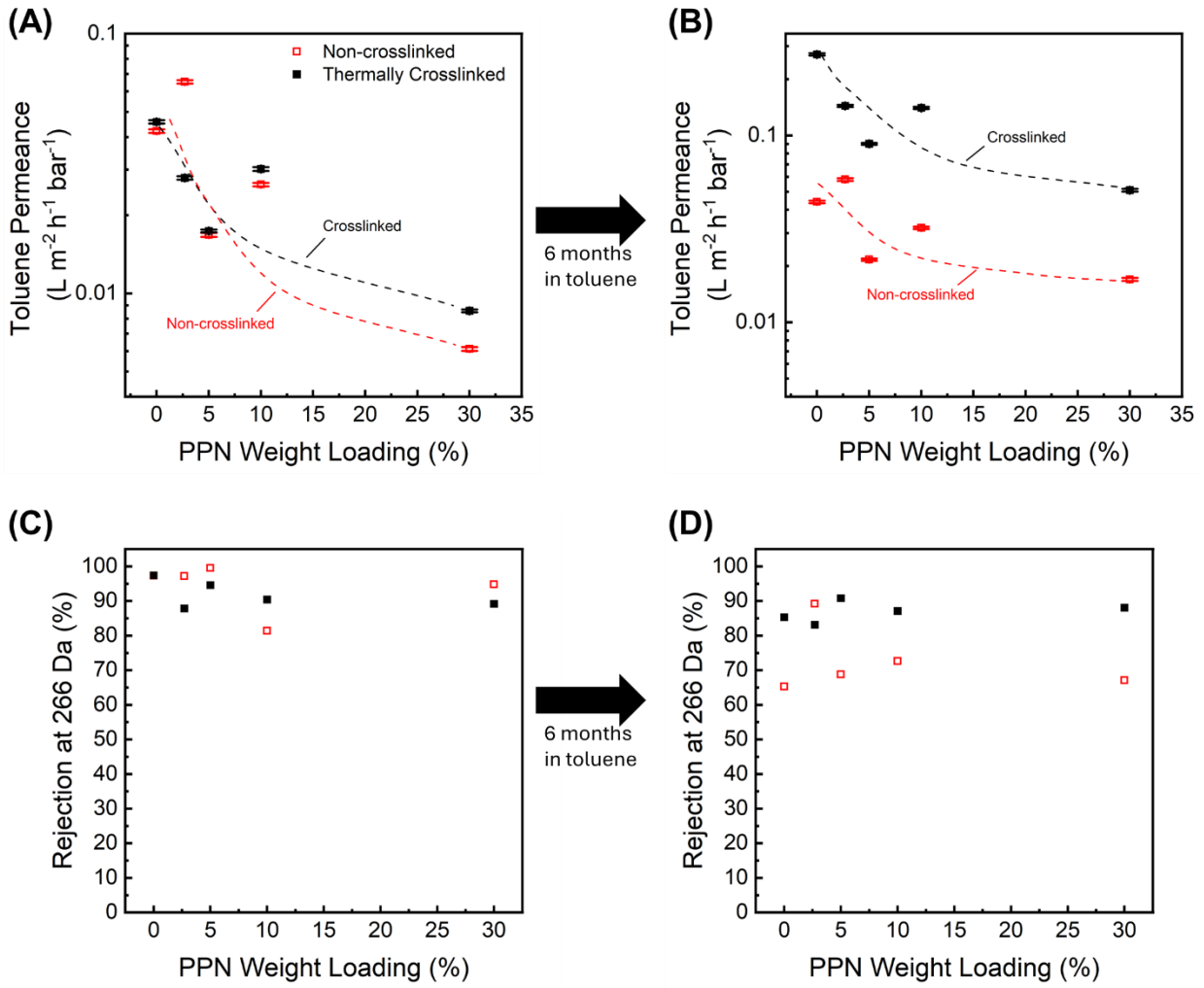


Figure C5. Trends in TFC membrane performance with thermal treatment, filler loading, and solvent exposure time. TFC membranes toluene permeance of (A) fresh samples and (B) after 6 months exposure to toluene. Rejection of the 266 Da Styrene oligomer of (C) fresh samples and (D) after 6 months exposure to toluene.

Table C3. OSN performance of fresh TFC membranes. Δp = 31 bar, ambient temperature, <3% stage cuts, with <500 ppm styrene oligomers. Error bars are calculated using linear error propagation.

Sample	Permeance ($L\ m^{-2}\ h^{-1}\ bar^{-1}$)	MWCO (Da)
CPIM	0.0422 ± 0.0007	200
MMM2.7	0.065 ± 0.001	162
MMM5	0.0168 ± 0.0003	162
MMM10	0.0263 ± 0.0004	370
MMM30	0.0061 ± 0.0001	162
CPIMTT	0.0458 ± 0.0007	162
IcMMM2.7	0.0278 ± 0.0004	280
IcMMM5	0.0174 ± 0.0002	162
IcMMM10	0.0301 ± 0.0005	266
IcMMM30	0.0086 ± 0.0001	270

Table C4. OSN performance of TFC membranes as in Table C3 after 6 months exposure to toluene, using the same testing conditions. Error bars are calculated using linear error propagation.

Sample	Permeance ($L\ m^{-2}\ h^{-1}\ bar^{-1}$)	MWCO (Da)
CPIM	0.0441 ± 0.0007	N/A[a]
MMM2.7	0.0581 ± 0.0009	295
MMM5	0.0217 ± 0.0003	667
MMM10	0.0320 ± 0.0005	660
MMM30	0.0170 ± 0.0003	709
CPIMTT	0.271 ± 0.004	316
IcMMM2.7	0.144 ± 0.002	330

IcMMM5	*0.090 ± 0.001*	*266*
IcMMM10	*0.140 ± 0.002*	*310*
IcMMM30	*0.0509 ± 0.0008*	*297*

[a]*Sample did not attain 90% rejection for any oligomer.*

Table C5. OSRO performance of samples after ~18 months exposure to toluene. Error bars are calculated using linear error propagation.

Sample	*Permeance* *(L m^{-2} h^{-1} bar^{-1})*	*Toluene/TIPB Separation Factor* *(-)*
CPIMTT	*0.293 ± 0.006*	*3.19 ± 0.44*
IcMMM2.7	*0.178 ± 0.003*	*4.14 ± 0.39*
IcMMM5[a]	*N/A*	*N/A*
IcMMM10	*0.145 ± 0.003*	*4.84 ± 0.40*
IcMMM30	*0.0512 ± 0.0009*	*6.06 ± 0.33*

[a]*Sample was defective and did not demonstrate any separation of toluene/TIPB.*

Table C6. Hydrocarbon rejection of IcMMM30 after ~21 months of exposure to toluene in a crossflow permeation test of a dilute 9-component mixture (1 mol% each dissolved in toluene, Δp = 50 bar). The permeance of IcMMM30 during this test was 0.038 L m^{-2} h^{-1} bar^{-1}.

No.	Component	Molecular Weight (Da)	Simulated Diameter (Å)[a]	Approx. Boiling Point (°C)	IcMMM30 Rejection (%)
1	Toluene	92.1	5.48	110.6	-7.4 ± 0.2
2	Isooctane	114.2	6.57	99.3	42.5 ± 0.5
3	Propylbenzene	120.2	6.14	159.2	6.5 ± 0.8
4	Tetralin	132.2	6.26	207	14.1 ± 1.4
5	1-Methylnapthalene	142.2	6.65	242	18.7 ± 1.9
6	*n*-Butylcyclohexane	172.3	6.90	179	38.8 ± 0.7
7	TIPB	204.4	7.60	234	82.2 ± 0.5
8	Dodecylbenzene	246.4	8.12	328	63.4 ± 1.3
9	Pristane	268.5	8.82	296	85.8 ±0.7

[a]*Simulated diameters were calculated by ChemDraw 3D software assuming a spherical shape, as reported in reference* [184].

C6. OSN Performance Stability at 578 Da

Changes in the rejection of the mid-molecular weight 578 Da styrene oligomer after 6 months exposure in toluene are shown in Figure C6. As can be seen, all the thermally crosslinked samples exhibit significantly more stable performance than the non-crosslinked samples.

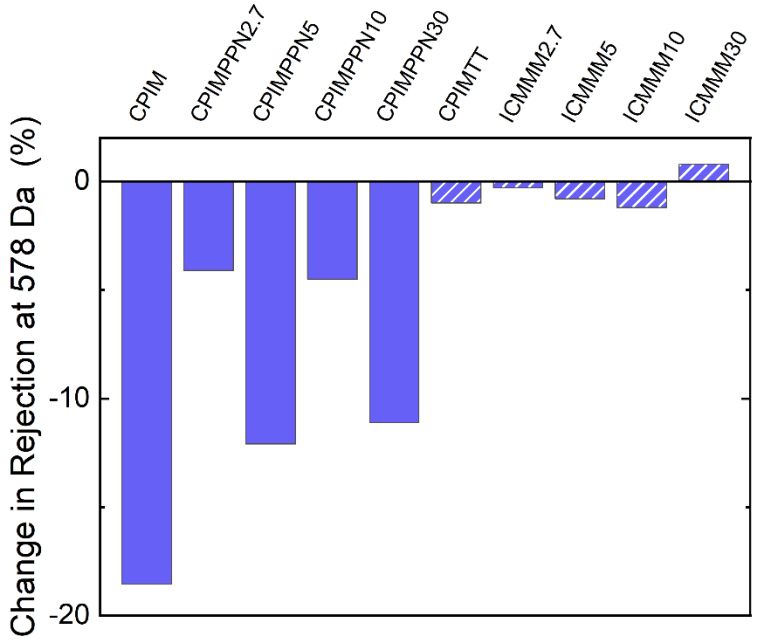


Figure C6. Changes in rejection for the 578 Da styrene oligomer after the 6-month stability test.

C7. Mechanism of Free Amine Formation

The mechanism for free amine formation in the porous supports is depicted in Figure C7. After a molecule of *p*-xylylenediamine reacts with Matrimid® at the imide linkage, it may react with another proximal imide linkage, forming the disubstituted diamine (crosslink). If another imide linkage is not available nearby, then the amine will remain unreacted, i.e., a free amine group is left available.

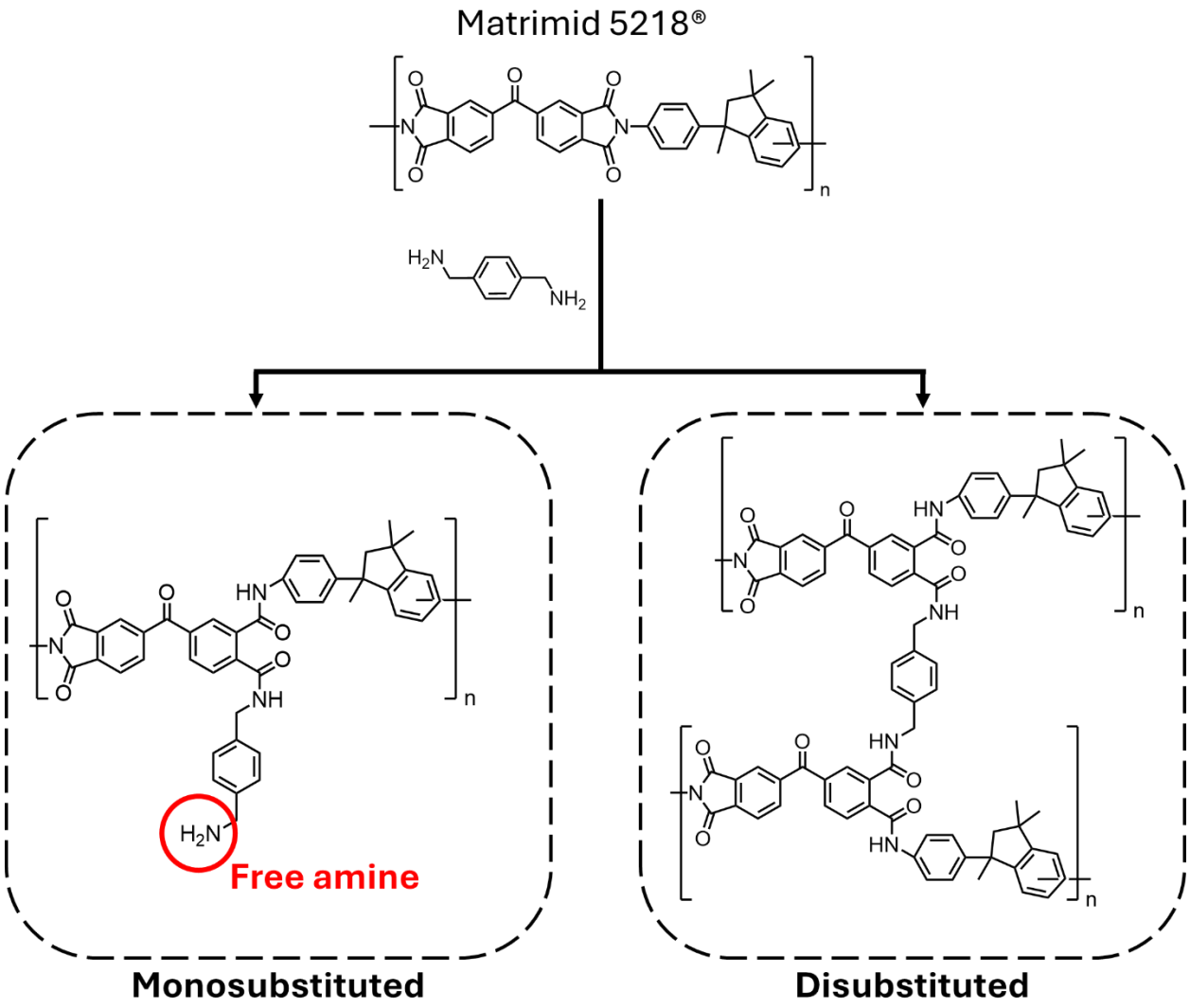


Figure C7. Mechanism of free amine formation during support crosslinking.

C8. Data for Toluene Permeability-Sorption Correlation

Table C7. Experimental datapoints used to validate the toluene permeability-sorption correlation.

Material	*Toluene Uptake (g_{solv}/g_{pol} * 100 %)*	*Toluene Weight Fraction*	*Permeability (L m^{-2} h^{-1} bar^{-1} nm)*	*Thickness (nm)*	*Reference*
CPIM	*49.2*	*0.3297*	*124.2*	*300*	*This work*
Torlon	*5.14*	*0.04890*	*4.88*	*350*	*190*
SBAD-1	*28.6*	*0.2226*	*40*	*200*	*177*
PIM-1	*124.5*	*0.5547*	*2138*	*300*	*187*
Matrimid	*55.08*	*0.3552*	*181.5*	*400*	*15*
DUCKY-9	*37.398*	*0.2722*	*94*	*200*	*178*
DUCKY-10	*51.49*	*0.3399*	*290*	*250*	*178*
Puramem 280	*41.278*	*0.2922*	*120*	*200*	*233,234*
Natural Rubber	*399.6*	*0.7998*	*75269*	*265 x 10^3*	*235,236*
Butyl Rubber	*256*	*0.7191*	*41445*	*342.9 x 10^3*	*237*
LDPE	*20.956*	*0.1733*	*85.8*	*50 x 10^3*	*238*
PDMS	*114*	*0.5327*	*3986*	*1385*	*239*
FRPAA-1	*22.2*	*0.1817*	*48.42*	*269*	*183*
FRPAA-2	*31.4*	*0.2390*	*63.25*	*253*	*183*
FRPAA-3	*21.9*	*0.1797*	*104.85*	*233*	*183*

FRPAA-4	*36.4*	*0.2669*	*142.68*	*246*	*183*
MPD-TFS	*21.8*	*0.1790*	*28.28*	*202*	*14*
Trip-TFB	*23.8*	*0.1922*	*24.96*	*192*	*14*
Trip-TFS	*27.1*	*0.2132*	*100.45*	*245*	*14*
MPD-SBF	*20.1*	*0.1674*	*82.0*	*332*	*14*
MPD-TMC	*22.5*	*0.1837*	*25.48*	*274*	*14*

C9. Elemental Analysis Results

Elemental analysis was performed to determine the *p*-xylylenediamine loading on the supports. Matrimid® has a C:N = 15 (mass ratio), while *p*-xylylenediamine has a C:N = 3.43. Thus, as more diamine is loaded into the supports, the C:N ratio will decrease. For example, at a 1:1 molar ratio of the repeat unit in Matrimid® to the diamine, the C:N = 9.2. The C:N mass ratios and diamine loadings are shown in Table C8.

Supports were washed with a mixture of 50:50 v:v toluene/methanol mixtures to desorb any unreacted diamine. After washing, the C:N ratio increased slightly, indicating that some fraction of the loaded diamine was only adsorbed (i.e., not reacted at either amine). The 10% crosslinked supports had 4.9% of the diamines adsorbed, while the 5% crosslinked supports had 1.1% of their diamines adsorbed.

Table C8. Combustion elemental analysis results for supports crosslinked with varying crosslinking solutions, before and after washing repeatedly with 50:50 v:v toluene/methanol solutions to remove adsorbed diamine.

Sample	*C:N Mass Ratio*	*Stoichiometric Diamine Loading (Amine:Imide)*
10% Crosslinked Supports	*7.53 ± 0.02*	*1.83 ± 0.01*
10% Crosslinked Supports, Washed	*7.66 ± 0.03*	*1.74 ± 0.02*
5% Crosslinked Supports	*8.88 ± 0.01*	*1.124 ± 0.004*
5% Crosslinked Supports, Washed	*8.91 ± 0.02*	*1.112 ± 0.009*

C10. Solution-Diffusion Prediction of Toluene Permeabilities

The solution-diffusion model is formulated based on Fick's law of diffusion:

$$J_i = -\rho D_i \frac{d\omega_i}{dx} \qquad (C2)$$

where J_i is the diffusive flux of penetrant i in the membrane with respect to the center of mass of the polymer-penetrant system, ρ is the mass density of the solvent/membrane mixture, ω_i is the penetrant mass fraction in the membrane, and x is the coordinate direction along which transport is occurring, assuming a unidirectional gradient that runs along the membrane thickness.[20] For the sake of simplicity, ρ was assumed to be that of toluene to make predictions, but ρ may be estimated using simple additive models if the density of the polymer being predicted is known.

Since ω_i can reach significant values in solvent-swollen polymers, any flux in the polymer-penetrant system will carry the laden solvent with it. This is expressed in the 'frame-of-reference' correction[20]:

$$n_i = J_i + \omega_i n_i \qquad (C3)$$

where n_i is the total flux in the membrane system. Combining the two above equations and integrating from $x = 0$ to $x = l$, the following expression can be derived:

$$n_i l = \rho \overline{D}_i \ln\left(\frac{1-\omega_i|_{x=l}}{1-\omega_i|_{x=0}}\right) \qquad (C4)$$

where $\overline{D}_i$ is the average diffusion coefficient of penetrant i in the membrane. This can be combined with the definition of permeability:

$$P_i = \frac{n_i l}{\Delta p} \qquad (C5)$$

where Δp is the hydraulic transmembrane pressure. Combining this definition with the expression for flux:

$$P_i = \frac{\rho \bar{D}_i \, ln\left(\frac{1-\omega_i|_{x=l}}{1-\omega_i|_{x=0}}\right)}{\Delta p} \qquad (C6)$$

In order to make predictions using this model, tools to estimate ω_i at the downstream interface (i.e., $x = l$) and $\bar{D}_i$ are required. Using Paul's model[235–237] and the assumption that the penetrant activity coefficient is relatively constant in the membrane, the following expression provides the downstream interface mass fraction:

$$\omega_i|_{x=l} = \omega_i|_{x=0} \exp\left(-\frac{\bar{V}_i \Delta p}{RT}\right) \qquad (C7)$$

where $\bar{V}_i$ is the partial molar volume of the penetrant in the membrane, which, for the sake of simplicity, is assumed to be equal to the molar volume, $\tilde{V}_i$. R is the ideal gas constant, and T is temperature.

Finally, the diffusion coefficient in the membrane can be estimated using the Mackie-Meares model, which predicts diffusivity to be a reduced factor of the self-diffusion coefficient ($D_{i,s}$) as volume fraction of the solvent (ϕ_i) decreases[240]:

$$\frac{\bar{D}_i}{D_{i,s}} = \left(\frac{\phi_i}{2-\phi_i}\right)^2 \qquad (C8)$$

Substituting all the elements into the expression for permeability yields the following expression, which makes predictions for a membrane given that you know its pure solvent uptake in the membrane ($\omega_i|_{x=0}$) and basic properties of the pure solvent:

$$P_i = \frac{\rho D_{i,s} \left(\frac{\phi_i}{2-\phi_i}\right)^2 \ln\left(\frac{1-\omega_i|_{x=0} \exp\left(-\frac{\tilde{V}_i \Delta p}{RT}\right)}{1-\omega_i|_{x=0}}\right)}{\Delta p} \quad (C9)$$

As can be seen in Figure C8, the solution-diffusion prediction has an R^2 of 0.91 on the experimental data, indicating that toluene fits the assumptions above, namely, has a relatively constant diffusion coefficient in the membrane, exhibits a partial molar volume in the membrane close to its molar volume, has a relatively constant activity coefficient in the membrane (i.e., behaves ideally), and its diffusivity in the membrane scales primarily with tortuosity effects. Given that toluene is a rigid molecule that does not exhibit varying conformations (that could lead to varying diffusivities), does not exhibit strong interactions such as hydrogen bonding, and is not too elongated, it makes sense that toluene transport behavior fits these assumptions. Negative deviations from the solution-diffusion predictions are systematically observed for a number of the TFC membranes; this bias towards negative deviations may be due to some combination of lateral diffusion limitations in these membranes and the fact that material properties begin to change drastically as the film thickness enters the nanometer range (e.g., solvent uptake could be lower in thin films due to denser packing). For more complicated hydrocarbons (e.g., long chain or branched hydrocarbons) or hydrogen bonding molecules such as alcohols or polar aprotic solvents, these assumptions presumably may not hold true.

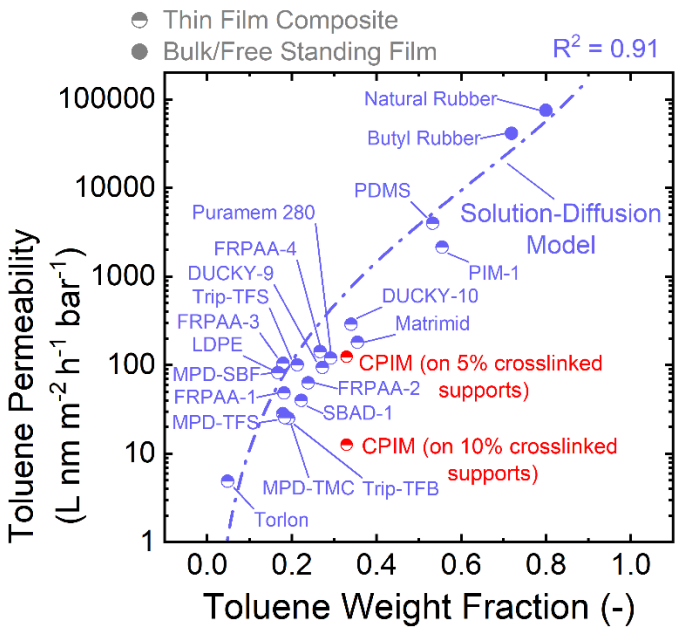


Figure C8. Solution-diffusion a priori predictions of experimental toluene permeabilities.

C11. Normalized Toluene Liquid Dilation Curves

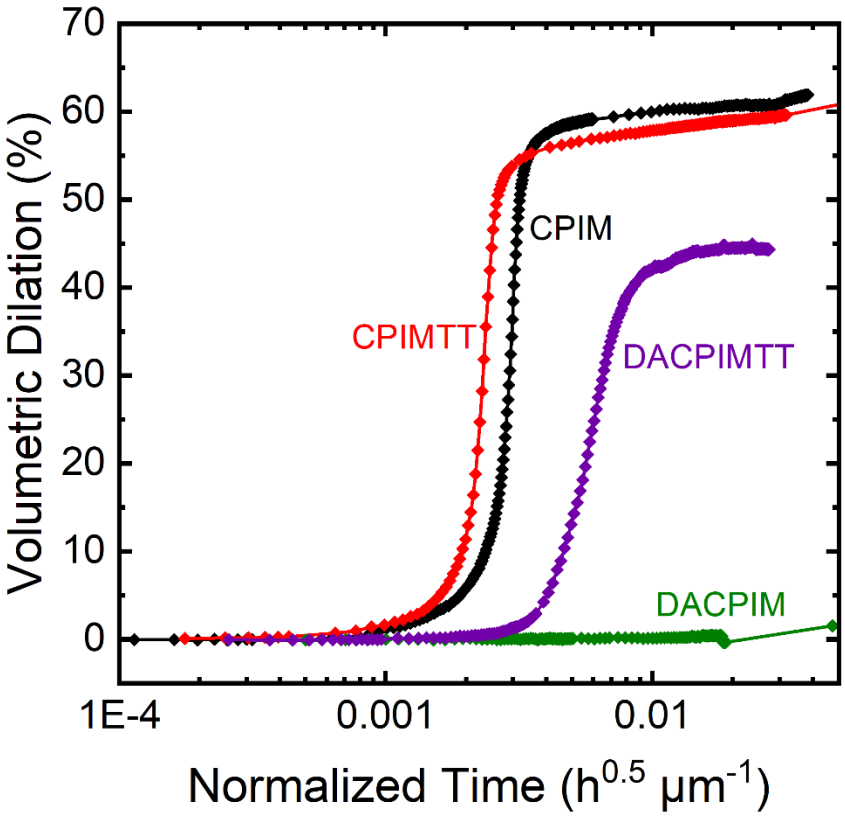


Figure C9. Volumetric dilation curves of CPIM, CPIMTT, DACPIMTT, and DACPIM in liquid toluene plotted against a normalized time parameter. The purpose of normalization is to create kinetically comparable curves (since thicker samples will dilate more slowly).

C12. Correlation of Dilation to Solvent Molar Volume

In order to relate dilation measurements to permeability predictions, an intermediary conversion of volumetric dilation to solvent uptake is required. Volumetric dilation is defined as follows:

$$\frac{\Delta V}{V} = \frac{V_f - V_i}{V_i} \tag{C10}$$

where $\frac{\Delta V}{V}$ is the volumetric dilation, V_f is the final polymer phase volume, and V_i is the initial (dry) polymer volume.

Assuming that the volume of incorporated solvent is much larger than the free volume in the dry polymer, it can be hypothesized that the change in volume of the polymer phase is directly proportional to the incorporated solvent volume:

$$\Delta V = n_i * \tilde{V}_i \tag{C11}$$

where n_i is the number of incorporated moles and $\tilde{V}_i$ is the solvent molar volume. This allows for substitution into the expression for dilation:

$$\frac{\Delta V}{V} = \frac{n_i * \tilde{V}_i}{V_i} \tag{C12}$$

In this expression, $\frac{n_i}{V_i}$ is the volumetric basis molar concentration; if the density of the polymer is known, it can be converted to a gravimetric basis molar concentration. Taking the loose assumption that $\rho_i \approx 1 \frac{g}{cm^3}$ yields a final expression to be empirically validated:

$$\frac{\left(\frac{\Delta V}{V}\right)}{\tilde{V}_i} = C_i \tag{C13}$$

where C_i is the gravimetric basis molar concentration (e.g., $\frac{mol_{solv}}{g_{pol}}$). Numerical validation of this expression is shown in Figure C10. 16 different datapoints with 15 different solvents in 3 different polymers shows excellent agreement with the relationship, indicating that this expression provides a reasonably accurate method to convert between volumetric dilation and solvent uptake.

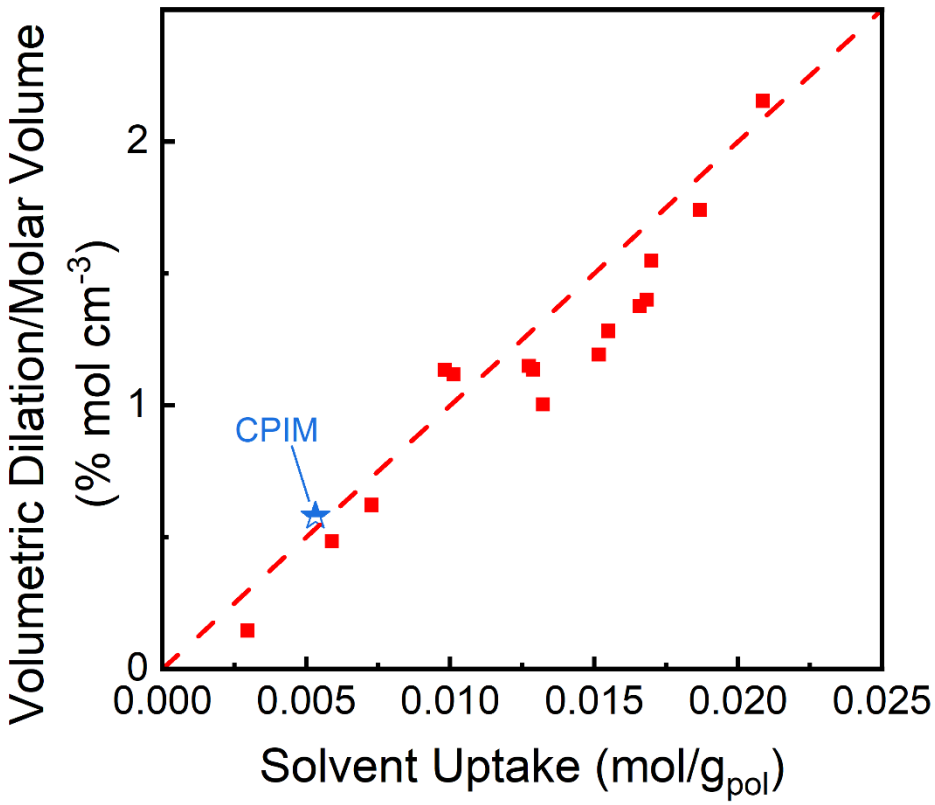


Figure C10. Validation of the derived relationship between volumetric dilation and incorporated solvent volume. The labelled point for CPIM was cross-validated using gravimetric uptake measurements and optical liquid dilation measurements.

Table C9. Polymers, solvent uptakes, and volumetric dilation data used to validate the derived expression used to convert dilation to solvent uptake.

Polymer	*Solvent*	*Molar Volume* ($cm^3\ mol^{-1}$)	*Solvent Uptake* ($mol\ g_{pol}^{-1}$)	*Volumetric Dilation* (%)	*Reference*
PBI	*water*	*18*	*0.0129*	*20.4*	[62]
PBI	*methanol*	*40.7*	*0.0127*	*46.8*	[62]
PBI	*ethanol*	*58.5*	*0.0098*	*66.4*	[62]
PBI	*1-propanol*	*75.2*	*0.0101*	*84.0*	[62]
PBI	*2-propanol*	*76.8*	*0.0030*	*11.2*	[62]
PBI	*acetone*	*74.1*	*0.0059*	*36.0*	[62]
PIM-1	*propylene carbonate*	*84.7*	*0.0132*	*85*	[241]
PIM-1	*Dimethylsulfoxide*	*71.0*	*0.0155*	*91*	[241]
PIM-1	*Dimethylformamide*	*77.1*	*0.0168*	*108*	[241]
PIM-1	*Triethylene Glycol*	*133.4*	*0.0073*	*83*	[241]
PIM-1	*Dimethylacetamide*	*93.0*	*0.0170*	*144*	[241]
PIM-1	*Toluene*	*106.9*	*0.0187*	*186*	[241]
PIM-1	*p-Xylene*	*123.3*	*0.0152*	*147*	[241]
PIM-1	*м-Xylene*	*123.5*	*0.0166*	*170*	[241]
PIM-1	*Benzene*	*89.1*	*0.0209*	*192*	[241]
CPIM	*Toluene*	*106.9*	*0.0053*	*62*	*This work*

References

(1) Lopez-Iglesias, B.; Suárez-García, F.; Aguilar-Lugo, C.; González Ortega, A.; Bartolomé, C.; Martínez-Ilarduya, J. M.; de la Campa, J. G.; Lozano, Á. E.; Álvarez, C. Microporous Polymer Networks for Carbon Capture Applications. *ACS Appl. Mater. Interfaces* **2018**, *10* (31), 26195–26205. https://doi.org/10.1021/acsami.8b05854.

(2) Smil, V. *Energy Transitions: Global and National Perspectives*; Bloomsbury Publishing USA, 2016.

(3) Murphy, T. W. Limits to Economic Growth. *Nat. Phys.* **2022**, *18* (8), 844–847. https://doi.org/10.1038/s41567-022-01652-6.

(4) Sholl, D. S.; Lively, R. P. Seven Chemical Separations to Change the World. *Nature* **2016**, *532* (7600), 435–437. https://doi.org/10.1038/532435a.

(5) Lee, K. P.; Arnot, T. C.; Mattia, D. A Review of Reverse Osmosis Membrane Materials for Desalination—Development to Date and Future Potential. *Journal of Membrane Science* **2011**, *370* (1), 1–22. https://doi.org/10.1016/j.memsci.2010.12.036.

(6) Glater, J. The Early History of Reverse Osmosis Membrane Development. *Desalination* **1998**, *117* (1), 297–309. https://doi.org/10.1016/S0011-9164(98)00122-2.

(7) Jones, E.; Qadir, M.; van Vliet, M. T. H.; Smakhtin, V.; Kang, S. The State of Desalination and Brine Production: A Global Outlook. *Science of The Total Environment* **2019**, *657*, 1343–1356. https://doi.org/10.1016/j.scitotenv.2018.12.076.

(8) Galizia, M.; Chi, W. S.; Smith, Z. P.; Merkel, T. C.; Baker, R. W.; Freeman, B. D. *50th Anniversary Perspective* : Polymers and Mixed Matrix Membranes for Gas and Vapor Separation: A Review and Prospective Opportunities. *Macromolecules* **2017**, *50* (20), 7809–7843. https://doi.org/10.1021/acs.macromol.7b01718.

(9) Lee, Y. J.; Lively, R. P. A Transition in Diffusion Behaviors of Organic Liquid Mixtures in Dense Polymer Membranes. *Journal of Membrane Science* **2025**, *713*, 123346. https://doi.org/10.1016/j.memsci.2024.123346.

(10) Rodriguez, K. M.; Lin, S.; X. Wu, A.; R. Storme, K.; Joo, T.; F. Grosz, A.; Roy, N.; Syar, D.; M. Benedetti, F.; P. Smith, Z. Penetrant-Induced Plasticization in Microporous Polymer Membranes. *Chemical Society Reviews* **2024**, *53* (5), 2435–2529. https://doi.org/10.1039/D3CS00235G.

(11) Liu, C.; Dong, G.; Tsuru, T.; Matsuyama, H. Organic Solvent Reverse Osmosis Membranes for Organic Liquid Mixture Separation: A Review. *Journal of Membrane Science* **2021**, *620*, 118882. https://doi.org/10.1016/j.memsci.2020.118882.

(12) Marchetti, P.; Jimenez Solomon, M. F.; Szekely, G.; Livingston, A. G. Molecular Separation with Organic Solvent Nanofiltration: A Critical Review. *Chem. Rev.* **2014**, *114* (21), 10735–10806. https://doi.org/10.1021/cr500006j.

(13) Galizia, M.; Bye, K. P. Advances in Organic Solvent Nanofiltration Rely on Physical Chemistry and Polymer Chemistry. *Front. Chem.* **2018**, *6*, 511. https://doi.org/10.3389/fchem.2018.00511.

(14) Lee, T. H.; Balcik, M.; Ali, Z.; Joo, T.; Rivera, M. P.; Pinnau, I.; Smith, Z. P. Microporous Polyimine Membranes for Efficient Separation of Liquid Hydrocarbon Mixtures. **2025**.

(15) Rivera, M. P.; Bruno, N. C.; Finn, M. G.; Lively, R. P. Organic Solvent Reverse Osmosis Using CuAAC-Crosslinked Molecularly-Mixed Composite Membranes. *Journal of Membrane Science* **2021**, *638*, 119700. https://doi.org/10.1016/j.memsci.2021.119700.

(16) Zhu, G.; Zhang, F.; Rivera, M. P.; Hu, X.; Zhang, G.; Jones, C. W.; Lively, R. P. Molecularly Mixed Composite Membranes for Advanced Separation Processes. *Angewandte Chemie International Edition* **2019**, *58* (9), 2638–2643. https://doi.org/10.1002/anie.201811341.
(17) Feliachi, Y.; Roy, A.; Ren, Y.; Finn, M. G.; Lively, R. P. Solid-State Crosslinking of Thin Film Composite Membranes for Organic Solvent Reverse Osmosis Separations. *Journal of Membrane Science* **2024**, *695*, 122462. https://doi.org/10.1016/j.memsci.2024.122462.
(18) Condes, L. C.; Landry, A. E.; Webb, M. T.; Box, W. J.; Gali, A.; Galizia, M. Inter-Crosslinked Spirocyclic Mixed Matrix Membranes Exhibiting Enhanced Gas Permeability, Selectivity, and Plasticization Resistance. *Journal of Membrane Science* **2024**, *709*, 123081. https://doi.org/10.1016/j.memsci.2024.123081.
(19) McGuinness, E. K.; Zhang, F.; Ma, Y.; Lively, R. P.; Losego, M. D. Vapor Phase Infiltration of Metal Oxides into Nanoporous Polymers for Organic Solvent Separation Membranes. *Chem. Mater.* **2019**, *31* (15), 5509–5518. https://doi.org/10.1021/acs.chemmater.9b01141.
(20) Bye, K. P.; Galizia, M. Fundamental Origin of Flux Non-Linearity in Organic Solvent Nanofiltration: Formulation of a Thermodynamic/Diffusion Framework. *Journal of Membrane Science* **2020**, *603*, 118020. https://doi.org/10.1016/j.memsci.2020.118020.
(21) Robeson, L. M.; Liu, Q.; Freeman, B. D.; Paul, D. R. Comparison of Transport Properties of Rubbery and Glassy Polymers and the Relevance to the Upper Bound Relationship. *Journal of Membrane Science* **2015**, *476*, 421–431. https://doi.org/10.1016/j.memsci.2014.11.058.
(22) Merrick, M. M.; Sujanani, R.; Freeman, B. D. Glassy Polymers: Historical Findings, Membrane Applications, and Unresolved Questions Regarding Physical Aging. *Polymer* **2020**, *211*, 123176. https://doi.org/10.1016/j.polymer.2020.123176.
(23) Mizrahi Rodriguez, K.; Wu, A. X.; Qian, Q.; Han, G.; Lin, S.; Benedetti, F. M.; Lee, H.; Chi, W. S.; Doherty, C. M.; Smith, Z. P. Facile and Time-Efficient Carboxylic Acid Functionalization of PIM-1: Effect on Molecular Packing and Gas Separation Performance. *Macromolecules* **2020**, *53* (15), 6220–6234. https://doi.org/10.1021/acs.macromol.0c00933.
(24) Koros, W. J.; Paul, D. R.; Rocha, A. A. Carbon Dioxide Sorption and Transport in Polycarbonate. *J. Polym. Sci. Polym. Phys. Ed.* **1976**, *14* (4), 687–702. https://doi.org/10.1002/pol.1976.180140410.
(25) Merkel, T. C.; Bondar, V. I.; Nagai, K.; Freeman, B. D.; Pinnau, I. Gas Sorption, Diffusion, and Permeation in Poly(Dimethylsiloxane). *Journal of Polymer Science Part B: Polymer Physics* **2000**, *38* (3), 415–434. https://doi.org/10.1002/(SICI)1099-0488(20000201)38:3%253C415::AID-POLB8%253E3.0.CO;2-Z.
(26) Merkel, T. C.; Bondar, V.; Nagai, K.; Freeman, B. D.; Yampolskii, Yu. P. Gas Sorption, Diffusion, and Permeation in Poly(2,2-Bis(Trifluoromethyl)-4,5-Difluoro-1,3-Dioxole-Co-Tetrafluoroethylene). *Macromolecules* **1999**, *32* (25), 8427–8440. https://doi.org/10.1021/ma990685r.
(27) Paul, D. R.; Koros, W. J. Effect of Partially Immobilizing Sorption on Permeability and the Diffusion Time Lag. *J. Polym. Sci. Polym. Phys. Ed.* **1976**, *14* (4), 675–685. https://doi.org/10.1002/pol.1976.180140409.
(28) Koros, W. J.; Paul, D. R.; Huvard, G. S. Energetics of Gas Sorption in Glassy Polymers. *Polymer* **1979**, *20* (8), 956–960. https://doi.org/10.1016/0032-3861(79)90192-7.
(29) Robeson, L. M. Correlation of Separation Factor versus Permeability for Polymeric Membranes. *Journal of Membrane Science* **1991**, *62* (2), 165–185. https://doi.org/10.1016/0376-7388(91)80060-J.

(30) Freeman, B. D. Basis of Permeability/Selectivity Tradeoff Relations in Polymeric Gas Separation Membranes. *Macromolecules* **1999**, *32* (2), 375–380. https://doi.org/10.1021/ma9814548.
(31) Budd, P. M.; Elabas, E. S.; Ghanem, B. S.; Makhseed, S.; McKeown, N. B.; Msayib, K. J.; Tattershall, C. E.; Wang, D. Solution-Processed, Organophilic Membrane Derived from a Polymer of Intrinsic Microporosity. *Advanced Materials* **2004**, *16* (5), 456–459. https://doi.org/10.1002/adma.200306053.
(32) Box, W. J.; Huang, Z.; Guo, R.; Galizia, M. Evidence for Size-Sieving Driven Vapor Sorption and Diffusion in a Glassy Polybenzoxazole Exhibiting Configurational Free Volume. *Ind. Eng. Chem. Res.* **2021**, *60* (36), 13326–13337. https://doi.org/10.1021/acs.iecr.1c02660.
(33) Swaidan, R.; Ghanem, B.; Litwiller, E.; Pinnau, I. Physical Aging, Plasticization and Their Effects on Gas Permeation in "Rigid" Polymers of Intrinsic Microporosity. *Macromolecules* **2015**, *48* (18), 6553–6561. https://doi.org/10.1021/acs.macromol.5b01581.
(34) Huang, Y.; Merkel, T. C.; Baker, R. W. Pressure Ratio and Its Impact on Membrane Gas Separation Processes. *Journal of Membrane Science* **2014**, *463*, 33–40. https://doi.org/10.1016/j.memsci.2014.03.016.
(35) Cangialosi, D.; Boucher, V. M.; Alegría, A.; Colmenero, J. Physical Aging in Polymers and Polymer Nanocomposites: Recent Results and Open Questions. *Soft Matter* **2013**, *9* (36), 8619. https://doi.org/10.1039/c3sm51077h.
(36) Lau, C. H.; Nguyen, P. T.; Hill, M. R.; Thornton, A. W.; Konstas, K.; Doherty, C. M.; Mulder, R. J.; Bourgeois, L.; Liu, A. C. Y.; Sprouster, D. J.; Sullivan, J. P.; Bastow, T. J.; Hill, A. J.; Gin, D. L.; Noble, R. D. Ending Aging in Super Glassy Polymer Membranes. *Angew. Chem. Int. Ed.* **2014**, *53* (21), 5322–5326. https://doi.org/10.1002/anie.201402234.
(37) Cangialosi, D.; Boucher, V. M.; Alegría, A.; Colmenero, J. Physical Aging in Polymers and Polymer Nanocomposites: Recent Results and Open Questions. *Soft Matter* **2013**, *9* (36), 8619. https://doi.org/10.1039/c3sm51077h.
(38) Mahajan, R.; Koros, W. J. Factors Controlling Successful Formation of Mixed-Matrix Gas Separation Materials. *Ind. Eng. Chem. Res.* **2000**, *39* (8), 2692–2696. https://doi.org/10.1021/ie990799r.
(39) Hussain, M.; König, A. Mixed-Matrix Membrane for Gas Separation: Polydimethylsiloxane Filled with Zeolite. *Chem Eng & Technol* **2012**, *35* (3), 561–569. https://doi.org/10.1002/ceat.201100419.
(40) Cheng, Y.; Ying, Y.; Japip, S.; Jiang, S.-D.; Chung, T.-S.; Zhang, S.; Zhao, D. Advanced Porous Materials in Mixed Matrix Membranes. *Advanced Materials* **2018**, *30* (47), 1802401. https://doi.org/10.1002/adma.201802401.
(41) Dechnik, J.; Gascon, J.; Doonan, C. J.; Janiak, C.; Sumby, C. J. Mixed-Matrix Membranes. *Angewandte Chemie International Edition* **2017**, *56* (32), 9292–9310. https://doi.org/10.1002/anie.201701109.
(42) Soto, C.; Torres-Cuevas, E. S.; González-Ortega, A.; Palacio, L.; Lozano, Á. E.; Freeman, B. D.; Prádanos, P.; Hernández, A. Gas Separation by Mixed Matrix Membranes with Porous Organic Polymer Inclusions within O-Hydroxypolyamides Containing m-Terphenyl Moieties. *Polymers* **2021**, *13* (6), 931. https://doi.org/10.3390/polym13060931.
(43) Aguilar-Lugo, C.; Suárez-García, F.; Hernández, A.; Miguel, J. A.; Lozano, Á. E.; de la Campa, J. G.; Álvarez, C. New Materials for Gas Separation Applications: Mixed Matrix Membranes Made from Linear Polyimides and Porous Polymer Networks Having Lactam

Groups. *Ind. Eng. Chem. Res.* **2019**, *58* (22), 9585–9595. https://doi.org/10.1021/acs.iecr.9b01402.
(44) Soto, C.; Aguilar Lugo, C.; Rodríguez, S.; Palacio, L.; Lozano, Á. E.; Prádanos, P.; Hernandez, A. Enhancement of CO2/CH4 Permselectivity via Thermal Rearrangement of Mixed Matrix Membranes Made from an o-Hydroxy Polyamide with an Optimal Load of a Porous Polymer Network. *Separation and Purification Technology* **2020**, *247*, 116895. https://doi.org/10.1016/j.seppur.2020.116895.
(45) Soto, C.; Cicuttin, N.; Carmona, F. J.; de la Viuda, M.; Tena, A.; Lozano, Á. E.; Hernández, A.; Palacio, L.; Prádanos, P. Gas Adsorption Isotherm, Pore Size Distribution, and Free Volume Fraction of Polymer-Polymer Mixed Matrix Membranes before and after Thermal Rearrangement. *Journal of Membrane Science* **2023**, *683*, 121841. https://doi.org/10.1016/j.memsci.2023.121841.
(46) Soto, C.; Torres-Cuevas, E. S.; Palacio, L.; Prádanos, P.; Freeman, B. D.; Lozano, Á. E.; Hernández, A.; Comesaña-Gándara, B. Gas Permeability, Fractional Free Volume and Molecular Kinetic Diameters: The Effect of Thermal Rearrangement on Ortho-Hydroxy Polyamide Membranes Loaded with a Porous Polymer Network. *Membranes* **2022**, *12* (2), 200. https://doi.org/10.3390/membranes12020200.
(47) Matesanz-Niño, L.; Webb, M. T.; González-Ortega, A.; Palacio, L.; Álvarez, C.; Lozano, Á. E.; Galizia, M. Plasticization Resistant Gas Separation Membranes Derived from Polyimides Exhibiting Polyethylene-Oxide Moieties. *Polymer* **2024**, *290*, 126535. https://doi.org/10.1016/j.polymer.2023.126535.
(48) Condes, L. C.; Webb, M. T.; Le, T. T. B.; Box, W. J.; Doherty, C. M.; Gali, A.; Garrido, L.; Deng, J.; Matesanz-Niño, L.; Lozano, A. E.; Alvarez, C.; Buongiorno Nardelli, M.; Striolo, A.; Hill, A. J.; Galizia, M. Elucidating the Molecular Mechanisms by Which Porous Polymer Networks Affect Structure, Aging Propensity, and Selectivity of Microporous Glassy Polymer Membranes Using a Multiscale Approach. *ACS Appl. Mater. Interfaces* **2024**, *16* (40), 53843–53854. https://doi.org/10.1021/acsami.4c11472.
(49) Hillock, A. M. W.; Koros, W. J. Cross-Linkable Polyimide Membrane for Natural Gas Purification and Carbon Dioxide Plasticization Reduction. *Macromolecules* **2007**, *40* (3), 583–587. https://doi.org/10.1021/ma062180o.
(50) Zhang, C. Decarboxylation Crosslinking of Polyimides with High CO2/CH4 Separation Performance and Plasticization Resistance. *Journal of Membrane Science* **2017**, 11.
(51) Du, N.; Dal-Cin, M. M.; Robertson, G. P.; Guiver, M. D. Decarboxylation-Induced Cross-Linking of Polymers of Intrinsic Microporosity (PIMs) for Membrane Gas Separation. *Macromolecules* **2012**, *45* (12), 5134–5139. https://doi.org/10.1021/ma300751s.
(52) Kratochvil, A. M.; Koros, W. J. Decarboxylation-Induced Cross-Linking of a Polyimide for Enhanced CO2 Plasticization Resistance. *Macromolecules* **2008**, *41* (21), 7920–7927. https://doi.org/10.1021/ma801586f.
(53) Qiu, W.; Chen, C.-C.; Xu, L.; Cui, L.; Paul, D. R.; Koros, W. J. Sub-Tg Cross-Linking of a Polyimide Membrane for Enhanced CO2 Plasticization Resistance for Natural Gas Separation. *Macromolecules* **2011**, *44* (15), 6046–6056. https://doi.org/10.1021/ma201033j.
(54) Wu, W.-N.; Lee, T. H.; Hernandez, A.; Dovranova, G.; Smith, Z. P. MOF Instability and Polymer Infiltration in Amine-Functionalized UiO MOFs/PIM-COOH-Based MMMs for Solvent-Based Separations. *Ind. Eng. Chem. Res.* **2025**, *64* (20), 10012–10021. https://doi.org/10.1021/acs.iecr.5c00174.

(55) Tien-Binh, N.; Vinh-Thang, H.; Chen, X. Y.; Rodrigue, D.; Kaliaguine, S. Crosslinked MOF-Polymer to Enhance Gas Separation of Mixed Matrix Membranes. *Journal of Membrane Science* **2016**, *520*, 941–950. https://doi.org/10.1016/j.memsci.2016.08.045.
(56) Wu, W.-N.; Mizrahi Rodriguez, K.; Roy, N.; Teesdale, J. J.; Han, G.; Liu, A.; Smith, Z. P. Engineering the Polymer–MOF Interface in Microporous Composites to Address Complex Mixture Separations. *ACS Appl. Mater. Interfaces* **2023**, *15* (45), 52893–52907. https://doi.org/10.1021/acsami.3c11300.
(57) Deng, J.; Huang, Z.; Sundell, B. J.; Harrigan, D. J.; Sharber, S. A.; Zhang, K.; Guo, R.; Galizia, M. State of the Art and Prospects of Chemically and Thermally Aggressive Membrane Gas Separations: Insights from Polymer Science. *Polymer* **2021**, *229*, 123988. https://doi.org/10.1016/j.polymer.2021.123988.
(58) Robeson, L. M. The Upper Bound Revisited. *Journal of Membrane Science* **2008**, *320* (1–2), 390–400. https://doi.org/10.1016/j.memsci.2008.04.030.
(59) Comesaña-Gándara, B.; Chen, J.; Grazia Bezzu, C.; Carta, M.; Rose, I.; Ferrari, M.-C.; Esposito, E.; Fuoco, A.; C. Jansen, J.; B. McKeown, N. Redefining the Robeson Upper Bounds for CO 2 /CH 4 and CO 2 /N 2 Separations Using a Series of Ultrapermeable Benzotriptycene-Based Polymers of Intrinsic Microporosity. *Energy & Environmental Science* **2019**, *12* (9), 2733–2740. https://doi.org/10.1039/C9EE01384A.
(60) Medicine, N. A. of S., Engineering, and; Studies, D. on E. and L.; Technology, B. on C. S. and; Science, C. on a R. A. for a N. E. in S. *A Research Agenda for Transforming Separation Science*; National Academies Press, 2019.
(61) Swaidan, R.; Ghanem, B.; Al-Saeedi, M.; Litwiller, E.; Pinnau, I. Role of Intrachain Rigidity in the Plasticization of Intrinsically Microporous Triptycene-Based Polyimide Membranes in Mixed-Gas CO2/CH4 Separations. *Macromolecules* **2014**, *47* (21), 7453–7462. https://doi.org/10.1021/ma501798v.
(62) Bye, K. P.; Loianno, V.; Pham, T. N.; Liu, R.; Riffle, J. S.; Galizia, M. Pure and Mixed Fluid Sorption and Transport in Celazole® Polybenzimidazole: Effect of Plasticization. *Journal of Membrane Science* **2019**, *580*, 235–247. https://doi.org/10.1016/j.memsci.2019.03.031.
(63) Huang, M.; Lu, K.; Wang, Z.; Bi, X.; Zhang, Y.; Jin, J. Thermally Cross-Linked Amidoxime-Functionalized Polymers of Intrinsic Microporosity Membranes for Highly Selective Hydrogen Separation. *ACS Sustainable Chem. Eng.* **2021**, *9* (28), 9426–9435. https://doi.org/10.1021/acssuschemeng.1c02784.
(64) Swaidan, R.; Ghanem, B. S.; Litwiller, E.; Pinnau, I. Pure- and Mixed-Gas CO2/CH4 Separation Properties of PIM-1 and an Amidoxime-Functionalized PIM-1. *Journal of Membrane Science* **2014**, *457*, 95–102. https://doi.org/10.1016/j.memsci.2014.01.055.
(65) Du, N.; Robertson, G. P.; Song, J.; Pinnau, I.; Guiver, M. D. High-Performance Carboxylated Polymers of Intrinsic Microporosity (PIMs) with Tunable Gas Transport Properties. *Macromolecules* **2009**, *42* (16), 6038–6043. https://doi.org/10.1021/ma9009017.
(66) Mizrahi Rodriguez, K.; Benedetti, F. M.; Roy, N.; Wu, A. X.; Smith, Z. P. Sorption-Enhanced Mixed-Gas Transport in Amine Functionalized Polymers of Intrinsic Microporosity (PIMs). *J. Mater. Chem. A* **2021**, *9* (41), 23631–23642. https://doi.org/10.1039/D1TA06530K.
(67) Mason, C. R.; Maynard-Atem, L.; Heard, K. W. J.; Satilmis, B.; Budd, P. M.; Friess, K.; Lanč, M.; Bernardo, P.; Clarizia, G.; Jansen, J. C. Enhancement of CO2 Affinity in a Polymer of Intrinsic Microporosity by Amine Modification. *Macromolecules* **2014**, *47* (3), 1021–1029. https://doi.org/10.1021/ma401869p.

(68) Satilmis, B.; Lanč, M.; Fuoco, A.; Rizzuto, C.; Tocci, E.; Bernardo, P.; Clarizia, G.; Esposito, E.; Monteleone, M.; Dendisová, M.; Friess, K.; Budd, P. M.; Jansen, J. C. Temperature and Pressure Dependence of Gas Permeation in Amine-Modified PIM-1. *Journal of Membrane Science* **2018**, *555*, 483–496. https://doi.org/10.1016/j.memsci.2018.03.039.
(69) Satilmis, B.; M. Budd, P. Base-Catalysed Hydrolysis of PIM-1: Amide versus Carboxylate Formation. *RSC Advances* **2014**, *4* (94), 52189–52198. https://doi.org/10.1039/C4RA09907A.
(70) Yanaranop, P.; Santoso, B.; Etzion, R.; Jin, J. Facile Conversion of Nitrile to Amide on Polymers of Intrinsic Microporosity (PIM-1). *Polymer* **2016**, *98*, 244–251. https://doi.org/10.1016/j.polymer.2016.06.041.
(71) Mason, C. R.; Maynard-Atem, L.; Al-Harbi, N. M.; Budd, P. M.; Bernardo, P.; Bazzarelli, F.; Clarizia, G.; Jansen, J. C. Polymer of Intrinsic Microporosity Incorporating Thioamide Functionality: Preparation and Gas Transport Properties. *Macromolecules* **2011**, *44* (16), 6471–6479. https://doi.org/10.1021/ma200918h.
(72) Du, N.; Robertson, G. P.; Dal-Cin, M. M.; Scoles, L.; Guiver, M. D. Polymers of Intrinsic Microporosity (PIMs) Substituted with Methyl Tetrazole. *Polymer* **2012**, *53* (20), 4367–4372. https://doi.org/10.1016/j.polymer.2012.07.055.
(73) Koros, W. J.; Zhang, C. Materials for Next-Generation Molecularly Selective Synthetic Membranes. *Nature Mater* **2017**, *16* (3), 289–297. https://doi.org/10.1038/nmat4805.
(74) Jue, M. L.; Lively, R. P. PIM Hybrids and Derivatives: How to Make a Good Thing Better. *Current Opinion in Chemical Engineering* **2022**, *35*, 100750. https://doi.org/10.1016/j.coche.2021.100750.
(75) Chang, Y. S.; Kumari, P.; Munro, C. J.; Szekely, G.; Vega, L. F.; Nunes, S.; Dumée, L. F. Plasticization Mitigation Strategies for Gas and Liquid Filtration Membranes - A Review. *Journal of Membrane Science* **2023**, *666*, 121125. https://doi.org/10.1016/j.memsci.2022.121125.
(76) Kadirkhan, F.; Goh, P. S.; Ismail, A. F.; Wan Mustapa, W. N. F.; Halim, M. H. M.; Soh, W. K.; Yeo, S. Y. Recent Advances of Polymeric Membranes in Tackling Plasticization and Aging for Practical Industrial CO2/CH4 Applications—A Review. *Membranes* **2022**, *12* (1), 71. https://doi.org/10.3390/membranes12010071.
(77) Wind, J. D.; Staudt-Bickel, C.; Paul, D. R.; Koros, W. J. The Effects of Crosslinking Chemistry on CO2 Plasticization of Polyimide Gas Separation Membranes. *Ind. Eng. Chem. Res.* **2002**, *41* (24), 6139–6148. https://doi.org/10.1021/ie0204639.
(78) Wind, J. D.; Staudt-Bickel, C.; Paul, D. R.; Koros, W. J. Solid-State Covalent Cross-Linking of Polyimide Membranes for Carbon Dioxide Plasticization Reduction. *Macromolecules* **2003**, *36* (6), 1882–1888. https://doi.org/10.1021/ma025938m.
(79) Cui, L.; Qiu, W.; Paul, D. R.; Koros, W. J. Responses of 6FDA-Based Polyimide Thin Membranes to CO2 Exposure and Physical Aging as Monitored by Gas Permeability. *Polymer* **2011**, *52* (24), 5528–5537. https://doi.org/10.1016/j.polymer.2011.10.008.
(80) Yu, H. J.; Chan, C.-H.; Nam, S. Y.; Kim, S.-J.; Yoo, J. S.; Lee, J. S. Thermally Cross-Linked Ultra-Robust Membranes for Plasticization Resistance and Permeation Enhancement – A Combined Theoretical and Experimental Study. *Journal of Membrane Science* **2022**, *646*, 120250. https://doi.org/10.1016/j.memsci.2021.120250.
(81) Shi, Y.; Wang, Z.; Shi, Y.; Zhu, S.; Zhang, Y.; Jin, J. Synergistic Design of Enhanced π–π Interaction and Decarboxylation Cross-Linking of Polyimide Membranes for Natural Gas

Separation. *Macromolecules* **2022**, *55* (7), 2970–2982. https://doi.org/10.1021/acs.macromol.1c02573.
(82) Zhang, T.; Deng, L.; Li, P. Decarboxylation Cross-Linking of Triptycene-Based Tröger's Base Polymers for Gas Separation. *Ind. Eng. Chem. Res.* **2020**, 9.
(83) Calle, M.; Jo, H. J.; Doherty, C. M.; Hill, A. J.; Lee, Y. M. Cross-Linked Thermally Rearranged Poly(Benzoxazole-Co-Imide) Membranes Prepared from Ortho-Hydroxycopolyimides Containing Pendant Carboxyl Groups and Gas Separation Properties. *Macromolecules* **2015**, *48* (8), 2603–2613. https://doi.org/10.1021/acs.macromol.5b00298.
(84) Tien-Binh, N.; Rodrigue, D.; Kaliaguine, S. In-Situ Cross Interface Linking of PIM-1 Polymer and UiO-66-NH2 for Outstanding Gas Separation and Physical Aging Control. *Journal of Membrane Science* **2018**, *548*, 429–438. https://doi.org/10.1016/j.memsci.2017.11.054.
(85) Lau, C. H.; Konstas, K.; Doherty, C. M.; Kanehashi, S.; Ozcelik, B.; Kentish, S. E.; Hill, A. J.; Hill, M. R. Tailoring Physical Aging in Super Glassy Polymers with Functionalized Porous Aromatic Frameworks for CO2 Capture. *Chem. Mater.* **2015**, *27* (13), 4756–4762. https://doi.org/10.1021/acs.chemmater.5b01537.
(86) Box, W. J.; Huang, Z.; Guo, R.; Galizia, M. The Mechanism of Light Gas Transport through Configurational Free Volume in Glassy Polymers. *Journal of Membrane Science* **2022**, *656*, 120608. https://doi.org/10.1016/j.memsci.2022.120608.
(87) Box, W. J.; Condes, L. C.; Webb, M. T.; Suleiman, A.; Guo, R.; Galizia, M. Computer Vision-Based Measurement of Pure- and Mixed-Gas Swelling in Polymer Membranes: Individual and Synergistic Effects of Configurational Free Volume and Thermal Rearrangement. *Journal of Membrane Science* **2024**, *Under Review*.
(88) Puleo, A. C.; Paul, D. R.; Kelley, S. S. The Effect of Degree of Acetylation on Gas Sorption and Transport Behavior in Cellulose Acetate. *Journal of Membrane Science* **1989**, *47* (3), 301–332. https://doi.org/10.1016/S0376-7388(00)83083-5.
(89) Box, W. J.; Webb, M. T.; Galizia, M. Evaluating the Experimental Uncertainty in Gas and Vapor Sorption/Adsorption Measurements: Fundamental Considerations and Experimental Design Implications. *Ind. Eng. Chem. Res.* **2022**, *61* (27), 9856–9868. https://doi.org/10.1021/acs.iecr.2c01414.
(90) Galizia, M.; Smith, Z. P.; Sarti, G. C.; Freeman, B. D.; Paul, D. R. Predictive Calculation of Hydrogen and Helium Solubility in Glassy and Rubbery Polymers. *Journal of Membrane Science* **2015**, *475*, 110–121. https://doi.org/10.1016/j.memsci.2014.10.009.
(91) Mahato, M.; Tabassian, R.; Nguyen, V. H.; Oh, S.; Nam, S.; Hwang, W.-J.; Oh, I.-K. CTF-Based Soft Touch Actuator for Playing Electronic Piano. *Nat Commun* **2020**, *11* (1), 5358. https://doi.org/10.1038/s41467-020-19180-3.
(92) Hao, L.; Liao, K.-S.; Chung, T.-S. Photo-Oxidative PIM-1 Based Mixed Matrix Membranes with Superior Gas Separation Performance. *J. Mater. Chem. A* **2015**, *3* (33), 17273–17281. https://doi.org/10.1039/C5TA03776J.
(93) Wang, P.; Li, X.; Liu, Z.; Peng, J.; Shi, C.; Li, T.; Yang, J.; Shan, C.; Hu, W.; Liu, B. Construction of Highly Conductive PBI-Based Alloy Membranes by Incorporating PIMs with Optimized Molecular Weights for High-Temperature Proton Exchange Membrane Fuel Cells. *Journal of Membrane Science* **2022**, *659*, 120790. https://doi.org/10.1016/j.memsci.2022.120790.

(94) Muldoon, P. F.; Venna, S. R.; Gidley, D. W.; Baker, J. S.; Zhu, L.; Tong, Z.; Xiang, F.; Hopkinson, D. P.; Yi, S.; Sekizkardes, A. K.; Rosi, N. L. Mixed Matrix Membranes from a Microporous Polymer Blend and Nanosized Metal–Organic Frameworks with Exceptional CO2/N2 Separation Performance. *ACS Materials Lett.* **2020**, *2* (7), 821–828. https://doi.org/10.1021/acsmaterialslett.0c00156.

(95) Alentiev, A. Yu.; Bondarenko, G. N.; Kostina, Yu. V.; Shantarovich, V. P.; Klyamkin, S. N.; Fedin, V. P.; Kovalenko, K. A.; Yampolskii, Yu. P. PIM-1/MIL-101 Hybrid Composite Membrane Material: Transport Properties and Free Volume. *Pet. Chem.* **2014**, *54* (7), 477–481. https://doi.org/10.1134/S0965544114070020.

(96) Yahia, M.; Phan Le, Q. N.; Ismail, N.; Essalhi, M.; Sundman, O.; Rahimpour, A.; Dal-Cin, M. M.; Tavajohi, N. Effect of Incorporating Different ZIF-8 Crystal Sizes in the Polymer of Intrinsic Microporosity, PIM-1, for CO2/CH4 Separation. *Microporous and Mesoporous Materials* **2021**, *312*, 110761. https://doi.org/10.1016/j.micromeso.2020.110761.

(97) Yu, M.; Foster, A. B.; Alshurafa, M.; Luque-Alled, J. M.; Gorgojo, P.; Kentish, S. E.; Scholes, C. A.; Budd, P. M. CO2 Separation Using Thin Film Composite Membranes of Acid-Hydrolyzed PIM-1. *Journal of Membrane Science* **2023**, *679*, 121697. https://doi.org/10.1016/j.memsci.2023.121697.

(98) Santoso, B.; Yanaranop, P.; Kang, H.; Leung, I. K. H.; Jin, J. A Critical Update on the Synthesis of Carboxylated Polymers of Intrinsic Microporosity (C-PIMs). *Macromolecules* **2017**, *50* (7), 3043–3050. https://doi.org/10.1021/acs.macromol.7b00344.

(99) Kokko, J. P.; Mandell, Leon.; Goldstein, J. H. An N.m.r. Investigation of Proton Mobility in Substituted Uracils. *J. Am. Chem. Soc.* **1962**, *84* (6), 1042–1047. https://doi.org/10.1021/ja00865a035.

(100) Eskay, T. P.; Britt, P. F.; Iii, A. C. B. Pyrolysis of Aromatic Carboxylic Acids: Potential Involvement of Anhydrides in Retrograde Reactions in Low-Rank Coal. *Energy Fuels* **1997**, *11* (6), 1278–1287.

(101) Li, F. Y.; Xiao, Y.; Chung, T.-S.; Kawi, S. High-Performance Thermally Self-Cross-Linked Polymer of Intrinsic Microporosity (PIM-1) Membranes for Energy Development. *Macromolecules* **2012**, *45* (3), 1427–1437. https://doi.org/10.1021/ma202667y.

(102) Wang, L.; Guo, X.; Zhang, F.; Li, N. Blending and *in Situ* Thermally Crosslinking of Dual Rigid Polymers for Anti-Plasticized Gas Separation Membranes. *Journal of Membrane Science* **2021**, *638*, 119668. https://doi.org/10.1016/j.memsci.2021.119668.

(103) Eriksen, T. K.; Hansen, B. K. V.; Spanget-Larsen, J. The Vibrational Structure of Dibenzo-p-Dioxin. IR Linear Dichroism, Raman Spectroscopy, and Quantum Chemical Calculations. *Polish Journal of Chemistry* **2008**, *82* (4), 921–934.

(104) Chen, W.; Zhang, Z.; Hou, L.; Yang, C.; Shen, H.; Yang, K.; Wang, Z. Metal-Organic Framework MOF-801/PIM-1 Mixed-Matrix Membranes for Enhanced CO2/N2 Separation Performance. *Separation and Purification Technology* **2020**, *250*, 117198. https://doi.org/10.1016/j.seppur.2020.117198.

(105) Hou, L.; Wang, Z.; Chen, Z.; Chen, W.; Yang, C. PIM-1 as an Organic Filler to Enhance CO2 Separation Performance of Poly (Arylene Fluorene Ether Ketone). *Separation and Purification Technology* **2020**, *242*, 116766. https://doi.org/10.1016/j.seppur.2020.116766.

(106) Mkhatresh, O. A.; Heatley, F. Thermal Oxidative and Photo-Oxidative Degradation of Polytetrahydrofuran Studied Using 1H NMR, 13C NMR and GPC. *Polymer International* **2004**, *53* (7), 959–971. https://doi.org/10.1002/pi.1483.

(107) Matsuda, K.; Tanaka, Y.; Sakai, T. Effect of Perchloric Acid on the Molecular Weight and Yield of poly-THF. *J of Applied Polymer Sci* **1976**, *20* (10), 2821–2827. https://doi.org/10.1002/app.1976.070201016.
(108) Chang, T. C.; Wu, K. H.; Chen, H. B.; Ho, S. Y.; Chiu, Y. S. Thermal Degradation of Aged Polytetrahydrofuran and Its Copolymers with 3-Azidomethyl-3′-Methyloxetane and 3-Nitratomethyl-3′-Methyloxetane by Thermogravimetry. *Journal of Polymer Science Part A: Polymer Chemistry* **1996**, *34* (16), 3337–3343. https://doi.org/10.1002/(SICI)1099-0518(19961130)34:16%253C3337::AID-POLA10%253E3.0.CO;2-H.
(109) Wallace, W. E. Mass Spectra. In *NIST Chemistry WebBook, NIST Standard Reference Database Number 69*; National Institute of Standards and Technology: Gaithersburg MD, 20899.
(110) Tago, K.; Tsuchiya, M.; Gondo, Y.; Ishimaru, K.; Kojima, T. Thermal Decomposition of Poly(Oxytetramethylene) Glycol. *Journal of Applied Polymer Science* **2000**, *77* (7), 1538–1544. https://doi.org/10.1002/1097-4628(20000815)77:7%253C1538::AID-APP15%253E3.0.CO;2-J.
(111)Ghosal, K.; Chern, R. T.; Freeman, B. D.; Daly, W. H.; Negulescu, I. I. Effect of Basic Substituents on Gas Sorption and Permeation in Polysulfone. *Macromolecules* **1996**, *29* (12), 4360–4369. https://doi.org/10.1021/ma951310i.
(112) Kim, H. W.; Park, H. B. Gas Diffusivity, Solubility and Permeability in Polysulfone–Poly(Ethylene Oxide) Random Copolymer Membranes. *Journal of Membrane Science* **2011**, *372* (1), 116–124. https://doi.org/10.1016/j.memsci.2011.01.053.
(113) Jordan, S. M.; Koros, W. J.; Fleming, G. K. The Effects of CO2 Exposure on Pure and Mixed Gas Permeation Behavior: Comparison of Glassy Polycarbonate and Silicone Rubber. *Journal of Membrane Science* **1987**, *30* (2), 191–212. https://doi.org/10.1016/S0376-7388(00)81351-4.
(114) Chung, T.-S.; Chan, S. S.; Wang, R.; Lu, Z.; He, C. Characterization of Permeability and Sorption in Matrimid/C60 Mixed Matrix Membranes. *Journal of Membrane Science* **2003**, *211* (1), 91–99. https://doi.org/10.1016/S0376-7388(02)00385-X.
(115) Esposito, E.; Mazzei, I.; Monteleone, M.; Fuoco, A.; Carta, M.; McKeown, N. B.; Malpass-Evans, R.; Jansen, J. C. Highly Permeable Matrimid®/PIM-EA(H2)-TB Blend Membrane for Gas Separation. *Polymers* **2019**, *11* (1), 46. https://doi.org/10.3390/polym11010046.
(116) Webb, M. T.; Condes, L. C.; Ly, H. G.; Galizia, M.; Razavi, S. Rational Design, Synthesis, and Characterization of Facilitated Transport Membranes Exhibiting Enhanced Permeability, Selectivity and Stability. *Journal of Membrane Science* **2023**, *685*, 121910. https://doi.org/10.1016/j.memsci.2023.121910.
(117) Kinoshita, Y.; Wakimoto, K.; Gibbons, A. H.; Isfahani, A. P.; Kusuda, H.; Sivaniah, E.; Ghalei, B. Enhanced PIM-1 Membrane Gas Separation Selectivity through Efficient Dispersion of Functionalized POSS Fillers. *Journal of Membrane Science* **2017**, *539*, 178–186. https://doi.org/10.1016/j.memsci.2017.05.072.
(118) Bushell, A. F.; Budd, P. M.; Attfield, M. P.; Jones, J. T. A.; Hasell, T.; Cooper, A. I.; Bernardo, P.; Bazzarelli, F.; Clarizia, G.; Jansen, J. C. Nanoporous Organic Polymer/Cage Composite Membranes. *Angewandte Chemie International Edition* **2013**, *52* (4), 1253–1256. https://doi.org/10.1002/anie.201206339.
(119) Wu, X.; Tian, Z.; Wang, S.; Peng, D.; Yang, L.; Wu, Y.; Xin, Q.; Wu, H.; Jiang, Z. Mixed Matrix Membranes Comprising Polymers of Intrinsic Microporosity and Covalent Organic

Framework for Gas Separation. *Journal of Membrane Science* **2017**, *528*, 273–283. https://doi.org/10.1016/j.memsci.2017.01.042.

(120) Hou, R.; Smith, S. J. D.; Wood, C. D.; Mulder, R. J.; Lau, C. H.; Wang, H.; Hill, M. R. Solvation Effects on the Permeation and Aging Performance of PIM-1-Based MMMs for Gas Separation. *ACS Appl. Mater. Interfaces* **2019**, *11* (6), 6502–6511. https://doi.org/10.1021/acsami.8b19207.

(121) Han, W.; Zhang, C.; Zhao, M.; Yang, F.; Yang, Y.; Weng, Y. Post-Modification of PIM-1 and Simultaneously in Situ Synthesis of Porous Polymer Networks into PIM-1 Matrix to Enhance CO2 Separation Performance. *Journal of Membrane Science* **2021**, *636*, 119544. https://doi.org/10.1016/j.memsci.2021.119544.

(122) Smith, Z. P.; Sanders, D. F.; Ribeiro, C. P.; Guo, R.; Freeman, B. D.; Paul, D. R.; McGrath, J. E.; Swinnea, S. Gas Sorption and Characterization of Thermally Rearranged Polyimides Based on 3,3′-Dihydroxy-4,4′-Diamino-Biphenyl (HAB) and 2,2′-Bis-(3,4-Dicarboxyphenyl) Hexafluoropropane Dianhydride (6FDA). *Journal of Membrane Science* **2012**, *415–416*, 558–567. https://doi.org/10.1016/j.memsci.2012.05.050.

(123) Matesanz-Niño, L.; Webb, M. T.; González-Ortega, A.; Palacio, L.; Álvarez, C.; Lozano, Á. E.; Galizia, M. Plasticization Resistant Gas Separation Membranes Derived from Polyimides Exhibiting Polyethylene-Oxide Moieties. *Polymer* **2024**, *290*, 126535. https://doi.org/10.1016/j.polymer.2023.126535.

(124) Chi, W. S.; Sundell, B. J.; Zhang, K.; Harrigan, D. J.; Hayden, S. C.; Smith, Z. P. Mixed-Matrix Membranes Formed from Multi-Dimensional Metal–Organic Frameworks for Enhanced Gas Transport and Plasticization Resistance. *ChemSusChem* **2019**, *12* (11), 2355–2360. https://doi.org/10.1002/cssc.201900623.

(125) He, Y.; Benedetti, F. M.; Lin, S.; Liu, C.; Zhao, Y.; Ye, H.-Z.; Van Voorhis, T.; De Angelis, M. G.; Swager, T. M.; Smith, Z. P. Polymers with Side Chain Porosity for Ultrapermeable and Plasticization Resistant Materials for Gas Separations. *Advanced Materials* **2019**, *31* (21), 1807871. https://doi.org/10.1002/adma.201807871.

(126) Jiang, X.; Li, S.; He, S.; Bai, Y.; Shao, L. Interface Manipulation of CO 2 –Philic Composite Membranes Containing Designed UiO-66 Derivatives towards Highly Efficient CO 2 Capture. *Journal of Materials Chemistry A* **2018**, *6* (31), 15064–15073. https://doi.org/10.1039/C8TA03872D.

(127) Yin, H.; Chua, Y. Z.; Yang, B.; Schick, C.; Harrison, W. J.; Budd, P. M.; Böhning, M.; Schönhals, A. First Clear-Cut Experimental Evidence of a Glass Transition in a Polymer with Intrinsic Microporosity: PIM-1. *J. Phys. Chem. Lett.* **2018**, *9* (8), 2003–2008. https://doi.org/10.1021/acs.jpclett.8b00422.

(128) Bevington, P. R.; Robinson, D. K. *Data Reduction and Error Analysis for the Physical Sciences*, 3rd ed.; McGraw-Hill: Boston, 2003.

(129) Bos, A.; Pünt, I. G. M.; Wessling, M.; Strathmann, H. CO2-Induced Plasticization Phenomena in Glassy Polymers. *Journal of Membrane Science* **1999**, *155* (1), 67–78. https://doi.org/10.1016/S0376-7388(98)00299-3.

(130) Intergovernmental Panel On Climate Change. *Climate Change 2021 – The Physical Science Basis: Working Group I Contribution to the Sixth Assessment Report of the Intergovernmental Panel on Climate Change*, 1st ed.; Cambridge University Press, 2023. https://doi.org/10.1017/9781009157896.

(131) Rockström, J.; Gupta, J.; Qin, D.; Lade, S. J.; Abrams, J. F.; Andersen, L. S.; Armstrong McKay, D. I.; Bai, X.; Bala, G.; Bunn, S. E.; Ciobanu, D.; DeClerck, F.; Ebi, K.; Gifford, L.; Gordon, C.; Hasan, S.; Kanie, N.; Lenton, T. M.; Loriani, S.; Liverman, D. M.; Mohamed, A.; Nakicenovic, N.; Obura, D.; Ospina, D.; Prodani, K.; Rammelt, C.; Sakschewski, B.; Scholtens, J.; Stewart-Koster, B.; Tharammal, T.; van Vuuren, D.; Verburg, P. H.; Winkelmann, R.; Zimm, C.; Bennett, E. M.; Bringezu, S.; Broadgate, W.; Green, P. A.; Huang, L.; Jacobson, L.; Ndehedehe, C.; Pedde, S.; Rocha, J.; Scheffer, M.; Schulte-Uebbing, L.; de Vries, W.; Xiao, C.; Xu, C.; Xu, X.; Zafra-Calvo, N.; Zhang, X. Safe and Just Earth System Boundaries. *Nature* **2023**, *619* (7968), 102–111. https://doi.org/10.1038/s41586-023-06083-8.

(132) Huang, Y.; Paul, D. R. Physical Aging of Thin Glassy Polymer Films Monitored by Gas Permeability. *Polymer* **2004**, *45* (25), 8377–8393. https://doi.org/10.1016/j.polymer.2004.10.019.

(133) Hutchinson, J. M. Physical Aging of Polymers. *Progress in Polymer Science* **1995**, *20* (4), 703–760. https://doi.org/10.1016/0079-6700(94)00001-I.

(134) Hodge, I. M. Physical Aging in Polymer Glasses. *Science* **1995**, *267* (5206), 1945–1947. https://doi.org/10.1126/science.267.5206.1945.

(135) Corrado, T.; Guo, R. Macromolecular Design Strategies toward Tailoring Free Volume in Glassy Polymers for High Performance Gas Separation Membranes. *Molecular Systems Design & Engineering* **2020**, *5* (1), 22–48. https://doi.org/10.1039/C9ME00099B.

(136) Rowe, B. W.; Freeman, B. D.; Paul, D. R. Physical Aging of Ultrathin Glassy Polymer Films Tracked by Gas Permeability. *Polymer* **2009**, *50* (23), 5565–5575. https://doi.org/10.1016/j.polymer.2009.09.037.

(137) Dorkenoo, K. D.; Pfromm, P. H. Experimental Evidence and Theoretical Analysis of Physical Aging in Thin and Thick Amorphous Glassy Polymer Films. *Journal of Polymer Science Part B: Polymer Physics* **1999**, *37* (16), 2239–2251. https://doi.org/10.1002/(SICI)1099-0488(19990815)37:16%253C2239::AID-POLB26%253E3.0.CO;2-8.

(138) Luo, S.; Zhang, Q.; Zhu, L.; Lin, H.; Kazanowska, B. A.; Doherty, C. M.; Hill, A. J.; Gao, P.; Guo, R. Highly Selective and Permeable Microporous Polymer Membranes for Hydrogen Purification and CO_2 Removal from Natural Gas. *Chem. Mater.* **2018**, *30* (15), 5322–5332. https://doi.org/10.1021/acs.chemmater.8b02102.

(139) Wiegand, J. R.; Smith, Z. P.; Liu, Q.; Patterson, C. T.; Freeman, B. D.; Guo, R. Synthesis and Characterization of Triptycene-Based Polyimides with Tunable High Fractional Free Volume for Gas Separation Membranes. *J. Mater. Chem. A* **2014**, *2* (33), 13309–13320. https://doi.org/10.1039/C4TA02303J.

(140) Weidman, J. R.; Guo, R. The Use of Iptycenes in Rational Macromolecular Design for Gas Separation Membrane Applications. *Ind. Eng. Chem. Res.* **2017**, *56* (15), 4220–4236. https://doi.org/10.1021/acs.iecr.7b00540.

(141) Weidman, J. R.; Luo, S.; Doherty, C. M.; Hill, A. J.; Gao, P.; Guo, R. Analysis of Governing Factors Controlling Gas Transport through Fresh and Aged Triptycene-Based Polyimide Films. *Journal of Membrane Science* **2017**, *522*, 12–22. https://doi.org/10.1016/j.memsci.2016.09.013.

(142) Wang, Y.; Ghanem, B. S.; Han, Y.; Pinnau, I. State-of-the-Art Polymers of Intrinsic Microporosity for High-Performance Gas Separation Membranes. *Current Opinion in Chemical Engineering* **2022**, *35*, 100755. https://doi.org/10.1016/j.coche.2021.100755.
(143) Crist, R. D.; Huang, Z.; Guo, R.; Galizia, M. Effect of Thermal Treatment on the Structure and Gas Transport Properties of a Triptycene-Based Polybenzoxazole Exhibiting Configurational Free Volume. *Journal of Membrane Science* **2020**, *597*, 117759. https://doi.org/10.1016/j.memsci.2019.117759.
(144) Corrado, T. J.; Huang, Z.; Huang, D.; Wamble, N.; Luo, T.; Guo, R. Pentiptycene-Based Ladder Polymers with Configurational Free Volume for Enhanced Gas Separation Performance and Physical Aging Resistance. *Proceedings of the National Academy of Sciences* **2021**, *118* (37), e2022204118. https://doi.org/10.1073/pnas.2022204118.
(145) Ben, T.; Ren, H.; Ma, S.; Cao, D.; Lan, J.; Jing, X.; Wang, W.; Xu, J.; Deng, F.; Simmons, J. M.; Qiu, S.; Zhu, G. Targeted Synthesis of a Porous Aromatic Framework with High Stability and Exceptionally High Surface Area. *Angewandte Chemie International Edition* **2009**, *48* (50), 9457–9460. https://doi.org/10.1002/anie.200904637.
(146) Baker, R. W.; Low, B. T. Gas Separation Membrane Materials: A Perspective. *Macromolecules* **2014**, *47* (20), 6999–7013. https://doi.org/10.1021/ma501488s.
(147) Aguilar-Lugo, C.; Lee, W. H.; Miguel, J. A.; de la Campa, J. G.; Prádanos, P.; Bae, J. Y.; Lee, Y. M.; Álvarez, C.; Lozano, Á. E. Highly Permeable Mixed Matrix Membranes of Thermally Rearranged Polymers and Porous Polymer Networks for Gas Separations. *ACS Appl. Polym. Mater.* **2021**, *3* (10), 5224–5235. https://doi.org/10.1021/acsapm.1c01012.
(148) Bastani, D.; Esmaeili, N.; Asadollahi, M. Polymeric Mixed Matrix Membranes Containing Zeolites as a Filler for Gas Separation Applications: A Review. *Journal of Industrial and Engineering Chemistry* **2013**, *19* (2), 375–393. https://doi.org/10.1016/j.jiec.2012.09.019.
(149) Tiwari, R. R.; Smith, Z. P.; Lin, H.; Freeman, B. D.; Paul, D. R. Gas Permeation in Thin Films of "High Free-Volume" Glassy Perfluoropolymers: Part I. Physical Aging. *Polymer* **2014**, *55* (22), 5788–5800. https://doi.org/10.1016/j.polymer.2014.09.022.
(150) Luo, S.; Stevens, K. A.; Park, J. S.; Moon, J. D.; Liu, Q.; Freeman, B. D.; Guo, R. Highly CO2-Selective Gas Separation Membranes Based on Segmented Copolymers of Poly(Ethylene Oxide) Reinforced with Pentiptycene-Containing Polyimide Hard Segments. *ACS Appl. Mater. Interfaces* **2016**, *8* (3), 2306–2317. https://doi.org/10.1021/acsami.5b11355.
(151) Wu, A. X.; Lin, S.; Mizrahi Rodriguez, K.; Benedetti, F. M.; Joo, T.; Grosz, A. F.; Storme, K. R.; Roy, N.; Syar, D.; Smith, Z. P. Revisiting Group Contribution Theory for Estimating Fractional Free Volume of Microporous Polymer Membranes. *Journal of Membrane Science* **2021**, *636*, 119526. https://doi.org/10.1016/j.memsci.2021.119526.
(152) Mahajan, R.; Burns, R.; Schaeffer, M.; Koros, W. J. Challenges in Forming Successful Mixed Matrix Membranes with Rigid Polymeric Materials. *J. Appl. Polym. Sci.* **2002**, *86* (4), 881–890. https://doi.org/10.1002/app.10998.
(153) Dull, T. L.; Frieze, W. E.; Gidley, D. W.; Sun, J. N.; Yee, A. F. Determination of Pore Size in Mesoporous Thin Films from the Annihilation Lifetime of Positronium. *J. Phys. Chem. B* **2001**, *105* (20), 4657–4662. https://doi.org/10.1021/jp004182v.
(154) Tao, S. J. Positronium Annihilation in Molecular Substances. *The Journal of Chemical Physics* **1972**, *56* (11), 5499–5510. https://doi.org/10.1063/1.1677067.

(155) Koschine, T.; Rätzke, K.; Faupel, F.; Khan, M. M.; Emmler, T.; Filiz, V.; Abetz, V.; Ravelli, L.; Egger, W. Correlation of Gas Permeation and Free Volume in New and Used High Free Volume Thin Film Composite Membranes. *J Polym Sci B Polym Phys* **2015**, *53* (3), 213–217. https://doi.org/10.1002/polb.23616.

(156) Wang, X.-Y.; Willmore, F. T.; Raharjo, R. D.; Wang, X.; Freeman, B. D.; Hill, A. J.; Sanchez, I. C. Molecular Simulations of Physical Aging in Polymer Membrane Materials. *J. Phys. Chem. B* **2006**, *110* (33), 16685–16693. https://doi.org/10.1021/jp0622334.

(157) Staiger, C. L.; Pas, S. J.; Hill, A. J.; Cornelius, C. J. Gas Separation, Free Volume Distribution, and Physical Aging of a Highly Microporous Spirobisindane Polymer. *Chem. Mater.* **2008**, *20* (8), 2606–2608. https://doi.org/10.1021/cm071722t.

(158) Yampol'Skii, Yu. P.; Shishatskii, S. M.; Shantorovich, V. P.; Antipov, E. M.; Kuzmin, N. N.; Rykov, S. V.; Khodjaeva, V. L.; Platé, N. A. Transport Characteristics and Other Physicochemical Properties of Aged Poly(1-(Trimethylsilyl)-1-;Propyne). *Journal of Applied Polymer Science* **1993**, *48* (11), 1935–1944. https://doi.org/10.1002/app.1993.070481107.

(159) Consolati, G.; Genco, I.; Pegoraro, M.; Zanderighi, L. Positron Annihilation Lifetime (PAL) in Poly[1-(Trimethyl-Silyl)Propine] (PTMSP): Free Volume Determination and Time Dependence of Permeability. *J. Polym. Sci. B Polym. Phys.* **1996**, *34* (2), 357–367. https://doi.org/10.1002/(SICI)1099-0488(19960130)34:2%253C357::AID-POLB17%253E3.0.CO;2-I.

(160) Struik, L. C. E. Physical Aging in Plastics and Other Glassy Materials. *Polymer Engineering & Science* **1977**, *17* (3), 165–173. https://doi.org/10.1002/pen.760170305.

(161) Nagai, K.; Masuda, T.; Nakagawa, T.; Freeman, B. D.; Pinnau, I. Poly[1-(Trimethylsilyl)-1-Propyne] and Related Polymers: Synthesis, Properties and Functions. *Progress in Polymer Science* **2001**, *26* (5), 721–798. https://doi.org/10.1016/S0079-6700(01)00008-9.

(162) Tsui, N. T.; Paraskos, A. J.; Torun, L.; Swager, T. M.; Thomas, E. L. Minimization of Internal Molecular Free Volume: A Mechanism for the Simultaneous Enhancement of Polymer Stiffness, Strength, and Ductility. *Macromolecules* **2006**, *39* (9), 3350–3358. https://doi.org/10.1021/ma060047q.

(163) Boyer, R. F.; Miller, R. L. Polymer Chain Stiffness Parameter, σ, and Cross-Sectional Area per Chain. *Macromolecules* **1977**, *10* (5), 1167–1169.

(164) Brennan, G.; Bergamino, S.; Pescio, M.; Tofail, S. A. M.; Silien, C. The Effects of a Varied Gold Shell Thickness on Iron Oxide Nanoparticle Cores in Magnetic Manipulation, T1 and T2 MRI Contrasting, and Magnetic Hyperthermia. *Nanomaterials* **2020**, *10* (12), 2424. https://doi.org/10.3390/nano10122424.

(165) Nagai, K.; Watanabe, T.; Nakagawa, T. Effects of Aging on Molecular Motion of Poly(1-Trimethylsilyl-1-Propyne) Membranes Synthesized Using Vanous Catalysts. *Polym J* **1996**, *28* (10), 933–935. https://doi.org/10.1295/polymj.28.933.

(166) Garrido, L.; Benito, E.; López-González, M. Probing In-Situ the Molecular Dynamics of Gas-Poly(1-Trimethylsilyl-1-Propyne) (polyTMSP) Systems with Dielectric and NMR Spectroscopies. *Polymer* **2024**, *290*, 126555. https://doi.org/10.1016/j.polymer.2023.126555.

(167) Hill, A. J.; Pas, S. J.; Bastow, T. J.; Burgar, M. I.; Nagai, K.; Toy, L. G.; Freeman, B. D. Influence of Methanol Conditioning and Physical Aging on Carbon Spin-Lattice Relaxation Times of Poly(1-Trimethylsilyl-1-Propyne). *Journal of Membrane Science* **2004**, *243* (1), 37–44. https://doi.org/10.1016/j.memsci.2004.06.007.

(168) Nakagawa, T.; Watanabe, T.; Mori, M.; Nagai, K. Aging of Gas Permeability in Poly[1-(Trimethylsilyl)-1-Propyne] (PTMSP) and PTMSP-Poly(Tert-Butylacetylene) Blends. In *Polymer Membranes for Gas and Vapor Separation*; ACS Symposium Series; American Chemical Society, 1999; Vol. 733, pp 68–84. https://doi.org/10.1021/bk-1999-0733.ch005.
(169) Garrido, L.; Guzmán, J. Influence of Diffusion Time on the Diffusion Coefficients of Gases in Polymers Determined by Pulsed Gradient Spin Echo NMR. *Macromolecules* **2018**, *51* (21), 8681–8688. https://doi.org/10.1021/acs.macromol.8b02107.
(170) Chiarotti, G.; Cristiani, G.; Giulotto, L. Proton Relaxation in Pure Liquids and in Liquids Containing Paramagnetic Gases in Solution. *Nuovo Cim* **1955**, *1* (5), 863–873. https://doi.org/10.1007/BF02731333.
(171) Merkel, T. C.; He, Z.; Pinnau, I.; Freeman, B. D.; Meakin, P.; Hill, A. J. Effect of Nanoparticles on Gas Sorption and Transport in Poly(1-Trimethylsilyl-1-Propyne). *Macromolecules* **2003**, *36* (18), 6844–6855. https://doi.org/10.1021/ma0341566.
(172) Prabhakar, R. S.; Merkel, T. C.; Freeman, B. D.; Imizu, T.; Higuchi, A. Sorption and Transport Properties of Propane and Perfluoropropane in Poly(Dimethylsiloxane) and Poly(1-Trimethylsilyl-1-Propyne). *Macromolecules* **2005**, *38* (5), 1899–1910. https://doi.org/10.1021/ma048032k.
(173) Cowan, G. *Statistical Data Analysis*; Oxford University Press, 1998.
(174) Loianno, V.; Luo, S.; Zhang, Q.; Guo, R.; Galizia, M. Gas and Water Vapor Sorption and Diffusion in a Triptycene-Based Polybenzoxazole: Effect of Temperature and Pressure and Predicting of Mixed Gas Sorption. *Journal of Membrane Science* **2019**, *574*, 100–111. https://doi.org/10.1016/j.memsci.2018.12.054.
(175) Merkel, T. C.; Bondar, V.; Nagai, K.; Freeman, B. D. Sorption and Transport of Hydrocarbon and Perfluorocarbon Gases in Poly(1-Trimethylsilyl-1-Propyne). *J. Polym. Sci. B Polym. Phys.* **2000**, *38* (2), 273–296. https://doi.org/10.1002/(SICI)1099-0488(20000115)38:2%253C273::AID-POLB1%253E3.0.CO;2-X.
(176) Baker, R. W. *Membrane Technology and Applications*, 3rd ed.; Wiley-Blackwell: Oxford, 2012. https://doi.org/10.1002/9781118359686.
(177) Thompson, K. A.; Mathias, R.; Kim, D.; Kim, J.; Rangnekar, N.; Johnson, J. R.; Hoy, S. J.; Bechis, I.; Tarzia, A.; Jelfs, K. E.; McCool, B. A.; Livingston, A. G.; Lively, R. P.; Finn, M. G. *N* -Aryl–Linked Spirocyclic Polymers for Membrane Separations of Complex Hydrocarbon Mixtures. *Science* **2020**, *369* (6501), 310–315. https://doi.org/10.1126/science.aba9806.
(178) Bruno, N. C.; Mathias, R.; Lee, Y. J.; Zhu, G.; Ahn, Y.-H.; Rangnekar, N. D.; Johnson, J. R.; Hoy, S.; Bechis, I.; Tarzia, A.; Jelfs, K. E.; McCool, B. A.; Lively, R.; Finn, M. G. Solution-Processable Polytriazoles from Spirocyclic Monomers for Membrane-Based Hydrocarbon Separations. *Nat. Mater.* **2023**, *22* (12), 1540–1547. https://doi.org/10.1038/s41563-023-01682-2.
(179) Alduraiei, F.; Manchanda, P.; Pulido, B.; Szekely, G.; Nunes, S. P. Fluorinated Thin-Film Composite Membranes for Nonpolar Organic Solvent Nanofiltration. *Separation and Purification Technology* **2021**, *279*, 119777. https://doi.org/10.1016/j.seppur.2021.119777.
(180) Vanherck, K.; Vandezande, P.; Aldea, S. O.; Vankelecom, I. F. J. Cross-Linked Polyimide Membranes for Solvent Resistant Nanofiltration in Aprotic Solvents. *Journal of Membrane Science* **2008**, *320* (1), 468–476. https://doi.org/10.1016/j.memsci.2008.04.026.

(181) Karan, S.; Jiang, Z.; Livingston, A. G. Sub–10 Nm Polyamide Nanofilms with Ultrafast Solvent Transport for Molecular Separation. *Science* **2015**, *348* (6241), 1347–1351. https://doi.org/10.1126/science.aaa5058.
(182) Feliachi, Y.; Roy, A.; Ren, Y.; Finn, M. G.; Lively, R. P. Solid-State Crosslinking of Thin Film Composite Membranes for Organic Solvent Reverse Osmosis Separations. *Journal of Membrane Science* **2024**, *695*, 122462. https://doi.org/10.1016/j.memsci.2024.122462.
(183) Ren, Y.; Ma, H.; Kim, J.; Al Otmi, M.; Lin, P.; Dai, C.; Lee, Y. J.; Zhai, Z.; Jang, W. J.; Yang, S.; Sarswat, A.; Feliachi, Y.; Sampath, J.; Realff, M. J.; Lively, R. P.; Guo, S. Fluorine-Rich Poly(Arylene Amine) Membranes for the Separation of Liquid Aliphatic Compounds. *Science* **2025**, *387* (6730), 208–214. https://doi.org/10.1126/science.adp2619.
(184) Lee, T. H.; Balcik, M.; Wu, W.-N.; Pinnau, I.; Smith, Z. P. Dual-Phase Microporous Polymer Nanofilms by Interfacial Polymerization for Ultrafast Molecular Separation. *Science Advances* **2024**, *10* (33), eadp6666. https://doi.org/10.1126/sciadv.adp6666.
(185) Giordano, M. Uncertainty Propagation with Functionally Correlated Quantities. arXiv October 27, 2016. https://doi.org/10.48550/arXiv.1610.08716.
(186) Sholl, D. S.; Lively, R. P. Exemplar Mixtures for Studying Complex Mixture Effects in Practical Chemical Separations. *JACS Au* **2022**, *2* (2), 322–327. https://doi.org/10.1021/jacsau.1c00490.
(187) Cook, M.; Gaffney, P. R. J.; Peeva, L. G.; Livingston, A. G. Roll-to-Roll Dip Coating of Three Different PIMs for Organic Solvent Nanofiltration. *Journal of Membrane Science* **2018**, *558*, 52–63. https://doi.org/10.1016/j.memsci.2018.04.046.
(188) Fritsch, D.; Merten, P.; Heinrich, K.; Lazar, M.; Priske, M. High Performance Organic Solvent Nanofiltration Membranes: Development and Thorough Testing of Thin Film Composite Membranes Made of Polymers of Intrinsic Microporosity (PIMs). *Journal of Membrane Science* **2012**, *401–402*, 222–231. https://doi.org/10.1016/j.memsci.2012.02.008.
(189) See Toh, Y. H.; Lim, F. W.; Livingston, A. G. Polymeric Membranes for Nanofiltration in Polar Aprotic Solvents. *Journal of Membrane Science* **2007**, *301* (1), 3–10. https://doi.org/10.1016/j.memsci.2007.06.034.
(190) Jang, H.; Johnson, J. R.; Ma, Y.; Mathias, R.; Bhandari, D. A.; Lively, R. P. Torlon® Hollow Fiber Membranes for Organic Solvent Reverse Osmosis Separation of Complex Aromatic Hydrocarbon Mixtures. *AIChE Journal* **2019**, *65* (12), e16757. https://doi.org/10.1002/aic.16757.
(191) Luo, S.; Zhang, Q.; Zhu, L.; Lin, H.; Kazanowska, B. A.; Doherty, C. M.; Hill, A. J.; Gao, P.; Guo, R. Highly Selective and Permeable Microporous Polymer Membranes for Hydrogen Purification and CO2 Removal from Natural Gas. *Chem. Mater.* **2018**, *30* (15), 5322–5332. https://doi.org/10.1021/acs.chemmater.8b02102.
(192) Marshall, B. D.; Johnson, J. R.; Lee, Y. J.; Moser, D.; Lively, R. P. Organic Solvent Reverse Osmosis Separations of Hydrocarbon-Alcohol Mixtures Using Matrimid Membranes. *Journal of Membrane Science* **2024**, *689*, 122168. https://doi.org/10.1016/j.memsci.2023.122168.
(193) Lee, Y. J.; Chen, L.; Nistane, J.; Jang, H. Y.; Weber, D. J.; Scott, J. K.; Rangnekar, N. D.; Marshall, B. D.; Li, W.; Johnson, J. R.; Bruno, N. C.; Finn, M. G.; Ramprasad, R.; Lively, R. P. Data-Driven Predictions of Complex Organic Mixture Permeation in Polymer Membranes. *Nat Commun* **2023**, *14* (1), 4931. https://doi.org/10.1038/s41467-023-40257-2.

(194) Charville, H.; Jackson, D. A.; Hodges, G.; Whiting, A.; Wilson, M. R. The Uncatalyzed Direct Amide Formation Reaction – Mechanism Studies and the Key Role of Carboxylic Acid H-Bonding. *Eur J Org Chem* **2011**, *2011* (30), 5981–5990. https://doi.org/10.1002/ejoc.201100714.
(195) Charville, H.; Jackson, D.; Hodges, G.; Whiting, A. The Thermal and Boron-Catalysed Direct Amide Formation Reactions: Mechanistically Understudied yet Important Processes. *Chem. Commun.* **2010**, *46* (11), 1813–1823. https://doi.org/10.1039/B923093A.
(196) Mitchell, J. A.; Reid, E. Emmet. THE PREPARATION OF ALIPHATIC AMIDES. *J. Am. Chem. Soc.* **1931**, *53* (5), 1879–1883. https://doi.org/10.1021/ja01356a037.
(197) March's Advanced Organic Chemistry: Reactions, Mechanisms and Structure, 5th Ed by M. B. Smith and J. March. Wiley Interscience: New York. 2001. 2112 Pp. $69.95. ISBN 0-471-58589-0. *Org. Process Res. Dev.* **2001**, *5* (6), 669–669. https://doi.org/10.1021/op010074a.
(198) Allen, C. L.; Chhatwal, A. R.; Williams, J. M. J. Direct Amide Formation from Unactivated Carboxylic Acids and Amines. *Chem. Commun.* **2011**, *48* (5), 666–668. https://doi.org/10.1039/C1CC15210F.
(199) Jursic, B. S.; Zdravkovski, Z. A Simple Preparation of Amides from Acids and Amines by Heating of Their Mixture. *Synthetic Communications* **1993**, *23* (19), 2761–2770. https://doi.org/10.1080/00397919308013807.
(200) Zhou, S.; Zhao, Y.; Zheng, J.; Zhang, S. High-Performance Functionalized Polymer of Intrinsic Microporosity (PIM) Composite Membranes with Thin and Stable Interconnected Layer for Organic Solvent Nanofiltration. *Journal of Membrane Science* **2019**, *591*, 117347. https://doi.org/10.1016/j.memsci.2019.117347.
(201) Mackie, J. S.; Meares, P. The Diffusion of Electrolytes in a Cation-Exchange Resin Membrane I. Theoretical. *Theoretical Proc. R. Soc. London, Ser. A* **1955**, *232* (1191), 498–509.
(202) Jung, D.; Chen, Z.; Alayoglu, S.; Mian, M. R.; Goetjen, T. A.; Idrees, K. B.; Kirlikovali, K. O.; Islamoglu, T.; Farha, O. K. Postsynthetically Modified Polymers of Intrinsic Microporosity (PIMs) for Capturing Toxic Gases. *ACS Appl. Mater. Interfaces* **2021**, *13* (8), 10409–10415. https://doi.org/10.1021/acsami.0c21741.
(203) Bevington, P. R. *Data Reduction and Error Analysis for the Physical Sciences*; McGraw-Hill: London, 1969.
(204) Torchia, D. A. The Measurement of Proton-Enhanced Carbon-13 T1 Values by a Method Which Suppresses Artifacts. *Journal of Magnetic Resonance (1969)* **1978**, *30* (3), 613–616. https://doi.org/10.1016/0022-2364(78)90288-3.
(205) Giordano, M. Uncertainty Propagation with Functionally Correlated Quantities. *arXiv:1610.08716 [physics]* **2016**.
(206) Kansy, J. Microcomputer Program for Analysis of Positron Annihilation Lifetime Spectra. *Nuclear Instruments and Methods in Physics Research Section A: Accelerators, Spectrometers, Detectors and Associated Equipment* **1996**, *374* (2), 235–244. https://doi.org/10.1016/0168-9002(96)00075-7.
(207) Pascual-Izarra, C.; Dong, A. W.; Pas, S. J.; Hill, A. J.; Boyd, B. J.; Drummond, C. J. Advanced Fitting Algorithms for Analysing Positron Annihilation Lifetime Spectra. *Nuclear Instruments and Methods in Physics Research Section A: Accelerators, Spectrometers,*

Detectors and Associated Equipment **2009**, *603* (3), 456–466. https://doi.org/10.1016/j.nima.2009.01.205.
(208) Bondi, A. A. Physical Properties of Molecular Crystals, Liquids, and Glasses. *(No Title)*.
(209) Toy, L. G.; Nagai, K.; Freeman, B. D.; Pinnau, I.; He, Z.; Masuda, T.; Teraguchi, M.; Yampolskii, Yu. P. Pure-Gas and Vapor Permeation and Sorption Properties of Poly[1-Phenyl-2-[p-(Trimethylsilyl)Phenyl]Acetylene] (PTMSDPA). *Macromolecules* **2000**, *33* (7), 2516–2524. https://doi.org/10.1021/ma991566e.
(210) Schmid, N.; Eichenberger, A. P.; Choutko, A.; Riniker, S.; Winger, M.; Mark, A. E.; Van Gunsteren, W. F. Definition and Testing of the GROMOS Force-Field Versions 54A7 and 54B7. *Eur Biophys J* **2011**, *40* (7), 843–856. https://doi.org/10.1007/s00249-011-0700-9.
(211) Automated Topology Builder (ATB) and Repository. https://atb.uq.edu.au.
(212) Chen, B.; Siepmann, J. I. Transferable Potentials for Phase Equilibria. 3. Explicit-Hydrogen Description of Normal Alkanes. *J. Phys. Chem. B* **1999**, *103* (25), 5370–5379. https://doi.org/10.1021/jp990822m.
(213) Cygan, R. T.; Romanov, V. N.; Myshakin, E. M. Molecular Simulation of Carbon Dioxide Capture by Montmorillonite Using an Accurate and Flexible Force Field. *J. Phys. Chem. C* **2012**, *116* (24), 13079–13091. https://doi.org/10.1021/jp3007574.
(214) Essmann, U.; Perera, L.; Berkowitz, M. L.; Darden, T.; Lee, H.; Pedersen, L. G. A Smooth Particle Mesh Ewald Method. *The Journal of Chemical Physics* **1995**, *103* (19), 8577–8593. https://doi.org/10.1063/1.470117.
(215) Allen, M. P.; Tildesley, D. J. *Computer Simulation of Liquids*; Oxford University Press, 2017.
(216) Van Der Spoel, D.; Lindahl, E.; Hess, B.; Groenhof, G.; Mark, A. E.; Berendsen, H. J. C. GROMACS: Fast, Flexible, and Free. *J Comput Chem* **2005**, *26* (16), 1701–1718. https://doi.org/10.1002/jcc.20291.
(217) Hess, B.; Kutzner, C.; Van Der Spoel, D.; Lindahl, E. GROMACS 4: Algorithms for Highly Efficient, Load-Balanced, and Scalable Molecular Simulation. *J. Chem. Theory Comput.* **2008**, *4* (3), 435–447. https://doi.org/10.1021/ct700301q.
(218) Hockney, R. W.; Goel, S. P.; Eastwood, J. W. Quiet High-Resolution Computer Models of a Plasma. *Journal of Computational Physics* **1974**, *14* (2), 148–158. https://doi.org/10.1016/0021-9991(74)90010-2.
(219) Nosé, S. A Molecular Dynamics Method for Simulations in the Canonical Ensemble. *Molecular Physics* **1984**, *52* (2), 255–268. https://doi.org/10.1080/00268978400101201.
(220) Hoover, W. G. Canonical Dynamics: Equilibrium Phase-Space Distributions. *Phys. Rev. A* **1985**, *31* (3), 1695–1697. https://doi.org/10.1103/PhysRevA.31.1695.
(221) Parrinello, M.; Rahman, A. Polymorphic Transitions in Single Crystals: A New Molecular Dynamics Method. *Journal of Applied Physics* **1981**, *52* (12), 7182–7190. https://doi.org/10.1063/1.328693.
(222) Kinaci, A.; Haskins, J. B.; Çağın, T. On Calculation of Thermal Conductivity from Einstein Relation in Equilibrium Molecular Dynamics. *The Journal of Chemical Physics* **2012**, *137* (1), 014106. https://doi.org/10.1063/1.4731450.
(223) Yampol'Skii, Yu. P.; Shishatskii, S. M.; Shantorovich, V. P.; Antipov, E. M.; Kuzmin, N. N.; Rykov, S. V.; Khodjaeva, V. L.; Platé, N. A. Transport Characteristics and Other Physicochemical Properties of Aged Poly(1-(Trimethylsilyl)-1-;Propyne). *Journal of Applied Polymer Science* **1993**, *48* (11), 1935–1944. https://doi.org/10.1002/app.1993.070481107.

(224) K Mogensen, P.; N Riseth, A. Optim: A Mathematical Optimization Package for Julia. *JOSS* **2018**, *3* (24), 615. https://doi.org/10.21105/joss.00615.
(225) Zhu, C.; Byrd, R. H.; Lu, P.; Nocedal, J. Algorithm 778: L-BFGS-B: Fortran Subroutines for Large-Scale Bound-Constrained Optimization. *ACM Trans. Math. Softw.* **1997**, *23* (4), 550–560. https://doi.org/10.1145/279232.279236.
(226) Kochenderfer, M. J.; Wheeler, T. A. Algorithms for Optimization.
(227) Kwong, T. *Hands-on Design Patterns and Best Practices with Julia: Proven Solutions to Common Problems in Software Design for Julia 1.x*; Packt: Birmingham Mumbai, 2020.
(228) Caceci, M. S. Estimating Error Limits in Parametric Curve Fitting. *Anal. Chem.* **1989**, *61* (20), 2324–2327. https://doi.org/10.1021/ac00195a023.
(229) Tellinghuisen, J. Statistical Error Propagation. *J. Phys. Chem. A* **2001**, *105* (15), 3917–3921. https://doi.org/10.1021/jp003484u.
(230) Rice, F. *Physical Data Analysis, A Primer*; 2018.
(231) Eldrup, M.; Lightbody, D.; Sherwood, J. N. The Temperature Dependence of Positron Lifetimes in Solid Pivalic Acid. *Chemical Physics* **1981**, *63* (1), 51–58. https://doi.org/10.1016/0301-0104(81)80307-2.
(232) Pascual-Izarra, C.; Dong, A. W.; Pas, S. J.; Hill, A. J.; Boyd, B. J.; Drummond, C. J. Advanced Fitting Algorithms for Analysing Positron Annihilation Lifetime Spectra. *Nuclear Instruments and Methods in Physics Research Section A: Accelerators, Spectrometers, Detectors and Associated Equipment* **2009**, *603* (3), 456–466. https://doi.org/10.1016/j.nima.2009.01.205.
(233) Low, Z.-X.; Shen, J. Determining Stability of Organic Solvent Nanofiltration Membranes by Cross-Flow Aging. *Separation and Purification Technology* **2021**, *256*, 117840. https://doi.org/10.1016/j.seppur.2020.117840.
(234) Shi, G. M.; Davood Abadi Farahani, M. H.; Liu, J. Y.; Chung, T.-S. Separation of Vegetable Oil Compounds and Solvent Recovery Using Commercial Organic Solvent Nanofiltration Membranes. *Journal of Membrane Science* **2019**, *588*, 117202. https://doi.org/10.1016/j.memsci.2019.117202.
(235) Paul, D. R.; Ebra-Lima, O. M. The Mechanism of Liquid Transport through Swollen Polymer Membranes. *Journal of Applied Polymer Science* **1971**, *15* (9), 2199–2210. https://doi.org/10.1002/app.1971.070150912.
(236) Paul, D. R.; Ebra-Lima, O. M. Pressure-Induced Diffusion of Organic Liquids through Highly Swollen Polymer Membranes. *Journal of Applied Polymer Science* **1970**, *14* (9), 2201–2224. https://doi.org/10.1002/app.1970.070140903.
(237) Paul, D. R.; Carranza, D. H. Pressure-Induced Diffusion in Swollen Butyl Rubber Membranes. *Journal of Polymer Science: Polymer Symposia* **1973**, *41* (1), 69–78. https://doi.org/10.1002/polc.5070410108.
(238) Friess, K.; Jansen, J. C.; Vopička, O.; Randová, A.; Hynek, V.; Šípek, M.; Bartovská, L.; Izák, P.; Dingemans, M.; Dewulf, J.; Van Langenhove, H.; Drioli, E. Comparative Study of Sorption and Permeation Techniques for the Determination of Heptane and Toluene Transport in Polyethylene Membranes. *Journal of Membrane Science* **2009**, *338* (1), 161–174. https://doi.org/10.1016/j.memsci.2009.04.030.
(239) Ben Soltane, H.; Roizard, D.; Favre, E. Effect of Pressure on the Swelling and Fluxes of Dense PDMS Membranes in Nanofiltration: An Experimental Study. *Journal of Membrane Science* **2013**, *435*, 110–119. https://doi.org/10.1016/j.memsci.2013.01.053.

(240) Galizia, M.; Paul, D. R.; Freeman, B. D. Liquid Methanol Sorption, Diffusion and Permeation in Charged and Uncharged Polymers. *Polymer* **2016**, *102*, 281–291. https://doi.org/10.1016/j.polymer.2016.09.010.
(241) Yushkin, A. A.; Anokhina, T. S.; Bazhenov, S. D.; Borisov, I. L.; Budd, P. M.; Volkov, A. V. Sorption and Nanofiltration Characteristics of PIM-1 Material in Polar and Non-Polar Solvents. *Pet. Chem.* **2018**, *58* (13), 1154–1158. https://doi.org/10.1134/S096554411813011X.